agriculture

Special Issue Reprint

Precision Planting Technology and Equipment in Advanced Crop Cultivation

Edited by
Xiaojun Gao, Qinghui Lai and Tao Cui

mdpi.com/journal/agriculture

MDPI

Precision Planting Technology and Equipment in Advanced Crop Cultivation

Precision Planting Technology and Equipment in Advanced Crop Cultivation

Guest Editors

Xiaojun Gao
Qinghui Lai
Tao Cui

MDPI

Basel • Beijing • Wuhan • Barcelona • Belgrade • Novi Sad • Cluj • Manchester

Guest Editors
Xiaojun Gao
College of Engineering
Nanjing Agricultural University
Nanjing
China

Qinghui Lai
School of Energy and Environment Science
Yunnan Normal University
Kunming
China

Tao Cui
College of Engineering
China Agricultural University
Beijing
China

Editorial Office
MDPI AG
Grosspeteranlage 5
4052 Basel, Switzerland

This is a reprint of the Special Issue, published open access by the journal *Agriculture* (ISSN 2077-0472), freely accessible at: https://www.mdpi.com/journal/agriculture/special_issues/J881G82LXU.

For citation purposes, cite each article independently as indicated on the article page online and as indicated below:

Lastname, A.A.; Lastname, B.B. Article Title. *Journal Name* **Year**, *Volume Number*, Page Range.

ISBN 978-3-7258-3893-6 (Hbk)
ISBN 978-3-7258-3894-3 (PDF)
https://doi.org/10.3390/books978-3-7258-3894-3

Contents

agriculture

Article

Design and Testing of Electric Drive System for Maize Precision Seeder

Lin Ling [1,†], Yuejin Xiao [2,3,†], Xinguang Huang [2,3], Guangwei Wu [3,4], Liwei Li [3,4], Bingxin Yan [3,*] and Duanyang Geng [2,*]

1 College of Engineering and Technology, Southwest University, Chongqing 400716, China; mike-lin0923@outlook.com
2 School of Agricultural Engineering and Food Science, Shandong University of Technology, Zibo 255049, China; xiaoyj@nercita.org.cn (Y.X.); delicate-521@outlook.com (X.H.)
3 Intelligent Equipment Research Center, Beijing Academy of Agriculture and Forestry Sciences, Beijing 100097, China; wugw@nercita.org.cn (G.W.); lilw@nercita.org.cn (L.L.)
4 State Key Laboratory of Intelligent Agricultural Power Equipment, Beijing 100097, China
* Correspondence: yanbx@nercita.org.cn (B.Y.); dygxt@sdut.edu.cn (D.G.)
† These authors contributed equally to this work.

Abstract: To improve the expandability, seeding accuracy, and operating speed range of the electric drive system (EDS) of precision seeders, this study constructed an EDS based on a controller area network (CAN) bus and designed a motor controller based on a field-orientated control (FOC) algorithm. Full-factorial bench and field tests based on seed spacing (0.1, 0.2, and 0.3 m) and operating speed (3, 6, 9, 12, and 15 km/h) were carried out to evaluate the performance of the EDS. The results of bench tests showed that seeding quality varied inversely with operating speed and positively with seed spacing. The average quality of feed index (QFI) at 0.1, 0.2, and 0.3 m seed spacing in bench tests was 88.38%, 96.67%, and 97.36%, with the average coefficient of variation (CV) being 20.13%, 16.27%, and 13.20%. Analysis of variance confirmed that both operating speed and seed spacing had a significant effect on QFI and CV ($p < 0.001$). The analysis of motor rotational speed accuracy showed that the relative error of motor rotational speed above 410 rpm did not exceed 2.24%, and the relative error had less influence on the seeding quality. The average QFI was 85.93%, 95.91%, and 96.24%, with the average CV being 21.12%, 15.50%, and 16.49% at 0.1, 0.2, and 0.3 m seed spacing in field tests. The methods and results of this study can provide a reference for the design and optimization of the EDS in a maize precision seeder and provide an effective solution for the improvement of maize yields.

Keywords: CAN bus; field-orientated control; electric drive system; seeding quality; maize

Citation: Ling, L.; Xiao, Y.; Huang, X.; Wu, G.; Li, L.; Yan, B.; Geng, D. Design and Testing of Electric Drive System for Maize Precision Seeder. *Agriculture* **2024**, *14*, 1778. https://doi.org/10.3390/agriculture14101778

Academic Editor: Maohua Xiao

Received: 10 September 2024
Revised: 1 October 2024
Accepted: 2 October 2024
Published: 9 October 2024

1. Introduction

Land desertification and population growth have left most countries facing a severe food shortage in the future [1,2]. In this context, improving crop yields has become one of the important research hotspots at present [3–5]. Of the many ways to increase yields, improving seed spacing uniformity is especially critical [4,6,7]. The main reason for this is that seed spacing uniform effectively reduces competition for water, nutrients, and light during seed growth and development, which in turn results in higher yields and increased returns [8–12].

A precision seeder is the main carrier to achieve uniformity in seed spacing, and its seed spacing uniformity can effectively ensure a yield [13]. Traditional precision seeders use a mechanical drive system (MDS) to achieve the rotation of the seed meter plate. The MDS consists of a ground wheel, chain, and sprocket. Ground wheel slippage and chain jumping in MDS lead to fluctuations in the rotational speed of the seed meter plate, which in turn can lead to poor seeding quality in precision seeders [13–15]. In order to improve the impact of MDSs, EDSs with electric motors as drive elements have become a current research hotspot [2,16].

EDSs are common in developed countries [16]. The EDS developed by Horsch of Germany can achieve an operating speed of 15 km/h while ensuring seeding quality [17]. The vDrive motor developed by American Precision planting company can meet the operation demand of 16 km/h, which greatly improves the operation efficiency [18]. In Italy, the company Maschio launched the CHRONO high-speed seeder with an EDS that can achieve seeding in 15 km/h [19]. The above EDSs meet the high-speed requirements at the same time, with the use of a controller area network (CAN) bus based on the ISOBUS 11783 protocol, which can achieve the expansion of different rows of seeders, further improving the scope of their application. Meanwhile, the EDS with advanced motor control algorithm ensures seed spacing uniformity.

The widespread use of precision seeders with an MDS in developing countries is a serious constraint on increasing yields and is not conducive to improving farmers' incomes and ameliorating possible future food shortages. Although the use of EDSs in developing countries in applications is relatively lacking, their superiority has attracted the attention of many researchers. Yang et al. [20] designed an EDS for a four-row precision seeder and carried out experiments, and the results of these experiments showed that under the three operating speeds of 9, 11, and 12 km/h, the quality of feed index (QFI) of the EDS was increased by an average of 4.7% compared with that of the MDS, and the miss index (MI) was reduced by an average of 3.54%, which proved that the EDS was better adapted to seeding. Cay et al. [21] found that the EDS had a lower fuel consumption, with a 22% year-over-year reduction in fuel consumption. In the above studies, EDSs were designed and found to be advantageous, but the expandability of the system was not considered, and the designed EDSs were only adapted to seeders with the corresponding number of rows. Therefore, He et al. [22], Ding et al. [23], and Yang et al. [24], on the other hand, designed an expandable EDS based on a CAN bus to adapt to different rows of seeders. However, they neglected the improvement of seeding quality by the control algorithm. Also, the operating speeds in the above EDS were within 12 km/h, and high-speed operating situations were not considered. Du et al. [25] designed an electric drive unit, and bench experiments were conducted to compare the effects of square wave control and field-orientated control (FOC) algorithms on motor control and seeding quality, and the results proved that the FOC algorithm could achieve a higher seeding quality by virtue of its good rotational speed accuracy. However, they did not apply the algorithm to the actual EDS, and there is still a large upside in terms of the seeding quality.

The high cost of products of developed countries has prevented EDSs from spreading rapidly in developing countries. Moreover, the EDS in developing countries is deficient in terms of expandability, seeding accuracy, and operating speed. Therefore, the adaptability and high efficiency of the EDS cannot be further improved, which could be the main reason limiting the rapid promotion and application of EDSs in developing countries.

In order to solve the above problems, this study aims to achieve the following objectives: (1) construct an expandable EDS based on a CAN bus to adapt to maize seeders with different row units; (2) design a motor controller based on the FOC algorithm for precise control of the motor rotational speed; (3) conduct an testing study to validate the system performance.

2. Materials and Methods

2.1. System Components

The EDS structure is shown in Figure 1. The EDS consists of a master control unit, a seeder lift status detection unit, and several seeding control units. The master control unit includes an Android terminal (Nongxin Technology Co., Ltd., Beijing, China), a GNSS antenna, and a 4G antenna, which is mainly responsible for receiving satellite signals, network signals and human–machine interaction. The seeder lift status detection unit includes a seeder lift status detection controller and a travel switch, which is mainly responsible for detecting the lift and fall status of the seeder. The seeding control unit includes a permanent magnet synchronous motor (PMSM) (Nongxin Technology Co., Ltd., Beijing, China), a motor controller, and an air-suction seed meter (Shandong Dahua Machinery Co., Ltd., Jining, China), and the PMSM is coaxially connected to the seed meter. The motor controller is installed at the end of the motor. Communication between the motor controllers and the terminal via the CAN bus allows the EDS to be adapted to precision seeders with different row units. The 120 Ω termination resistors at both ends of the CAN bus are used for impedance matching to improve the CAN bus interference immunity.

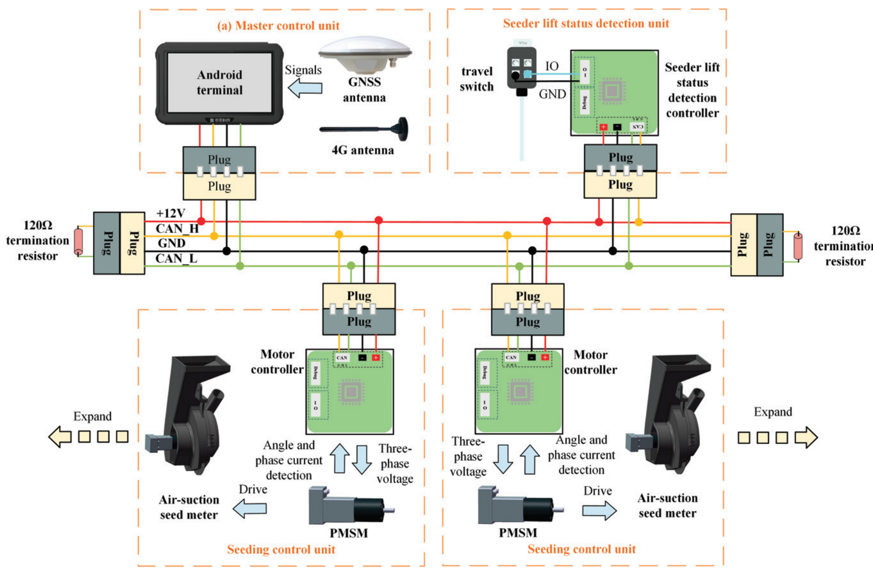

Figure 1. Structure of the EDS. Solid lines indicate connecting lines; dashed lines indicate system component units; notes are labeled near arrows and lines.

When the motor rotates, the seed meter plate connected to the motor rotates synchronously. The reduction ratio between the two is 32, and the diameter of the seed meter plate is 220 mm. The seeds are adsorbed on the seed meter plate (4.5 mm in diameter) under the action of negative pressure (4 to 6 kPa) and then pass through the double-sided seed-cleaning knives to scrape off the excess seeds. The seeds are finally transported to a seed feeding point, which operates without negative pressure, and placed into the seed tube under the influence of gravity and initial speed.

2.2. Working Principle

The working principle of the EDS is shown in Figure 2. The seeder lift status detection controller obtains the status of the tractor's three-point suspension bar according to the travel switch and then identifies the seeder lift status and sends it to the CAN bus. The Android terminal, as the main controller, acquires the operational speed of the seeder through the built-in board, external GNSS antenna, and 4G antenna in network RTK mode and calculates the target rotational speed of the motor according to the seeding parameters based on Equation (1). At the same time, the terminal also receives the seeder lift status, and, in combination with the motor start/stop status input by the user, it determines the enable state of each motor and sends it, together with the motor target rotational speed, to the CAN bus.

$$R_m = \frac{50vi}{3n_{\mathfrak{p}}d} \tag{1}$$

where R_m is the motor target rotational speed, rpm; v is the operating speed, km/h; i is the reduction ratio between the motor and the seed meter, 32; n_{p} is the number of holes in the seed meter plate, 26; and d is the seed spacing, m.

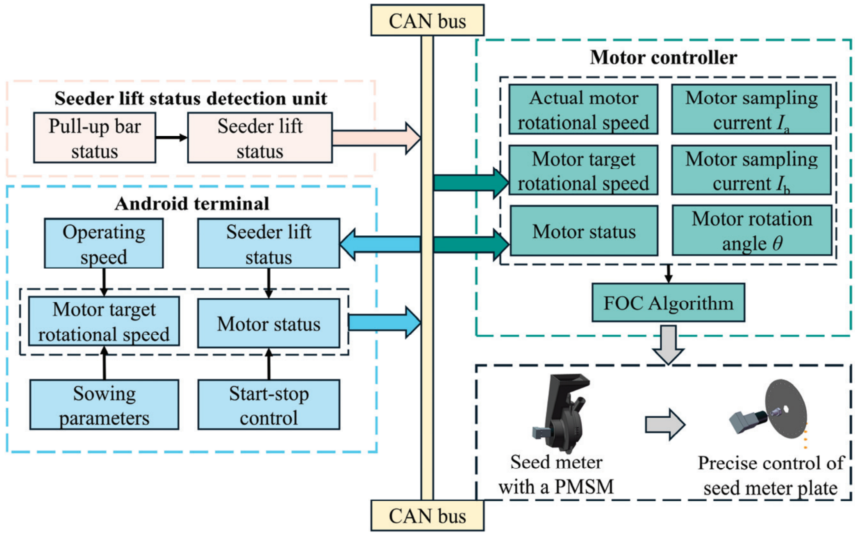

Figure 2. Working principle of the EDS.

2.3. Design of Communication Protocol

The communication protocol of the EDS is developed with reference to the ISO 11783 protocol. The ISO 11783 protocol is an international standard for communication between agricultural machinery and equipment [26]. The protocol data unit (PDU) is the basic unit of transmission in ISO 11783 [24]. The PDU consists of seven parts including the priority (P), reserved bit (R), data page (DP), protocol data unit format (PF), protocol specific data unit (PS), source address (SA), and data domain [27]. With reference to ISO 11783 regulations and the EDS architecture, the PDU information of the EDS is shown in Table 1.

Table 1. PDU information.

Equipment	P	R	DP	PF	PS	SA	Parameter Group PCN	PDU Identification
Controller	6	0	0	0xFF	0x22	0x80	00FF22	18FF2280
Android terminal	2	0	0	0xFF	0x23	0x26	00FF23	18FF2326

The data domain hosts the actual application data. According to the PDU identification, the EDS uses single-frame mode to transmit data, and the protocol is shown in Table 2. Among them, the row number is used to distinguish the type of controller; '0' means the seeder lift status detection sensor, '1' means the motor controller in the first row, '2' means the motor controller in the second row, and other sequential analogous types of controller.

Table 2. Data domain protocols.

Device	Byte1	Byte2	Byte3	Byte4	Byte5	Byte6	Byte7	Byte8
Controller	/	Row number	Motor/seeder lift status	Motor actual rotational speed		Motor target rotational speed		/
Android terminal	/	Row number	Motor status	Motor target rotational speed		/	/	/

2.4. Field-Orientated Control Algorithm

The schematic diagram of the FOC algorithm is shown in Figure 3. The currents I_a and I_b of PMSM are obtained by a current sampling process, and the current I_c can be obtained based on Kirchhoff's Law, as shown in Equation (2).

$$I_c = -(I_a + I_b) \tag{2}$$

The two currents are transformed by Clark's transformation to obtain the orthogonal axis currents I_α and I_β for the α-β coordinate system, and I_α, I_β are transformed by Park transformation to obtain the orthogonal axis currents I_{q} and I_{d} for the q-d coordinate system. I_{q} is the torque current component, and I_{d} is the excitation current component. Therefore, the target value of I_{d}, $I_{\text{d\_ref}}$, is usually set to zero for torque maximization. The difference between the actual rotational speed, speed_act, obtained by the sensor and the target rotational speed, speed_ref, is fed into the PI controller to find the quadrature axis current I_{q} reference value $I_{\text{q\_ref}}$. The actual ($I_{\text{q\_act}}$, $I_{\text{d\_act}}$) and reference ($I_{\text{q\_ref}}$, $I_{\text{d\_ref}}$) values of I_{q} and I_{d} are fed into the PI controller to find the quadrature axis voltages U_q and U_d, respectively. U_q and U_d are subjected to inverse Park transformation to obtain U_α and U_β for the α-β coordinate system, which are subjected to space voltage vector pulse width modulation (SVPWM) to obtain target voltage vectors (U_{a}, U_{b}, U_{c}) to achieve the FOC of the PMSM.

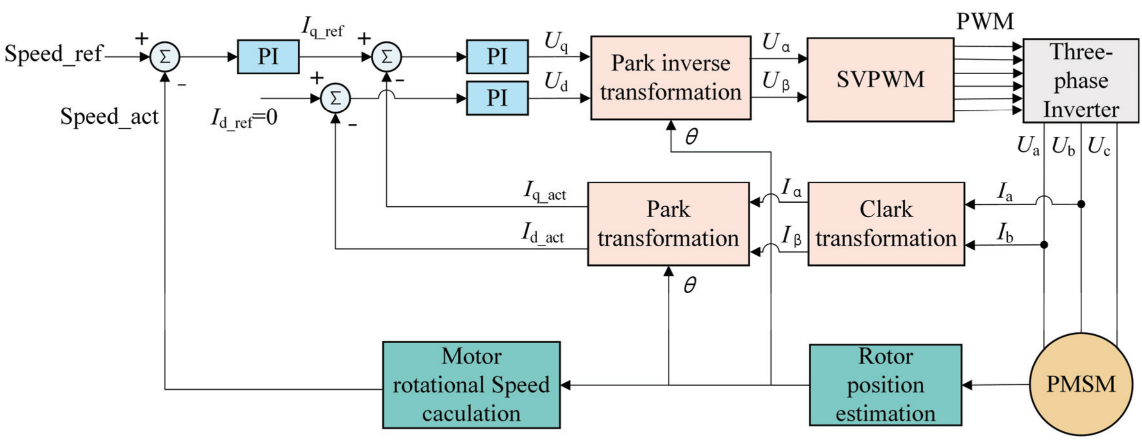

Figure 3. Schematic diagram of the FOC algorithm.

2.4.1. Coordinate Transformation

Coordinate transformation is used to solve the problem of the difficult calculation of AC quantities such as the voltage, current, and magnetic chain in the stator. The currents (I_a, I_b, I_c) in a three-phase stationary coordinate system (abc) are first projectively transformed into the two-phase orthogonal currents I_α and I_β in the two-phase stationary coordinate system (α-β) [25], as shown in Figure 4.

The relationship between the currents is shown in Equation (3).

$$\begin{bmatrix} I_\alpha \\ I_\beta \end{bmatrix} = \frac{2}{3}\begin{bmatrix} 1 & -\frac{1}{2} & -\frac{1}{2} \\ 0 & \frac{\sqrt{3}}{2} & -\frac{\sqrt{3}}{2} \end{bmatrix}\begin{bmatrix} I_a \\ I_b \\ I_c \end{bmatrix} \tag{3}$$

For the convenience of describing the motion of the rotor, I_α and I_β are projected onto the two-phase rotating coordinate system (q-d), as shown in Figure 5. Where θ is the rotation angle of the rotor, its value can be obtained by the sensor.

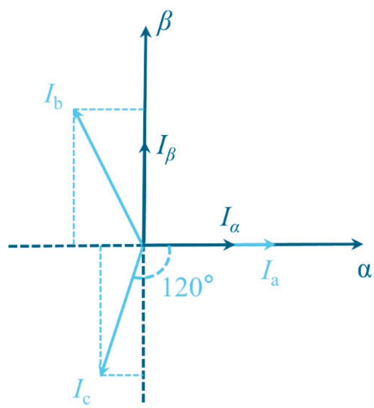

Figure 4. Two-phase stationary coordinate system.

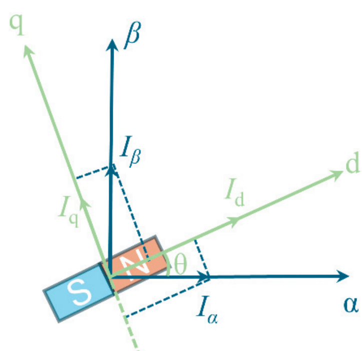

Figure 5. Two-phase rotating coordinate system.

The U_q and U_d in the qd coordinate system can be calculated by Equation (4), which is also known as the Park transformation.

$$\begin{bmatrix} U_d \\ U_q \end{bmatrix} = \begin{bmatrix} \cos\theta & \sin\theta \\ -\sin\theta & \cos\theta \end{bmatrix} \begin{bmatrix} U_a \\ U_\beta \end{bmatrix} \tag{4}$$

2.4.2. Space Voltage Vector Pulse Width Modulation

SVPWM outputs different space voltage vectors to drive the motor rotation by controlling the conduction of the MOSFET (Q1~Q6) in the three-phase inverter circuit (Figure 6) [28]. The three-phase inverter circuit consists of three sets of bridge arms, each of which contains two MOSFET arranged in upper and lower positions. There are eight combinations of upper and lower bridge arm switching, corresponding to eight space voltage vectors, including six non-zero vectors, U_1, U_2, U_3, U_4, U_5, and U_6, and two zero vectors, U_0 and U_7.

The magnitudes and positions of the eight space voltage vectors in the stationary coordinate system are shown in Figure 7, where six of the vectors divide the plane into six sectors (I, II, III, IV, V, and VI).

In each sector, two adjacent voltage vectors, as well as the zero vector, are selected to synthesize an arbitrary voltage vector according to the principle of volt–second balancing [29], as shown in Equation (5).

$$U_{ref} * T = U_x * T_x + U_y * T_y + U_0 * T_0 \tag{5}$$

where U_{ref} is the desired voltage vector, V; T is the PWM period, s; U_x and U_y are used to synthesize the two spatial voltage vectors of U_{ref}, corresponding to two of the six spatial voltage vectors mentioned above; and U_0 refers to the two zero vectors U_0 and U_7; and T_x, T_y, and T_0 are the action times corresponding to U_x, U_y, and U_0 in one PWM period, respectively.

The SVPWM allows the synthesis of space vectors of arbitrary direction and magnitude to achieve the FOC of PMSM [28].

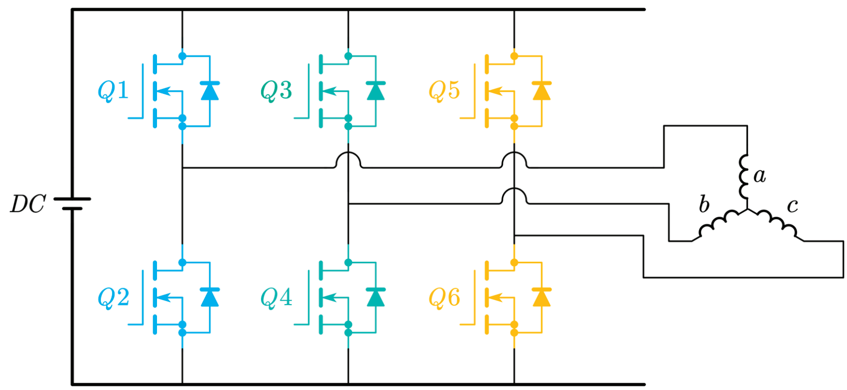

Figure 6. Three-phase inverter circuit. MOSFETs of the same color indicate the same bridge arm.

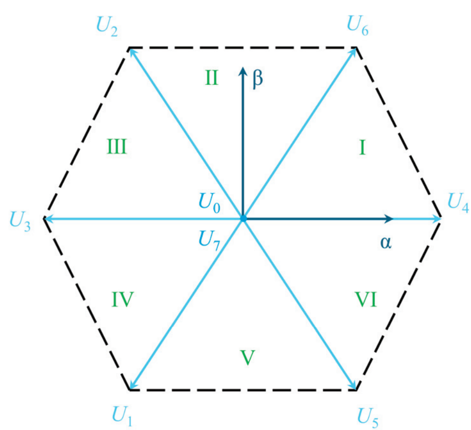

Figure 7. Space voltage vector. The triangular areas surrounded by neighboring arrows are sectors (I, II, III, IV, V, and VI).

2.5. Design of Motor Controller

The motor controller, tailored for the FOC in PMSM, comprises key components, as depicted in Figure 8. It incorporates two power supply modules (SCT2400, Silicon Content Technology Co., Ltd., Beijing, China) regulated to output 10 V (for gate drivers) and 3.3 V (for the MCU, magnetic encoder, and CAN transceiver). The heart of the system is an MCU (GD32C103CBT6, Zhaoyi Innovation Technology Group Co., Ltd., Beijing, China), leveraging USART, SWDIO for debugging, CAN (SN65HVD230, Texas Instruments Inc., Dallas, TX, USA) for communicating with Android terminal, TIMER0 for PWM generation, ADC for phase current sensing from operational amplifiers (OP-amp) (LVM324IPWR, Texas Instruments Inc., Dallas, TX, USA), and SPI for rotor angle acquisition from the magnetic encoder (MT6825, Magtek Inc., Shanghai, China). The PWMs were generated by the MCU drive gate drivers (FD6288Q, Texas Instruments Inc., Dallas, TX, USA), adjusting the MOSFETs (BSC0702LS, Infineon Technologies, Neubiberg, Germany) of the three-phase inverter circuit to achieve PMSM control.

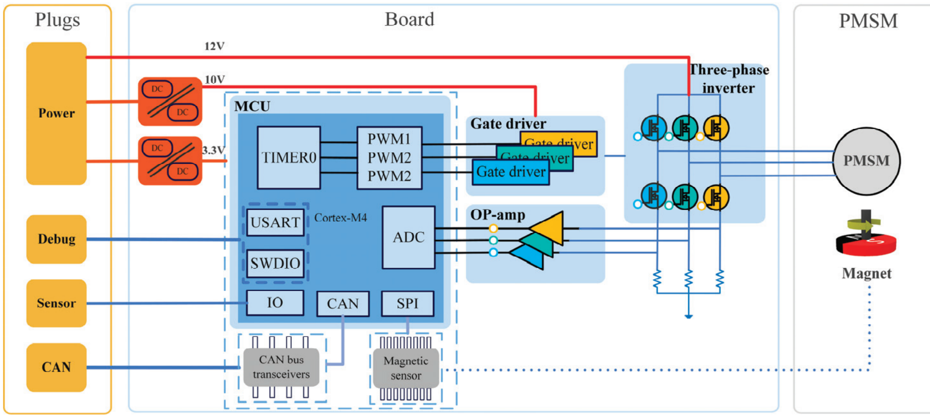

Figure 8. Controller structure and function.

The FOC process involves the MCU acquiring target speeds, rotor angle, and phase currents via CAN, SPI, and ADC. Based on these and the FOC algorithm (Figure 3), TIMER0 generates PWM signals, which, through SVPWM and gate drivers, produce a three-phase voltage to precisely control the PMSM.

It is worth mentioning that, in order to reduce the development period, the seeder lift status detection controller follows the motor controller, and the seeder lift status detection controller detects the triggering signal of the travel switch through the IO port and then obtains the lift status of the seeder.

3. Tests

In order to fully validate the seeding performance of the EDS, bench tests and field tests were carried out. The bench tests were used to evaluate the seed space uniformity of the EDS under a static environment and, at the same time, analyze the influence of the precision of motor rotational speed on seeding quality based on the relative error of the motor rotational speed. The field tests were used to validate the actual seeding performance of the EDS and to analyze the difference between bench tests and field tests regarding the seeding quality. NK815 maize seed was used in both bench tests and field tests. The seed had a half-horse tooth shape, and the 1000-seed weight was 312.05 g.

3.1. Bench Tests

Seed spacing and operating speed are important factors that affect seeding quality. Agronomy varies from region to region, and the seed spacing need is not consistent. In order to ensure the adaptability of the EDS, the range of seed spacing was set at 0.1–0.3 m. The operating speed greatly affects the operating efficiency, but due to the influence of the load of the seeder, the ground conditions, and the performance of the seed meter, the current seeder operating speed is generally within 15 km/h. Based on the range of seed spacing and operating speed, bench tests factor levels were set, as shown in Table 3.

Table 3. Bench tests factor levels.

Test Factor	Level
Seed spacing/m	0.1, 0.2, 0.3
Operating speed/(km/h)	3, 6, 9, 12, 15

Bench tests were conducted in September 2023. The bench tests equipment is shown in Figure 9 and included a seed meter detector [30], an air-suction seed meter (Shandong Dahua Machinery Co., Ltd., Jining, China), a PMSM (Nongxin Technology Co., Ltd., Beijing, China), a motor controller, a CAN tool (CANalyst-II, Chuangxin Technology, Zhuhai, China), and a terminal (Nongxin Technology Co., Ltd., Beijing, China). The air-suction seed meter is installed on the seed meter detector, which provides negative pressure (6kPa) via the seed meter detector, and the PMSM is connected coaxially to the seed meter plate. The outer seed cleaning knife of the seed meter is adjusted to the 9th position (14 positions in total), and the inner seed cleaning knife is adjusted to the 6th position (9 positions in total). The CAN tool is connected to the CAN bus between the motor controller and the terminal and is used to read CAN bus data.

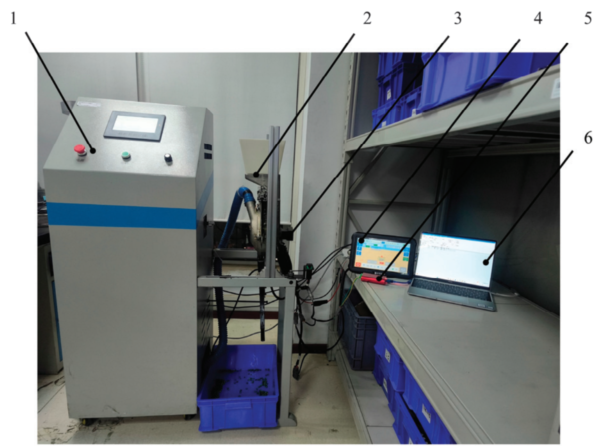

Figure 9. Bench tests equipment. 1. Seed meter detector, 2. air-suction seed meter, 3. PMSM, 4. Android terminal, 5. CAN tool, 6. computer.

Before the tests, the seed meter detector and the terminal were configured with the same operating speed and seed spacing according to Table 3, respectively. The seeding quality was recorded by the seed meter detector, and this was repeated three times at each factor level. The target number of seeds detected by the seed meter detector was set to 1000. At the same time, the motor rotational speed returned by the motor controller (return frequency of 20 Hz) through the CAN bus was read in real time by the CAN tool during the process, which is used to analyze the precision of motor rotational speed control.

3.2. Field Tests

Field tests were conducted to further explore the actual seeding performance of the EDS. The same factor levels as those used in the bench tests were selected for the field tests (Table 3). The field tests were conducted in October 2023. Before the tests, the soil (brown loam) was tilled by a rotary tiller working at a depth of 0.15 m, to ensure that the soil was soft. The tests equipment is shown in Figure 10, including a 2104 tractor (Case IH, Racine, WI, USA), a six-row precision seeder (2BMYFQ-6D, Shandong Dahua Machinery Co., Ltd., Jining, China), and an EDS. The EDS was installed on the seeder. The double-sided seed cleaning knife configuration was consistent with that used in the bench tests. The parameters of the seeder are shown in Table 4.

Figure 10. Field tests equipment. ① Antenna mounting method; ② Terminal mounting method; ③ Seeder lift detection unit mounting method; ④ PMSM and controller mounting method.

Table 4. Parameters of the seeder.

Name	Parameter
Overall dimensions/mm	2000 × 5900 × 1800
Weights/kg	1500
Working width/m	3.9
Number of rows	6
Row spacing/m	0.65
Seeding depth/mm	50
Fertilizer opener type	Double disk
Suppression wheel	V-shaped
Hitch way with tractor	Three-point suspension
Profiling mechanism	Machinery

Before the tests, six PMSMs were divided into three groups, and the three groups of motors were configured to 0.1, 0.2, and 0.3 m seed spacing, respectively. The seeding depth of each seeding unit was set at 0.05 m. The tractor rear hydraulic output was adjusted so that the rotational speed of the hydraulic motor of the seeder fan was increased as needed to ensure that the vacuum pressure of the seed meter was maintained at not less than 6.0 kPa. After the tests, 100 seed spacings per row were collected by digging out the seeds (Figure 11), translating to 200 seed spacings per group.

Figure 11. Seed digging and measuring.

3.3. Evaluation Index

The quality of feed index (QFI), miss index (MI), multiple index (MUL), and coefficient of variation (CV) specified in ISO 7256-1:1984, "Sowing equipment—Test methods Part 1: Single seed drills" [31], were used as evaluation indexes in both the bench tests and the field tests. The difference is that the evaluation indexes in the bench tests were given by direct calculations from the seed meter detector, and the results of the field tests were manually calculated based on seed spacings.

4. Analysis and Discussion of Results

4.1. Analysis and Discussion of Bench Tests

4.1.1. Seeding Quality of Bench Tests

The seeding quality at three seed spacings (0.1, 0.2, and 0.3 m) and five operating speeds (3, 6, 9, 12, and 15 km/h) is shown in Figure 12. With the increase in operating speed, the overall trend of QFI decreased, and the trend of MI, MUL and CV increased; with the increase in seed spacing, the trend of QFI decreased, and the trend of CV decreased.

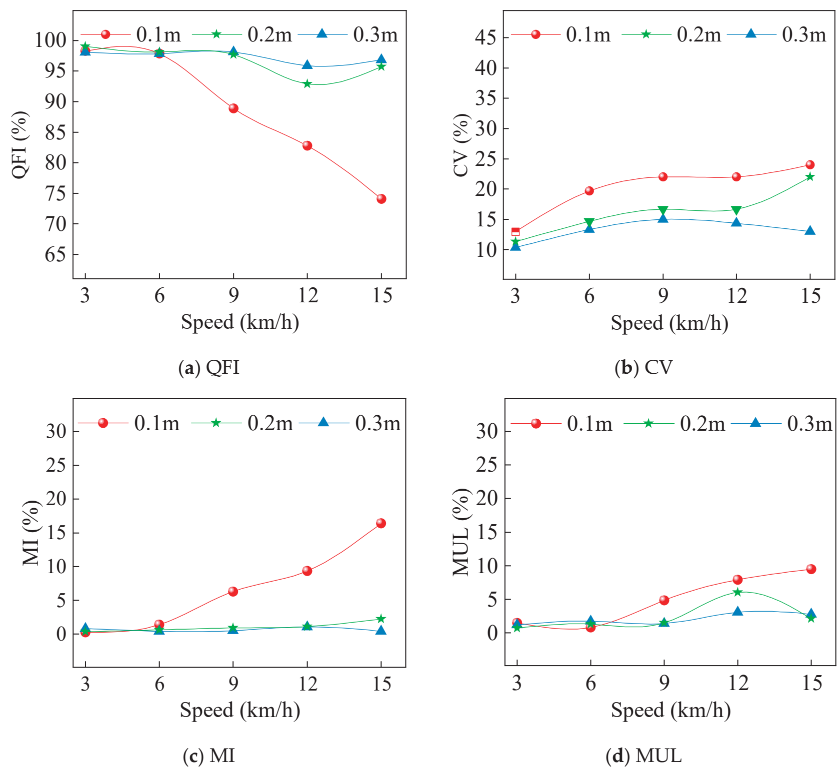

Figure 12. Seeding quality of bench tests.

Table 5 shows the results of bench tests. In the range of 3–15 km/h, the QFI varied from 74.10% to 98.30%, 92.87% to 99.00%, and 95.90% to 98.07% at 0.1, 0.2, and 0.3 m seed spacing, respectively. The average QFI was 88.38%, 96.67%, and 97.36%, respectively; the extreme difference (ED) in the QFI was 24.20%, 6.13%, and 2.23%, respectively. The CV varied from 13.00% to 24.00%, 11.33% to 22.00%, and 10.33% to 15.00% at 0.1, 0.2, and 0.3 m seed spacing, respectively; the average CV was 20.13%, 16.27%, and 13.20%, respectively; and the ED in the CV was 11.00%, 10.67%, and 4.67%, respectively.

Table 5. Results of the bench tests.

Seed Spacing/m	Operating Speed/(km/h)	QFI/%	Average QFI/%	ED of QFI/%	CV/%	Average CV/%	ED of CV/%
0.1	3	98.30	88.38	24.20	13.00	20.13	11.00
	6	97.83			19.67		
	9	88.90			22.00		
	12	82.77			22.00		
	15	74.10			24.00		
0.2	3	99.00	96.67	6.13	11.33	16.27	10.67
	6	98.10			14.67		
	9	97.67			16.67		
	12	92.87			16.67		
	15	95.70			22.00		
0.3	3	98.07	97.36	2.23	10.33	13.20	4.67
	6	97.87			13.33		
	9	98.13			15.00		
	12	95.90			14.33		
	15	96.83			13.00		

Based on the extreme difference data for QFI, it can be seen that the effect of increasing seed spacing on the decrease in QFI is not linear, but rather an accelerated deterioration process. The extreme difference in QFI at 0.1 m and 0.2 m seed spacing is 2.75 times and 10.84 times of that at 0.3 m seed spacing, respectively. The cause of this condition may be related to the rotational speed of seed meter plate and seed bouncing [2,16,32]. The decrease in seed spacing and the increase in operating speed lead to an increase in the rotational speed of the seed meter plate, which will result in less time for the seed adsorption and clearing process [16], thereby causing a decrease in QFI. Moreover, the increase in the rotational speed leads to an increase in the initial velocity of the seed when it is put into the seed tube, and the seed bouncing in the seed tube becomes violent, which leads to a decrease in QFI and an increase in CV.

4.1.2. Analysis of Variance

To further explore the effect of operating speed and seed spacing on seeding quality, an analysis of variance (ANOVA) was conducted, and the results of the ANOVA are shown in Table 6.

Table 6. ANOVA of bench tests results.

Index	Factor	SS	Df	MS	F	p
Seed spacing	QFI	748.950	2	374.475	655.695	0.000
	CV	362.133	2	181.067	94.744	0.000
Operating speed	QFI	670.056	4	167.514	293.313	0.000
	CV	343.200	4	85.800	44.895	0.000

Table 6 shows that both operating speed and seed spacing had a significant effect on QFI and CV ($p < 0.001$). From the F-values, it can be seen that both seed spacing and operating speed had a greater effect on QFI than on CV, and seed spacing had a greater effect on QFI and CV than operating speed had on QFI and CV.

4.1.3. Accuracy Analysis of Motor Rotational Speed

The decrease in seeding quality may be related to seed spacing and operating speed on the one hand, but there may also be a correlation with motor rotational speed accuracy [15,33]. In order to clarify the effect of motor rotational speed accuracy on seeding quality, the motor rotational speed accuracy in the tests was analyzed. The motor target rotational speed, relative error of motor rotational speed, QFI, and CV value correspondences during the tests are shown in Figure 13.

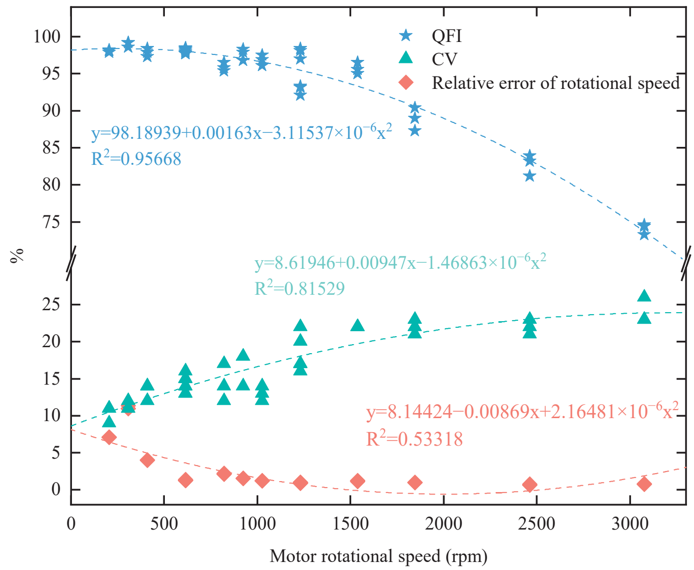

Figure 13. Correspondence between the relative error of motor rotational speed, QFI and CV.

Figure 13 shows that as the motor rotational speed increases, the QFI and the relative error of the motor rotational speed gradually decrease and the CV gradually increases. Among them, the relative error of the motor rotational speed does not exceed 2.24% when the motor rotational speed is more than 410 rpm; when the motor rotational speed is less than 410 rpm, the relative error of the motor rotational speed does not exceed 11.34%.

The reason for this condition is that at low motor rotational speeds, the resolution of the magnetic encoder is insufficient to accurately measure speed changes [34]. At the same time, the phase currents are small and the current sampling process is susceptible to noise. However, the QFI and CV corresponding to the low motor rotational speeds are at a high level. It can be assumed that the relative error of the motor rotational speed is low, having little effect on the seeding quality. The EDS's motor rotational speed accuracy can meet the demands for precision seeding of maize within the ranges of 3–15 km/h and 0.1–0.3 m seed spacing. Therefore, the reduction in QFI and the increase in CV are mainly due to the seed meter and seed bouncing. The seed adsorption and clearing time decreases at higher motor rotational speeds, leading to a reduction in QFI. At the same time, excessive rotational speed in the seed meter plate will make the seed bouncing in the seed tube become more violent, resulting in a decrease in the seeding quality and an increase in CV.

4.2. Analysis and Discussion of Field Tests

4.2.1. Seeding Quality of Field Tests

The seeding quality of field tests at three seed spacings (0.1, 0.2, and 0.3 m) and five operating speeds (3, 6, 9, 12, and 15 km/h) is shown in Figure 14. With the increase in operation speed, the overall trend of the QFI was decreasing, and the MI, MUL, and CV increased. With the increase in seed spacing, the QFI first increased rapidly and then stabilized, and the MI, MUL, and CV first decreased rapidly and then stabilized. The overall trend is similar to that of the indexes in the bench tests.

Table 7 shows the results of field tests. In the range of 3–15 km/h, the QFI varied from 66.37% to 98.02%, 91.79% to 98.52%, and 92.68% to 99.50% at 0.1, 0.2, and 0.3 m seed spacing, respectively. The average QFI was 85.93%, 95.91%, and 96.24%, respectively; the extreme difference in the QFI was 31.65%, 6.73%, and 6.82%, respectively. The CV varied from 17.94% to 24.02%, 10.43% to 20.65%, and 12.19% to 20.8% at 0.1, 0.2, and 0.3 m seed spacing, respectively; the average CV was 21.12%, 15.50%, and 16.49%, respectively; and the extreme difference in the CV was 6.08%, 10.22%, and 8.61%, respectively.

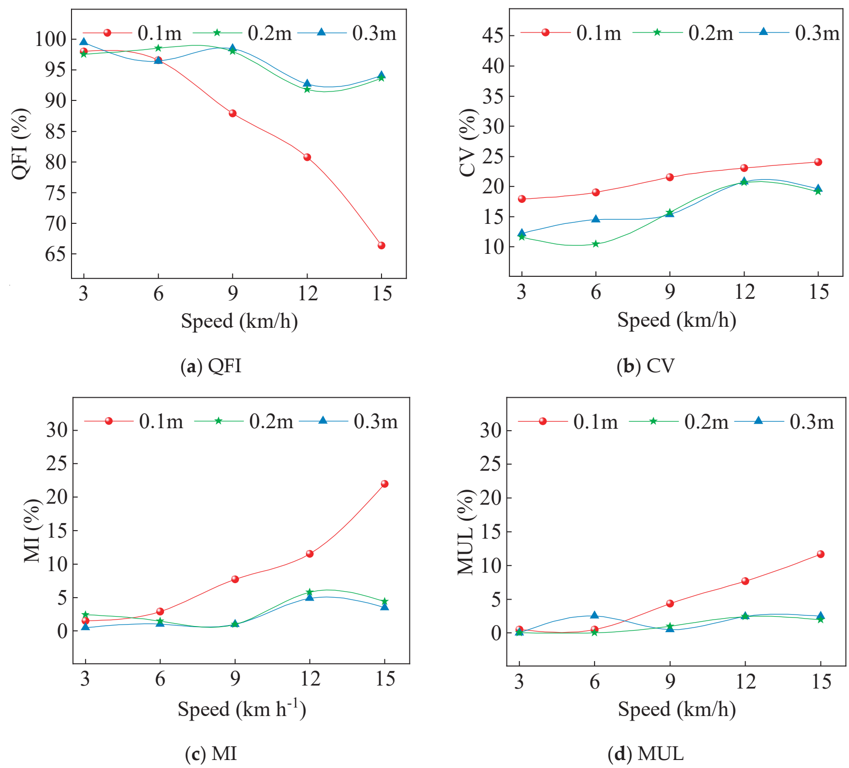

Figure 14. Seeding quality in field tests.

Table 7. Results of the field tests.

Seed Spacing/m	Operating Speed/(km/h)	QFI/%	Average QFI/%	ED of QFI	CV	Average CV	ED of CV
	3	98.02			17.94		
	6	96.59			19.05		
0.1	9	87.92	85.93	31.65	21.54	21.12	6.08
	12	80.77			23.05		
	15	66.37			24.02		
	3	97.56			11.61		
	6	98.52			10.43		
0.2	9	98	95.91	6.73	15.69	15.50	10.22
	12	91.79			20.65		
	15	93.66			19.13		
	3	99.5			12.19		
	6	96.45			14.49		
0.3	9	98.51	96.24	6.82	15.38	16.49	8.61
	12	92.68			20.8		
	15	94.06			19.58		

4.2.2. Comparison of Bench and Field Tests Results

Based on the extreme difference data of QFI in field tests, it is clear that smaller seed spacing has a significant effect on QFI. The extreme difference in QFI at 0.1 m seed spacing was 4.64 times that at 0.3 m seed spacing. In contrast, the extreme differences in QFI at 0.2 m and 0.3 m were similar, which may be related to the method used to obtain the seeding quality. Seeds were monitored in the bench tests by a monitoring sensor mounted on the seed tube, while, in the field tests, seeds were dug out manually. There was relatively little seed bouncing within the seed tube in the bench tests, whereas in the field tests seed bouncing was present throughout the seed tube and in the seed furrow. Seed bouncing affects seed spacing [35]; the effect of seed bouncing is more pronounced when seed spacing is small and less pronounced when seed spacing is large. As a result, the extreme differences in QFI are close at seed spacings of 0.2 and 0.3 m.

More seed bouncing in the field tests resulted in an overall decrease in seeding quality, with the average QFI at 0.1 m, 0.2 m, and 0.3 m seed spacing decreasing by 2.45%, 0.76%, and 1.12% compared to the average QFI in the bench tests and the average CV increasing by 0.98%, −0.77%, and 3.29% compared to the increase in the bench tests.

Overall, the EDS can meet the needs of a wide operating speed range (3–15 km/h) and a wide seed spacing range (0.1–0.3 m), and the motor controller designed based on the FOC algorithm can achieve high control accuracy. However, the seed meter performance and seed bouncing are important constraints that could limit further improvement in seeding quality, especially at high operating speeds. Therefore, it is necessary to optimize the seed meter based on the demand for high speeds and to improve seed bouncing in the seed tube and the furrow, which will help improve the yield in the future.

5. Conclusions

In this study, an EDS for a maize precision seeder based on a CAN bus was designed and a seeding controller based on FOC algorithm was developed to achieve the FOC of the PMSM. The seeding quality change rule for the EDS under different seed spacings and operating speeds was studied to determine the seeding performance of the system. Specific conclusions are as follows:

1. To improve the expandability, seeding accuracy, and operating speed range, an EDS for a maize precision seeder was designed based on the CAN bus and FOC algorithm. A CAN bus communication protocol designed based on ISO 11783 standard can be applied to different row seeders. The seeding controller based on the FOC algorithm can effectively ensure the seeding accuracy and speed range.
2. To explore the performance of the EDS and the change rule for seeding quality, bench tests were carried out. The results of the bench tests showed that seeding quality varied inversely with operating speed and positively with seed spacing. over a range of seed spacings (0.1, 0.2, and 0.3 m) and operating speeds (3, 6, 9, 12, and 15 km/h). The average QFI at 0.1, 0.2, and 0.3 m seed spacing in bench tests was 88.38%, 96.67%, and 97.36%, with the average CV being 20.13%, 16.27%, and 13.20%.
3. To explore the effect of tests factors on seeding quality, ANOVA and rotational speed accuracy were conducted based on bench tests. ANOVA showed that both operating speed and seed spacing have a significant effect on QFI and CV ($p < 0.001$). Both seed spacing and operating speed have a greater effect on QFI than on CV, and the effect of seed spacing on QFI and CV is greater than the effect of operating speed on QFI and CV. The analysis of motor rotational speed accuracy showed that the relative error of motor rotational speed above 410 rpm does not exceed 2.24% and the rotational speed control error has less influence on the seeding quality.
4. To further determine the performance of the system, field tests were conducted. The results of the field tests showed that the average QFI was 85.93%, 95.91%, and 96.24% at 0.1, 0.2, and 0.3 m seed spacing, and the average CV was 21.12%, 15.50%, and 16.49% in the range of operating speeds of 3, 6, 9, 12, and 15 km/h. Compared with the bench tests, the average QFI at 0.1 m, 0.2 m, and 0.3 m seed spacing decreasing by

2.45%, 0.76%, and 1.12%, and the average CV increased by 0.98%, −0.77%, and 3.29%, respectively.

Synthesizing the results of the above tests, the EDS meets the demand for expandability, seeding accuracy, and operating speed range. The seed meter performance and seed bouncing can limit seeding quality at high operating speeds, and further optimization of the seed meter and seed guide mechanism will be needed in the future.

Author Contributions: Conceptualization, D.G.; Data curation, X.H.; Formal analysis, L.L. (Lin Ling); Funding acquisition, B.Y.; Investigation, L.L. (Lin Ling) and Y.X.; Methodology, L.L. (Lin Ling); Project administration, B.Y.; Resources, B.Y. and D.G.; Software, Y.X.; Supervision, G.W.; Validation, B.Y.; Visualization, L.L. (Lin Ling) and L.L. (Liwei Li); Writing—original draft, L.L. (Lin Ling); Writing—review and editing, L.L. (Lin Ling) and Y.X. All authors have read and agreed to the published version of the manuscript.

Funding: This research was funded by Next Generation Artificial Intelligence National Science and Technology Major Project (No. 2022ZD0115800), Modern AgricuituraIndustrial System of Shandong Province (No. SDAIT-02-12), and National Natural Science Foundation of China (No. 32301705).

Data Availability Statement: Data are contained within the article. The data presented in this study can be requested from the authors.

Conflicts of Interest: The authors declare no conflicts of interest.

References

1. Zhang, Q.; Dong, W.; Wen, C.; Li, T. Study on Factors Affecting Corn Yield Based on the Cobb-Douglas Production Function. *Agric. Water Manag.* **2020**, *228*, 105869. [CrossRef]
2. Ling, L.; Wu, G.; Wen, C.; Xiao, Y.; Fu, W.; Dong, J.; Ding, J.; Meng, Z.; Yan, B. Influence of Speed Measurement Method on Performance of an Electric-Drive Maize Precision Planter. *Biosyst. Eng.* **2024**, *238*, 175–187. [CrossRef]
3. Ding, Y.; He, X.; Yang, L.; Zhang, D.; Cui, T.; Li, Y.; Zhong, X.; Xie, C.; Du, Z.; Yu, T. Low-Cost Turn Compensation Control System for Conserving Seeds and Increasing Yields from Maize Precision Planters. *Comput. Electron. Agric.* **2022**, *199*, 107118. [CrossRef]
4. Yang, S.; Zhai, C.; Gao, Y.; Dou, H.; Zhao, X.; He, Y.; Wang, X. Planting Uniformity Performance of Motor-Driven Maize Precision Seeding Systems. *Int. J. Agric. Biol. Eng.* **2022**, *15*, 101–108. [CrossRef]
5. Wang, H.; Yang, L.; Zhang, D.; Cui, T.; He, X.; Xiao, T.; Li, H.; Du, Z.; Xie, C. Comparative Investigation and Evaluation of Electric-Drive Seed-Metering Systems across Diverse Speed Ranges for Enhanced High-Precision Seeding Applications. *Comput. Electron. Agric.* **2024**, *222*, 108976. [CrossRef]
6. He, X.; Zhang, D.; Yang, L.; Cui, T.; Ding, Y.; Zhong, X. Design and Experiment of a GPS-Based Turn Compensation System for Improving the Seeding Uniformity of Maize Planter. *Comput. Electron. Agric.* **2021**, *187*, 106250. [CrossRef]
7. Mishler, B.D. Quantifying Seed Uniformity and Yield Advantage of Precision Planter Technologies through Use of Field Tests and Machine Data. Master's Thesis, Kansas State University, Manhattan, KS, USA, 2021.
8. Nørremark, M.; Griepentrog, H.W.; Nielsen, J.; Søgaard, H.T. The Development and Assessment of the Accuracy of an Autonomous GPS-Based System for Intra-Row Mechanical Weed Control in Row Crops. *Biosyst. Eng.* **2008**, *101*, 396–410. [CrossRef]
9. Yang, L.; Yan, B.; Zhang, D.; Zhang, T.; Wang, Y.; Cui, T. Research Progress on Precision Planting Technology of Maize. *Trans. Chin. Soc. Agric. Mach.* **2016**, *47*, 38–48. [CrossRef]
10. Griepentrog, H.W. Seed Distribution Over The Area. In Proceedings of the AgEng. 1998: International Conference on Agricultural Engineering, Oslo, Norway, 24–27 August 1998; p. 98-A-059.
11. Panning, J.; Kocher, M.; Smith, J.; Kachman, S. Laboratory and Field Testing of Seed Spacing Uniformity for Sugarbeet Planters. *Appl. Eng. Agric.* **2000**, *16*, 7–13. [CrossRef]
12. Valentin, M.T.; Białowiec, A.; Karayel, D.; Jasinskas, A.; Ciolkosz, D.; Lavarias, J.A. Investigation of the Performance of a Cylindrical Hopper and Metering Device of a Carrot Seeder. *Sci. Rep.* **2023**, *13*, 813. [CrossRef] [PubMed]
13. Kamgar, S. Eslami Design, Development and Evaluation of a Mechatronic Transmission System for Upgrading Performance of a Row Crop Planter. *Int. J. Agron. Plant Prod.* **2013**, *4*, 480–487.
14. Wang, Y.; Zhang, W.; Qi, B.; Xia, Q. Comparison of Field Performance of Different Driving Systems and Forward Speed Measuring Methods for a Wet Direct Seeder of Rice. *Agronomy* **2022**, *12*, 1655. [CrossRef]
15. He, X.; Cui, T.; Zhang, D.; Wei, J.; Wang, M.; Yu, Y.; Liu, Q.; Yan, B.; Zhao, D.; Yang, L. Development of an Electric-Driven Control System for a Precision Planter Based on a Closed-Loop PID Algorithm. *Comput. Electron. Agric.* **2017**, *136*, 184–192. [CrossRef]
16. Wang, Y.; Zhang, W.; Qi, B.; Ding, Y.; Xia, Q. Research on Control System of Corn Planter Based on Radar Speed Measurement. *Agronomy* **2024**, *14*, 1043. [CrossRef]
17. MAESTRO SV/SX. Available online: https://www.horsch.com/en-ca/products/planting/maestro/maestro-sv/sx (accessed on 10 September 2024).

18. vDrive | Drive Systems. Available online: https://www.precisionplanting.com/products/planters/vdrive (accessed on 10 September 2024).
19. CHRONO—International—Corporate Website. Available online: https://www.maschiogaspardo.com/en/web/international/chrono (accessed on 10 September 2024).
20. Li, Y.; Xiantao, H.; Tao, C.; Dongxing, Z.; Song, S.; Zhang, R.; Mantao, W. Development of Mechatronic Driving System for Seed Meters Equipped on Conventional Precision Corn Planter. *Int. J. Agric. Biol. Eng.* **2015**, *8*, 1–9. [CrossRef]
21. Cay, A.; Kocabiyik, H.; May, S. Development of an Electro-Mechanic Control System for Seed-Metering Unit of Single Seed Corn Planters Part II: Field Performance. *Comput. Electron. Agric.* **2018**, *145*, 11–17. [CrossRef]
22. He, X.; Ding, Y.; Zhang, D.; Yang, L.; Cui, T.; Zhong, X. Development of a Variable-Rate Seeding Control System for Corn Planters Part I: Design and Laboratory Experiment. *Comput. Electron. Agric.* **2019**, *162*, 318–327. [CrossRef]
23. Ding, Y.; Yang, L.; Zhang, D.; Cui, T.; Li, Y.; Zhong, X.; Xie, C.; Ding, Z. Novel Low-Cost Control System for Large High-Speed Corn Precision Planters. *Int. J. Agric. Biol. Eng.* **2021**, *14*, 151–158. [CrossRef]
24. Yang, S.; Wang, X.; Gao, Y.; Zhao, X.; Dou, H.; Zhao, C. Design and Experiment of Motor Driving Bus Control System for Corn Vacuum Seed Meter. *Nongye Jixie Xuebao/Trans. Chin. Soc. Agric. Mach.* **2019**, *50*, 57–67. [CrossRef]
25. Du, Z.; Yang, L.; Zhang, D.; Cui, T.; He, X.; Xiao, T.; Xing, S.; Xie, C.; Li, H. Development and Testing of a Motor Drive and Control Unit Based on the Field-Oriented Control Algorithm for the Seed-Metering Device. *Comput. Electron. Agric.* **2023**, *211*, 108024. [CrossRef]
26. Paraforos, D.S.; Sharipov, G.M.; Griepentrog, H.W. ISO 11783—Compatible Industrial Sensor and Control Systems and Related Research: A Review. *Comput. Electron. Agric.* **2019**, *163*, 104863. [CrossRef]
27. Gao, Y.; Wang, X.; Yang, S.; Zhai, C.; Zhao, X.; Zhao, C. Development of CAN-Based Sowing Depth Monitoring and Evaluation System. *Nongye Jixie Xuebao/Trans. Chin. Soc. Agric. Mach.* **2019**, *50*, 15–28. [CrossRef]
28. Ramesh, P.; Umavathi, M.; Bharatiraja, C.; Ramanathan, G.; Athikkal, S. Development of a PMSM Motor Field-Oriented Control Algorithm for Electrical Vehicles. *Mater. Today Proc.* **2022**, *65*, 176–187. [CrossRef]
29. Wang, X.; Liu, N.; Na, R. Simulation of PMSM Field-Oriented Control Based on SVPWM. In Proceedings of the 2009 IEEE Vehicle Power and Propulsion Conference, Dearborn, MI, USA, 7–10 September 2009; pp. 1465–1469.
30. Hao, Y.; Cui, T.; Bora, G.; Zhang, D.; Wei, J.; He, X.; Wang, M.; Yang, L. Development of an Instrument to Measure Planter Seed Meter Performance. *Appl. Eng. Agric.* **2017**, *33*, 31–40. [CrossRef]
31. *ISO 7256-1:1984*; Sowing Equipment—Test Methods Part 1: Single Seed Drills (Precision Drills). ISO: Geneva, Switzerland, 1984.
32. Yan, B.; Wu, G.; Xiao, Y.; Mei, H.; Meng, Z. Development and Evaluation of a Seed Position Mapping System. *Comput. Electron. Agric.* **2021**, *190*, 106446. [CrossRef]
33. Wang, S.; Zhao, B.; Yi, S.; Zhou, Z.; Zhao, X. GAPSO-Optimized Fuzzy PID Controller for Electric-Driven Seeding. *Sensors* **2022**, *22*, 6678. [CrossRef]
34. Wang, Y.; Xie, W.; Chen, H.; Day-Uei, L.D. High-Resolution Time-to-Digital Converters (TDCs) with a Bidirectional Encoder. *Measurement* **2023**, *206*, 112258. [CrossRef]
35. Parish, R.L.; Bracy, R.P. An Attempt to Improve Uniformity of a Gaspardo Precision Seeder. *Horttech* **2003**, *13*, 100–103. [CrossRef]

agriculture

MDPI

Article

Design and Experiment of Compound Transplanter for Sweet Potato Seedling Belt

Wei Yan [1,2], Wenyi Zhang [1], Minjuan Hu [1], Yao Ji [1], Kun Li [1], Zhaoyang Ren [1,2] and Chongyou Wu [1,*]

1 Nanjing Institute of Agricultural Mechanization, Ministry of Agriculture and Rural Affairs, Nanjing 210014, China; yanwei@caas.cn (W.Y.); zhangwenyi@caas.cn (W.Z.); huminjuan@caas.cn (M.H.); jiyao@caas.cn (Y.J.); likun03@caas.cn (K.L.); 82101222108@caas.cn (Z.R.)
2 Graduate School, Chinese Academy of Agricultural Sciences, Beijing 100083, China
* Correspondence: wuchongyou@caas.cn

Abstract: To address the issues of high labor intensity, excessive manpower requirements, low planting spacing qualification rates, low planting depth qualification rates, and low operational efficiency associated with sweet potato transplanting, a sweet potato seedling belt transplanter has been designed. This machine can perform multiple processes: precision tillage and ridge shaping, orderly seedling feeding from rolls, the efficient separation of seedlings from the belt, flexible gripping and shaping, precise soil covering and the mechanism of exposing seedling tips. A three-factor, three-level orthogonal test was carried out using the forward speed of the machine, the pitch of the screw belt and the rotational speed of the screw as the influencing factors of the performance test, and the qualified rate of planting spacing and the qualified rate of planting depth as the evaluation indexes. The test results indicated that the significance order of the factors affecting the qualification rate for planting spacing with the optimal combination of factors was as follows: a forward speed of 0.3 m·s^{-1}, a ribbon spacing of 60 mm, and a screw speed of 160 rpm. Field trials confirmed that under optimal conditions, the average qualification rate for planting spacing was 90.37%, meeting relevant technical standards and agronomic requirements.

Keywords: sweet potato; seedling belt transplanting; horizontal planting; seedling belt separation; mulching and matting tips

Citation: Yan, W.; Zhang, W.; Hu, M.; Ji, Y.; Li, K.; Ren, Z.; Wu, C. Design and Experiment of Compound Transplanter for Sweet Potato Seedling Belt. *Agriculture* **2024**, *14*, 1738. https://doi.org/10.3390/agriculture14101738

Academic Editor: John Fielke

Received: 5 September 2024
Revised: 29 September 2024
Accepted: 1 October 2024
Published: 2 October 2024

1. Introduction

China is the largest producer of sweet potatoes globally, with an annual planting area of approximately 2.2 million hectares, accounting for about 30% of the world's total, and an annual output of 48 million tons, approximately 53% of global production [1]. In recent years, with rising living standards and growing health awareness, the demand for fresh sweet potatoes has increased significantly, placing higher quality requirements on sweet potato production and consumption [2]. With the rapid development of social and economic as well as rural labor transfer, labor costs increase year by year, and the mechanized transplanting technology and equipment needs in sweet potato production areas urgently need more and more machinery to replace the dependence on many workers [3]. Currently, sweet potato transplanting accounts for about 23% of the labor used in the entire production process. Consequently, a substantial amount of transplanting is still carried out by labor, which is costly and uneven in quality, resulting in poor product marketability and low planting efficiency, thereby hindering the healthy and high-quality development of China's sweet potato industry [4]. Due to the requirement of bare-root transplanting, the morphology of sweet potato seedlings is complex, with tangled vines and inconsistent shapes, which complicates the mechanization of horizontal transplantation. Currently, transplantation primarily relies on manual labor or semi-automatic methods involving manual single-seedling placement. Semi-automatic transplanting requires two to three workers per row, with an average planting spacing pass rate of 85%, a planting depth pass rate of 80%, and an average transplanting machine operating efficiency of 35 plants per minute. The transplanting link has become an urgent issue in sweet potato production.

In order to solve the above problems, the author developed a sweet potato belt transplanter based on artificial seedling feeding, which solved the problem of a low qualified rate of planting distance and planting depth of transplanter. In terms of employment, the single-line operation has changed from the original two to one. In the production process, it is found that although the working efficiency of the transplanter is improved by 10% compared with the existing transplanter, it is difficult to popularize it. On this basis, in order to improve the working efficiency of the transplanter, an innovative technical solution has been proposed, incorporating "seedling belt feeding from rolls + automatic seedling belt separation + adaptive speed matching for the belt + flexible grip adjustment + stable shaping of seedlings". This technological approach involves breakthroughs in key techniques such as tension stability control, adaptive speed matching, seedling feeding from rolls, the automatic separation of seedlings, flexible gripping, and the shaping of seedlings. The design of the sweet potato seedling belt transplanter effectively reduces production costs, lessens labor intensity, enhances product quality, and increases economic efficiency. This development is significant for stabilizing planting scales, improving comprehensive benefits, enhancing market competitiveness, and promoting the green and efficient development of the sweet potato industry in China. Furthermore, it also provides an effective solution for the efficient transplantation of seedling cuttings.

2. Sweet Potato Seedling Transplanting Agronomy

2.1. Sweet Potato Seedling Mechanization Cultivation Model

In terms of cultivation methods, both ridge and flat systems are practiced in sweet potato production, predominantly with ridges. Various ridge configurations are used depending on production scenarios [5]. To address the compatibility issues related to suitable mechanized production operations, this proposal encompasses various stages, including ridging, transplanting, tillage, vine shredding, and harvesting. The approach emphasizes cost-effectiveness while integrating diverse operational scenarios and existing tractor availability across different regions, fostering the integration of agricultural machinery and agronomy. The recommended mechanized cultivation modes include single-ridge single-row, single-ridge double-row, and large-ridge double-row cultivation. From the perspective of mechanization, a single-ridge single-row cultivation model is recommended, as illustrated in Figure 1.

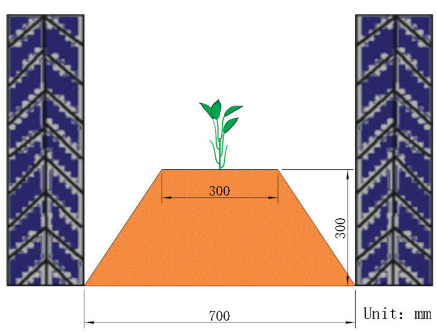

Figure 1. Single-ridge single-row cultivation model.

This model allows for the full mechanization of tillage, planting, management, and harvesting using a single tractor. It offers advantages such as high economic efficiency, simplicity in setup, broad adaptability, and low investment requirements, making it suitable for medium- and small-plot operations in most regions. In flat lowland areas, it can be paired with medium-sized four-wheeled tractors, while in hilly or small plots, walking tractors or mini tillers can be utilized. However, for larger fields, the machinery can be configured for multi-row operations to enhance efficiency.

2.2. Sweet Potato Seedling Transplanting Methods

Due to the tuber formation characteristics of sweet potatoes, sweet potato seedlings cannot be transplanted in soil-covered plug trays like vegetables. Instead, they must undergo a seedling cultivation process followed by cutting and then bare-root transplantation. Sweet potato mainly has five traditional planting methods: horizontal planting, diagonal planting, boat-bottom shaped planting, straight planting, and vine-pressing planting [6], as shown in Figure 2. The horizontal planting method requires the seedling to be planted in the soil part of the horizontal posture in the basic conditions of the potato, where each section is mostly occupied by rooting potato, with a less empty section having more potatoes, potato size uniformity, and other advantages. The oblique planting method requires the seedling to be planted in the soil part of the vertical direction at a certain angle, where the number of single-plant potatoes compared with the horizontal planting method is less than the number of larger potatoes in the upper nodes, and the lower nodes have smaller potatoes or even no potatoes. The ship-bottom-shaped planting method requires the seedling to be planted in the soil part of the middle of the pressure, where the head and tail ends of the two thus resemble the bottom of a ship. The seedling is implanted into the soil section more, causing more nodes to be close to the soil surface, which is conducive to the potatoes and leads to higher yields; however, at the central part of the seedling in the soil, the deeper nodes tend to be small and have fewer potatoes, or they can even become empty nodes. The direct planting method requires that the seedling be inserted directly into the soil. Due to the deeper direct insertion into the soil, only a few nodes are distributed in the topsoil layer of the potato species; the general number of single-plant potatoes is small; the potato has more than a few kinds of nodes in the upper part of the plant; expansion is fast; and the rate of large potatoes is high. The pressure vine planting method requires the top of the potato seedlings to be buried in the soil at both ends. The leaves are all exposed to the ground and results in more potatoes that are large; the stems and leaves are not easy to grow. It has high yield advantages, but poor drought resistance, and requires more planting labor with only a small area of high-yield cultivation.

Figure 2. Five traditional methods of planting sweet potato: 1. horizontal planting; 2. inclined planting; 3. boat-shaped planting; 4. vertical planting; and 5. layering planting.

A comparative analysis of these five different planting methods, in conjunction with high-yield cultivation techniques, indicates that the current predominant practices involve horizontal, inclined, and vertical planting methods. Horizontal and inclined planting methods are primarily suitable for fresh sweet potato seedlings, while vertical planting is mainly used for waxy sweet potato seedlings. Horizontal planting has advantages over inclined planting, including higher tuber yield, uniformity in tuber size, better marketability, and an overall higher productivity, making it the leading method for fresh sweet potato seedling transplantation. For horizontal planting, the seedling length should be approximately 30 cm, with a horizontal planting depth of about 15 cm and a planting depth of 5~8 cm.

3. Design of the Sweet Potato Seedling Belt with Compound Transplanter

3.1. General Structure of the Machine

The overall structure of the sweet potato seedling belt with compound transplanter is schematically shown in Figure 3, which mainly consists of key components such as sliding rail, suspension device, hydraulic oil pipe, hydraulic cylinder, seedling roll belt, seat, angle adjustment, seedling tray, motor, support wheel, suppression wheel, mulching screw, furrow opener, seedling conveyor belt, frame, tension roller, monopoly shaping plate, soil crushing roller, rotary tillage cutter shaft and so on.

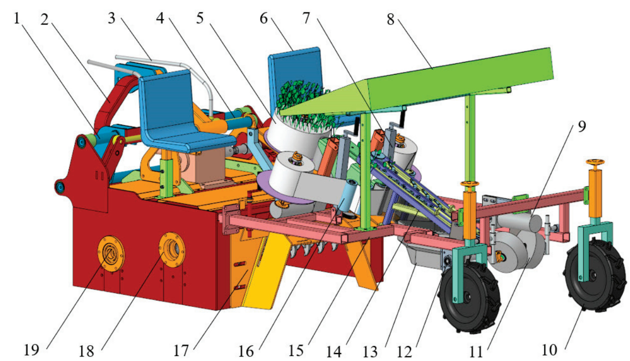

Figure 3. Structural diagram of the sweet potato seedling belt with compound transplanter: 1. sliding rail; 2. suspension device; 3. hydraulic oil pipe; 4. hydraulic cylinder; 5. seedling roll belt; 6. seat; 7. angle adjustment; 8. seedling tray; 9. motor; 10. support wheel; 11. suppression wheel; 12. mulching screw; 13. furrow opener; 14. seedling conveyor belt; 15. frame; 16. tension roller; 17. monopoly shaping plate; 18. soil crushing roller; and 19. rotary tillage cutter shaft.

3.2. Working Principle

During operation, the machine is connected to the rear of a tractor via a three-point hitch and coupled to the tractor's power output shaft using a universal joint. The rotary tillage part cuts and pulverizes the soil and throws it to the crusher rollers, which further crush the soil before the ridge shaping plate shapes it, completing the ridge-making operation. Manually, the rolled seedling belt is loaded onto the carrying device, and the dual-layer seedling belt is initially separated and bonded to the separation roller. A motor drives the separation roller to separate and collect the seedling belt. Once separated, the seedlings belt enters a conveyor belt driven by a motor, which transports the seedlings diagonally downward into the prepared seedling ditch. Once the roots touch the bottom of the ditch, the seedlings continuously bend and take a horizontal position. After the seedlings detach from the conveyor belt, the soil covering device performs soil covering and exposes the seedling tips to complete the seedling transplantation. Simultaneously, the bidirectional offset mechanism can be adjusted, allowing the equipment to operate along the edges of the field, between ridges, and in "S"-shaped operations.

3.3. Main Technical Parameters

According to the appropriate mechanization mode of operation and sweet potato horizontal planting agronomic requirements in sweet potato production, the design of the transplanting machine needs to meet the operation requirements of a ridge height of 300 mm and a distance between the center of the two ridges (ridge spacing) of 900 mm. According to the requirements of the planting of fresh potatoes, a planting spacing of 200~300 mm, a planting depth of 50~80 mm, and a planting spacing qualification rate of

≥90% are needed. In order to adapt to small-field operations, the machine needs to be compact and have low power consumption. The main technical parameters of sweet potato seedling with the compound transplanter are shown in Table 1.

Table 1. Main parameters of sweet potato seedling with compound transplanter.

Item	Parameter
Dimension of whole machine/(mm × mm × mm)	2450 × 1100 × 1150
Power requirements/kW	≥36
Ridge height/mm	300
Ridge spacing/mm	900
Planting spacing/mm	200~300
Planting depth/mm	50~80
Number of working rows	1
Qualified rate of planting spacing/%	≥90

4. Design of Key Component Parameters

4.1. Design of Key Parameters for Seedling Belt Carrying Device

4.1.1. Design of Seedling Belt Loading Program

Currently, sweet potato seedling transplanting machines primarily operate as semi-automatic systems with manual seedling feeding. The single-row operational efficiency of the equipment is limited by the manual feeding efficiency, resulting in relatively low overall productivity. Without improvements in feeding efficiency, significant enhancements in the machine's single-row operation efficiency are unlikely. To address these challenges, this section focuses on improving seedling feeding efficiency by innovatively proposing a seedling belt feeding technology solution. This approach constrains irregular and unordered sweet potato seedlings to the seedling belt in a standardized, orderly manner, allowing for specification and organization of the seedlings. The feeding method transitions from individual manual feeding to feeding entire rolls of the seedling belt. These seedling belt carrying devices can accommodate 50, 100, 200, or more seedlings as needed, leading to substantial improvements in feeding efficiency. Based on the previously measured geometric parameters and mechanical characteristics of sweet potato seedling plants, the seedling belt design was developed, as illustrated in Figure 4.

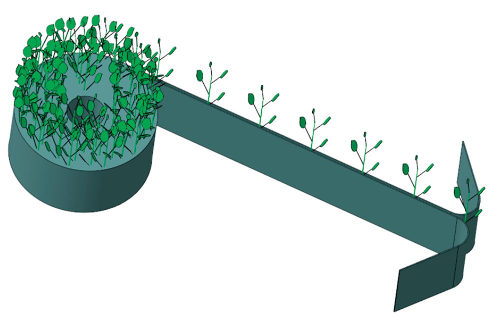

Figure 4. Design of the sweet potato seedling belt carrying device.

The designed seedling belt carrying device consists of two layers with a width of 150 mm, featuring designated planting positions at specified intervals. To facilitate manual planting, the upper openings of these positions have a width of 40 mm, while the lower openings measure 20 mm. The seedlings are placed from the upper opening to the lower opening, with roots positioned at the bottom of the lower opening, ensuring a spacing of 200 mm between seedlings. The preliminary selection of the seedling belt's materials includes paper-based and polymer-based dual-layer belts. The bonding methods for the seedlings belts can be continuous, intermittent, or dot-style. Experimental research has shown that under the same temperature, pressure, and sealing time conditions, the dot-style structure is easier to separate. Therefore, the bonding points of the seedling belt are designed as semicircular structures, with bonding methods chosen based on the materials used—either adhesive or point-sealing techniques. In conclusion, the differing sizes of the upper and lower openings and the semicircular design of the bonding points facilitate manual seedling placement. Additionally, the dual-layer seedling belt requires only minimal separation force during detachment. The specific structural design of the seedling belt carrying device is shown in Figure 5.

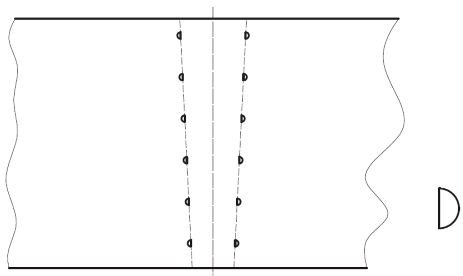

Figure 5. Structural configuration of the sweet potato seedling belt carrying device.

4.1.2. Experimental Research on Seedling Belt Carrying Device

To verify the suitability of different materials for the seedling belt carrying device and to determine the optimal material, experiments were conducted on paper-based carrier belts and polymer-composite carrier belts for sweet potato seedlings.

The paper-based carrier belt is constructed by bonding two layers of paper with adhesive, allowing for the manual insertion of the sweet potato seedlings into the designated slots of the belt. Experimental results indicate that sweet potato seedlings tend to lose moisture and wilt after a period when placed in the paper-based carrier belt. Additionally, the paper belt can easily break when exposed to water, making it unsuitable for watering or moisture-retaining operations, ultimately failing to maintain the freshness of the seedlings. Furthermore, the separation of the two layers of the paper carrier belt post-bonding is challenging, the bonding process is complex, and the cost of paper belts is relatively high, as shown in Figure 6.

Figure 6. Paper seedling carrier.

In contrast, the polymer-composite carrier belt is bonded using a thermal pressing technique to secure the two layers at specified points and distances. This method also allows for the manual insertion of the seedlings into the carrier belt's designated slots before rolling into rolls of polymer-composite carrier belts. To ensure the vitality of the seedlings, these polymer-composite rolls can be placed in a water tray or nutrient solution; however, care must be taken not to submerge them for too long, as prolonged exposure can lead to root bending, negatively affecting the subsequent growth of the tubers. Experimental findings demonstrate that the polymer-composite belts exhibit high strength, excellent flexibility, and low cost. When planting at a density of 3000~4000 seedlings per acre, the cost of the carrier belt is estimated to be between 40 and 50 RMB per acre, which aligns well with user production requirements. Consequently, polymer-composite carrier belts are preferred, as illustrated in Figure 7.

Figure 7. Polymer seedling carrier.

4.2. Design of Key Parameters for Offset Tillage and Ridge Formation

4.2.1. Design of the Bidirectional Offset Device

To address issues such as the mismatched wheel spacing of tractors, incomplete coverage in hilly or small plots, and difficulties in switching rows during ridge cultivation operations [7], a hydraulic bidirectional offset mechanism has been designed. This mechanism allows the equipment to operate close to field edges and rows, as well as execute "S"-shaped movements. Furthermore, it enables the equipment to align with the ridge edges during the end-of-row operations, minimizing the distance between neighboring ridges, improving equipment adaptability, and enhancing plot utilization.

The hydraulic bidirectional offset mechanism derives its power from the tractor. During operation, a hydraulic oil line connects to the tractor's hydraulic interface. Depending on the specific offset operation required, a manual directional valve controls the flow of hydraulic oil in and out of the left and right hydraulic cylinders, enabling lateral movement of the hydraulic rod, which is connected to the frame. This configuration allows the bidirectional offset mechanism to pivot around the three-point hitch to achieve lateral offset, as depicted in the schematic in Figure 8.

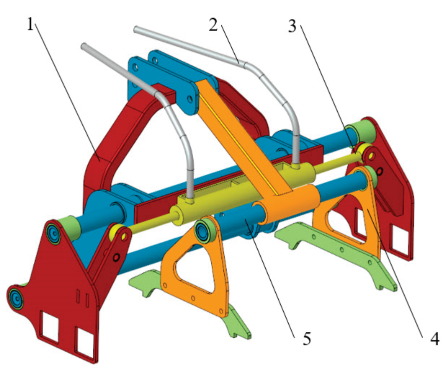

Figure 8. Structural diagram of the bidirectional offset mechanism: 1. linking device; 2. hydraulic oil hose; 3. hydraulic cylinder; 4. slide guide; and 5. connection plate.

Based on the parameters of tractors with power ratings between 50 and 70 horsepower, the left and right offset length of the mechanism is set at 20 cm, facilitating edge and aligned operations [8]. The hydraulic cylinder's body length is approximately 60 cm, while the stroke of the single-sided hydraulic rod is 20 cm. The load capacity of the hydraulic cylinder mainly arises from the sliding friction between the unit during translational movement and the frame. Based on trials of the initial prototype, the equipment weight is around 320 kg, translating to a gravitational force of approximately 3200 N. The installation position of the bidirectional offset mechanism is centrally located within the width of the three-point hitch with no imbalanced forces set for operation. The load force can be calculated using the following formula:

$$F = \mu G \tag{1}$$

In the formula, F is load force, N; μ is the coefficient of sliding friction; and G is the weight of the individual unit, N.

According to the Mechanical Design Handbook, the inner diameter of a hydraulic cylinder can be calculated using the following formula:

$$D = \sqrt{\frac{4F}{\pi P \times 10^6} + d^2} \tag{2}$$

In the formula, D—inner diameter, m; d—rod diameter, m; and P—actual load pressure, Mpa.

During actual operation, when the coefficient of sliding friction μ is 0.1, the rated output pressure of a hydraulic system on a 50~70 horsepower tractor is 16 MPa. Based on the Mechanical Design Handbook, if the gear ratio φ is taken as 1.46, d can be determined using the following formula:

$$d = D\sqrt{\frac{\varphi - 1}{\varphi}} \tag{3}$$

From this, Formula (3) can be expressed as follows:

$$D = \sqrt{\frac{146F}{25\pi P \times 10^6}} \tag{4}$$

By solving Equation (4), the result is calculated to be 6.09 mm. This indicates that a hydraulic cylinder inner diameter of 6.09 mm is sufficient to meet the operational requirements for bidirectional offset. Based on commonly used hydraulic cylinder specifications, a double-rod hydraulic cylinder with equal speed and stroke is selected. The main working parameters of the hydraulic cylinder are shown in Table 2.

Table 2. Hydraulic cylinder working parameters.

Name	Inner Diameter/mm	Rod Diameter/mm	Piston Stroke/mm
Double-rod hydraulic cylinder	40	20	200

4.2.2. Design of the Precision Tillage Device

Soil fragmentation is a critical factor affecting the quality of ridge shaping and transplanting [9,10]. To enhance soil fragmentation and improve the quality of ridge shaping and transplanting, this study utilizes a dual-structured "rotary tillage + soil crushing" precision tillage device. The dual-rotation mechanism is also effective in minimizing the effect of root stubble in the soil on the quality of starting and transplanting, as demonstrated in Figure 9.

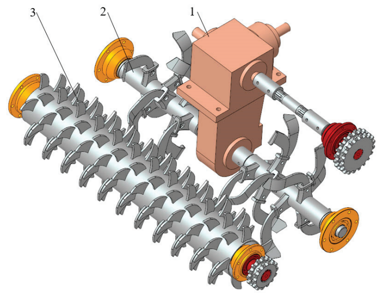

Figure 9. Structural schematic of the precision tillage device: 1. gearbox; 2. rotary tillage device; 3. soil crushing device.

The power for the fine tillage device is provided by the tractor, with a universal joint connecting the tractor's rear power output shaft to the gearbox of the rotary tiller. The gearbox, through gear transmission, supplies power to the rotary tillage device, while the side axle of the gearbox provides power to the soil crushing mechanism. During operation, the rotary tillage device throws the soil and root residues into the crushing device, where the soil clumps and residues are further cut into finer pieces. To optimize the soil crushing rate, the crushing blades of the device are arranged in an interleaved spiral configuration. Based on the preliminary transplanting test results, the lateral spacing for the crushing blades is designed to be 30 mm, satisfying the demands of the transplanting operations.

4.2.3. Design of the Ridge Shaping Device

The ridge shaping device primarily consists of a ridge shaping plate and an adjustment mechanism, as shown in Figure 10.

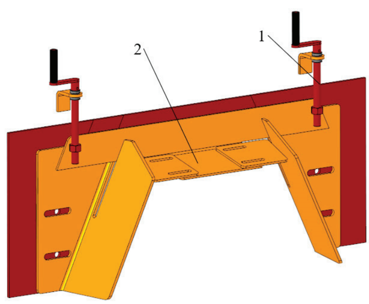

Figure 10. Structural diagram of the ridge shaping device: 1. ridge shaping plate and 2. adjustment mechanism.

To ensure soil permeability and ridge compaction, the formation plate is designed with a "trumpet" shape, with dimensions configured according to mechanized operational modes. The entrance of the ridge shaping plate is designed for a ridge height of 350 mm, a bottom width of 800 mm, and a top width of 350 mm, while the exit plate is designed for a ridge height of 300 mm, a bottom width of 700 mm, and a top width of 300 mm. Furthermore, to enhance the adaptability of the equipment, the ridge shaping plate can be adjusted laterally, and its height can be modulated via an adjustment lever.

4.3. Design of Key Parameters for Seedling Separation

4.3.1. Design of the Seedling Separation System

The seedling separation process refers to the stable separation and recovery of the double-layer seedling belt, allowing the sweet potato seedlings to be extracted from the roll and transferred in a single, orderly manner to the seedling transport belt. The key components of the seedling separation apparatus mainly include the active separation mechanism, the seedling holding mechanism, and the seedling belt tensioning mechanism, as shown in Figure 11.

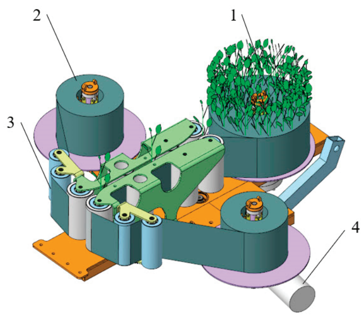

Figure 11. Structural diagram of the seedling separation device: 1. sweet potato seedling belt; 2. seedling separation device; 3. tensioning device; and 4. drive motor.

During operation, a motor drives the separation mechanism to perform a rotational motion. Through this rotational movement, the double-layer seedling belt is separated and collected into a roll. The seedling holding mechanism rotates around the axis of rotation to facilitate the seedling separation operation. To ensure an orderly and precise transfer of the separated seed potatoes to the transport device, it is essential to maintain continuous tension in the seedling belt throughout the process. This requires that both the active separation mechanism and the seedling holding mechanism rotate without self-rotation during their movements under the tensioning condition. Additionally, to enable the rapid loading and unloading of the rolled seedling belt and facilitate the quick detachment of the collected rolls by the separation mechanism, research on rapid replacement devices needs to be conducted.

4.3.2. Design and Selection of the Constant Tension Device

Seedling separation refers to the process of stably separating and recovering the double-layered seedling belt, allowing the sweet potato seedlings to be extracted from the carrier and conveyed individually and orderly onto the seedling delivery belt.

The seedling carrying mechanism produces a rotational motion under the influence of the separation mechanism. In the absence of a damping device, the rotational axis may easily self-rotate due to inertia, preventing the seedling belt from remaining in a tensioned state. To eliminate this issue and ensure that the seedling belt maintains constant tension during the separation process, a magnetic particle brake is designed, as illustrated in Figure 12.

Figure 12. Magnetic particle brake.

The magnetic particle brake utilizes a magnetic particle clutch, which transmits torque using magnetic particle clutches under the effect of electromagnetic force. When current flows through the coil, a magnetic field is generated, magnetizing the internal powder and causing it to attract itself, forming a strong magnetic coupling surface. As the current increases, the powder is activated in the magnetic field, which increases the friction of the clutch and enhances torque transmission between the input and output shafts. Conversely, when the current decreases or is cut off, the magnetization of the powder decreases, reducing the coupling force and thereby decreasing or disconnecting torque transmission. Therefore, by adjusting the current intensity, one can accurately control the friction and torque output of the clutch, enabling adjustments to the tension or rotational speed.

The constant tension is related to the characteristics of the seedling belt material, calculated using a specific formula:

$$F = k\sigma_s bh \tag{5}$$

In the formula, k is the tension coefficient; σ_s is the yield strength, MPa; b is the width of the seedling carrier, mm; and h is the thickness of the seedling carrier, mm. Here, $k < 1$; when $k = 1$, the tension in the carrier reaches the yield limit. After field adjustments, k is set to 0.4; σ_s = 21 MPa = 21 N·mm^{-2}; b = 150 mm, h = 0.07 mm, leading to a calculated constant tension F = 88 N.

According to the definition of torque, the maximum torque M_{max} for the film unwind roll can be calculated using the following formula:

$$M_{max} = \frac{F \times D_{max}}{2} \tag{6}$$

In the formula, M is the torque of the film unwind roll, N·m; F is the tension in the seedling carrier, N; and D is the diameter of the film unwind roll, m. With the maximum seedling carrier roll diameter D_{max} being 0.5 m, the calculated maximum torque M_{max} for the film unwind roll is 22 N·m. Therefore, when selecting a dual-shaft magnetic particle clutch, its rated torque must not be less than 22 N·m. The FL-25-S dual-shaft magnetic particle clutch is selected, with its performance parameters listed in Table 3 below.

Table 3. Magnetic particle clutch performance parameters.

Name	Parameter
Product model	FL-25-S
Rated torque/(N·m)	25
Rated voltage (V)	24
Rated speed (rpm)	1400
Rated current (A)	1.5

This paper selects the FL-25-S dual-shaft magnetic particle clutches, which allows adjustable torque ranging from 0 to 25 N·m and a rotational speed of 0~1400 rpm, meeting the requirements for maintaining constant tension in the seedling belt during roll operations.

Experimental studies indicate that the electromagnetic damping device maintains stable tension during the rotation of the seedling belt, keeping it in a tensioned state. The damping device ensures constant tension, which can also be adjusted based on need, possessing advantages of convenience, stability, and reliability.

4.3.3. Design of the Quick-Change Device

Through research, it has been found that the core shaft of the seedling roll production companies is commonly a cylindrical shape with a certain wall thickness, in accordance with relevant standards. The square coordinate fit for the core shaft is relatively rare. When using a cylindrical core shaft, a hinged quick replacement device has been designed to achieve the rapid switching of the rolled seedling belt and separation mechanism after coiling, while also preventing the rolling of the seedling belt and the coiled collection belt, as shown in Figure 13.

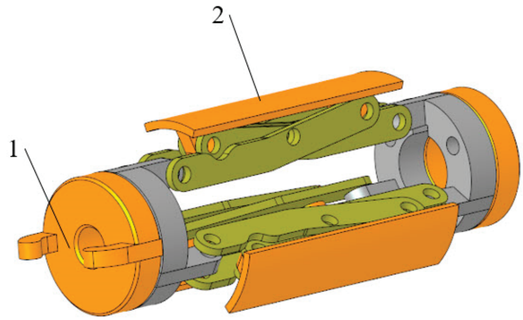

Figure 13. Structural diagram of the quick-change device: 1. locking mechanism and 2. support device.

The inner diameter of the seedling core shaft is 60 mm, and to standardize dimensions, the inner diameter of the collection belt shaft is also set to 60 mm. The design of the quick replacement device allows for a contraction and expansion range of 59~61 mm. During operation, the cylindrical core shaft is fitted into the replacement device, and by rotating the adjustment mechanism, the hinged structure is raised to facilitate quick replacement, which also prevents self-rotation. Conversely, the hinged structure can be contracted for rapid disassembly.

4.4. Design of Key Parameters for Horizontal Positioning and Shaping

4.4.1. Principle of Horizontal Positioning and Shaping

The process of achieving a horizontal posture of the seedlings refers to the horizontal positioning of the portion of the seed potatoes that is planted in the soil, as illustrated in Figure 14. During this horizontal positioning process, it is crucial to avoid damage to the seedling caused by the gripping components, as well as to prevent bending damage to the seedling roots when they touch the ground. To minimize gripping damage to the seedlings, the gripping component employs a flexible design made with double-layer sponge belts. Based on the previous experiments on seedling bending, it was determined that when the bending angle of the seedlings exceeds 90 degrees, bending damage is likely to occur. To avoid this, after achieving a horizontal posture, it is optimal for the angle between the seedling tip and the horizontal direction to be around 80 degrees. Furthermore, considering the physical characteristics of the seedlings, the width of the gripping component should not be excessively wide, as a wider grip may lead to the phenomenon where the stem separates from the transport belt while the leaf petiole and leaves remain attached. Through experimental research on different widths of the seedling belt, a width of 30 mm has been determined as suitable.

After the seedlings are separated from the seedling belt, they are conveyed downward at an angle by the grabbing component until the seedling roots touch the ground and bend to meet the horizontal planting requirement. To ensure a smooth transition of the seedlings onto the transport belt, the transport belt must simultaneously grip the seedlings before separation. Additionally, during the angled downward transportation of the seedlings, to guarantee the stability of the gripping posture and prevent the seedlings from falling during transport, an elastic pressing device should be added to the inner side of the transport belt to maintain stable gripping on the seedlings.

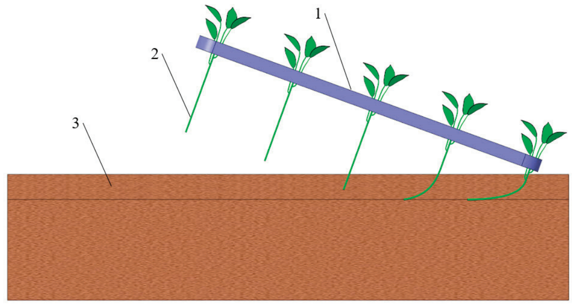

Figure 14. Schematic diagram of horizontal positioning and shaping: 1. seedling delivery belt; 2. sweet potato seedlings; and 3. ridge body.

4.4.2. Motion Analysis for Horizontal Positioning and Shaping

The movement relationships during the downward transportation of the seedlings on the transport belt are illustrated in Figure 15.

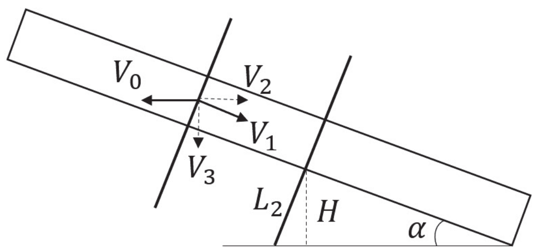

Figure 15. Motion analysis diagram for horizontal positioning and shaping.

In the figure, V_0 represents the forward speed of the machinery, V_1 is the speed of the transport belt, V_2 is the horizontal component speed of the transport belt, and V_3 is the vertical component speed of the transport belt. The length from the seedling root to the edge of the transport belt is L_2, and the distance from the edge of the transport belt to the bottom of the ditch is H. Once the machinery is operating stably, for the seedlings to achieve a horizontal posture when the roots touch the ground, the seedlings must exhibit a tendency to move in the opposite direction of the machinery's forward motion. The following conditions must be met:

$$V_2 = V_1 \cos\alpha > V_0 \tag{7}$$

If the specified planting distance for the seedlings is L_0, and the spacing between seedlings on the belt is L_1, the time required to plant the next seedling after the previous one is Δt. The transplanting machine must maintain stable planting spacing throughout the process, then

$$\Delta t = \frac{L_1 \sin\alpha}{V_3} \tag{8}$$

V_3 is the vertical speed of the transport belt, then

$$V_3 = V_1 \sin\alpha \tag{9}$$

Substituting Equation (9) into (8) yields

$$\Delta t = \frac{L_1}{V_1} \tag{10}$$

Based on the characteristics of horizontal posture formation, the planting distance can be expressed as

$$L_0 = L\cos\alpha - (V_2 - V_0)\Delta t \tag{11}$$

After simplification,

$$V_1 = \frac{L_1}{L_0} \times V_0 \tag{12}$$

When the seedlings separate from the transport belt, the conditions to achieve a horizontal posture must also be satisfied:

$$V_1 \sin\alpha\Delta t \geq H \tag{13}$$

That is,

$$V_1 \sin\alpha\Delta t \geq L_2 \cos\alpha \tag{14}$$

After simplification,

$$L_1 \sin\alpha \geq L_2 \cos\alpha \tag{15}$$

$$\cos\alpha \geq \sin\alpha \tag{16}$$

In summary, the angle between the transport belt and the horizontal is $\alpha \leq 45°$; this paper designates the angle between the transport belt and the horizontal to be 25°.

4.5. Design of Key Parameters for Planting Upright Seedlings

4.5.1. Design of the Ditching and Depth-Fixing Part

The main function of the grooving and depth setting parts is to open the seedling groove to prepare for the potato seedling to land on the bed, mainly including the grooving piece, connecting plate, etc. According to the potato seedling and seedling conveyor belt, the groove opener is designed as a large upper and small lower structure, as shown in Figure 16. The ditching and depth-fixing part is firmly attached to the frame through connecting plates. According to the agronomic requirements for sweet potato seedling planting, the ditch depth is designed to be 80 mm, with an adjustable ditch depth range of 0~80 mm. According to the physical characteristics of the potato seedlings, in order to minimize the collision of the seedlings with the side wall of the groove opener when they are transported diagonally downward, the width of the groove is designed to be 50 mm. To allow the seedling transport component to be submerged into the ditch opener, the upper opening of the ditch device is designed to be 190 mm wide. In order to make the trenching and depth setting parts have better soil breaking performance, after trenching to form a “clean zone” inside the trenching and depth setting parts, the design of the two trenching pieces into the soil at an angle of 35° can effectively reduce the impact of the soil, weeds, etc., on the transplanting [11–13], and the position of its position before and after is adjustable, with an adjustable range of 0~50 mm.

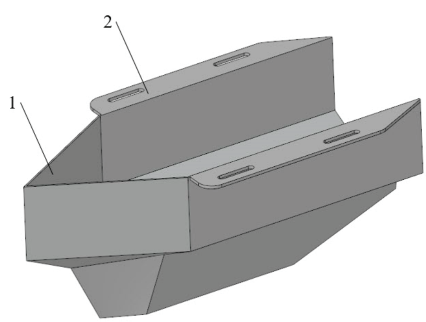

Figure 16. Structural diagram of the ditching and depth-fixing mechanism: 1. opening blade and 2. connection plate.

4.5.2. Design of Key Parameters for Soil Covering and Exposing Seedling Tips

Once the seedlings have achieved a horizontal posture and are about to be released from the seedling transport belt, soil covering of the seedling roots is required while ensuring that the seedling tips remain exposed above the soil surface, referred to as the "soil covering and exposing seedling tips". To achieve this operation, an active screw soil covering and tip exposure mechanism has been designed.

The active screw soil covering and exposing seedling tip mechanism mainly consists of a driving motor, connecting plate, screw mechanism, transmission shaft, chain case, and position adjustment plate, as shown in Figure 17. The motor drives the screw mechanism to perform the soil covering and exposes the seedling tips via chain transmission. The position of the screw mechanism can be adjusted both vertically and horizontally using the adjustment plate.

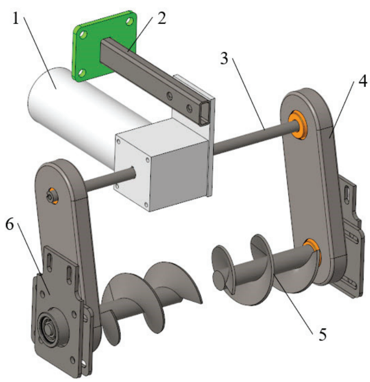

Figure 17. Active spiral soil covering and exposing seedling tip components: 1. drive motor; 2. connection plate; 3. drive shaft; 4. chain cover; 5. spiral mechanism; and 6. position adjustment plate.

Parameter Design of the Screw Mechanism

The soil covering process requires soil particles to move outward along the axial direction, meaning that the velocity vector of the particles must move from the inside toward the outside (with a friction angle relative to the normal of the screw surface) [14–17]. The conditions for this are as follows:

$$\tan\alpha \leq 1/\tan\varphi \tag{17}$$

In the formula, α is the screw angle (°) and φ is the friction angle between the soil and the steel plate (°). Since the screw angle varies at different points along the blade, with the maximum screw angle at the minimum radius, it is sufficient for the screw angle at the inner diameter to meet the conditions.

The theoretical volume of soil moved by the screw mechanism in the ditch can be considered as the volume of the furrow created, which can be modeled as a rectangular prism. The volume of soil required to cover the ditch can be expressed as

$$V = bvh \tag{18}$$

where b is the working width (m); v is the forward speed (m·s^{-1}); and h is the tillage depth (m). Based on the agronomic requirements for the sweet potato seedling transplanter and to improve transplanting efficiency, the operational speed of the tractor is set to be between 0.1 and 0.4 m·s^{-1}. With a ditch width of 50 mm and a ditch depth of 80 mm, the volume of soil required to cover the ditch is calculated to be approximately 4×10^{-4}~1.6×10^{-3} m^3·s^{-1}.

Referencing the design methods for open screw conveyors, to ensure stable soil movement and prevent clogging, the screw covering mechanism must meet the following requirements:

The conveying capacity of the screw mechanism must exceed the soil input rate, or sludging may occur.

The soil must not exhibit vertical jumping or rolling perpendicular to the direction of conveyance.

The soil must be conveyed axially, meaning that both axial forces and axial velocity must be greater than 0.

Based on the design principles of screw conveyors, the formulas for the design parameters of the screw mechanism are as follows:

Spiral outer diameter:

$$D \geq K \sqrt[2.5]{\frac{V}{\varphi \varepsilon \rho}} \tag{19}$$

Shaft diameter:

$$d = (0.2 \sim 0.35)D \tag{20}$$

Spiral speed:

$$n \leq n_{max} = \frac{A}{\sqrt{D}} \tag{21}$$

Screw pitch:

$$S_{max} = (0.5 \sim 2.2)D \tag{22}$$

In the formula, V is the amount of mud transported, $m^3 \cdot s^{-1}$; K is the comprehensive characteristic coefficient of the mud; φ is the filling coefficient; ε is the slope coefficient; ρ is the bulk density of the conveyed material, $t \cdot m^{-3}$; and A is the comprehensive characteristic coefficient of the material.

Since the left and right soil covering screws are arranged symmetrically, the mud transport capacity of each screw mechanism should be half of the total soil required to fill the seedling ditch, and thus is set to range between 2×10^{-4} and 0.8×10^{-3} $m^3 \cdot s^{-1}$. The topsoil for sweet potato seedling transplanting has a certain fluidity, referring to the design standards for screw conveyors, and the estimated comprehensive characteristic coefficient for the soil K is taken as 0.0415. The filling factor φ is set to 0.4; since the spirals are positioned horizontally, the inclination coefficient ε is set to 1.0; the comprehensive characteristic coefficient A for the soil is taken as 75; and the bulk density ρ of the soil is set at 1.8 $t \cdot m^{-3}$.

From Equation (19), the outer diameter of the screw is calculated to be $D \geq 72$ mm. Considering the overall mass of the machine and its compatibility with the tractor, the outer diameter is determined to be $D = 100$ mm. From Equation (20), the screw shaft diameter is determined to be between 20 and 35 mm. To minimize the entanglement of grass on the shaft and to enhance soil transport capacity, the screw shaft diameter is chosen as $d = 30$ mm. The pitch from Equation (22) is determined to be in the range of 50 to 220 mm. To ensure smooth soil transport within the screw and to prevent mud accumulation, the soil transport amount of each pitch section must exceed the combined mud input from the current and previous pitch sections. Therefore, this study adopts a variable-pitch, constant-diameter screw, where the pitch increases along the helices towards the furrow, with the largest pitch closest to the furrow. Based on the structure and configuration dimensions of the machine, the maximum operational rotational speed from Equation (21) is calculated to be 237 rpm.

5. Performance Testing and Analysis

To achieve efficient and sustainable sweet potato seedling planting, the performance of the sweet potato seedling belt transplanter is evaluated.

5.1. Testing Conditions and Equipment

In May 2023, a sweet potato seedling transplanting test was conducted in Qingzhou City, Shandong Province, where the test site was an idle winter field, consisting of sandy soil with a moisture content of approximately 16% to 18% (0~100 mm). The sweet potato seedlings used in the test were 300 to 350 mm in length and 4 to 6 in diameter. The test equipment primarily consisted of a Dongfanghong 504 tractor, sweet potato seedling belt transplanter, moisture meter, calculators, ruler, tape measure, tachometer, etc.

5.2. Experimental Design and Methods

To improve planting quality, achieve horizontal planting of the sweet potato seedlings, and enhance yield, quality, and uniformity of sweet potato seedling tubers, several key parameters affecting the whole machine's performance and operational effectiveness were selected as test factors: the forward speed of the machine v, the screw speed n, and the spacing of the ribbons τ (the distance between the centerline of the screw shaft and the end of the conveyor belt, hereinafter referred to as the pitch of the screw belt). The planting spacing Z was taken as the evaluation index to characterize the operation quality of the machine. According to the above experimental plan, single-factor tests were conducted to identify the factors influencing the qualified rate of planting spacing and their respective ranges. A three-factor, three-level orthogonal test ($L^9(3^4)$) [18,19] was designed, with factor levels shown in Table 4.

Table 4. Factors and levels of the orthogonal test.

Test Level	The Forward Speed of the Machine v/m·s^{-1}	Spacing of the Ribbons τ/mm	The Screw Speed n/rpm
1	0.20	40	120
2	0.30	60	140
3	0.40	80	160

During the tests, different combinations of forward speed, spacing of the ribbons, and screw speeds were adjusted to calculate the qualified rate of planting spacing Z, thus analyzing and evaluating the operational performance of the machine. Each experimental group was repeated three times to take an average value [20]. The assessment criteria for the experiments were based on GB/T 5262 standards [21]. Three measurement areas were randomly selected within the test site, where each area must contain two adjacent operational widths. In each area, one row was chosen, and 120 consecutive planting spacings were measured [22]. A standard planting spacing of D = 200 mm was established, with measured spacings considered qualified if they fell within D(1 ± 10%). The percentage of qualified spacings relative to the total measured count was calculated to determine the qualified rate of spacings [23,24], based on Equations (23) and (24):

$$Z_i = \frac{N_{zi}}{N} \times 100 \tag{23}$$

$$Z = \frac{\sum_{i=1}^{n} z_i}{n} \times 100 \tag{24}$$

In the above formulas, the following notations are used:
N_{zi}—The number of qualified plant spacings in the testing area;
N—Total number of samples determined in the detection area, N = 120;
Z_i—The qualified rate of planting spacing in the detection area (%);
Z—The qualified rate of planting spacing (%);
n—The number of detection areas, n= 3.

5.3. Test Results and Analysis

The experimental results obtained from the orthogonal performance tests are presented in Table 5, where A, B and C represent the levels of the parameters v, τ and n, respectively.

Table 5. Results and orthogonal test.

Test Number		Test Factor *A*	*B*	*C*	Test Index Planting Spacing Qualification Rate *Z*/%
1		1	1	1	85.56
2		1	2	2	91.78
3		1	3	3	87.57
4		2	1	2	91.17
5		2	2	3	95.33
6		2	3	1	87.86
7		3	1	3	91.21
8		3	2	1	91.95
9		3	3	2	88.42
Z	k_1	88.30	89.31	88.46	
	k_2	91.45	93.02	90.46	
	k_3	90.53	87.95	91.37	
	R	3.15	5.07	2.91	

An analysis of the range values for each factor in Table 5 indicates that [25], regarding the evaluation indicators, the order of significance for each factor's influence is as follows: B, A, C, with the optimal combination of factor levels identified as $A_2B_2C_3$.

Using SPSS 21.0 data processing software, a variance analysis was performed on the experimental results, as shown in Table 6 [26]. As can be seen from Table 6, the value of the sum of squares of the error terms is much smaller than the sum of squares of the influencing factors, indicating that the interaction between the test factors does not have a significant effect on the test assessment indicators [27,28]. When analyzing the qualified rate of planting spacing Z, it is evident from the F-value that the experimental factors A, B and C have a significant impact on the evaluation indicator Z. From $F_B > F_A > F_C$, it is evident that the experimental factor B has the greatest impact on the evaluation indicators, followed by factor A, while factor C has the least influence, which is consistent with the results of the range analysis.

Table 6. Analysis of variance.

Evaluation Indicators	Source of Variation	Sum of Squares	Degrees of Freedom	Sum of Mean Squares	*F*	*p*
Z	calibration model	70.35	6	11.73	49.06	0.020 *
	A	15.72	2	7.86	32.90	0.029 *
	B	41.30	2	20.65	86.42	0.011 *
	C	13.32	2	6.67	27.87	0.035 *
	error	0.48	2	0.24		

Note: $R^2 = 0.995$; * is significant ($p < 0.05$).

Combining the results of the range analysis and the variance analysis, it can be concluded that the best parameter combination for transplanting performance was $A_2B_2C_3$, which corresponds to a forward speed of 0.3 $m \cdot s^{-1}$, a ribbon spacing of 60 mm, and a screw speed of 160 rpm.

5.4. Field Experiment

In order to verify the working performance of the transplanter in the above results, a field trial was conducted in May 2023 at the sweet potato planting base in Qingzhou City, Shandong Province, China. Prior to the experiments, the machine's operational parameters were adjusted to the optimal combination: a forward speed of 0.3 $m \cdot s^{-1}$, a ribbon spacing of 60 mm, and a screw speed of 160 rpm. A total of six sets of repeated experiments were conducted, with each set containing 120 measured planting spacings. The results of these experiments are presented in Table 7 and in Figure 18.

Table 7. Results of the field test.

Test Serial Number	Planting Spacing Qualification Rate Z/%
1	90.21
2	89.63
3	91.32
4	89.74
5	90.96
6	90.38
mean	90.37

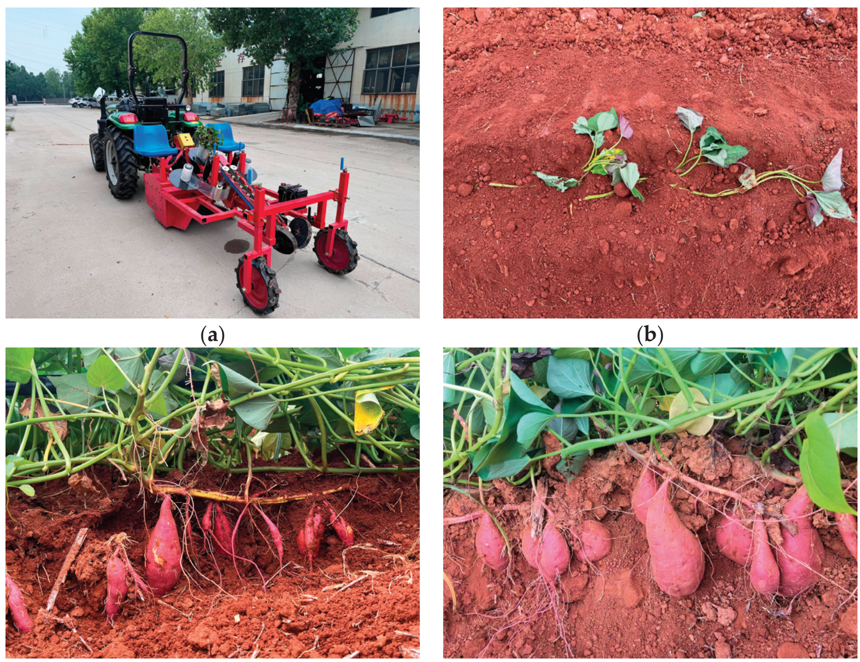
(**a**) (**b**) (**c**) (**d**)

Figure 18. Field experiment results: (**a**) field experiment equipment; (**b**) experiment result; (**c**) growth situation; and (**d**) growth situation.

The test results show that the average planting distance of the sweet potato bare seedling horizontal transplanter is 90.37%, which is in line with the relevant agricultural machinery industry technology and standards and local agronomic production requirements. The horizontal planting of potato seedlings can be realized, which is beneficial to improve the uniformity and yield of sweet potato.

6. Discussion

In this paper, the effects of machine advance speed, spacing between spirals and the screw speed on the planting spacing qualification rate were studied. Further optimization and improvement of the machine is needed in later experiments for indexes such as the planting depth qualification rate and planting spacing variation coefficient.

Additionally, it was observed during the experiments that, with the planting spacing fixed, there is a need to match the seedling delivery speed with the forward speed. However, as the roll diameter of the seedling conveyor increases, the relationship between the seedling separation line speed and the forward speed changes continuously, which affects the planting spacing to some extent.

The sweet potato seedling belt transplanter has preliminarily achieved automation in sweet potato seedling transplanting; however, manual intervention is still required to thread the seedlings onto the conveyor belt. Future research could focus on developing key technologies for automatic seedling bundling.

7. Conclusions

The designed sweet potato seedling belt replica transplanter initially realizes automatic and horizontal planting of sweet potato. The machine saves the labor of one to two people, and at an operating speed of 0.3 $m \cdot s^{-1}$, the machine plants 90 plants per minute, which improves the efficiency by more than 40% compared with the semi-automatic transplanting machine.

The main parameters affecting the working performance and operational effectiveness of the whole machine were obtained. Tests on the main parameters affecting the working performance and operational effectiveness of the whole machine were carried out. The test results show that the primary and secondary orders of the Z significance of the qualified rate of planting spacing for the impact evaluation index are B, A and C, the optimal level combination of influencing factors is $A_2B_2C_3$, the forward speed of the machine is 0.3 $m \cdot s^{-1}$, the spacing of the ribbons is 60 mm, and the screw speed is 160 rpm.

Transplanters meet sweet potato production requirements. The field test results show that under the optimal combination of factor levels, the Z-average rate of planting spacing was 90.37%, which met the relevant technical standards and agronomic requirements.

Author Contributions: Conceptualization, W.Y. and M.H.; methodology, W.Y.; software, K.L.; validation, W.Y., M.H. and C.W.; formal analysis, W.Y.; investigation, K.L.; resources, Y.J.; data curation, W.Y.; writing—original draft preparation, W.Y.; writing—review and editing, W.Y. and Z.R.; visualization, C.W.; supervision, Z.R.; project administration, W.Z. All authors have read and agreed to the published version of the manuscript.

Funding: This research was funded by the Key R&D Plan of Jiangsu Province (Grant No. BE2021311) and China Agriculture Research System of MOF and MARA (Grant No. CARS-10-B19).

Institutional Review Board Statement: Not applicable.

Data Availability Statement: The datasets used and/or analyzed during the current study are available from the corresponding author on reasonable request.

Conflicts of Interest: The authors declare no conflicts of interest.

References

1. Li, Q.; Zhao, H.; Jin, Y.L.; Zhu, J.C.; Ma, D.F. Analysis and perspectives of sweetpotato industry contributing to national food security in China. *Jiangsu JOAS* **2022**, *38*, 1484–1491.
2. Ma, D.F.; Li, Q.; Cao, Q.H.; Niu, F.X.; Xie, Y.P.; Tang, J.; Li, H.M. Development and prospect of sweetpotato industry and its technologies in China. *Jiangsu JOAS* **2012**, *28*, 969–973.
3. Hu, L.L.; Ji, F.L.; Wang, B.; Ling, X.Y.; Hu, Z.C.; Yu, X.T. Latest developments of sweet potato mechanical transplanting in China. *J. Chin. Agric.* **2015**, *36*, 289–291, 317.
4. Yan, W.; Zhang, W.Y.; Hu, M.J.; Ji, Y.; Li, K.; Qi, B. Present situation of research and expectation on plant mechanization of sweet potato in China and abroad. *J. Chin. Agric.* **2018**, *39*, 12–16.
5. Sarkar, P.; Upadhyay, G.; Raheman, H. Active-passive and passive-passive configurations of combined tillage implements for improved tillage and tractive performance. *Span. J. Agric. Res.* **2021**, *19*, e02R01. [CrossRef]
6. Ma, D.F.; Liu, Q.C.; Zhang, L.M. China Sweet Potato. *Jiangsu PSTP* **2021**, *3*, 337–340.
7. Upadhyay, G.; Raheman, H. Performance of combined offset disc harrow (front active and rear passive set configuration) in soil bin. *J. Terramech.* **2018**, *78*, 27–37. [CrossRef]
8. Zhang, L.M.; Ma, D.F. *Main Cultivation Modes of Sweet Potato in China*, 1st ed.; China Agricultural Science and Technology Press: Beijing, China, 2012; pp. 102–108.
9. Zhao, H.; Liu, X.X.; Pan, Z.G.; Li, L.; Sun, Y. Agronomic characteristics and mechanized planting technology of sweet potato. *J. Chin. Agric* **2021**, *42*, 21–26.

10. Shao, Y.Y.; Xuan, G.T.; Hou, J.L.; Hu, Z.C.; Wang, Y.X.; Liu, Y. Design and Simulation of sweet potato mulched transplanting mechanism with "boat"-shape. *ASABE* **2018**, *39*, 2–6.
11. Zhao, S.H.; Gu, Z.Y.; Yuan, Y.W.; Lu, J.Q. Bionic Design and Experiment of Potato Curved Surface Sowing Furrow Opener. *Trans. CSAM* **2021**, *52*, 32–42.
12. Zhao, S.H.; Yang, L.L.; Zhang, X.; Hou, L.T.; Yuan, Y.W.; Yang, Y.Q. Design and Experiment of Zigzag Opener for Double-row No-tillage Seeding on Soybean Ridge. *Trans. CSAM* **2022**, *53*, 74–84.
13. Zeng, S.; Tang, H.T.; Luo, X.W.; Ma, G.H.; Wang, Z.M.; Zang, Y.; Zhang, M.H. Design and experiment of precision rice hill-drop drilling machine for dry land with synchronous fertilizing. *Trans. CSAE* **2012**, *28*, 12–19.
14. Qi, J.T.; Meng, H.W.; Kan, Z.; Li, C.S.; Li, Y.P. Analysis and test of feeding performance of dual-spiral cow feeding device based on EDEM. *Trans. CSAE* **2017**, *33*, 65–71.
15. Yang, W.W.; Luo, X.W.; Wang, Z.M.; Zhang, M.H.; Zeng, S.; Zang, Y. Design and experiment of track filling assembly mounted on wheeled-tractor for paddy fields. *Trans. CSAE* **2016**, *32*, 26–31.
16. Meng, H.W.; Gao, Z.J.; Kan, Z.; Lin, H. Design and experiment on dairy cow precision-feeding device based on equal-diameter and variable-pitch. *Trans. CSAE* **2011**, *27*, 103–107.
17. Dai, F.; Zhang, S.L.; Song, X.F.; Zhao, W.Y.; Ma, H.J.; Zhang, F.W. Design and Test of Combined Operation Machine for Double Width Filming and Covering Soil on Double Ridges. *Trans. CSAM* **2020**, *51*, 108–117.
18. Chen, K. *Experimental Design and Analysis*, 2nd ed.; Tsinghua University Press: Beijing, China, 2015; pp. 172–188.
19. Shao, Y.Y.; Liu, Y.; Xuan, G.T.; Hu, Z.C.; Han, X.; Wang, Y.X.; Chen, B.; Wang, W.Y. Design and Test of Multifunctional Vegetable Transplanting Machine. *IFAC* **2019**, *52*, 92–97. [CrossRef]
20. Shi, Y.Y.; Luo, W.W.; Hu, Z.C.; Wu, F.; Gu, F.W.; Chen, Y.Q. Design and Test of Equipment for Straw Crushing with Strip-laying and Seed-belt Classification with Cleaning under Full Straw Mulching. *Trans. CSAM* **2019**, *50*, 58–67.
21. *GB/T 5262*; Measuring Methods for Agricultural Machinery Testing Conditions-General Rules. SAC: Beijing, China, 2008.
22. Dai, F.; Zhao, W.Y.; Song, X.F.; Xin, S.L.; Liu, F.J.; Xin, B.B. Operating Parameter Optimization and Experiment of Device with Elevating and Covering Soil on Plastic-film. *Trans. CSAM* **2017**, *48*, 88–96.
23. Yan, W.; Hu, Z.C.; Wu, N.; Xu, H.B.; You, Z.Y.; Zhou, X.X. Parameter optimization and experiment for plastic film transport mechanism of shovel screen type plastic film residue collector. *Trans. CSAE* **2017**, *33*, 17–24.
24. Yan, W.; Hu, M.J.; Li, K.; Wang, J.; Zhang, W.Y. Design and experiment of horizontal transplanter for sweet potato seedlings. *Agriculture* **2022**, *12*, 675. [CrossRef]
25. Hu, L.L.; Wang, B.; Wang, G.P.; Yu, Z.Y.; You, Z.Y.; Hu, Z.C.; Wang, B.K.; Gao, X.M. Design and experiment of type 2ZGF-2 duplex sweet potato transplanter. *Trans. CSAE* **2016**, *32*, 8–16.
26. Xiang, W.; Wu, M.L.; Guan, C.Y.; Xu, Y.J. Design and experiment of planting hole forming device of crawler transplanter for rape (*Brassica napus*) seedlings. *Trans. CSAE* **2015**, *31*, 12–18.
27. Xu, H.B.; Hu, Z.C.; Zhang, P.; Gu, F.W.; Song, W.L.; Wang, C.C. Optimization and Experiment of Straw Back-Throwing Device of No-Tillage Drill Using Multi-Objective QPSO Algorithm. *Agriculture* **2021**, *11*, 986. [CrossRef]
28. Yang, H.G.; Yan, J.C.; Wei, H.; Wu, H.C.; Wang, S.Y.; Ji, L.L.; Xu, X.W.; Xie, H.X. Gradient Cleaning Method of Potato Based on Multi-Step Operation of Dry-Cleaning and Wet Cleaning. *Agriculture* **2021**, *11*, 1139. [CrossRef]

agriculture

Article

Design and Testing of Soybean Double-Row Seed-Metering Device with Double-Beveled Seed Guide Groove

Huajiang Zhu [1], Sihao Zhang [1], Wenjun Wang [1,*], Hongqian Lv [1], Yulong Chen [1], Long Zhou [1], Mingwei Li [1] and Jinhui Zhao [2]

[1] School of Agricultural Engineering and Food Science, Shandong University of Technology, Zibo 255000, China; 22503030045@stumail.sdut.edu.cn (H.Z.); 22403010040@stumail.sdut.edu.cn (S.Z.); 23403010309@stumail.sdut.edu.cn (H.L.); cyl06471@sdut.edu.cn (Y.C.); zhoulong21@sdut.edu.cn (L.Z.); lmw271314@sdut.edu.cn (M.L.)

[2] State Key Laboratory of Agricultural Equipment Technology, Beijing 100083, China; zhaojinhui@caams.org.cn

* Correspondence: wjwang2016@163.com

Abstract: During the operation of a shaped hole seed-metering device, poor seed-filling quality and inconsistent seed-casting points lead to poor seed spacing uniformity, especially in a one-chamber double-row seed-metering device. To solve this problem, a soybean double-row seed-metering device with double-beveled seed guide groove was designed to ensure a high single-seed rate and seed-casting point consistency. Through the theoretical analysis of the working process of the seed-metering device, dynamic and kinematic models of the seeds were established, and the main structural parameters of the seed discharge ring, triage convex ridge, shaped hole, and seed guide groove were determined. The main factors affecting the seeding performance were obtained as the following: the inclination angle of the triage convex ridge, the radius of the shaped hole, and the depth of the seed guide groove. A single-factor test was carried out by discrete element simulation to obtain the inclination angle of the triage convex ridge α_3 = 29°, the radius of the shaped hole r_1 = 4.16–4.5 mm, and the depth of the seed guide groove l_1 = 0.49–1.89 mm. A two-factor, five-level, second-order, orthogonal rotation combination test was conducted to further optimize the structural parameters of the seed-metering device. The two test factors were the radius of the shaped hole and the depth of the seed guide groove, and the evaluation indices were the qualified rate, replay rate, and missed seeding rate. The results showed that the optimal combinations of the structural parameters were the radius of the shaped hole r_1 = 4.33 mm and the depth of the seed guide groove l_1 = 1.20 mm. Subsequent bench testing demonstrated that the seed discharge's qualified rate was above 94% at operating speeds of 6–10 km/h, and the seeding performance was stable. The final results of the soil trench test showed that the seed-metering device exhibited a qualified rate of 93.31%, replay rate of 2.04%, and missed seeding rate of 4.65% at an operating speed of 8 km/h. This research outcome may serve as a valuable reference and source of inspiration for the innovative design of precision seed-metering devices.

Keywords: soybean; double-row planting; seed-metering device; guide filling; discrete element method

Citation: Zhu, H.; Zhang, S.; Wang, W.; Lv, H.; Chen, Y.; Zhou, L.; Li, M.; Zhao, J. Design and Testing of Soybean Double-Row Seed-Metering Device with Double-Beveled Seed Guide Groove. *Agriculture* **2024**, *14*, 1595. https://doi.org/10.3390/agriculture14091595

Academic Editors: Xiaojun Gao, Qinghui Lai and Tao Cui

Received: 20 July 2024
Revised: 7 September 2024
Accepted: 9 September 2024
Published: 13 September 2024

1. Introduction

Precision seeding represents a pivotal developmental trajectory and prevailing trend within the realm of contemporary seeding technology, embodying a commitment to enhancing agricultural efficiency. A seed-metering device is the core component of a precision seeding system, directly influencing the seeding quality and working efficiency [1,2]. Precision seed-metering devices are categorized into mechanical and pneumatic types based on the principle of operation [3]. A mechanical seed-metering device features a simple structure, an ease of maintenance, and low processing costs, making it widely utilized in China.

Researchers have extensively researched on how different filling ways and shaped hole structures affect the filling effect of seed-metering devices [4–9]. Zhang et al. [10] aimed to improve the probability of seeds entering the holes of disc seeders, addressing the issue of empty planting by designing a height difference at the edges of the holes. Meng et al. [11] developed a fixed disturbance ring to enhance the activity of seed populations, which subsequently facilitated the design of a fixed disturbance-assisted soybean seeder. To identify the pivotal parameters of a seed-metering device, Li et al. [12] analyzed the movement process and state of the seeds. Li et al. [13] adopted a centrifugal cone disc-pushing seed-filling method to improve the stability of seeding quality, adjusting the seed orientation through friction and vibration. Zhang et al. [14] developed a pneumatic, mechanical, combination single-disc double-row seeder that minimizes seed damage while simultaneously reducing production costs. Li et al. [15] investigated the structure of a seed disc and seed-cleaning device, leading to the design of a double-row pneumatic disc seeder that significantly enhanced the seed-filling rate. Guo et al. [16] improved seeding quality by utilizing a seed guide groove and an auxiliary air-assisted seed-filling shaped hole structure. Chen et al. [17] employed discrete element simulation software to dissect the factors and their combinations influencing seeding performance, ultimately guiding the design of a convex scoop seed-metering device. Dun et al. [18] studied a shaped hole structure. Huang et al. [19] improved the filling force and seeding stability by altering the structure of a seed-filling shaped hole. Their study provided a reference for the design of shaped hole structures. Foreign researchers designed a secondary seed-casting device based on the principle of orderly seeding, with seeds discharged from the same position [20–23]. Maschio Company (Campodarsego, Italy) uses airflow to ensure uniform plant spacing when seed-casting [24]. Researchers in China have also been researching the uniformity of seed-casting. A seed-guiding mechanism designed by Dong et al. [25] significantly enhanced the seed-casting performance of a seed-metering device under high-speed operating conditions. Chen et al. [26] designed a belt-type seed delivery device aimed at improving the uniformity of the seed-casting process. Li et al. [27,28] designed a linear seed-pushing mechanism for an air-aspirated seed-metering device. This mechanism served to prevent the seed from changing position due to colliding with the seed tube's interior. Their proposed end toggle mechanism to disengage the seed and the straight-line seed-casting method were effective in resolving lateral seed displacement from the seed-casting effect. The above research directions mainly focused on two aspects of realizing orderly seed-filling and precise seed-casting. These studies effectively improved the performance of seed-metering devices. The problems of the above seed-metering devices mainly include the following: (1) the seed is in an unconstrained state before it enters the shaped hole, and the stability of seed-filling is poor and (2) by solely relying on its own gravity to disperse the seed, the device leads to irregular seed-casting points, thereby impacting the uniformity of spacing among the sown seeds.

Therefore, a soybean double-row seed-metering device with double-beveled seed guide groove was designed. The precision seed-metering device enables the systematic and orderly introduction of seeds into individual holes, thus ensuring the singular presence of one seed per hole. Furthermore, the seeding wheel guarantees the achievement of a consistent seed-casting point.

2. Materials and Methods

2.1. Overall Structure and Working Principle of the Seed-Metering Device

2.1.1. Overall Structure

Figure 1 illustrates the design of a soybean double-row seed-metering device, featuring a double-beveled seed guide groove. It consists of a front cover, front seed chamber, seed discharge ring, rear seed chamber, drive disc, seed guard, rear shell, drive shaft, and other components.

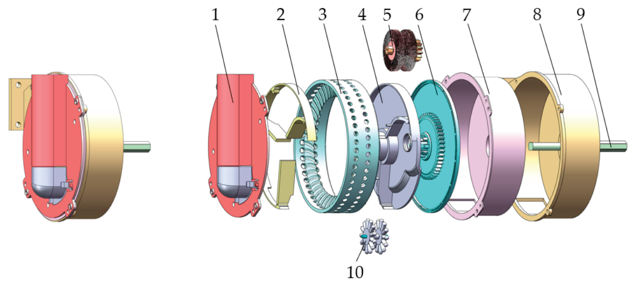

Figure 1. Diagram of the structural principles of a soybean double-row seed-metering device with double-beveled seed guide groove, where 1 is the front cover; 2 is the front seed chamber; 3 is the seed discharge ring; 4 is the rear seed chamber; 5 is the brush wheel; 6 is the drive disc; 7 is the seed guard; 8 is the rear shell; 9 is the drive shaft; and 10 is the seeding wheel.

The drive shaft initiates the rotation of the drive disc, which in turn propels the seed discharge ring into circular motion for the purpose of sowing. Simultaneously, the brush wheel, powered by the drive disc, rotates to execute seed-clearing operations. The teeth of the seeding wheel are strategically positioned within the contoured holes of the seed discharge ring, which, upon being rotated by the latter, performs the crucial task of seed-casting. Except for the above three sets of rotating parts, all other parts are non-rotating fixed parts. The triage convex ridge on the seed discharge ring has the capacity to divide the seed population into two distinct portions, which can then be filled independently, which improves the seed-filling efficiency. The seed guide grooves on the triage convex ridge effectively guide the seeds into the shaped holes using the restraining effect of the grooves on the seeds to enhance the seed-filling rate. The teeth of the seeding wheel push the seed to reach the seed-casting point out of the shaped hole, keeping the seed-casting point consistent.

2.1.2. Working Principle

The working process of the seed-metering device is mainly divided into four areas: seed-filling area I, seed-clearing area II, seed transport area III, and seed-casting area IV. The working process is shown in Figure 2.

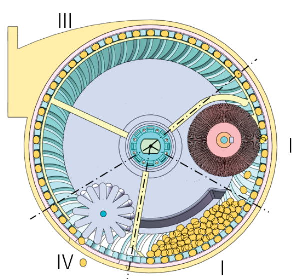

Figure 2. Schematic diagram of the division of the working process area of the seed-metering device, where I is seed-filling area; II is seed-clearing area; III is seed transport area; IV is seed-casting area.

When the seed-metering device operates, the seed falls into seed-filling area I. The connection between seed-filling area I and seed-casting area IV is divided by a partition on the front and rear seed discharge chambers. The partition serves to prevent the seed from entering seed-casting area IV directly from seed-filling area I. The seeds within the population traverse along the seed guide groove toward the shaped holes. The constraints and propulsion provided by the seed guide groove facilitate a smoother entry of the seeds into the shaped holes, thereby enabling effective guidance. This mechanism results in a significant increase in the seed-filling rate compared to seed-metering devices that rely solely on the seeds' gravity for filling. The seeds in the shaped holes follow the seed discharge ring as it rotates counterclockwise. When the seed reaches seed-clearing area II, the excess seed falls back to seed-filling area I under the action of the brush wheel and gravity. Afterward, the seeds waiting to be discharged follow the movement of the seed-discharging ring and pass through seed transport area III to seed-casting area IV. The teeth of the seeding wheel extend into the shaped holes on the seed discharge ring. When the seeds reach the seed-casting point, the teeth of the seed discharge ring immediately push the seeds out of the shaped holes, completing the seed-casting operation. Since the position of the seeding wheel remains fixed, the location of the seed-casting point also remains constant, ensuring consistency in the seed-casting point.

2.2. Key Component Design and Related Parameter Analysis

2.2.1. Overall Structure of the Seed Discharge Ring

The seed discharge ring, as depicted in Figure 3, constitutes the core functional element of the seed-metering device, playing a pivotal role in its operation. The seed discharge ring structure comprises a triage convex ridge, seed guide groove, shaped hole, and limiting convex ridge. Triage convex ridges, seed guide grooves, and shaped holes form the seed-filling structure. Double rows of seed guide grooves are staggered on both sides of the triage convex ridge of the seed discharge ring. The shaped holes are designed with rounded corners where they come into contact with the inner circle of the seed discharge ring. This not only effectively reduces seed damage but also facilitates the removal of excess seed from the shaped holes by the brush wheel. The seed discharge ring was designed with a limiting convex ridge on one side, fitting into a slot on the edge of the drive disc to form a whole.

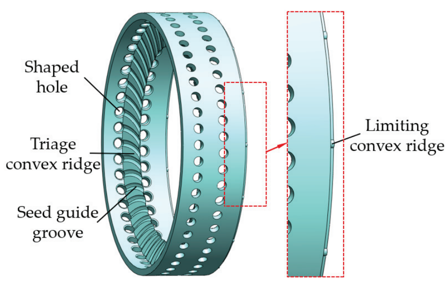

Figure 3. Schematic diagram of the structure of the seed discharge ring.

2.2.2. Analysis of the Force Acting on Soybean Seeds

During the seed-filling process, the origin is defined by the center of mass of the seed, with the *x*-axis aligned to the tangent direction of the seed discharge ring's rotation, the *y*-axis to its normal direction, and the *z*-axis perpendicular to the plane of the seed discharge ring. The three-dimensional coordinate system *oxyz* is shown in Figure 4.

In the *xoy* plane, forces acting on the seed include friction from the slanting surface of the seed guide, thrust perpendicular to the surface, friction of the seed cluster on the seed in the tangential direction of the triage convex ridge, and gravity. The equation of equilibrium is as follows.

$$F_{c1}\cos\alpha_1 + f_{m1}\sin\alpha_1 = f_{m2}\cos\alpha_2 \tag{1}$$

where F_{c1} is the thrust perpendicular to the seed guide groove, N; f_{m1} is the friction force along the incline, N; f_{m2} is the population friction along the tangent to the triage convex ridge, N; α_1 is the angle between the slant of the seed guide groove and the *x*-axis, (°); and α_2 is the angle between the tangent to the triage convex ridge and the *x*-axis, (°).

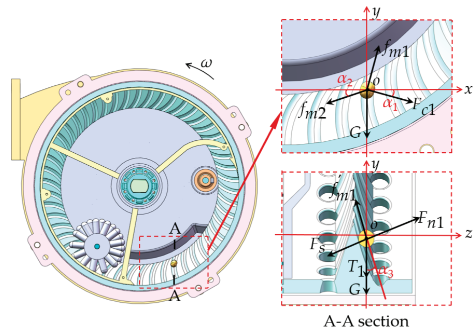

Figure 4. Schematic diagram of the forces on the seeds during seed-filling.

In the *yoz* plane, forces acting on the seed include the crowding force on the seed cluster perpendicular to the incline, supporting force perpendicular to the incline, combined force along the y-axis, and gravity. Forces on the seed are in equilibrium in the z-axis direction. The equation of equilibrium is as follows.

$$F_{n2}\cos\alpha_1 = F_s\cos\alpha_1 + f_{m1}\sin\alpha_1 \tag{2}$$

The f_{m1} in Equation (2) is given in Equation (3) below.

$$f_{m1} = \mu F_{n1} \tag{3}$$

where F_{n1} is the support force perpendicular to the incline, N; F_s is the crowding force from the seed cluster perpendicular to the inclined plane, N; and μ is the sliding friction factor between the seed and the seed discharge ring.

To facilitate the seamless downward progression of the seed within the designated guide groove, the resultant force acting upon the seed must be oriented consistently downward, conforming to the inclined plane of the triage convex ridge. The force equation is as follows.

$$G\cos\alpha_3 + T_1\cos\alpha_3 > f_{m1} \tag{4}$$

where G is the gravitational force acting on the seed, N; T_1 is the combined force along the y-axis, N; and α_3 is the inclination angle of the triage convex ridge, (°). The T_1 in Equation (4) is given in Equation (5) below.

$$T_1 = F_{c1}\sin\alpha_1 + f_{m2}\sin\alpha_2 - f_{m1}\cos\alpha_1 \tag{5}$$

A comprehensive analysis was conducted on both the internal architecture of the seed-metering device and the configuration of the seed discharge ring. It was found that when the inclination angle of the triage convex ridge α_3 was taken as 0°, the crowding pressure on the seeds on both sides of it by the seed population increased with time. Consequently, the seeds may be prone to breakage or erratic movements, ultimately compromising the quality of the seed-filling process. However, according to Equation (4), the larger the inclination angle of the triage convex ridge α_3, the smaller the $G\cos\alpha_3$ and $T_1\cos\alpha_3$. Therefore, the lower the guiding force is on the seeds, and thus the less favorable the seed-filling. Further tests are necessary to definitively determine the optimal range of the inclination angle of the triage convex ridge α_3.

As soybean seeds rotate concurrently with the seed discharge ring, transitioning from the seed transport area to the seed-casting area, they relinquish the supportive force provided by the seed guard, enabling their steady ejection under the impetus of the seeding wheel. At this time, the seed is subjected to forces, including the thrust of the shaped hole F_{c2}, the thrust of the seeding wheel F_{c3}, centrifugal force J, and gravity G, which make up the combined force T_2. The combined force T_2 provides the seed with a plane velocity v of motion, which can be decomposed into a horizontal velocity v_x and a vertical velocity v_y. A schematic diagram of the seed-casting process is shown in Figure 5.

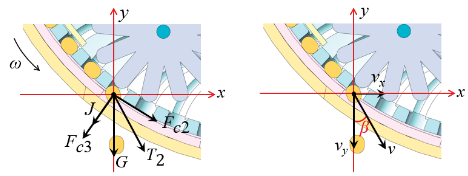

Figure 5. Schematic diagram of seed force and speed in the process of seed-casting.

A Cartesian coordinate system *xoy* was established in the plane of the rotating seed discharge ring, with the center of gravity of the soybean seeds designated as the origin. The trajectory of the soybean seed is as follows.

$$\begin{cases} x = v_x t_1 \\ y = v_y t_1 + \frac{g t_1^2}{2} \end{cases} \tag{6}$$

where x is the displacement of the soybean seed in the horizontal direction, mm; y is the displacement of the soybean seed in the vertical direction, mm; v_x is the velocity of the soybean seed in the horizontal direction, m/s; v_y is the velocity of the soybean seed in the vertical direction, m/s; and t_1 is the seed-casting time, s. The v_x, and v_y in Equation (6) are given in Equations (7) and (8) below.

$$v_x = v \sin \beta \tag{7}$$

$$v_y = v \cos \beta \tag{8}$$

The v in Equations (7) and (8) is given in Equation (9) below.

$$v = \frac{n_p \pi r_1}{30} \tag{9}$$

where β is the angle of the seed-casting, (°); n_p is the rotational speed of the seed discharge ring, r/min; and r_1 is the radius of the shaped hole, mm.

According to Equations (6)–(9), the equations for the trajectory of the soybean seed in the *xoy* plane were obtained as follows.

$$\begin{cases} x = \frac{n_p \pi r_1 \sin \beta}{30} t_1 \\ y = \frac{n_p \pi r_1 \cos \beta}{30} t_1 + \frac{g t_1}{2} \end{cases} \tag{10}$$

Under constant structural parameters of both the seed discharge ring and seeding wheel, the rotational velocity n_p of the ring governs the seed trajectory. Rigorous mechanical characterization is imperative for the rational design of the seed discharge ring, facilitating the precise analysis and calculation of its crucial parameters.

2.2.3. Design of the Seed Discharge Ring

The diameter of the seed discharge ring is instrumental in determining not only its overall size but also the magnitude of linear velocity and centrifugal force during its operation. Hence, its design necessitates meticulous consideration of specific operational conditions. It was found that the diameter of the seed discharge ring was directly proportional to the number of seed guide grooves and shaped holes [29]. Therefore, after determining the forward speed of the seeder and the seed spacing, the diameter of the seed discharge ring can be increased accordingly to reduce the rotation speed of the seed discharge ring.

The diameter range of the seed discharge ring is usually 140–260 mm [30]. For this study, the diameter of the seed discharge ring was taken as 240 mm and the width of the seed discharge ring was taken as 52 mm. The distance between the centers of the shaped holes on both sides of the seed discharge ring was designed to be 20 mm. 3D-printed technology was utilized for the fabrication of seed discharge rings using resin materials.

(1) Design of the triage convex ridge

The structure of the triage convex ridge is shown in Figure 6. The triage convex ridge ensures that the seeds on either side are filled independently, without interference, during the seed-filling operations of the seed-metering device. An optimal angle of inclination for the triage convex ridge is beneficial for seed-filling operations. However, if the angle of inclination is excessively large, the height of the ridge becomes constrained, which impairs the ability of the seed cluster to separate into both sides simultaneously, thereby reducing its guiding capability. This reduces the ability of the seeds to fill the shaped holes.

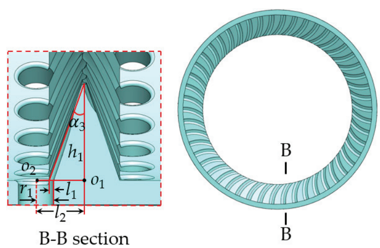

Figure 6. Schematic diagram of the structure of the triage convex ridge.

The formula for the inclination angle of the triage convex ridge was obtained from Figure 6.

$$\alpha_3 = \arctan\left(\frac{l_2 - (r_1 - l_1)}{h_1}\right) \tag{11}$$

where l_1 is the depth of the seed guide groove, mm; l_2 is the distance from o_2 to o_1, mm; h_1 is the height of the triage convex ridge, mm; o_1 is the midpoint of the distance between the centers of the shaped holes on both sides; and o_2 is the center of the shaped holes on one of the sides

The distance between points o_2 and o_1 is half the distance between the centers of the shaped holes on both sides, and therefore l_2 was taken as 10 mm. The triage convex ridge is limited by the positions of the brush wheel and the seeding wheel. Hence, the maximum height of the triage convex ridge was designed to be 25 mm, ensuring uninterrupted rotation of the brush and seeding wheels. The minimum height, exceeding the largest seed dimension, was set at 15 mm to facilitate seed separation on both sides and ensure guidance into the shaped holes via the seed guide groove. Therefore, the height of the triage convex ridge h_1 was taken in the range of 15–25 mm. The presence of diversion ridges effectively segmented the seed population into two distinct groups, each facilitated independently for seed-filling. As the rotary seed discharge ring rotates, the seed guide grooves adjacent to the diversion ridges meticulously direct the seeds toward their respective shaped holes. The inherent diversity among soybean varieties results in variations in their physical attributes, particularly in their dimensions. Consequently, larger seeds experience enhanced guiding forces during their trajectory, increasing their likelihood of successfully accessing the shaped holes. In contrast, smaller seeds encounter less pronounced guiding forces, which leads to a comparatively lower seed-filling efficiency. The determination of the range of height of the triage convex ridge provides the basis for the determination of the range of inclination angle of the triage convex ridge in a single-factor test.

(2) Design of the shaped holes

- Structure and dimensions of the shaped hole

The structure of the shaped hole has a great influence on a seed-metering device's seeding performance. A right-angled configuration at the shaped hole entrance may inflict damage on seeds during both the filling and cleaning processes. Therefore, the shaped holes were designed with chamfered corners with a radius of 1 mm, as shown in Figure 7.

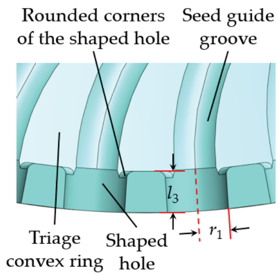

Figure 7. Schematic diagram of the structure of the shaped hole.

The radius of a shaped hole being too large will lead to multiple smaller seeds entering, while the radius of a shaped hole being too small will result in larger seeds being unable to enter. The depth of the shaped hole was designed to hold one seed and only one seed to ensure a smooth seed-filling and seed-clearing process [31]. It was essential to adhere to the following constraints for the individual dimensions.

$$\begin{cases} 0.75d_{\max} > r_1 > 0.5d_{\max} \\ \overline{X}_W > l_3 > d_{\min} \end{cases} \tag{12}$$

where $d_{\max}$ is the maximum size of the seed, mm; $\overline{X}_W$ is the average of the width of the seed, mm; $d_{\min}$ is the minimum size of the seed, mm; and l_3 is the depth of the shaped hole, mm.

The widely cultivated Zhonghuang 37 soybean seed was employed in the test procedure. A sample of 100 seeds were randomly extracted from the seed cluster, and their dimensions (length L, width W, and thickness T) were meticulously measured. The measurements were recorded and subsequently processed. The outcomes of the processing are summarized in Table 1.

Table 1. Statistical results of the soybean seeds' geometric size.

Parameter	Length L/mm	Width W/mm	Thickness T/mm
Maximum value	10.18	8.18	7.38
Minimum value	7.06	6.4	5.22
Average value	8.19	7.49	6.55

Table 1 shows that the average values of the dimensions of the soybean seeds were 8.19 mm in length, 7.49 mm in width, and 6.55 mm in thickness. Upon substituting the dimensions into Equation (12), it was determined that the range of values for the radius of the shaped hole was 4.1–6.14 mm. Thus, when the seed size was excessively large (L > 6.14 mm), there was an elevated risk of missed seeding occurring. Conversely, if the seed size was overly small (L < 4.1 mm), there was an increased likelihood of replay phenomena taking place. The 1 mm gap between the seed discharge ring and the seed guard serves to prevent friction, with the seed that fills the shaped holes subsequently dropping down to the seed guard. Therefore, the depth of the shaped hole was reduced by 1 mm. The value of l_3 was taken to be within the range of 5.56–6.49 mm, and the depth of the shaped hole was rounded up to l_3 = 6 mm. The range of the shaped hole's radius was subsequently determined through a rigorous single-factor test.

- Distribution of the shaped hole

The diameter of the seed discharge ring directly determines the number of shaped holes. When the operating speed and plant spacing are constant, the decrease in the rotation speed of the seed discharge ring can increase the number of shaped holes. Equation (13) shows the relationship between the rotation speed of the seed discharge ring, the number of shaped holes, and the forward speed of the seeder.

$$v = \frac{6zmn}{10000} \tag{13}$$

where v is the forward speed of the seeder, km/h; z is the seed spacing, calculated by taking 10 cm; n is the rotation speed of the seed discharge shaft, r/min; and m is the number of shaped holes, piece.

Based on Equation (13), it was evident that the drive shaft's rotational speed inversely correlated with the number of shaped holes, given constant seeder forward speed and plant spacing. Maintaining a constant diameter of the seed discharge ring, a reduced drive shaft speed translates to an increased number of shaped holes, enhancing seed-filling efficiency. However, an overly high number of holes may impede seed-filling. Therefore, determining the optimal maximum number of holes and the minimum spacing between them is crucial for ensuring smooth and efficient seed-filling. This simplifies the seed-filling process of a seed-metering device, as shown in Figure 8.

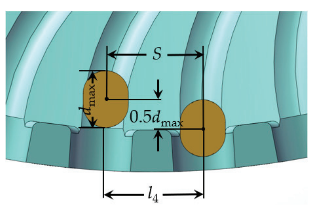

Figure 8. Schematic diagram of distribution distance of the shaped hole.

We assumed that the seed underwent horizontal projectile motion before entering the shaped hole from the seed guide groove. Then, the conditions for successful seed-filling would entail that the portion of the seed entering the shaped hole exceeded half of the seed itself, which corresponded to a drop height of more than $0.5d_{\max}$. The fall time required for successful seed-filling was $t_2 = \sqrt{\frac{d_{max}}{g}}$, and the displacement in the horizontal direction $S = v_0 t_2$. According to the reference literature [17], Equations (14)–(16) are necessary conditions for smooth seed-filling.

$$l_4 \geq S + 0.5d_{\max} \tag{14}$$

$$v_0 = \frac{\omega D}{2} \tag{15}$$

$$l_4 \approx \frac{\pi D}{m} \tag{16}$$

where S is the distance the seed traveled in the horizontal direction, mm; l_4 is the distance between the shaped holes, mm; v_0 is the linear velocity of the seed discharge ring, rad/s; ω is the angular velocity of the seed discharge ring, rad/s; and D is the diameter of the seed discharge ring, mm.

The following relationship was obtained from Equations (14)–(16).

$$m \leq \frac{60\pi}{\pi n \sqrt{\frac{d_{\max}}{g}} + \frac{30 d_{\max}}{D}} \tag{17}$$

Equation (17) indicates that the number of shaped holes is directly proportional to the diameter of the seed discharge ring and inversely proportional to both the rotational speed of the drive shaft and the seed size. When the distance between the shaped holes is the smallest, the number of shaped holes is the largest and the following relationship was obtained.

$$l_4 \approx \frac{\sqrt{3}+1}{2} d_{\max} \tag{18}$$

$$m l_4 \approx m \frac{\sqrt{3}+1}{2} d_{\max} \approx \pi D \tag{19}$$

Collation yielded the following relationships.

$$m \approx \frac{2\pi D}{\left(\sqrt{3}+1\right)} d_{\max} \tag{20}$$

$$v_0 t \leq l_4 \tag{21}$$

Substituting Equation (15) into Equation (21) yielded Equation (22).

$$n \leq \frac{\sqrt{g d_{\max}}\left(\sqrt{3}+1\right) \times 30}{\pi D} \tag{22}$$

Given a seed discharge ring diameter of 240 mm and a maximum seed size of 8.19 mm, the calculated maximum rotational speed for the seed discharge ring, as determined by Equation (22), was 58.43 r/min. Calculation according to Equation (20) gave $m \approx 67.39$ when the neighboring shaped holes were next to each other. To have enough space between the shaped holes during seed-filling, the number of shaped holes on one side of the triage convex ridge was taken as 50. At a seeder forward speed of 10 km/h, the seed discharge ring speed was 33.33 r/min, less than 58.43 r/min, and met the design requirements.

(3) Design of the seed guide groove

The reasonable structure of the seed guide groove not only guides the seed into the shaped hole but also enhances the disturbance of the seed cluster. As the seed discharge ring rotates, the seed guide groove and seed cluster exert pressure on the seed in the seed guide groove. This force ensures that the seed outside the seed guide groove cannot influence the seed in the seed guide groove to enter the shaped hole. This ensures that the seed-filling is effective.

A Cartesian coordinate system *XOY* was established, with the origin positioned at the center *O* of the seed discharge ring, as depicted in Figure 9. To guarantee seamless seed entry into the shaped hole, the absolute trajectory of the seed must align precisely with the tangent of the circle defined by the top of the seed guide groove. At time t_4, point A_1 moves to point A_2, and the seed moves from point A_1 to point A_3.

After time t_4, point A_1 rotates to point A_3, at which point the velocity at this position is as follows.

$$v_1 = v_2 / \cos \gamma_2 \tag{23}$$

$$\begin{cases} v_2 = r_3 \omega \\ \gamma_2 = k \omega t_3 \\ r_3 = r_2 / \cos \gamma_2 \end{cases} \tag{24}$$

where v_1 is the velocity of the seed at point A_3, m/s; v_2 is the velocity component of the seed in the direction tangent to point A_3, m/s; γ_2 is the angle between line segment OA_1

and line segment OA_3, (°); r_2 is the radius of the base circle of the seed guide groove, mm; r_3 is the radius of the circle at point A_3, mm; k is the angular rate coefficient for soybeans, which was taken as 0.1 to 0.9; and t_3 is the time of movement of the soybean seed, s.

According to Equations (23) and (24), the following results were obtained.

$$v_1 = r_2\omega / \cos^2(k\omega t_3) \tag{25}$$

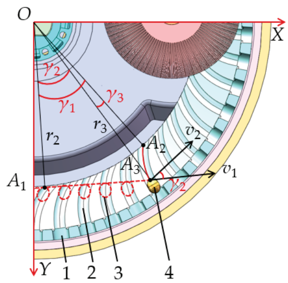

Figure 9. Schematic diagram of the curve equation of the guide groove on the seed-metering ring, where 1 is the shaped hole; 2 is the seed guide groove; 3 is seeds in the process of moving; 4 is the position the soybean seed needs to reach at time t_4; the dotted line A_1A_3 segment is the absolute motion trajectory of the soybean seed; and the Arc A_2A_3 segment is the relative motion trajectory of the soybean seed.

After time t_4, the absolute motion trajectory of the soybean seed following the movement of the seed discharge ring is represented by the following equation.

$$l_{A_1A_3} = \int_0^{t_4} \frac{r_2\omega}{\cos^2(k\omega t_3)} dt_3 = r_2 \tan(k\gamma_1)/k \tag{26}$$

where t_4 is the actual movement time of the soybean seed, s, and γ_1 is the angle between line segment OA_1 and line segment OA_2, (°).

The soybean seeds have a defined trajectory as the seed discharge ring rotates. To maximize the ability of the seed guide groove to guide the seed-filling, the curve equation of the seed guide groove was made to coincide with the relative motion trajectory of the seed. The expression of the curve equation is as follows.

$$\begin{cases} x_{A_3} = r_2 \cos\gamma_3 \\ y_{A_3} = r_2 \sin\gamma_3 \end{cases} \tag{27}$$

$$\gamma_3 = \gamma_1 - \gamma_2 \tag{28}$$

$$r_2 = r_3 \cos\gamma_2 \tag{29}$$

where γ_3 is the angle between line segment OA_2 and line segment OA_3, (°).

The following equation was obtained by combining Equations (27)–(29).

$$\begin{cases} x_{A_3} = r_2(\cos\gamma_1 + \tan\gamma_2 \sin\gamma_1) \\ y_{A_3} = r_2(\sin\gamma_1 - \tan\gamma_2 \cos\gamma_1) \end{cases} \tag{30}$$

$$\tan\gamma_2 = l_{A_1A_3}/r_2 \tag{31}$$

The result of the simplification of Equation (30) is as follows.

$$\begin{cases} x_{A_3} = r_2\left(\cos\gamma_2 + \frac{\tan(k\gamma_1)\sin\gamma_1}{k}\right) \\ y_{A_3} = r_2\left(\sin\gamma_2 + \frac{\tan(k\gamma_1)\cos\gamma_1}{k}\right) \end{cases} \quad (\gamma_1 \in (0, \zeta)) \tag{32}$$

where x_{A_3} is the coordinate of point A_3 on the x-axis in the absolute coordinate system, mm; y_{A_3} is the coordinate of point A_3 on the y-axis in the absolute coordinate system, mm; and ζ is the upper bound of the range, (°).

The expression for r_3 is as follows.

$$r_3 = r_2\sqrt{1 + (\tan(k\gamma_1)/k)^2} \tag{33}$$

Equation (32) is the relative motion trajectory of the soybean seeds. The radius of the circumference in which the shaped hole is located must exceed r_3, so the value of γ_1 was in the range $37.17° < \gamma_1 < 42.02°$. The optimal depth range for the seed guide groove was established to prioritize its role in guiding seed-filling over its tangential function in pushing the seed. This prevents the excessive depth of the seed guide groove from compromising the efficiency of seed-filling. The depth of the seed guide groove l_1 must be less than $0.5T_{\min}$, and according to Table 1, $T_{\min}$ = 5.22 mm, so the range of values for l_1: $l_1 < 2.61$ mm.

2.3. Test Conditions and Methods

2.3.1. Modeling and Parameter Setting

The operation of the seed-metering device was simulated using Altair EDEM 2021 discrete element simulation software. Soybean seeds were modeled using 5-ball collocation based on the known dimensional parameters of the soybean seeds [32]. The Hertz–Mindlin non-slip contact model was used for the seed-to-seed and seed-to-component contact models [33–36]. The parameters of the simulation model are presented in Table 2.

Table 2. Simulation of model parameters.

Item	Parameters	Numerical Values
Soybean seed	Density/(kg·m^{-3})	0.4
	Shear modulus/MPa	11
	Poisson's ratio	1053
	Moisture content/%	10.2
Resin	Density/(kg·m^{-3})	1454.80
	Shear modulus/MPa	120
	Poisson's ratio	0.35
Soybean–soybean	Static friction coefficient	0.5
	Rolling friction coefficient	0.01
	Coefficient of restitution	0.6
Soybean–resin	Static friction coefficient	0.32
	Rolling friction coefficient	0.04
	Coefficient of restitution	0.35

In the parameter settings of EDEM, the 3D particle sizes were set to be generated according to a normal distribution based on the distribution of the three-axis sizes of the seeds. The coefficient of variation for the seed population was 0.157, with a total seed count of 1500. The total time of the simulation was 10 s, where the step size of the simulation was 0.0000314 s, and the data were saved at intervals of 0.01 s. The simulation's boundary conditions were the following: (1) During the simulation, the operating speed was 8 km/h. The seed discharge ring, the drive disc, and the drive shaft rotated together counterclockwise in the same direction and their rotation speed was set to 160 deg/s. The brush wheel rotated clockwise at −525.71 deg/s. The seeding wheel rotated counterclockwise at a speed of 615.38 deg/s. And the remaining seed-metering device components were fixed. (2) The simulation material, including the front cover, as well as the front and rear seed chambers, were all constructed of resin. The seed discharge ring and seeding wheel were also composed of resin material. The bristles of the brush wheel were manufactured from nylon. The seed guard was constructed from high-strength steel. Lastly, the rear shell of the device was made of cast iron, selected for its strength and resistance to wear and tear. (3) The computational domains were the following: x-axis (maximum: 210 mm, minimum: 90 mm); y-axis (maximum: 265 mm, minimum: −20 mm); and Z-axis (maximum: 120 mm, minimum: −160 mm). The scope of the computational domain was combined with the seed-metering device structure to meet the needs of the simulation. The simulation process is shown in Figure 10.

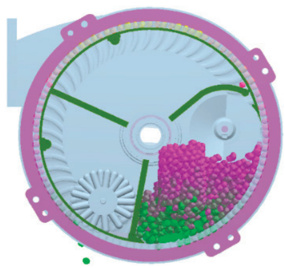

Figure 10. Seed-metering device model and discrete element simulation process.

2.3.2. Single-Factor Test

Following the structural design and theoretical analysis of the triage convex ridge, shaped hole, and seed guide groove, a targeted single-factor test was undertaken to refine the structural parameters. This endeavor sought to quantify the influence of diverse structural features on the performance index of the seed-metering device. In the single-factor test, the test factors were the inclination angle of the triage convex ridge α_3, the radius of the shaped hole r_1, and the depth of the seed guide groove l_1. The operational speed during the single-factor test was set at 8 km/h. When investigating the effect of the inclination angle of the triage convex ridge α_3 on seeding performance, each of the other factors took a fixed value: the radius of the shaped hole r_1 = 4.4 mm and the depth of the seed guide groove l_1 = 1.5 mm. When investigating the effect of the radius of the shaped hole r_1 on seeding performance, each of the other factors took a fixed value: the inclination angle of the triage convex ridge α_3 = 20.5° and the depth of the seed guide groove l_1 = 1.5 mm. When investigating the effect of the depth of the seed guide groove l_1 on seeding performance, each of the other factors took a fixed value: the inclination angle of the triage convex ridge α_3 = 20.5° and the radius of the shaped hole r_1 = 4.4 mm.

According to GB/T 6973-2005 [37] Testing methods of single seed drills (precision drills), the qualified rate, replay rate, and missed seeding rate were taken as test indices. The seeds discharged from the seed-casting point during the simulation were counted, and the qualified rate, replay rate, and missed seeding rate were calculated. When only one seed was found to have been discharged from the shaped hole, it was marked as passing. When two or more seeds were found to have been discharged from the shaped hole, they were marked as reseeding. When no seed was found to have been discharged from the shaped hole, it was marked as missed seeding.

The test methods for the qualified rate, replay rate, and missed seeding rate were the following: In the first step, the simulation was played back to record the total number of shaped holes that were traversed through the seed-casting point, starting from the first seed-filled shaped hole until the end of the simulation. This total is referred to as the total number of shaped holes turned through the seed-casting point. The number of shaped holes that dispensed only one seed while passing through the seed-casting point was designated as the qualified count. The number of shaped holes that dispensed two or more seeds was classified as the replay count, while the number of shaped holes that dispensed no seeds was termed the missed seeding count. In the second step, the recorded qualified count, replay count, and missed seeding count were divided by the total count to calculate the qualified rate, replay rate, and missed seeding rate, respectively. In the third step, the qualified rates, replay rates, and missed seeding rates from the three repeated simulation tests were averaged to yield the final test results.

2.3.3. Second-Order Orthogonal Rotation Combination Test

Based on the results of the single-factor test, the radius of the shaped hole and the depth of the seed guide groove were identified as pivotal test factors for further investigation. The range of values for the radius of the shaped hole was 4.16–4.5 mm and the range of values for the depth of the seed guide groove was 0.49–1.89 mm. A two-factor, five-level, second-order orthogonal rotation combination test was conducted with the qualified rate, replay rate, and missed seeding rate as test indicators. The measurement of test indicators was conducted in accordance with the methodology employed in the single-factor test, utilizing the two-factor level coding presented in Table 3. These parameters provided the basis for the successful implementation of the orthogonal test and were processed using the data analysis software Design-Expert 13.0.

Table 3. Test factor coding.

Code	Radius of the Hole X_1/mm	Depth of Seed Guide Groove X_2/mm
−1.414	4.09	0.2
−1	4.16	0.49
0	4.33	1.19
1	4.5	1.89
1.414	4.57	2.18

2.3.4. Bench Test

Bench tests are conducted to verify the reasonableness of the optimized results of parameters. The radius of the shaped hole was taken as 4.33 mm, and the depth of the seed guide groove was taken as 1.20 mm. The main working parts and the rear shell inside the 3D-printed seed-metering device formed the seed-metering device, which was mounted on a bench, as shown in Figure 11. According to GB/T 6973-2005 Testing methods of single seed drills (precision drills), the qualified rate, replay rate, and missed seeding rate were taken as test indicators. Bench test verification was carried out on the JSP-12 computer vision-measuring device performance test bench at 5 operating speeds of 6, 7, 8, 9, and 10 km/h. Each operating speed was tested three times and the results were recorded. Theoretical seed spacing was 10 cm. If the distance between two adjacent seeds in the row was greater than 5 cm and less than or equal to 15 cm, it was considered passing. Seed spacing less than or equal to 5 cm was considered to be reseeding. Seed spacing greater than 15 cm was considered to be a missed seeding.

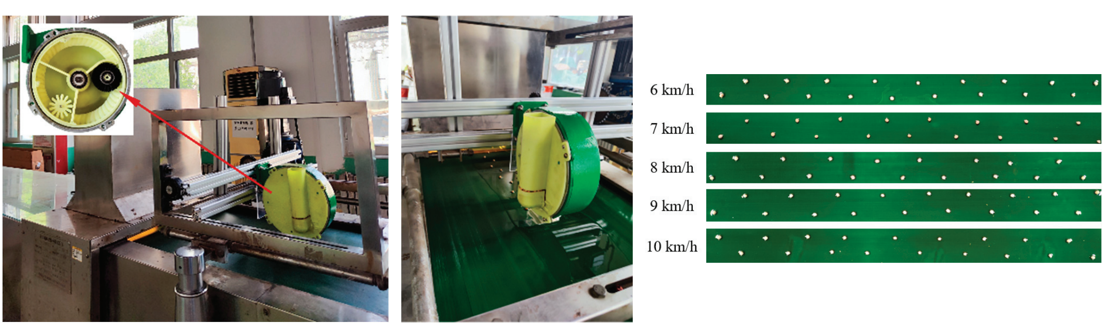

(**a**) (**b**) (**c**)

Figure 11. Bench validation test. (**a**) Bench test device; (**b**) Test process; (**c**) Test effect.

2.3.5. Soil Trench Test

Using two-factor optimum parameter combination, a soil trench validation test was carried out at an operating speed of 8 km/h to investigate the seeding performance of the seed-metering device on the soil. The soil trench was 30 m long, 2.8 m wide, and 25 cm deep. The tests were carried out from 16 April to 26 April 2024 on the soil trench test bench in the laboratory of Shandong University of Technology. The physical properties of the soil were measured before the test. The soil moisture content was 12.6% at 0–10 cm and 14.3% at 10–20 cm. The soil compactness was 1.98 MPa at 0–10 cm and 2.5 MPa at 10–20 cm. The physical properties of the soil in the soil trench tests fell within the range of those encountered in field operations [38,39]. The bench frame with the seed-metering device was fixedly installed on the rear suspension beam of the soil trench trolley, as shown in Figure 12. The test indicators included the qualified rate, replay rate, and missed seeding rate, which were measured in the same way as in the bench test.

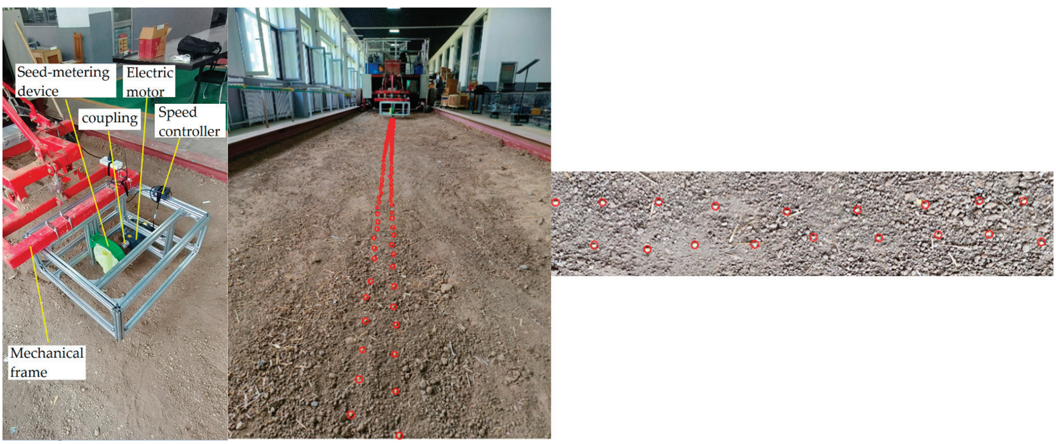

(**a**) (**b**) (**c**)

Figure 12. Soil trench validation test. (**a**) Soil trench test device; (**b**) Test process; (**c**) Test effect. where the red circles in (**b**,**c**) indicate the position of the seeds after landing.

3. Results and Discussion

3.1. Single-Factor Test Results and Analyses

The results of the single-factor test are shown in Table 4.

Table 4. Single-factor test results.

Factor	Level	Qualified Rate/%	Replay Rate/%	Missed Seeding Rate/%
Inclination angle of the triage convex ridge $\alpha_3/^\circ$	12	91.32	8.48	0.2
	16.25	93.96	5.07	0.97
	20.5	95.13	3.99	0.88
	24.75	96.3	1.85	1.85
	29	96.49	1.07	2.44
Radius of the shaped hole r_1/mm	4.1	93	1.22	5.78
	4.2	96.56	1.22	2.22
	4.3	95.67	2.55	1.78
	4.4	95.89	3.78	0.33
	4.5	95.11	4.67	0.22
	4.6	93.9	5.34	0.76
	4.7	93.34	6.11	0.55

Table 4. *Cont.*

Factor	Level	Qualified Rate/%	Replay Rate/%	Missed Seeding Rate/%
Depth of the seed guide groove l_1/mm	0.5	95.03	1.07	3.9
	1	96.98	1.36	1.66
	1.5	96.3	1.85	1.85
	2	94.64	4.78	0.59
	2.5	92.98	6.82	0.2

3.1.1. Effect of the Inclination Angle of the Triage Convex Ridge on the Test Index

It was known that l_2 = 10 mm, h_1 = 15–25 mm, r_1 = 4.4 mm, and l_1 = 1.5 mm. Substituting this into Equation (11), the range of values of the inclination angle of the triage convex ridge α_3 was calculated to be 11.97–29.57°. The inclination angles of the triage convex ridge were taken as 12°, 16.25°, 20.5°, 24.75°, and 29°. In order to more clearly show the change in the trend of the effect of the inclination angle of the triage convex ridge on the test index, the results of the test are shown in Figure 13.

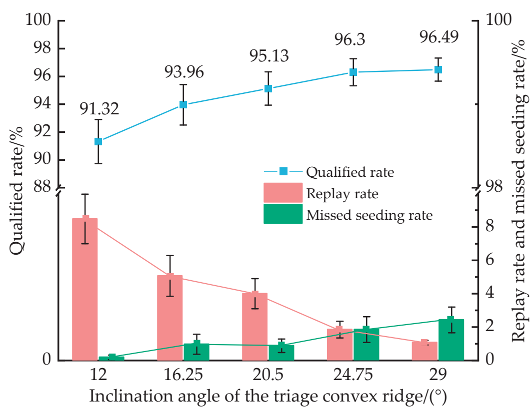

Figure 13. Effect curve of the inclination angle of the triage convex ridge on the test index.

Figure 13 shows that the qualified rate increased with the increased inclination angle of the triage convex ridge. When the inclination angle of the triage convex ridge increased to 24.75°, the changed trend of the qualified rate slowed down significantly.

The replay rate decreased with the increased inclination angle of the triage convex ridge and was lowest when the inclination angle of the triage convex ridge increased to 29°. The increase in the inclination angle of the triage convex ridge led to a reduction in the squeezing force on the seeds on both sides, which reduced the likelihood of multiple seeds entering the shaped hole.

The missed seeding rate gradually increased with the inclination angle of the triage convex ridge, peaking at 29°. At angles higher than this, the downward guiding force of the seed guide groove was diminished, thereby affecting the quality of seed filling. The optimal seeding performance was observed when the inclination angle was set at 29°, which was then chosen for conducting single-factor tests regarding the radius of the shaped hole and the depth of the seed guide groove.

Based on the observed trend in the qualified rate, as illustrated in Figure 13, it could be inferred that an increase in the inclination angle of the triage convex ridge resulted in improved seeding performance. Consequently, the maximum value of 29° was selected as the inclination angle of the triage convex ridge for subsequent testing.

3.1.2. Effect of the Radius of the Shaped Hole on the Test Index

Simulation pre-tests were performed for the radius range of the shaped hole due to the large radius range of the shaped hole. The pre-test results are shown in Figure 14a.

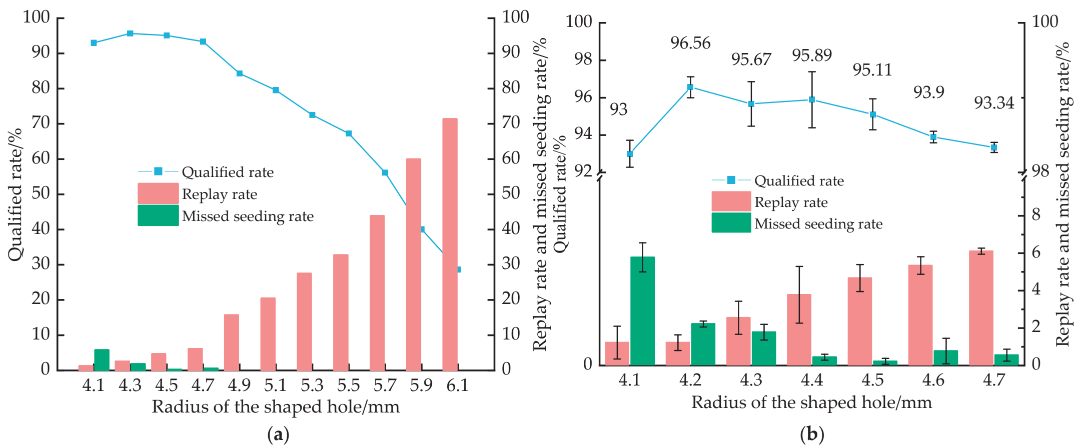

Figure 14. Effect curve of the radius of the shaped hole on the test index. (**a**) Pre-test results; (**b**) Test results.

The analysis of the test results, presented in Figure 14a, indicated that the radius of the shaped hole r_1 had to range from 4.1 to 4.71 mm to achieve a qualified rate exceeding 93%. Conversely, at a radius of 4.9 mm, the qualified rate was observed to be 84.33%. When the radius of the shaped hole was larger than 4.9 mm, the qualified rate continued to decrease, and the requirement for the precision operation of the seeder could not be met. The range of values for the radius of the shaped hole r_1 was determined to be 4.1–4.7 mm, and 4.1, 4.2, 4.3, 4.4, 4.5, 4.6, and 4.7 mm were selected for the single-factor test. The test outcomes are depicted in Figure 14b.

By analyzing the test results in Figure 14b, the following regression equation was obtained for the effect of the radius of the shaped hole on the seeding performance.

$$Y_1 = 99.167X_1^3 - 1337.8X_1^2 + 6004.4X_1 - 8871 \tag{34}$$

$$Y_2 = -37.5X_1^3 + 494.85X_1^2 - 2165.1X_1 + 3144.1 \tag{35}$$

$$Y_3 = -61.667X_1^3 + 842.44X_1^2 - 3834.8X_1 + 5816.8 \tag{36}$$

where Y_1, Y_2, and Y_3 are the qualified rate, replay rate, and missed seeding rate, respectively, %, and X_1 is the radius of the shaped hole, mm.

The qualified rate exhibited a pronounced variation with the augmentation of the radius of the shaped hole, attaining a peak value of 96.56% at a radius of precisely 4.2 mm. Subsequently, a decline was observed as the radius surpassed 4.2 mm, reaching 4.3 mm, whereupon a marginal yet discernible increase occurred between 4.3 mm and 4.4 mm. This slight elevation was attributed to the mitigation of seed collisions at the entry point, thereby facilitating enhanced seed ingress. Notably, this transient increase did not undermine the overarching trend of the radius of the shaped hole's influence on the qualified rate, which then resumed its continuous downward trajectory.

As the radius of the shaped hole increased, the replay rate augmented, with a deceleration in this trend observed when the radius surpassed 4.5 mm. As the radius of the shaped holes increased to a certain extent, the probability of multiple seeds entering the shaped holes continued to rise. However, the collisions among the seeds at the entrance of the shaped holes became more intense, resulting in a deceleration of this upward trend.

With the increase in the radius of the shaped holes, the missed seeding rate initially decreases. When the radius reaches 4.5 mm, the missed seeding rate begins to rise slightly. The reason for this is that the shaped hole size was excessive, exceeding 4.5 mm. This caused some seeds to collide at the mouth of the shaped hole and prevented them from entering the shaped hole.

According to regression Equations (34)–(36), when the radius of the shaped holes ranged from 4.1 to 4.5 mm, the qualified rate exceeded 95%, and the replay rate was below 5%. Furthermore, when the radius of the shaped holes ranged from 4.11 to 4.7 mm, the missed seeding rate was less than 5%. The highest qualified rate of 96.56% was achieved with a radius of the shaped hole of 4.2 mm.

3.1.3. Effect of the Depth of the Seed Guide Groove on the Test Index

In the single-factor test, the depth of the seed guide groove l_1 was taken as 0.5, 1, 1.5, 2, and 2.5 mm, where the seed guide grooves did not affect each other. To more clearly show the change in trend of the effect of the depth of the seed guide groove on the test index, the results of the test are depicted in Figure 15.

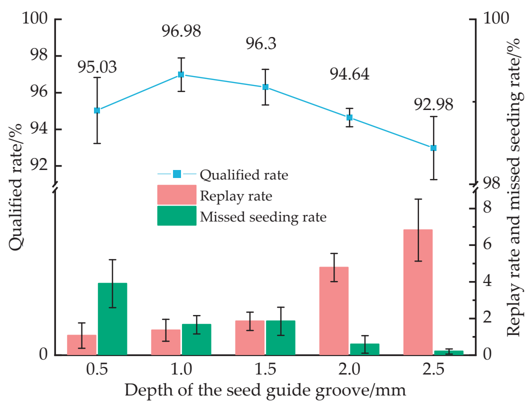

Figure 15. Effect curve of the depth of the seed guide groove on the test index.

By analyzing the test results in Figure 15, the following regression equation was obtained for the effect of the depth of the seed guide groove on the seeding performance.

$$Y_1 = 1.7533X_2^3 - 10.233X_2^2 + 16.085X_2 + 89.336 \quad (37)$$

$$Y_2 = -0.7267X_2^3 + 4.9671X_2^2 - 6.3948X_2 + 3.196 \quad (38)$$

$$Y_3 = -1.04X_2^3 + 5.3229X_2^2 - 9.7586X_2 + 7.49 \quad (39)$$

where Y_1, Y_2, and Y_3 are the qualified rate, replay rate, and missed seeding rate, respectively, %, and X_2 is the depth of the seed guide groove, mm.

The qualified rate increased with increasing depth of the seed guide groove, reaching a maximum value of 96.98% when the depth of the seed guide was increased to 1 mm, and then gradually decreased. As the depth of the seed guide groove increases, the capacity of the groove to direct seed movement toward the shaped hole is enhanced, thereby facilitating a more streamlined seed entry into the shaped hole. However, the depth of the seed guide groove was too large, causing multiple seeds to enter the same shaped hole, thereby reducing the qualified rate. The highest qualified rate of 97% was achieved with a depth of seed guide groove of 1.09 mm.

The replay rate increased slowly as the depth of the seed guide groove significantly increased when it increased to 1.5 mm. The lowest replay rate of 0.89% was achieved with a depth of the seed guide groove of 0.78 mm.

The missed seeding rate initially decreased with the depth of the seed guide groove; however, it augmented at 1–1.5 mm before resuming its downward trend beyond 1.5 mm. This increase in the missed seeding rate may be due to the increased ability of the seed guide groove to constrain the seed, resulting in some of the seeds colliding at the entrance of the shaped hole, thus failing to enter the shaped hole.

According to regression Equations (37)–(39), when the depth of the seed guide groove ranged from 0.49 to 1.89 mm, the qualified rate exceeded 95%. Additionally, when the depth of the seed guide groove was between 0.23 and 1.4 mm, the replay rate was below 2%. Finally, when the depth of the seed guide groove exceeded 1.01 mm, the missed seeding rate was below 2%.

3.2. Second-Order Orthogonal Rotation Combination Test Results and Analysis

Design-Expert 13.0 software was used to design a second-order orthogonal rotary combination test to investigate the effect of the radius of the shaped hole and the depth of the seed guide groove on the test indices. The test results are presented in Table 5.

Table 5. Second-order orthogonal rotating combination test design and results.

No.	X_1	X_2	Qualified Rate Y_1/%	Replay Rate Y_2/%	Missed Seeding Rate Y_3/%
1	−1	−1	91.23	0.29	8.48
2	1	−1	95.71	1.85	2.44
3	−1	1	96.39	2.92	0.69
4	1	1	95.03	4.39	0.58
5	−1.414	0	94.74	1.17	4.09
6	1.414	0	95.91	3.8	0.29
7	0	−1.414	92.69	0.58	5.27
8	0	1.414	95.32	4.39	0.29
9	0	0	96.2	1.46	2.34
10	0	0	96.49	2.15	1.36
11	0	0	96.3	1.27	2.43
12	0	0	96.49	1.75	1.76
13	0	0	96.79	1.66	1.55

Note: X_1 and X_2 are the factor-coded values for the radius of the shaped hole and the depth of the seed guide groove, respectively. The interaction between the radius of the shaped hole and the depth of the seed guide groove was significant. The effects of two factors on the test indices had a significant impact.

Regression analysis was conducted on the test results presented in Table 5, yielding the subsequent regression equations.

$$Y_1 = -0.5832X_1^2 - 1.24X_2^2 - 1.46X_1X_2 + 0.5968X_1 + 1.02X_2 + 96.45 \tag{40}$$

$$Y_2 = 0.3829X_1^2 + 0.3829X_2^2 - 0.0225X_1X_2 + 0.8437X_1 + 1.32X_2 + 1.66 \tag{41}$$

$$Y_3 = 0.2916X_1^2 + 0.5866X_2^2 + 1.48X_1X_2 - 1.44X_1 - 2.09X_2 + 1.89 \tag{42}$$

Analysis of variance was performed on the experimental data using Design-expert 13.0 software. The results are presented in Table 6.

The p-values of the models for qualified rate, replay rate, and missed seeding rate were all less than 0.001, and the differences were extremely significant. The respective F values for the lack of fit terms were 2.30, 0.2888, and 2.29, with corresponding p-values of 0.2187, 0.8323, and 0.2203, all exceeding the significance threshold of 0.05. The insignificant variations in the lack-of-fit terms indicate that the second-order regression equation, as fitted by the model, closely aligned with reality, offering a robust prediction of the test results. In the regression model for the qualified rate, replay rate, and missed seeding rate, the two factors and their interaction terms had extremely significant effects on the qualified rate, replay rate, and missed seeding rate.

Table 6. Analysis of variance.

Source	Qualified Rate/%		Replay Rate/%		Missed Seeding Rate/%	
	F **Value**	***p*-Value**	***F*** **Value**	***p*-Value**	***F*** **Value**	***p*-Value**
Model	80.08	<0.0001	56.02	<0.0001	35.75	<0.0001
X_1	35.90	0.0005	74.41	<0.0001	47.14	0.0002
X_2	105.86	<0.0001	182.10	<0.0001	98.90	<0.0001
X_1 X_2	107.40	<0.0001	0.0265	0.8754	24.96	0.0016
${X_1}^2$	29.81	0.0009	13.33	0.0082	1.68	0.2360
${X_2}^2$	135.45	<0.0001	13.33	0.0082	6.80	0.0351
Lack of Fit	2.30	0.2187	0.2888	0.8323	2.29	0.2203

Note: $0.01 < p < 0.05$ is generally significant, $0.001 < p < 0.01$ is significant, and $p < 0.001$ is extremely significant.

Response surface plots were generated in Design-expert 13.0 software to analyze the relationship between the effects of the two factors on the test indices, as shown in Figure 16.

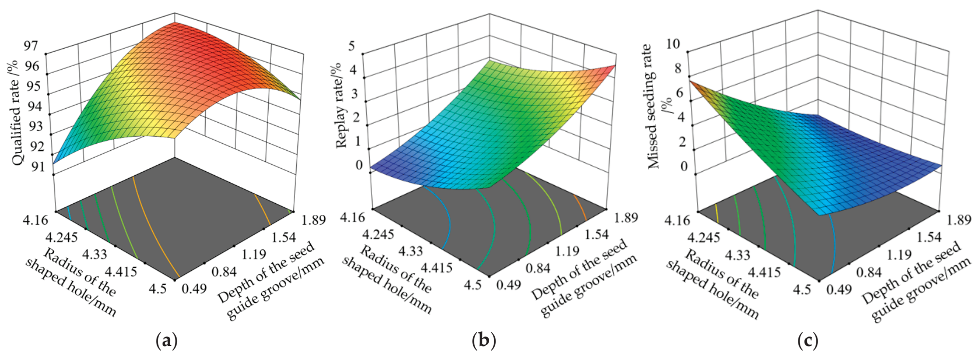

Figure 16. Response surface diagram: (**a**) the radius of the shaped hole and the depth of the seed guide groove on the qualified rate; (**b**) the radius of the shaped hole and the depth of the seed guide groove on the replay rate; and (**c**) the radius of the shaped hole and the depth of the seed guide groove on the missed seeding rate.

From Figure 16, it was evident that there was a significant interaction between the two factors. When the radius of the shaped hole was relatively small, both the qualified rate and replay rate increased with the depth of the seed guide groove, while the missed seeding rate decreased. This phenomenon can be attributed to the fact that an increased depth of the seed guide groove enhances the contact area with the seeds, thereby allowing for more effective guidance of the seeds into the shaped holes. Conversely, when the radius of the shaped hole was larger, seeds could more easily enter the shaped holes, resulting in an increase in both the qualified rate and replay rate, along with a decrease in the missed seeding rate. However, if the depth of the seed guide groove became excessively large, the guiding force exerted on the seeds may have become too strong, leading to a significant increase in the replay rate and, consequently, a decrease in the qualified rate.

When the depth of the seed guide groove was shallow, the qualified rate increased as the radius of the shaped hole expanded. This occurred because larger seeds encountered difficulties when attempting to enter smaller shaped holes, and a larger radius facilitated their entry, thereby enhancing seeding effectiveness. However, with a deeper seed guide groove, the qualified rate decreased as the radius increased. Although a larger radius allowed for easier entry, the deeper seed guide groove enhanced guidance, resulting in multiple seeds entering the same shaped hole more frequently. This phenomenon led to a higher replay rate and a subsequent decline in the qualified rate.

To explore the optimal parameter combination for each test factor and ensure that the conditions for optimization fell within a reasonable range of design parameters, an optimization solution was employed that aimed to maximize the qualified rate while minimizing the replay rate and missed seeding rate. Equation (43) presents the objective function along with the constraint range for the working parameters.

$$\begin{cases} \max Y_1(X_1, X_2) \\ \min Y_2(X_1, X_2) \\ s.t. \begin{cases} -1.414 \leq X_1 \leq 1.414 \\ -1.414 \leq X_2 \leq 1.414 \end{cases} \end{cases} \tag{43}$$

The optimization process was executed utilizing the "Optimization" module within Design-expert 13.0 software, yielding optimized parameters: the radius of the shaped hole was 4.33 mm and the depth of the seed guide groove was 1.20 mm. These conditions facilitated a qualified rate of 96.48%, a replay rate of 1.69%, and a missed seeding rate of 1.83%.

3.3. Bench Test Results and Analysis

A comparative analysis of the bench and simulation test results was conducted to validate the seeding quality achieved by the seed-metering device during actual operational conditions. The results of the test were averaged over three times, and the results are shown in Table 7 and Figure 17.

Table 7. Bench test results.

Factor	Level	Qualified Rate/%		Replay Rate/%		Missed Seeding Rate/%	
		Test Value	Simulation Value	Test Value	Simulation Value	Test Value	Simulation Value
Operating speed /(km·h^{-1})	6	96.18	96.65	1.24	1.81	2.58	1.54
	7	95.34	96.02	1.02	1.93	3.64	2.05
	8	95.63	95.61	1.08	2.44	3.29	1.95
	9	95.44	95.45	0.81	2.11	3.75	2.44
	10	94.91	95.33	0.54	1.7	4.55	2.97

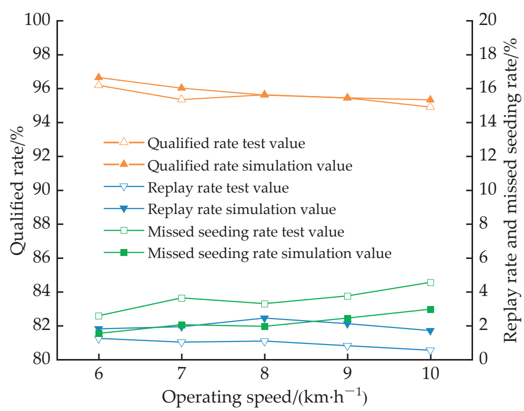

Figure 17. Bench test results.

According to Table 7 and Figure 17, the test results from the bench and simulation were found to be closely aligned. The bench tests, conducted at five operating speeds—6, 7, 8, 9, and 10 km/h—yielded relatively favorable outcomes, with all tests achieving a qualified rate exceeding 94%, demonstrating stable seeding performance. At a forward speed of 8 km/h, the bench test recorded a qualified rate of 95.12%, a replay rate of 1.08%, and a missed seeding rate of 3.80%. This result closely corresponds to the data obtained from the regression model calculations, indicating the reliability of the optimized parametric combination.

According to Table 7 and Figure 17, it was observed that with an increase in the operating speed, both the qualified rate and the replay rate decreased, and the missed seeding rate increased. An increase in the forward speed of the seeder may have induced vibrations in the seed-metering device, potentially impeding the efficient entry of seeds into the shaped hole. Concomitantly, as the working speed intensified, the seed-metering device's velocity escalated, curtailing the seed filling duration. This decrease in filling time resulted in a diminished seed-filling rate and a consequential rise in the missed seeding rate.

During the bench tests, the seed-metering device was mounted on a JSP-12 computer vision-measuring device performance test bench, with only the vibrations generated by the device's own operation acting as a source of disturbance. In comparison to actual field operations, the system exhibited superior performance, facilitated more effective filling of the shaped holes, and achieved greater uniformity in seed spacing.

3.4. Soil Trench Test Results and Analysis

The soil trench test results are shown in Table 8.

Table 8. Soil trench test results.

No.	Qualified Rate/%	Replay Rate/%	Missed Seeding Rate/%
1	93.50	2.28	4.22
2	93.11	1.71	5.18
3	93.33	2.12	4.55
Average value	93.31	2.04	4.65

According to Table 8, the seed-metering device operating at a speed of 8 km/h achieved a qualified rate of 93.31%, a replay rate of 2.04%, and a missed seeding rate of 4.65%. These findings suggest that the seed-metering device exhibits stable seeding performance, satisfying the criteria for precision sowing operations. The seeding quality of the seed-metering device in the soil trench test was reduced compared to the bench test. It may be that the vibration caused by the forward movement of the soil trench trolley during the soil trench test resulted in a more intense vibration of the seed-metering device, which reduced the quality of seed-filling and seed-casting. In addition, the bouncing roll of the seed as it hit the ground also reduced seeding quality. In the soil trench test, the soil trench trolley operated relatively smoothly and exhibited low vibration. In contrast, during field operations, the seeder may have experienced significant vibrations due to complex ground conditions, which could have adversely affected seeding outcomes. Therefore, the results of the soil trench test may have deviated from the empirical results obtained from the combined field tests.

4. Conclusions

(1) A soybean double-row seed-metering device with a double-beveled seed guide groove was designed. Through the theoretical analysis of the working process of the seed-metering device, dynamic and kinematic models of the seeds were established. The main factors affecting the seeding performance were obtained as the following: the inclination angle of the triage convex ridge, the radius of the shaped hole, and the depth of the seed guide groove. The ranges of values for the inclination angle of the triage convex ridge, the radius of the shaped hole, and the depth of the seed guide groove were determined to be 11.97–29.57°, 4.1–4.7 mm, and 0–2.61 mm, respectively.

(2) A discrete element simulation was employed to conduct a single-factor test, using the qualified rate, replay rate, and missed seeding rate as evaluation indicators. The test results were obtained as the following: the inclination angle of the triage convex ridge α_3 = 29°, the radius of the shaped hole r_1 = 4.16–4.5 mm, and the depth of the seed

guide l_1 = 0.49–1.89 mm. The qualified rates of the tests were all greater than 95%, meeting the operational requirements of precision seeding.

(3) A two-factor, five-level, second-order orthogonal rotation combination test was conducted with the radius of the shaped hole and the depth of the seed guide groove as test factors. A regression model between the evaluation indices of the radius of the shaped hole and the depth of the seed guide groove was developed. The test results showed that the radius of the shaped hole and the depth of the seed guide groove had a significant effect on each evaluation index. According to the regression model, the optimal parameter combination was 4.33 mm for the radius of the shaped hole and 1.20 mm for the depth of the seed guide groove. The qualified rate was 96.48%, the replay rate was 1.69%, and the missed seeding rate was 1.83%.

(4) Bench tests were carried out, and the results showed that the test results from the bench and simulation were consistent. At the operating speed of 6–10 km/h, the qualified rate of seeding was above 94%. A soil trench test was conducted, and the results showed that the seed spacing qualified rate of the seed-metering device was 93.31% at an operating speed of 8 km/h. The replay rate was 2.04% and the missed seeding rate was 4.65%. This met the requirements of precision sowing operation. These research results can provide a reference for the innovative design of precision seed-metering devices.

Author Contributions: Data curation, H.Z. and S.Z.; funding acquisition, W.W.; investigation, Y.C. and M.L.; methodology, L.Z. and J.Z.; project administration, W.W.; supervision, L.Z.; validation, H.Z. and H.L.; writing—original draft, H.Z.; writing—review and editing, W.W. All authors have read and agreed to the published version of the manuscript.

Funding: This work was supported by the National Natural Science Foundation of China (52005307), High-quality Development project for the Ministry of Industry and Information (2023ZY02009), and Opening Fund of the State Key Laboratory of Agricultural Equipment Technology (NKL-2023-010).

Institutional Review Board Statement: Not applicable.

Data Availability Statement: The data used to support the findings of this study are available from the corresponding author upon request.

Conflicts of Interest: The authors declare no conflicts of interest.

References

1. Gao, X.J.; Zhou, Z.Y.; Xu, Y.; Yu, Y.B.; Su, Y.; Cui, T. Numerical simulation of particle motion characteristics in quantitative seed feeding system. *Powder Technol.* **2020**, *367*, 643–658. [CrossRef]
2. Yang, L.; Yan, B.X.; Zhang, D.X.; Zhang, T.L.; Wang, Y.X.; Cui, T. Research Progress on Precision Planting Technology of Maize. *Trans. Chin. Soc. Agric. Mach.* **2016**, *47*, 38–48.
3. Yuan, Y.W.; Bai, H.J.; Fang, X.F.; Wang, D.C.; Zhou, L.M.; Niu, K. Research Progress on Maize Seeding and Its Measurement and Control Technology. *Trans. Chin. Soc. Agric. Mach.* **2018**, *49*, 1–18.
4. Li, Y.H.; Yang, L.; Han, Y.; Zhang, D.X.; Cui, T.; Yu, Y.M. Design and Experiment of Spoon-clamping Type Metering Device for Faba Beans. *Trans. Chin. Soc. Agric. Mach.* **2018**, *49*, 108–116.
5. Li, Y.H.; Wei, Y.N.; Yang, L.; Zhang, D.X.; Cui, T.; Zhang, K.L. Design and Experiment of Mung Bean Precision Seed-metering device with Disturbance for Promoting Seed-filling. *Trans. Chin. Soc. Agric. Mach.* **2020**, *51*, 43–53.
6. Liu, H.X.; Liu, J.X.; Tang, S.F.; Xu, X.M. Design on opposed inclined-plate high-speed precision seed-metering device and its working mechanism analysis. *Trans. Chin. Soc. Agric. Eng.* **2016**, *32*, 24–31.
7. Correia, T.P.; Sousa, S.F.; Silva, P.R.; Dias, P.P.; Gomes, A.R. Sowing performance by a metering mechanism of continuous flow indifferent slope conditions. *J. Agric. Eng.* **2016**, *36*, 839–845.
8. Wang, Y.C.; Sun, H.; Li, B.Q.; Han, X.; Chen, H.T. Design and Experiment of Centralized Belt Type Soybean Seed-metering Device. *Trans. Chin. Soc. Agric. Mach.* **2019**, *50*, 74–83.
9. Jia, H.L.; Chen, Y.L.; Zhao, J.L.; Guo, M.Z.; Huang, D.Y.; Zhuang, J. Design and key parameter optimization of an agitated soybean seed metering device with horizontal seed-filling. *Int. J. Agric. Biol. Eng.* **2018**, *11*, 76–87. [CrossRef]
10. Zhang, F.X.; Qing, C.L.; Wang, X. Study on Leak in Seeding Prevention and Seed Protection of Disc Precision Soybean Metering Device. *J. Agric. Mech. Res.* **2022**, *44*, 65–70.
11. Meng, H.; Wang, X.; Li, X.H.; Li, H.; Yu, Y.C. Design and experiment of soybean seed metering device with constant disturbance aided filling soybean. *J. China Agric. Mech. Chem.* **2023**, *44*, 18–25.

12. Li, W.; Xu, H.; Li, X.H.; Li, H.; Yu, Y.C. Design and Experiment of Soybean Side Nest Seed Meter Based on EDEM. *J. Agric. Mech. Res.* **2023**, *45*, 164–169.
13. Li, M.T.; Li, T.Y.; Guan, X.D.; Zhao, G.K.; Zhou, F.J. Design on Push Structure of Centrifugal Cone Seed-metering Device and Its Filling Mechanism Analysis. *Trans. Chin. Soc. Agric. Mach.* **2018**, *49*, 77–85.
14. Zhang, X.L.; Song, J.; Li, X.Y.; Xie, F.X.; Zhang, L. Design and simulation analysis of pneumatic mechanical combined single disc and double row seed meter. *J. China Agric. Mech. Chem.* **2020**, *41*, 30–34.
15. Li, B.H.; Li, H.; Qi, X.D.; Xu, S.Y.; Bai, M.C. Design and Test of Double—row Pneumatic Precision Metering Device for Brassica Chinensis. *J. Agric. Mech. Res.* **2022**, *44*, 71–77.
16. Guo, P.; Zheng, X.S.; Wang, D.W.; Hou, J.L.; Zhao, Z. Design and Experiment of Precision Seed-metering device with Pneumatic Assisted Seed-filling for Peanut. *Trans. Chin. Soc. Agric. Mach.* **2024**, *55*, 64–74.
17. Chen, Y.L.; Jia, H.L.; Wang, J.X.; Wang, Q.; Zhao, J.L.; Hu, B. Design and Experiment of Scoop Metering Device for Soybean High-speed and Precision Seeder. *Trans. Chin. Soc. Agric. Mach.* **2017**, *48*, 95–104.
18. Dun, G.Q.; Yu, C.L.; Yang, Y.Z.; Ye, J.; Du, J.X.; Zhang, J.T. Parameter simulation optimization and experiment of seed plate type hole for soybean breeding. *Trans. Chin. Soc. Agric. Eng.* **2019**, *35*, 62–73.
19. Huang, Y.X.; Li, P.; Dong, J.X.; Chen, X.H.; Zhang, S.L.; Liu, Y. Design and Experiment of Side-mounted Guided High Speed Precision Seed-metering device for Soybean. *Trans. Chin. Soc. Agric. Mach.* **2022**, *53*, 44–53+75.
20. Yazgi, A. Effect of seed tubes on corn planter performance. *Appl. Eng. Agric.* **2016**, *32*, 783–790.
21. Kocher, M.F.; Coleman, J.M.; Smith, J.A.; Kachman, S.D. Corn seed spacing uniformity as affected by seed tube condition. *Appl. Eng. Agric.* **2011**, *27*, 177–183. [CrossRef]
22. Yang, L.; Yan, B.X.; Cui, T.; Yu, Y.M.; He, X.T.; Liu, Q.W.; Liang, Z.J.; Yin, X.W.; Zhang, D.X. Global overview of research progress and development of precision maize planters. *Int. J. Agric. Biol. Eng.* **2016**, *9*, 9–26.
23. Liao, Y.T.; Li, C.L.; Liao, Q.X.; Wang, L. Research Progress of Seed Guiding Technology and Device of Planter. *Trans. Chin. Soc. Agric. Mach.* **2020**, *51*, 1–14.
24. Available online: https://www.maschio.com/en/web/international (accessed on 7 February 2020).
25. Dong, J.X.; Gao, X.J.; Zhang, S.L.; Huang, Y.X.; Zhang, C.Q.; Shi, J.T. Design and Test of Guiding Seed Throwing Mechanism for Maize Posture Control and Driving Metering Device. *Trans. Chin. Soc. Agric. Mach.* **2023**, *54*, 25–34.
26. Chen, X.G.; Zhong, L.M. Design and test on belt-type seed delivery of air-suction metering device. *Trans. Chin. Soc. Agric. Eng.* **2012**, *28*, 8–15.
27. Li, Y.H.; Yang, L.; Zhang, D.X.; Cui, T.; Zhang, K.L.; Xie, C.J.; Yang, R.M. Analysis and test of linear seeding process of maize high speed precision metering device with air suction. *Trans. Chin. Soc. Agric. Eng.* **2020**, *36*, 26–35.
28. Li, Y.H.; Yang, L.; Zhang, D.X.; Cui, T.; He, X.T.; Du, Z.H.; Wang, D.C. Performance analysis and structure optimization of the maize precision metering device with air suction at high-speed condition. *Trans. Chin. Soc. Agric. Eng.* **2022**, *38*, 1–11.
29. Wang, D.W.; Ji, R.Q.; He, X.N.; Guo, P.; Shi, Y.X.; Zhang, C.X. Drive-guided Combination Slot-assisted Seed-attached Air-absorbing Peanut High-speed Precision Seed Meter. *Trans. Chin. Soc. Agric. Mach.* **2023**, *54*, 59–70+149.
30. Zhao, L.J.; Yan, S.S.; Wang, Y.J.; Zhang, Y.X.; Han, Y.M.; Cai, X.H.; Xu, C.L. Experiment and Design on Air Suction Single and Double Row Precision Universal Metering Device. *J. Agric. Mech. Res.* **2019**, *41*, 136–141.
31. Gai, M.M.; Yang, J.; Li, X.H.; Qu, Z.; Li, H.; Yu, Y.C. Design and test of a guided horizontal disc soybean precision seed-metering device. *Jiangsu Agric. Sci.* **2023**, *51*, 200–206.
32. Yang, D.X. *Particle Modelling of Soybean Seeds and the Simulation Analysis and Experimental Study of the Seed-Throwing and Pressing*; Jilin University: Changchun, China, 2021.
33. Qu, Z.; Liu, L.; An, X.; Lu, Q.; Ding, L.; Yu, Y.C. Optimization Design and Experiment of Soybean Hole Wheel Seed Metering Device Besed on EDEM. *J. Agric. Mech. Res.* **2023**, *45*, 103–110.
34. Niu, Y.Y.; Xu, M.C.; Qu, Z.; An, X.; Li, H.; Yu, Y.C. Design and test of EDEM-based self-disturbing internal spoon type soybean precision seed-metering device. *Jiangsu Agric. Sci.* **2022**, *50*, 202–207.
35. Dun, G.Q.; Yang, Y.Z.; Guo, Y.L.; Liu, X.L.; Yu, C.L.; Du, J.X.; Zhang, J.T. Analysis of EDEM simulation of different soybean seed-filling characteristics. *J. Henan Agric. Univ.* **2019**, *53*, 93–98.
36. Xu, J.; Cai, Z.S.; Gan, Y.Q.; Zhang, L.L. Optimization study on seed-clearing process for declined disc-scoop-type soybean seed metering device based on EDEM. *J. Northeast Agric. Univ.* **2018**, *49*, 79–88.
37. *GB/T 6973-2005*; Testing Methods of Single Seed Drills (Precision Drills). AQSIQ-SAC: Beijing, China, 2005.
38. Zhang, S.J.; Qiu, Z.J.; Wang, F.H.; Zhao, H.M.; Zhang, H.H. Design and Test on the Field Soil Moisture and Compaction Acquisition Instrument. *Trans. Chin. Soc. Agric. Mach.* **2010**, *41*, 75–79.
39. Xu, S.; Kan, Y.C. Correlation of Soil Compactness and Water Content Under Different Fertility Levels. *Chin. Agric. Sci. Bu.* **2022**, *38*, 94–100.

agriculture

MDPI

Article

Simulation and Optimization of a Rotary Cotton Precision Dibbler Using DEM and MBD Coupling

Long Wang [1,2], Xuyang Ran [1,2], Lu Shi [1,2], Jianfei Xing [1,2], Xufeng Wang [1,2], Shulin Hou [3] and Hong Li [1,2,*]

1 College of Mechanical and Electronic Engineering, Tarim University, Alar 843300, China; 120140002@taru.edu.cn (L.W.); ranxuyang98@126.com (X.R.); fengleaf77@126.com (L.S.); 120200012@taru.edu.cn (J.X.); wxf@taru.edu.cn (X.W.)

2 Xinjiang Production and Construction Corps (XPCC) Key Laboratory of Utilization and Equipment of Special Agricultural and Forestry Products in Southern Xinjiang, Alar 843300, China

3 College of Engineering, China Agricultural University, Beijing 100083, China; h01520@cau.edu.cn

* Correspondence: 120140003@taru.edu.cn

Abstract: Investigating the seeding mechanism of precision seeders is of great significance for improving the quality of cotton sowing operations. This paper designs a rotary type-hole cotton precision mulching dibbler. The main factors influencing the entry of cotton seeds into the seed wheel holes during the seeding process are then theoretically analyzed. Following this, an accurate discrete element model of coated cotton seeds is established and combined with a discrete element method (DEM) and multi-body dynamics (MBD)-coupled simulation model of the seed drill for seed picking and planting. Simulation experiments on the seeding performance of the precision dibbler were performed to study the influence of the seed wheel structure and motion parameters on the picking and planting performance under different speeds. The optimal parameter combination for the seed wheel is obtained through optimization experiments, and a precision dibbler is manufactured for bench testing. The bench test results are consistent with the simulation test results. At the precision dibbler rotation speed of 16 r/min, the qualified index reaches a maximum value of 93.28%, the skip sowing index increases with the precision dibbler rotation speed, and the re-sowing index decreases as the speed increases. These optimization results significantly improved seeding precision and efficiency and are of great significance for the reliability and effectiveness of cotton sowing operations.

Keywords: discrete element method; multi-body dynamics; coupling simulation; dibbler

Citation: Wang, L.; Ran, X.; Shi, L.; Xing, J.; Wang, X.; Hou, S.; Li, H. Simulation and Optimization of a Rotary Cotton Precision Dibbler Using DEM and MBD Coupling. *Agriculture* **2024**, *14*, 1411. https://doi.org/10.3390/agriculture14081411

Academic Editor: Maohua Xiao

Received: 27 July 2024
Revised: 16 August 2024
Accepted: 18 August 2024
Published: 20 August 2024

1. Introduction

Coupling the discrete element method (DEM) with multi-body dynamics (MBD) to conduct dynamic simulations of complex mechanical structures containing granular materials can effectively improve the dynamic performance of mechanisms and optimize mechanical structures and motion parameters [1–3]. This coupling approach can determine the motion behavior of materials and equipment and also predicts the operational performance of equipment [4]. The DEM calculates the loads of bulk granular materials within the geometric bodies of the equipment. The determined values are then input into the MBD to obtain the relative motion of the bodies. Following this, the motion is transferred back to the DEM, which calculates the behavior of the particles and the loads on the geometric bodies based on the motion. This mutual transfer enables coupled calculations [5].

The application of MBD-DEM co-simulation techniques for analyzing the motion state of granular materials in complex structures was first applied in the field of engineering. Lu [6] and Coetzee [4] designed MBD-DEM-coupled simulation models for civil engineering and geotechnical engineering, respectively. Applications have also been presented in aerospace engineering [7] and mining engineering [8]. Ji [9] employed DEM-MBD-coupled simulations to analyze the impact of the landing method and cushioning mechanism on the landing process of the lunar lander. Mohajeri [10] simulated the grabbing process of iron ore under bonding and stress using MBD-DEM-coupled simulations. Shi [11,12] analyzed the influence of compaction operations on the mechanical quality and damage of ballast based on the DEM-MBD-coupled method. Lommen [5] established a framework for the development, validation, and application of combined MBD and DEM simulations. Xiao [13,14] employed one-way-coupled MBD-DEM simulations to determine the influence of damping particles on the dynamic response of gear transmission. Chung [15] and Wu [16] developed bidirectional-coupled MBD-DEM dynamic models for gear and bearing systems, with damping particles filled in the gear cavities, to analyze the system's dynamic response and conduct experimental validation. The South African company VR Steel optimized the bucket of a dragline through co-simulation using ADAMS-EDEM, increasing the bucket fill rate while reducing the driving forces of the equipment [17].

Recent studies have applied the coupling simulation analysis of DEM and MBD to agricultural engineering [18]. Xu [19] established a simulation analysis model for precision seeders based on DEM-MBD coupling to analyze the soil covering and compaction process during planting operations. There was a strong agreement between the simulation and experimental results, validating the feasibility and applicability of the coupled simulation method. Yan [20] realized simulation analysis of the soybean seeding monomer working process by coupling EDEM and RecurDyn. The simulation results agreed with the test results, proving the accuracy of the coupling method. Liu [21] employed coupled simulation analysis using EDEM and RecurDyn to analyze the load on the rotary tiller shaft of a micro-tiller. Lai [22] conducted a DEM-MBD-coupled simulation experiment to analyze the impact of different seeding chain tension, seeder structure, and operating parameters on the working performance of a chain spoon-type ginseng precision seeder. Kim [23] established a soil-tool coupling simulation model based on DEM-MBD coupling and conducted simulation experiments combined with field measurements. The results indicated the ability of the simulations to effectively and accurately replace on-site testing. Dong [24] used DEM-MBD coupling to simulate the vibration-deep loosening operation, analyzing the soil disturbance and velocity distribution during the operation. However, despite these advances, the application of DEM-MBD coupling specifically to cotton precision dibblers remains relatively limited. In light of this, we believe that exploring the use of DEM-MBD coupling for the design and optimization of cotton precision dibblers could provide new insights into improving seeding performance. The previous literature indicates that the DEM-MBD simulation method can effectively analyze the motion characteristics of seeds in a seeder and determine the main factors affecting the seeding performance of the seeder. Applying DEM-MBD coupling to the design and optimization of cotton precision dibblers differs from previous agricultural applications. This method allows for more accurate prediction of seeding performance by simulating the unique interactions between cotton seeds and the dibbler components, thereby improving the precision and efficiency of cotton sowing operations.

This study aims to improve the structural design of seeding machinery, optimizing the existing configurations to enhance the efficiency of seed picking and sowing processes. Based on the DEM-MBD-coupled simulation model for a cotton precision dibbler, this research analyzed the main factors influencing the seeder's performance and explored the effects of different rotational speeds and structural and motion parameters of the seed wheel on seeding performance. A consistent trend observed between the simulations and bench tests validates the feasibility of the coupled simulation approach and the effectiveness of the simulation parameters. This work provides a reference for the structural analysis and optimization of the seeding unit.

2. Structure Analysis and Modeling of the Dibbler

Figure 1 presents the rotary type-hole cotton precision dibbler structure designed for the mulching planting mode of cotton in the northwest region of China. The main components of the structure include a seed tube, waist belt, duckbill, seed wheel, disrupter, and a moving plate. The seed tube is designed to guide the cotton seeds falling from the seed box along the correct path into the seed chamber. The outer side of the belt is used to secure the duckbill of the rotary type-hole dibbler, while the inner side is employed to install the type-hole wheel. The cotton seeds fall into the duckbill through the type-hole wheel by gravity. The duckbill, which directly contacts the soil, is a critical component that ensures the cotton seeds are ultimately deposited into the soil. The type-hole wheel is an essential component of the rotary type-hole dibbler, responsible for precisely metering the seeds that enter the seed chamber. The disrupter stirs the seeds within the seed chamber, making them easier for the type-hole wheel to capture. The moving plate connects and secures all components, facilitating rotational seeding.

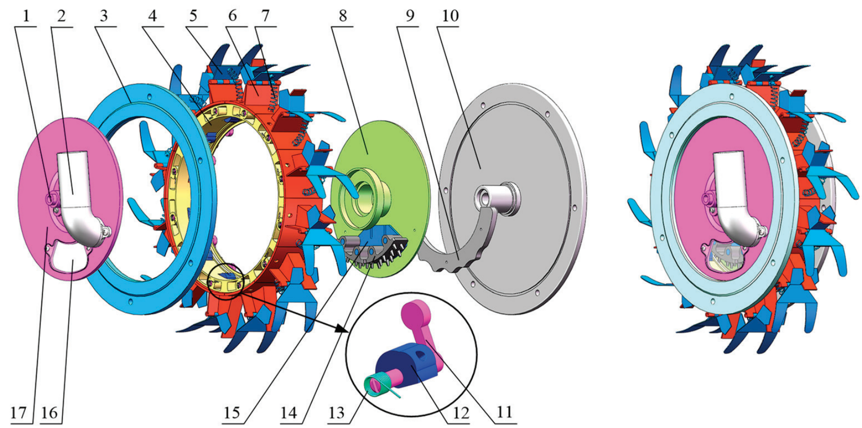

Figure 1. Structure of the rotary type-hole dibbler. (1) Shaft, (2) seed tube, (3) dynamic ring, (4) waist belt, (5) duckbill dynamic plate, (6) spring, (7) duckbill fixed plate, (8) fixed plate, (9) gear plate, (10) moving plate, (11) shifter, (12) type-hole wheel, (13) torsion spring, (14) disrupter, (15) disrupter support frame, (16) sight hole cover plate, and (17) end cover.

2.1. Working Principle of the Rotary Type-Hole Dibbler

The working process of a dibbler can be divided into three key stages: seed picking and cleaning; seed storage and dropping, and hole forming and seeding (Figure 2). During operation, the dibbler rolls on the mulch and soil at speed v under the drive of the main frame of the seeding machine. The cotton seeds in the seed box then enter the seed chamber through a seed-dropping pipe. The dibbler rotates as the main frame advances. When the type-hole wheel enters the seed picking and cleaning area, the gear plate moves the shifter, which connects with the type-hole wheel, causing the holes on the type-hole wheel to rotate in and out in the seed chamber as the belt rotates, achieving seed picking and cleaning. As the dibbler continues to rotate, the type-hole wheel enters the seed storage and dropping area, and the shifter disengages from the gear plate. The type-hole wheel then returns to its initial position under the action of the torsion spring, and the hole enters the seed storage chamber. As the dibbler continues to rotate, the hole opens downwards, and the cotton seeds slide out under the effect of gravity, passing through the seed storage chamber and entering the duckbill. At this point, the duckbill is in a closed state under the action of the spring. As the dibbler continues to rotate, it enters the seeding area and the duckbill reaches the bottom of the dibbler and inserts into the mulch and soil. The duckbill blade moves upwards under the pressure of the soil, causing the duckbill to open, and the cotton seeds are sown into the soil, thus completing the seeding operation.

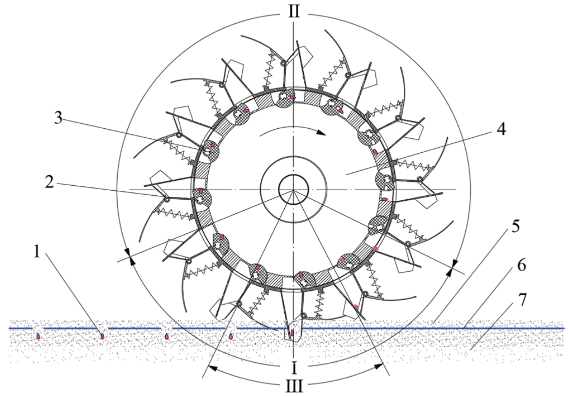

Figure 2. Working principle of the rotary type-hole dibbler. (I) Seed picking and cleaning, (II) seed storage and dropping, (III) hole forming and seeding. (1) cotton seeds, (2) duckbill, (3) type-hole wheel, (4) dibbler, (5) soil on plastic film, (6) plastic film, and (7) soil under plastic film.

2.2. Analysis of the Seed-Picking Movement of the Type-Hole Wheel

The successful seed picking of the dibbler-type hole wheel depends on the movement of the cotton seeds along the surface of the hole wheel. In particular, the cotton seeds can slide, roll, or exhibit a combination of both movements. The dibbler rotates and transfers at a certain speed to the lower layer of the cotton seeds that are in contact with the inner surface of the belt. This speed is less than or equal to the belt speed. The lower cotton seed layer then transfers a certain speed to the upper layer of cotton seeds, thereby transferring its speed to the cotton seeds inside the seed box. The relative speed of the cotton seeds is key in investigating the successful picking of seeds by the type-hole wheel. Without relative movement, successful seed picking cannot occur. Moreover, if the relative speed is too low, the frequency of successful seed picking is low, resulting in low sowing efficiency, while if the relative speed is too high, the type-hole wheel may not pick seeds in time, leading to missed sowing. Therefore, a precision dibbler must have a good seed-picking performance to clearly define the maximum limit speed at which cotton seeds can pass through the type holes of the type-hole wheel.

The motion trajectory equation of the hole wheel during the seed-picking process is described as follows:

$$\begin{cases} S = A\sin(2\pi f t) \\ f = \frac{360nz}{\tau} \end{cases} \tag{1}$$

where S is the harmonic motion displacement of the type-hole wheel (mm); A is the vibration amplitude of the type-hole wheel (mm); f is the vibration frequency of the type-hole wheel (Hz); n is the rotational speed of the seeder (r/min); z is the number of teeth on the gear plate; t is the time (min); and τ is the corresponding angular degree of the vibrating motion region of the seed-picking wheel (°).

By taking the first derivative of the motion trajectory equation of the hole wheel with respect to time t, the motion equation for harmonic motion velocity v_0 of the hole wheel can be obtained as follows:

$$v_0 = \frac{\mathrm{d}S}{\mathrm{d}t} = 2\pi A\cos(2\pi f) \tag{2}$$

In addition, the hole wheel moves in a circular motion along with the belt. The motion equation for its circular motion $v_r{}'$ is given by Equation (3):

$$v_r' = \omega R = 2\pi n R \tag{3}$$

The velocity of the hole wheel v' is the vector sum of its harmonic motion velocity v_0 and circular motion velocity v_r, expressed as Equation (4).

$$v' = \sqrt{v_0^2 + v_r'^2} = \sqrt{4\pi^2 n^2 R^2 + 4\pi^2 A^2 f^2 (\cos(2\pi f t))^2} \tag{4}$$

When the cotton seed is in an inverted position and needs to enter the type hole, the maximum distance of movement is required. We assume that the cotton seed approaches the type hole with its germ end, the coordinate origin is at the top right point of the type hole, the X-axis is the tangential direction of the seeding wheel rotation, and the Z-axis is the normal direction of the seeding wheel. When the center of gravity point O' moves directly above the edge of the type hole, a gap is generated between the lower side of the cotton seed's center of gravity and the edge of the type hole. Under the influence of gravity, the cotton seed begins to flip counterclockwise until it completely enters the type hole. As the cotton seed enters the type hole, its motion is similar to free falling and rotational motion, and the trajectory of the motion is approximately parabolic, as shown in Figure 3.

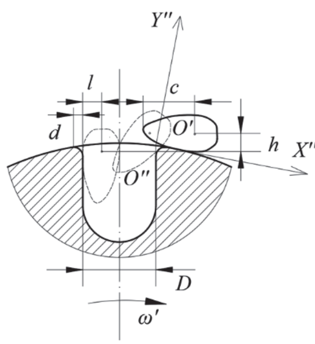

Figure 3. Motion state of the cotton seed falling into the type hole.

When the cotton seed enters the type hole at maximum speed $v_{\max}$, the motion trajectory of the cotton seed center is given by Equation (5):

$$\begin{cases} D + d - l = v_{\max} t_0 \\ h = \frac{1}{2} g t_0^2 \end{cases} \tag{5}$$

where l is the horizontal distance between the cotton seed center of mass and the type hole wall (mm); t_0 is the time taken by the cotton seed center of mass (from the beginning) to fall into the type hole (s); h is the vertical distance that the cotton seed center of mass passes through during the falling process into the type hole (mm); d is the chamfer width (mm); and g is the acceleration due to gravity (m/s^2).

From Equation (5), the required time t_0 for the cotton seed to fall into the type hole can be obtained as follows:

$$t_0 = \sqrt{\frac{2h}{g}} \tag{6}$$

Substituting Equation (6) into Equation (5) gives the terminal velocity $v_{\max}$ at which the cotton seed fills the type hole as Equation (7):

$$v_{\max} = (D + d - l)\sqrt{\frac{g}{2h}} \tag{7}$$

The relative movement velocity v of the cotton seed with respect to the type-hole wheel is the vector sum of the type-hole wheel movement velocity v' and the relative velocity of the cotton seed v_r with respect to the dibbler, expressed as Equation (8):

$$v = \sqrt{v'^2 + v_r^2} = \sqrt{4\pi^2 n^2 R^2 + 4\pi^2 A^2 f^2 (\cos(2\pi f t))^2 + v_r^2} \tag{8}$$

To ensure the seeding accuracy of the furrow opener, the movement velocity v of the cotton seed with respect to the type-hole wheel must be less than the terminal velocity $v_{\max}$ of the cotton seed filling the type hole:

$$\sqrt{4\pi^2 n^2 R^2 + 4\pi^2 A^2 f^2 (\cos(2\pi f t))^2 + v_r^2} < (D + d - l)\sqrt{\frac{g}{2h}} \tag{9}$$

Equation (9) reveals that when parameters such as the type hole diameter, hole chamfer size, cotton seed dimensions, cotton seed friction coefficient, cotton seed layer height inside the dibbler, and belt radius are constant, the successful filling of cotton seeds into the type-hole wheel is related to its vibration amplitude, the vibration frequency, and the rotation speed of the dibbler.

In the device design process, we used the equations derived in this paper to calculate the key parameters. These equations helped determine the optimal rotation speed of the seeder, the number of gear plate teeth, and the oscillation amplitude of the type-hole wheel to ensure efficient performance in actual operation.

2.3. Establishment of a Discrete Element Model for Coated Cotton Seeds

The coated cotton seeds are similar to ovals. This study utilized reverse engineering technology to obtain an accurate contour model of the cotton seeds. A Capture MINI scanner (3D Systems) was employed to perform a three-dimensional (3D) scan of the outer contour of the cotton seed, and Geomagic Wrap 3D 2017 (3D Systems) was used to process the 3D scanning data. Figure 4 presents the process adopted for the cotton seed contour model. The physical coated cotton seed is depicted in Figure 4a. The 3D scanning data were employed to derive the point clouds of the coated cotton seed. The point cloud data were preprocessed to remove noise points from the original point cloud and compress it. It was then encapsulated to form a polygon model. Automatic curvature repair was applied to the missing areas in the polygon model to obtain the contour model of the coated cotton seed, as shown in Figure 4b.

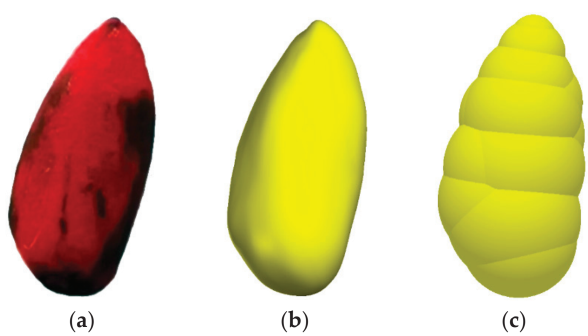

Figure 4. Processing of the coated cotton seed contour model: (**a**) coated cotton seed, (**b**) contour model, (**c**) multi-sphere aggregation particle model.

In the discrete element simulation software, spherical or other shaped particles are required to establish the discrete element model of the target materials. However, actual materials are mostly irregular in shape. In the EDEM discrete element software, the bonded particle [25] and multi-sphere [26] methods can be used to establish material models. The bonded particle model requires complex computations and a long simulation time due to the large number of particles used. The multi-sphere aggregation model has lower computational and simulation time requirements. Based on this, we adopt the multi-sphere aggregation model for the simulation experiments. The material contour model is imported into the EDEM software, and according to the model contour, several spherical particles with different diameters are overlapped and stacked to form the model. Figure 4c presents the cotton seed model established by this method, comprising 13 spherical particles with different diameters.

2.4. Establishment of the DEM-MBD Coupling Simulation Model

We implemented the MBD-DEM method using RecurDyn V9R2 (FunctionBay) and EDEM 2020 (DEM-Solutions). RecurDyn can simulate the complex motion of the planter, while EDEM simulates the motion between particles and components. Combining the RecurDyn and EDEM simulations can achieve real-time data transfer, enabling the bidirectional coupling of the cotton seed particles and furrow wheel planter. During the joint simulation, RecurDyn transfers the motion of the belt and seeding wheel components in the planter to EDEM. EDEM then calculates the forces and moments exerted by the cotton seed particles on the moving components of the planter and returns relevant information to RecurDyn. In the next time step, RecurDyn calculates the new displacements, velocities, accelerations, etc. of the components based on the new force, torque information, and planter motion, which are then transferred back to EDEM and implemented on the cotton seed particles. The data exchange process iterates back and forth to achieve bidirectional coupling calculations between RecurDyn and EDEM.

To ensure the reasonable and efficient simulation and calculation of the furrow wheel planter, the planter model is simplified by considering only the components in direct contact with the cotton seeds in the seed chamber, including end caps, fixed plates, belts, seeding wheels, and pushrods. The furrow wheel planter is modeled in 3D using SolidWorks 2018 (Dassault Systemes). The material properties, connections, forces, and contacts are set up in the multibody dynamics software RecurDyn. In the model, the end caps and fixed plates are stationary, the belt rotates clockwise around the axis, the seeding wheel rotates around the axis, and the motion is controlled by torsion springs and limit stops.

The direct target of the furrow wheel planter is the coated cotton seeds. The virtual simulation process uses the Hertz–Mindlin (no slip) model to calculate the interaction relationships between the coated cotton seeds. According to actual operation conditions, cotton seeds are first introduced into the seed chamber from the seed drop tube. Therefore, the mechanism does not move during the seed-filling process. A particle factory is set on the seed drop tube using pre-calibrated discrete element particles of coated cotton seeds with contact parameters. A total of 3000 cotton seed particles are generated at a rate of 1000 seeds/s and in the direction of gravity, with a volume proportional to a normal distribution.

The intrinsic and contact parameters of materials are crucial in the discrete element simulation process. The intrinsic parameters include material density, Poisson's ratio, elastic modulus, etc., while the contact parameters include the collision coefficient, sliding friction coefficient, and rolling friction coefficient between materials. Table 1 reports the values of the intrinsic and contact parameters of cotton seeds and resin materials, determined based on previous experimental results and references [27,28].

The total simulation time is set as the same value for EDEM and RecurDyn in the coupling interface, and the time step in RecurDyn is fixed as an integer multiple of that in EDEM. Here, the time steps in RecurDyn and EDEM are set as 0.01 s and 2.5×10^{-6} s, respectively. Once the parameters are set, the coupled simulation commences. After coupling, cotton seed particles also appear in RecurDyn, as shown in Figure 5. The movements of the components of the seeder and the cotton seed particles are simultaneously displayed in the two software, with arrows indicating the rotation direction of the conveyor belt.

Table 1. Simulation model parameters.

Parameter	Value
Density of cotton seed (g/cm^3)	0.981
Poisson's ratio of cotton seed	0.27
Shear modulus of cotton seed (MPa)	1.4×10^7
Density of resin (g/cm^3)	1.18
Poisson's ratio of resin	0.38
Shear modulus of resin (MPa)	177
Seed-to-seed static friction coefficient	0.130
Seed-to-seed dynamic friction coefficient	0.225
Seed-to-seed collision restoration coefficient	0.185
Seed-to-resin static friction coefficient	0.49
Seed-to-resin dynamic friction coefficient	0.21
Seed-to-resin collision restoration coefficient	0.25

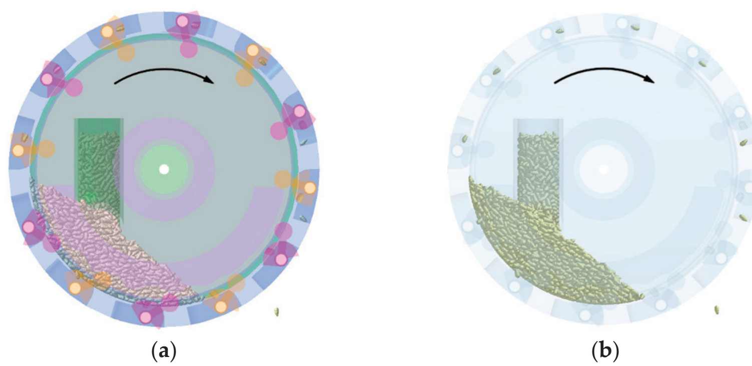

Figure 5. EDEM-RecurDyn-coupled simulation: (**a**) RecurDyn simulation; (**b**) EDEM simulation. The direction of the arrow indicates the direction of dibbler movement.

In EDEM, a cotton seed particle that has been successfully picked and discharged by the type-hole wheel is selected to generate the motion trajectory (Figure 6). The cotton seed enters the seed chamber from the seed drop tube, follows the rotation of the conveyor belt, and revolves with the seed group. It then moves from the bottom to the top of the conveyor belt, falls back to the bottom, and enters the hole of the type-hole wheel. When the hole of the type-hole wheel rotates back to the seed storage bin, the cotton seed reaches the seed storage bin and is discharged under the action of gravity.

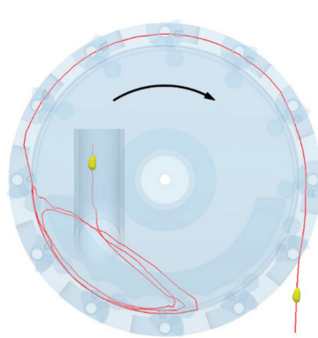

Figure 6. Motion trajectory of the cotton seed. Yellow represent cotton seed, and red lines represent the movement trajectory of cotton seed.

3. Simulation and Bench Tests

3.1. Simulation Test

The theoretical analysis in Section 2.2 reveals that the type-hole wheel structure has a certain disturbance effect on the seed population, and increasing the disturbance of the population can improve the probability of successful seed filling in the type-hole. To study the effect of the type-hole wheel structure on the seed population inside the seed cavity, this study designed three type-hole wheel structures, namely, a circular-type-hole wheel, a convex-type-hole wheel, and a corrugated-type-hole wheel. The basic structural parameters of these three type-hole wheels are the same, with a hole diameter of 7.0 mm and a depth of 10.0 mm. The convex and corrugated seed wheels have a surface wave amplitude of 2.0 mm, and a rounded corner is made at the upper edge of the shape hole with a radius of 0.5 mm (Figure 7). The dibbler speed, number of gear plate teeth, and vibration amplitude of the type-hole wheel are set as 20 r/min, 6, and 10 mm, respectively, and the working speed of the dibbler is controlled by setting the rotation speed of the belt.

(**a**) (**b**) (**c**)

Figure 7. Different type-hole wheel structures designed in this study: (**a**) circular-type-hole wheel, (**b**) convex-type-hole wheel, (**c**) corrugated-type-hole wheel.

The vibration frequency and oscillation amplitude of the type-hole wheel influence the cotton seed filling effect on the shape hole. In addition, the oscillation frequency corresponds to the number of teeth on the gear plate during the movement of the type-hole wheel in the seeding and clearing area, and the oscillation amplitude corresponds to the tooth surface fluctuation amplitude of the gear plate. To investigate the impact of the vibration frequency and oscillation amplitude of the type-hole wheel on the seeding performance of the dibbler, we design a simulation test plan based on an optimized design of the combined experimental method. The test plan is used to determine the combination of type-hole wheel motion parameters that can achieve the best seeding performance. The type-hole wheel structure is corrugated, and based on preliminary experiments, the type-hole wheel oscillation amplitude is selected as 8–12 mm and the number of gear plate teeth is 4–8 (Figure 8).

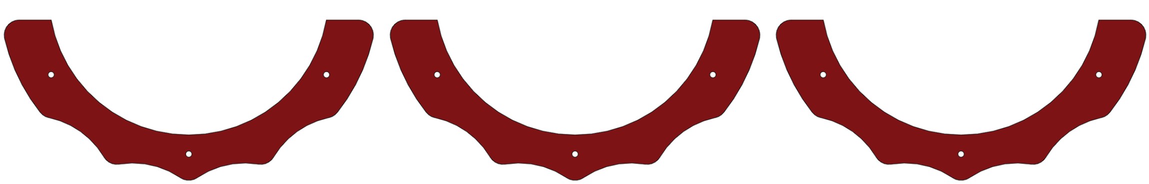

(**a**) (**b**) (**c**)

Figure 8. Gear plates of dibbler structures designed in this study: (**a**) Four teeth, (**b**) six teeth, (**c**) eight teeth.

To reduce the impact of the rotation speed on the seed population of the dibbler, the seeder rotation speed of 10–30 r/min was selected and the levels of seeding experiment factors were encoded (Table 2).

Table 2. Encoding of the seeding experiment factor levels.

Level	Rotation Speed of Dibbler X_1 (r/min)	Number of Teeth on the Gear Plate X_2	Oscillation Amplitude of the Type-Hole Wheel X_3 (mm)
−1	10	4	7
0	20	6	10
1	30	8	13

The simulation planting operation status has three key forms, namely single seeding (1 seed), double seeding (≥2 seeds), and missed seeding (no seed). To facilitate the observations of cotton seed movements, during the EDEM simulation process, only cotton seed particles within the seed disc thickness in the seed metering device are selected during seed retrieval. Moreover, the transparency of all mechanical components is set to 0.1 (Figure 9). Figure 9a depicts the qualified sowing state, where the type-hole wheel typically takes out a single cotton seed from the group of seed particles and transfers it to the seed storage bin through the type hole. Figure 9b shows the re-sowing state, where the type-hole wheel takes out multiple cotton seeds from the group of seed particles and transfers them to the seed storage bin through the seed-type hole. The cotton seed status in the type holes under multiple double-seeding states reveals that smaller cotton seeds are more prone to double-seeding. This is because when the size of cotton seeds around the type hole is small, it is easier for two or more cotton seeds to enter the hole under their own gravity and the compression of other cotton seeds. This makes it difficult for the seed cleaning plate to remove them from the type hole. Furthermore, in the double seeding state, the two cotton seeds in the type hole are mostly overlapping. Figure 9c presents the skip sowing state, where the type-hole wheel fails to smoothly remove the cotton seed from the group of seed particles. The cotton seed status around the type hole under multiple missed seeding states indicates that larger cotton seeds are more likely to experience missed seeding. This is because when the size of the cotton seeds around the type hole is large, the cotton seeds have difficulty entering the type hole under their own gravity and the compression of other cotton seeds, leading to unsuccessful seed retrieval. In addition, when a cotton seed is about to enter the type hole, it escapes from the hole due to the compression of the surrounding cotton seeds, resulting in failed seed retrieval.

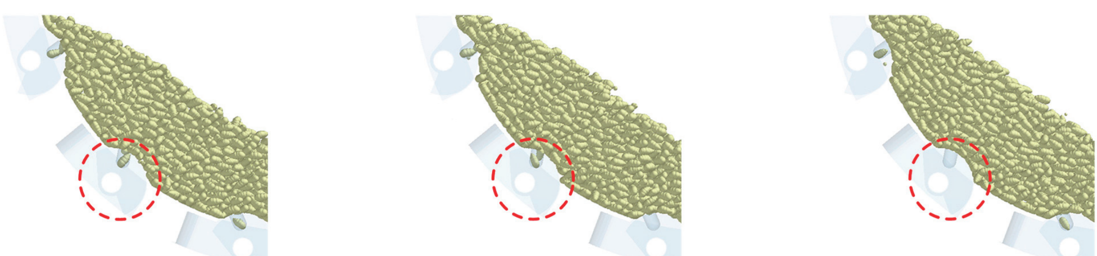

(**a**) (**b**) (**c**)

Figure 9. EDEM virtual simulation of seed sowing operation status: (**a**) qualified sowing state, (**b**) re-sowing state, (**c**) skip sowing state. The regions between red dashed lines represent seed sowing operation status.

According to the national standards GB/T 6976-2005 'Test Methods for Single-Granule (Precision) Seeders' and JB/T10293-2013 'Technical Conditions for Single-Granule (Precision) Seeders', this study selects the qualified index Y_1 (Y_1 represents the degree of matching between the number of seeds successfully sown by the seeder in each seeding cycle and the theoretical number of seeds), re-sowing index Y_2 (Y_2 refers to the proportion of instances where more than one seed is sown at a single seeding point during a seeding cycle), and skip sowing index Y_3 (Y_3 indicates the proportion of instances where no seeds are sown at a seeding point during the seeding process) as simulation test indicators to evaluate the quality of the seed metering device operation. These indices are calculated as follows:

$$Y_1 = \frac{N - n_1 - n_2}{N} \times 100\% \tag{10}$$

$$Y_2 = \frac{n_1}{N} \times 100\% \tag{11}$$

$$Y_3 = \frac{n_2}{N} \times 100\% \tag{12}$$

where N is the total number of cotton seeds counted in the experiment; n_1 is the number of cotton seeds that have a distance with adjacent seeds less than 0.5 times the theoretical seed distance; and n_2 is the number of cotton seeds that have a distance with adjacent seeds greater than 1.5 times the theoretical seed distance.

3.2. Bench Test

The JPS-12 seed metering device developed by the Heilongjiang Agricultural Machinery Research Institute was employed for the seeding performance test (Figure 10). During the test, the designed hole-type cotton seed metering device is installed on the test stand and the seedbed conveyor belt moves in the opposite direction to the seed metering device to simulate the actual field operation process. Cotton seeds are collected by the seed metering device and seeded on the seedbed conveyor belt coated with sticky oil to prevent the cotton seeds from bouncing on the seedbed conveyor belt. The image acquisition system of the test stand detects the cotton seeds in real-time to determine various seeding performance indicators and subsequently outputs the test results.

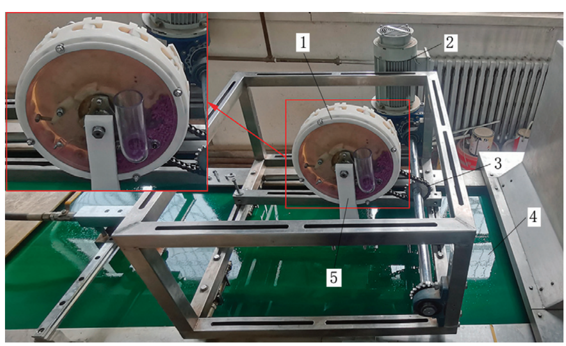

Figure 10. Seed planting performance evaluation test; (1) the rotary type-hole dibbler, (2) the motor, (3) the transmission shaft, (4) the conveyor belt, and (5) the fixed bracket. The red boxes and arrow represent enlarged view of the dibbler.

To validate the accuracy of the optimized simulation test results, the optimal parameter combination obtained from the simulation seeding test was used to create a gear plate, with a tooth number of 5.64 and a type-hole wheel swing amplitude of 9.71 mm. The components of the seeder were 3D printed using light-sensitive resin. Transparent resin materials were used for the seed-dropping tube and end cover to observe the seed movement inside the seeder. Xinlu Zhong 67 deseeded cotton seeds were selected for the experimental sample. The seeding device speeds were set to 12 r/min, 16 r/min, 20 r/min, 24 r/min, and

28 r/min for the seeding tests. In each test group, the number of seeding measurements was set to 250 (except for the start-up and stop phases), and each test group was repeated three times.

4. Results and Discussion

4.1. Impact of the Type-Hole Wheel Structure on the Seeding Performance

Figure 11 presents the vector diagram of the compression force of cotton seeds at 5.6 s when the rotational speed of the planter is 20 r/min. At this same time, the corrugated-type-hole wheel exhibits the maximum cotton seed compression force, reaching 0.317 N, followed by the convex-type-hole wheel (0.299 N) and the circular-type-hole wheel (0.212 N). The cotton seeds in the seed chamber of the circular-type-hole wheel generally move clockwise around the center. The cotton seeds at the bottom of the cotton seed group move to the upper right under the drive of the belt, and after reaching the top, they slide down to the left along the upper surface under the action of gravity and friction. The cotton seeds in the middle of the cotton seed group move clockwise under the drive of the upper and lower layer cotton seeds. The movement of the upper and lower layer cotton seeds in the seed chamber of the convex and corrugated-type-hole wheels is similar to that of the circular wheel. However, the movement of the cotton seeds in the middle of the cotton seed group exhibits an irregular trend, with a chaotic movement direction in some areas. Compared to the circular-type-hole wheel, the movements caused by the convex and corrugated-type-hole wheels are more irregular, indicating that they exert the greatest disturbance to the cotton seed particles, which is conducive to the filling of type holes by the cotton seeds.

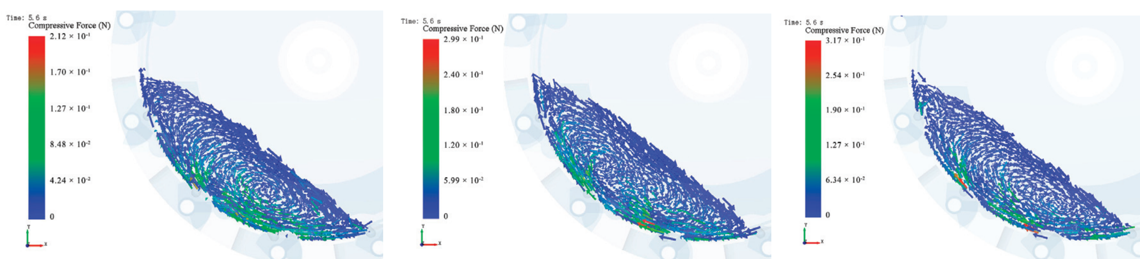

(**a**) (**b**) (**c**)

Figure 11. Vector plot of the cotton seed compression force at 5.6 s: (**a**) circular-type-hole wheel, (**b**) convex-type-hole wheel, (**c**) corrugated-type-hole wheel.

To further analyze the influence of the seeding wheel structure on the seeding process, the average velocity curves of cotton seed particles within the time steps of 3 to 15 s are shown in Figure 12. The cotton seed particle velocity with the circular-type-hole wheel is markedly lower than that of the convex and corrugated types. The fluctuation magnitude of the cotton seed particle velocity, from the largest to smallest, is as follows: convex-type-hole wheel (0.0284 m/s); circular-type-hole wheel (0.0276 m/s); and corrugated-type-hole wheel (0.0242 m/s). The relative velocity of cotton seed particles with the circular-type-hole wheel is low and the velocity fluctuates greatly. Although the convex-type-hole wheel can increase the relative velocity of the cotton seed particles, its velocity also exhibits large fluctuations. In contrast, the corrugated-type-hole wheel enhances the relative velocity of cotton seed particles while maintaining velocity fluctuations at a low level. This indicates the ability of the corrugated-type-hole wheel to improve the dibbler filling performance.

Therefore the structure of the type-hole wheel determines the mobility and compression force inside the dibbler. A well-designed type-hole wheel structure can effectively reduce the compression force between seeds, and increase the mobility of seeds, thereby improving filling efficiency. If the type-hole wheel structure is not optimized, the seeds may be subjected to excessive compression force, leading to seed damage or inadequate filling, which will further affect the quality and efficiency of seeding.

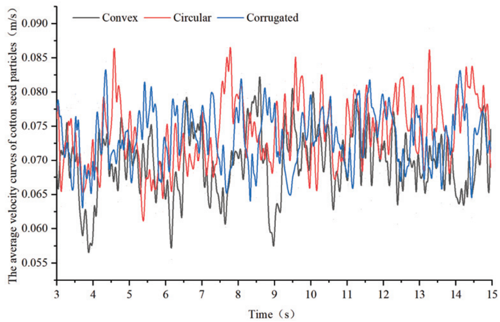

Figure 12. Average velocity of cotton seed particles under the action of different type-hole wheels with different structures.

4.2. Influence of the Dibbler Rotation Speed on Seeding Performance

To analyze the relationship between the speed of the type-hole wheel and the cotton seeds during the seed-picking process, two cotton seeds successfully filled into the type holes were randomly selected. When the dibbler rotation speed was 10 r/min, the selected seed numbers were 648 and 1472; when the planter rotation speed was 20 r/min, the selected seed numbers were 1088 and 1724; when the planter rotation speed was 30 r/min, the selected seed numbers were 564 and 116. The cotton seeds were marked in EDEM to obtain the speed of the cotton seeds and the corresponding type-hole wheels during the seed-picking process. The data were plotted using Origin 2018 (OriginLab Corporation, Indianapolis, United States) to present the speed change trends of the cotton seeds and the corresponding type-hole wheels at different rotation speeds, as shown in Figure 13.

Figure 13a,b reveal that when the dibbler rotation speed is 10 r/min, the duration of the type-hole wheel in the seed picking and cleaning area is approximately 2.65 s, with the speed fluctuating between 0.12 and 0.23 m/s. The time taken for cotton seeds no. 648 and no. 1472 to fill into the holes is 6.84 s and 10.52 s, with speeds of 0.0947 m/s and 0.1190 m/s, respectively. At this time, the corresponding speeds of the type-hole wheel are 0.1559 m/s and 0.1374 m/s, respectively. Under a rotation speed of 10 r/min, the speed fluctuation range of successfully picked cotton seeds is between 0.05 and 0.27 m/s, with the speed of the cotton seeds before filling into the holes generally higher than that of the type-hole wheel.

Figure 13c,d show that when the dibbler rotation speed is 20 r/min, the duration of the type-hole wheel in the seed picking and cleaning area is approximately 1.33 s, with the speed fluctuating between 0.25 and 0.45 m/s. The time taken for cotton seeds no. 1088 and no. 1724 to fill into the holes is 9.61 s and 12.64 s, with speeds of 0.1933 m/s and 0.1809 m/s, respectively. At this time, the corresponding speeds of the type-hole wheel are 0.2804 m/s and 0.2799 m/s, respectively. Under a rotation speed of 20 r/min, the speed fluctuation range of successfully picked cotton seeds is between 0.13 and 0.48 m/s, and the of the cotton seeds before filling into the holes is generally still higher than that of the type-hole wheel.

Figure 13e,f reveal that when the dibbler rotation speed is 30 r/min, the duration of the type-hole wheel in the seed picking and cleaning area is approximately 0.88 s, with the speed ranging from 0.37 to 0.66 m/s. The time taken for cotton seeds no. 564 and no. 116 to fill into the holes is 9.26 s and 12.28 s, with speeds of 0.3016 m/s and 0.4054 m/s, respectively. At this time, the corresponding speeds of the type-hole wheel are 0.4198 m/s and 0.4954 m/s, respectively. Under a rotation speed of 30 r/min, the speed fluctuation range of successfully picked cotton seeds is between 0.11 and 0.73 m/s, and the speed of the cotton seeds before filling into the holes is mostly lower than that of the type-hole wheel.

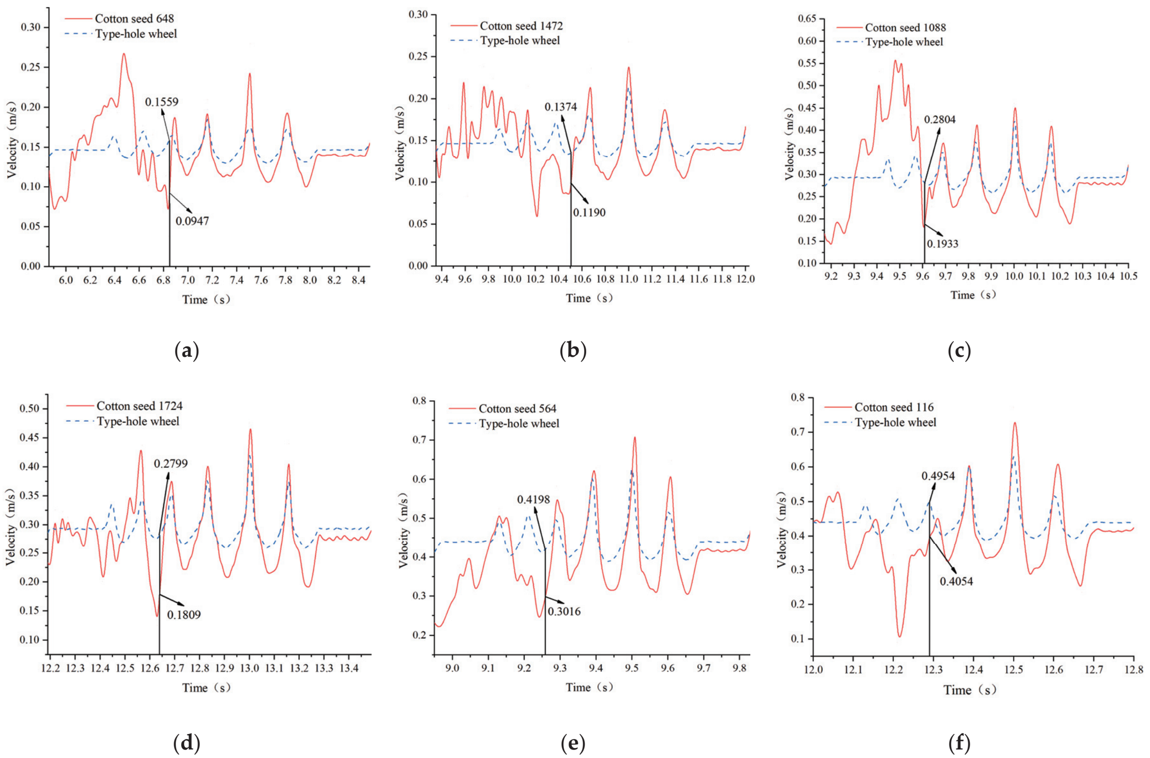

Figure 13. Speed of cotton seeds and type-hole wheels at different rotation speeds: (**a**) cotton seed 648 with the dibbler rotation speed at 10 r/min, (**b**) cotton seed 1472 with the dibbler rotation speed at 10 r/min, (**c**) cotton seed 1088 with the dibbler rotation speed at 20 r/min, (**d**) cotton seed 1724 with the dibbler rotation speed at 20 r/min, (**e**) cotton seed 564 with the dibbler rotation speed at 30 r/min, and (**f**) cotton seed 116 with the dibbler rotation speed at 30 r/min.

In summary, as the dibbler rotation speed increases, the duration of the type-hole wheel in the seed picking and cleaning area decreases, while the speed fluctuation range of the cotton seeds increases. Under the same dibbler rotation speed, the variation in the type-hole wheel speed is constant, but the cotton seed speed exhibits irregular random fluctuations. At different planter rotation speeds, a higher rotation speed results in a larger instantaneous speed of the cotton seeds. Before filling into the holes of the type-hole wheel, the speed changes are relatively chaotic and fluctuate greatly. However, after filling the holes, the speed of the cotton seeds follows a similar trend to that of the type-hole wheel speed, but with a larger speed fluctuation range than the type-hole wheel. After filling the holes, in addition to moving with the type-hole wheel, the cotton seeds also move within the holes. An improved planting effect is achieved when the relative speed between the cotton seeds and the type-hole wheel is smaller. Therefore, by adjusting the dibbler rotation speed, the relative speed of the cotton seeds within the dibbler can be changed, thereby improving the effectiveness of filling the cotton seeds into the holes.

4.3. Effects of the Motion Parameters of the Type-Hole Wheel on Seeding Performance

Based on the actual production situation, the qualified index Y_1, re-sowing index Y_2, and skip-sowing index Y_3 were selected as the experimental indicators for planting experiments. Table 3 reports the design of the Box–Behnken response surface experiment and the corresponding results.

Table 3. Design and results of the seeding experiment.

No.	Rotation Speed of Dibbler X_1 (r/min)	Number of Teeth on the Gear Plate X_2	Oscillation Amplitude of Type-Hole Wheel X_3 (mm)	Qualified Index Y_1 (%)	Re-Sowing Index Y_2 (%)	Skip Sowing Index Y_3 (%)
1	−1	1	0	89.69	7.25	3.06
2	0	−1	−1	89.16	5.39	5.45
3	0	−1	1	89.22	4.16	6.62
4	−1	0	1	90.43	6.52	3.05
5	0	1	−1	88.48	6.34	5.18
6	0	0	0	91.65	3.88	4.47
7	0	0	0	91.57	4.32	4.11
8	1	−1	0	86.58	4.49	8.93
9	0	1	1	86.96	6.89	6.15
10	0	0	0	91.52	4.21	4.27
11	1	0	−1	87.77	4.54	7.69
12	1	0	1	85.31	4.85	8.84
13	−1	0	−1	90.96	6.26	2.78
14	0	0	0	92.19	3.75	4.06
15	−1	−1	0	90.45	6.38	3.17
16	1	1	0	86.48	5.23	8.29
17	0	0	0	91.96	3.65	4.39

We employed Design-Expert 12.0 (Stat-Ease Inc., Minia Bonis, Minneapolis, MN, USA) to conduct polynomial regression analysis on the seeding experiment results. The second-order polynomial regression models for the qualified index, re-sowing index, and skip-sowing index are expressed in Equations (13)–(15):

$$\begin{aligned} Y_1 = {} & 91.78 - 1.92X_1 - 0.48X_2 - 0.56X_3 + 0.17X_1X_2 - 0.48X_1X_3 \\ & - 0.40X_2X_3 - 1.66X_1^2 - 1.82X_2^2 - 1.50X_3^2 \end{aligned} \tag{13}$$

$$\begin{aligned} Y_2 = {} & 3.96 - 0.91X_1 + 0.66X_2 - 0.01X_3 - 0.03X_1X_2 + 0.01X_1X_3 \\ & + 0.45X_2X_3 + 0.86X_1^2 + 1.01X_2^2 + 0.72X_3^2 \end{aligned} \tag{14}$$

$$\begin{aligned} Y_3 = {} & 4.26 + 2.71X_1 - 0.19X_2 + 0.45X_3 - 0.13X_1X_2 + 0.22X_1X_3 \\ & - 0.05X_2X_3 + 0.67X_1^2 + 0.93X_2^2 + 0.66X_3^2 \end{aligned} \tag{15}$$

Tables 4–6 report the results of the regression model variance analysis. The p-values of the regression models for the three indices are less than 0.0001, and the p-values of the lack-of-fit terms exceed 0.05. This indicates that the regression models are highly significant, the lack-of-fit of the models is not significant, and the regression models have a high fitting degree.

Table 4. Analysis of variance for the qualified index.

Source of Variance	Sum of Squares	Degrees of Freedom	F	p	Significance
Model	74.67	9	42.97	<0.0001	**
X_1	29.61	1	153.33	<0.0001	**
X_2	1.81	1	9.35	0.0184	*
X_3	2.48	1	12.82	0.0090	**
X_1X_2	0.1089	1	0.5640	0.4771	
X_1X_3	0.9312	1	4.82	0.0641	
X_2X_3	0.6241	1	3.23	0.1152	
X_1X_1	11.57	1	59.93	0.0001	**
X_2X_2	13.95	1	72.25	<0.0001	**
X_3X_3	9.51	1	49.24	0.0002	**
Residual	1.35	7			
Lack of fit	1.02	3	4.14	0.1017	
Error	0.3291	4			
Sum	76.02	16			

Note: ** denotes an extremely significant impact of the parameter ($p < 0.01$); and * represents a significant impact of the parameter ($p < 0.05$). The same as Tables 5 and 6.

Table 5. Analysis of variance for the re-sowing index.

Source of Variance	Sum of Squares	Degrees of Freedom	F	p	Significance
Model	21.69	9	15.29	0.0008	**
X_1	6.66	1	42.26	0.0003	**
X_2	3.50	1	22.19	0.0022	**
X_3	0.0015	1	0.0096	0.9247	
X_1X_2	0.0042	1	0.0268	0.8746	
X_1X_3	0.0006	1	0.0040	0.9516	
X_2X_3	0.7921	1	5.03	0.0599	
X_1X_1	3.12	1	19.82	0.0030	**
X_2X_2	4.33	1	27.46	0.0012	**
X_3X_3	2.18	1	13.81	0.0075	**
Residual	1.10	7			
Lack of fit	0.7647	3	3.01	0.1574	
Error	0.3387	4			
Sum	22.79	16			

Table 6. Analysis of variance for the skip sowing index.

Source of Variance	Sum of Squares	Degrees of Freedom	F	p	Significance
Model	69.15	9	270.38	<0.0001	**
X_1	58.81	1	2069.37	<0.0001	**
X_2	0.2775	1	9.77	0.0167	*
X_3	1.58	1	55.75	0.0001	**
X_1X_2	0.0702	1	2.47	0.1599	
X_1X_3	0.1936	1	6.81	0.0349	*
X_2X_3	0.0100	1	0.3519	0.5717	
X_1X_1	1.90	1	66.76	<0.0001	**
X_2X_2	3.65	1	128.49	<0.0001	**
X_3X_3	1.83	1	64.30	<0.0001	**
Residual	0.1989	7			
Lack of fit	0.0753	3	0.8126	0.5498	
Error	0.1236	4			
Sum	69.35	16			

Table 4 reveals that the interaction terms (X_1X_2, X_1X_3, and X_2X_3) between the rotation speed of the dibbler, the number of teeth on the gear plate, and the oscillation amplitude of type-hole wheel do not exert a significant influence ($p > 0.05$) on the qualified index model, while all other factors have a significant impact on the qualified index model. Table 5 indicates that the oscillation amplitude of the type-hole wheel does not significantly affect the re-sowing index model ($p > 0.05$), suggesting that the oscillation amplitude of the type-hole wheel has a minor impact on the re-sowing index. In addition, the interaction terms (X_1X_2, X_1X_3, and X_2X_3) between the rotation speed of the dibbler, the number of teeth on the gear plate, and the oscillation amplitude of the type-hole wheel also do not significantly influence ($p > 0.05$) the re-sowing index model, while all other factors have a significant impact on the re-sowing index model. Table 6 shows that the interaction term (X_1X_2) between the rotation speed of the dibbler and the number of teeth on the gear plate and the interaction term (X_2X_3) between the number of teeth on the gear plate, and the oscillation amplitude of type-hole wheel do not significantly impact ($p > 0.05$) the skip sowing index model, while all other factors have a significant impact on the skip sowing index model.

Removing the non-significant terms from the regression models of the qualified index, re-sowing index, and skip-sowing index results in the following simplified equations, respectively:

$$Y_1 = 91.78 - 1.92X_1 - 0.48X_2 - 0.56X_3 - 1.66X_1^2 - 1.82X_2^2 - 1.50X_3^2 \tag{16}$$

$$Y_2 = 3.96 - 0.91X_1 + 0.66X_2 - 0.01X_3 + 0.86X_1^2 + 1.01X_2^2 + 0.72X_3^2 \tag{17}$$

$$Y_3 = 4.26 + 2.71X_1 - 0.19X_2 + 0.45X_3 + 0.22X_1X_3 + 0.67X_1^2 + 0.93X_2^2 + 0.66X_3^2 \tag{18}$$

After simplification, the goodness of fit R^2 for the regression models of the qualified index, re-sowing index, and skip-sowing index are 0.9603, 0.9960, and 0.9166, respectively. This indicates that the predicted values of the regression model equations have a good fit with the actual values. Thus, the regression models for the seed selection qualified index, re-broadcast index, and missed broadcast index have high reliability.

To obtain the optimal parameter combination for the rotation speed of the dibbler, the number of teeth on the gear plate, and the oscillation amplitude of the type-hole wheel, this study takes the maximum value of the qualified index, and the minimum values of the re-sowing index and skip sowing index as the optimization objectives. The optimization objectives and constraints for the rotation speed of the dibbler, the number of teeth on the gear plate, and the oscillation amplitude of the type-hole wheel can be formulated as Equation (19):

$$\begin{cases} \max Y_1(X_1, X_2, X_3) \\ \min[Y_2(X_1, X_2, X_3), Y_3(X_1, X_2, X_3)] \\ 10 \le X_1 \le 30 \\ 4 \le X_2 \le 8 \\ 7 \le X_3 \le 13 \end{cases} \tag{19}$$

The optimization module of Design-Expert 12.0 is used to optimize the constrained objective function, obtaining the best parameter combination can be obtained. At the dibbler rotation speed of 16.34 r/min, the number of teeth on the gear plate is 5.64, the oscillation amplitude of the type-hole wheel is 9.71 mm, and the seeding performance of the seed planter reaches is optimized. At this point, the qualified index is 92.23%, the re-sowing index is 3.63%, and the skip-sowing index is 4.18%.

4.4. Optimization and Validation of Seeder Performance in Bench Tests

The qualified index, re-sowing index, and skip-sowing index were selected as the evaluation criteria for seeding performance. Table 7 presents the bench test results.

Table 7. The bench test results.

Rotation Speed of the Dibbler (r/min)	Qualified Index (%)	Re-Sowing Index (%)	Skip Sowing Index (%)
12	91.78	6.64	1.58
16	93.28	4.35	2.37
20	92.95	3.98	3.07
24	92.17	3.04	4.79
28	90.71	2.82	6.47

The experimental results presented in Table 7 show that as the dibbler rotation speed increases, the qualified index initially increases and then decreases, while the re-sowing index exhibits a decreasing trend and the skip-sowing index exhibits an increasing trend. As the rotation speed increases, the movement of seeds inside the seeder accelerates, improving filling efficiency and increasing the qualified index. However, when the speed increases further, the effect of centrifugal force becomes more pronounced, causing some seeds to fail to enter the seeding holes properly, which leads to a decrease in filling efficiency and a subsequent decline in the qualified index. When the rotation speed of the dibbler reaches 16 r/min, the qualified index reaches its maximum value of 93.28%, with the skip-sowing index at 2.37% and the re-sowing index at 4.35%. The qualified index from the bench test is slightly higher than that from the simulation test. This discrepancy may be attributed to the vibrations caused by the rotation of the motor and the chain gear transmission in the bench test, which intensifies the seed movement within the seeder and facilitates seed filling in the seed extraction wheel. The relative error between the bench test and simulation test results is not significant, indicating that the simulation test results are relatively accurate.

5. Conclusions

A simulation model of a type-hole wheel precision cotton dibbler was established based on the DEM-MBD-coupled algorithm to analyze the impact of the type-hole wheel structure and the motion parameters of the dibbler on its seed extraction and seeding performance. The main conclusions are as follows:

(1) Three different structures of the type-hole wheel were designed: circular; convex; and corrugated. The effects of the type-hole wheel structural designs and operating speed on the dibbler seeding performance were analyzed. The results showed that the average movement speed of the cotton seed particles in the seed chamber increased with the dibbler rotation speed. Among the three structures, the corrugated-type-hole wheel caused the greatest disturbance to the cotton seed population within the dibbler. In particular, the corrugated-type-hole wheel type increased the relative speed of the cotton seed particles and the seed population speed fluctuated less compared to the other type-hole wheel types, indicating it to be more conducive to filling the holes with the seeds.

(2) A combination design experiment was conducted to study the optimal motion parameter combination for the type-hole wheel and establish a mathematical model relating the seeding performance indicators to the experimental parameters. The rotation speed of the dibbler, the number of teeth on the gear plate, and the oscillation amplitude of the type-hole wheel were selected as experimental factors, and the qualified index, re-sowing index, and skip-sowing index were used as evaluation criteria. The regression mathematical model was optimized, yielding the following optimal parameter combination: dibbler rotation speed of 16.34 r/min; the number of gear plate teeth of 5.64; and type-hole wheel oscillation amplitude of 9.71 mm.

(3) A bench test of the seeder's seeding performance was conducted. The test results indicated that when the rotation speed of the dibbler was 16 r/min, the qualified index reached a maximum value of 93.28%, with a re-sowing index of 4.35% and a skip-sowing index of 2.37%. The results from the bench test were consistent with those from the simulation test, showing that the re-sowing index decreased with the increase in rotation speed, while the skip-sowing index increased with the dibbler rotation speed.

This study presents significant advancements in the seeding performance of the dibbler, achieved by optimizing both the structure of the type-hole wheel and the motion parameters of the device. The findings demonstrate that variations in type-hole wheel design considerably influence seed movement and speed fluctuations. Although these parameters exhibited strong performance under controlled experimental conditions, they may be influenced by real-world factors, including terrain variations, differences in soil conditions, and the maintenance of equipment during operational use. Therefore, to ensure sustained optimal performance across diverse operating environments, regular maintenance of the dibbler is recommended, along with the adjustment of parameters tailored to specific conditions. Future research should consider additional variables to further refine and optimize the dibbler's design, including the impact of seed type and shape, soil conditions, and fluctuations in the operational environment, thereby ensuring robust performance across a range of field conditions.

Author Contributions: Conceptualization, L.W. and H.L.; methodology, L.W. and X.R.; software, L.W. and X.R.; validation, L.W., X.W. and J.X.; formal analysis, L.S.; investigation, L.S. and X.R.; data curation, S.H.; writing—original draft preparation, L.W.; writing—review and editing, L.W. and H.L.; project administration, L.W. and H.L.; funding acquisition, L.W. All authors have read and agreed to the published version of the manuscript.

Funding: This research was supported by the Bintuan Science and Technology Program (2022CB001-06, 2023AB005-01) and the President Fund from Tarim University (TDZKYS202302).

Institutional Review Board Statement: Not applicable.

Data Availability Statement: The data presented in this study are available upon request from the authors.

Acknowledgments: The authors would like to thank their schools and colleges, as well as the funding providers of the project. All support and assistance are sincerely appreciated.

Conflicts of Interest: The authors declare no conflicts of interest.

References

1. Zhang, X.; Wu, B.; Niu, L.K.; Xiong, X.Y.; Dong, Z.X. Dynamic characteristics of two-way coupling between flip-flow screen and particles based on DEM. *Chin. Coal Soc.* **2019**, *44*, 1930–1940.
2. Gan, J.Q.; Zhou, Z.Y.; Yu, A.B.; Ellis, D.; Attwood, R.; Chen, W. Co-simulation of multibody dynamics and discrete element method for hydraulic excavators. *Powder Technol.* **2023**, *414*, 118001. [CrossRef]
3. Fang, J.; Zhao, C.F.; Lu, X.Y.; Xiong, W.H.; Shi, C. Dynamic behavior of railway Vehicle-Ballasted track system with unsupported sleepers based on the hybrid DEM-MBD method. *Constr. Build. Mater.* **2023**, *394*, 132091. [CrossRef]
4. Coetzee, C.J.; Els, D.N.J.; Dymond, G.F. Discrete element parameter calibration and the modelling of dragline bucket filling. *J. Terramech.* **2010**, *47*, 33–44. [CrossRef]
5. Lommen, S.; Lodewijks, G.; Schott, D.L. Co-simulation framework of discrete element method and multibody dynamics models. *Eng. Comput.* **2018**, *35*, 1481–1499. [CrossRef]
6. Lu, Z.; Lu, X.L.; Lu, W.S.; Masri, S.F. Studies of the performance of particle dampers under dynamic loads. *J. Sound Vib.* **2010**, *329*, 5415–5433. [CrossRef]
7. Ahmad, N.; Ranganath, R.; Ghosal, A. Modeling and experimental study of a honeycomb beam filled with damping particles. *J. Sound Vib.* **2017**, *391*, 20–34. [CrossRef]
8. Barrios, G.K.P.; Tavares, L.M. A preliminary model of high pressure roll grinding using the discrete element method and multi-body dynamics coupling. *Int. J. Miner. Process.* **2016**, *156*, 32–42. [CrossRef]
9. Ji, S.Y.; Liang, S.M. DEM-FEM-MBD coupling analysis of landing process of lunar lander considering landing mode and buffering mechanism. *Adv. Space Res.* **2021**, *68*, 1627–1643. [CrossRef]
10. Mohajeri, M.J.; de Kluijver, W.; Helmons, R.L.J.; van Rhee, C.; Schott, D.L. A validated co-simulation of grab and moist iron ore cargo: Replicating the cohesive and stress behaviour of bulk solids. *Adv. Powder Technol.* **2021**, *32*, 1157–1169. [CrossRef]
11. Shi, S.W.; Gao, L.; Xiao, H.; Xu, Y.; Yin, H. Research on ballast breakage under tamping operation based on DEM-MBD coupling approach. *Constr. Build. Mater.* **2021**, *272*, 1810–1822. [CrossRef]
12. Shi, S.W.; Gao, L.; Cai, X.P.; Yin, H.; Wang, X.L. Effect of tamping operation on mechanical qualities of ballast bed based on DEM-MBD coupling method. *Comput. Geotech.* **2020**, *124*, 103574. [CrossRef]
13. Xiao, W.Q.; Huang, Y.X.; Jiang, H.; Lin, H.; Li, J.L. Energy dissipation mechanism and experiment of particle dampers for gear transmission under centrifugal loads. *Particuology* **2016**, *27*, 40–50. [CrossRef]
14. Xiao, W.Q.; Li, J.N.; Pan, T.L.; Zhang, X.; Huang, Y.X. Investigation into the influence of particles' friction coefficient on vibration suppression in gear transmission. *Mech. Mach. Theory* **2017**, *108*, 217–230. [CrossRef]
15. Chung, Y.C.; Wu, Y.R. Dynamic modeling of a gear transmission system containing damping particles using coupled multi-body dynamics and discrete element method. *Nonlinear Dyn.* **2019**, *98*, 129–149. [CrossRef]
16. Wu, Y.R.; Chung, Y.C.; Wang, I.C. Two-way coupled MBD-DEM modeling and experimental validation for the dynamic response of mechanisms containing damping particles. *Mech. Mach. Theory* **2021**, *159*, 104257. [CrossRef]
17. Curry, D.R.; Deng, Y. Optimizing Heavy Equipment for Handling Bulk Materials with Adams-EDEM Co-simulation. In Proceedings of the 7th International Conference on Discrete Element Methods (DEM), Dalian, China, 15 December 2017.
18. Hu, J.P.; Pan, J.; Chen, F.; Yue, R.C.; Yao, M.J.; Li, J. Simulation Optimization and Experiment of Finger-clamping Seedling Picking Claw Based on EDEM RecurDyn. *Chin. Soc. Agric. Mach.* **2022**, *53*, 75–85+301.
19. Xu, T.Y.; Zhang, R.X.; Wang, Y.; Jiang, X.M.; Feng, W.Z.; Wang, J.L. Simulation and Analysis of the Working Process of Soil Covering and Compacting of Precision Seeding Units Based on the Coupling Model of DEM with MBD. *Processes* **2022**, *10*, 1103. [CrossRef]
20. Yan, D.X.; Xu, T.Y.; Yu, J.Q.; Wang, Y.; Guan, W.; Tian, Y.; Zhang, N. Test and Simulation Analysis of the Working Process of Soybean Seeding Monomer. *Agriculture* **2022**, *12*, 1464. [CrossRef]
21. Liu, Y.; Liu, Y.P.; Zhang, T. Load Analysis of Rotary Cutter Shaft for Power Tiller Based on DEM and MBD Theory. *J. Agric. Sci. Technol.* **2020**, *22*, 79–86.
22. Lai, Q.H.; Jia, G.X.; Su, W.; Zhao, L.J.; Qiu, X.B.; Lu, Q. Design and Test of Chain Spoom Type Precision Seed Metering Device for Ginseng Based onDEM-MBD Coupling. *Chin. Soc. Agric. Mach.* **2022**, *53*, 91–104.
23. Kim, Y.S.; Lee, S.D.; Baek, S.M.; Baek, S.Y.; Jeon, H.H.; Lee, J.H.; Siddique, M.A.; Kim, Y.J.; Kim, W.S.; Sim, T.; et al. Development of DEM-MBD coupling model for draft force prediction of agricultural tractor with plowing depth. *Comput. Electron. Agric.* **2022**, *202*, 107405. [CrossRef]

24. Dong, X.Q.; Su, C.; Zheng, H.N.; Han, R.Q.; Li, Y.L.; Wan, L.P.C.; Song, J.N.; Wang, J.C. Analysis of soil disturbance process by vibrating subsoiling based on DEM-MBD coupling algorithm. *Transact. Chin Soc. Agric. Eng.* **2022**, *38*, 34–43.
25. Yu, Q.X.; Liu, Y.; Chen, X.B.; Sun, K.; Lai, Q.H. Calibration and Experiment of Simulation Parameters for Panax notoginseng Seeds Based on DEM. *Chin. Soc. Agric. Mach.* **2020**, *51*, 123–132.
26. Abbaspour-Fard, M.H. Theoretical validation of a multi-sphere discrete element model suitable for biomaterials handling simulation. *Biosyst. Eng.* **2004**, *88*, 153–161. [CrossRef]
27. Wang, L.; He, X.W.; Hu, C.; Guo, W.S.; Wang, X.F.; Xing, J.F. Measurement of physical parameters of coated cotton seed and parameter calibration of discrete element. *Chin. Agric. Univ.* **2022**, *27*, 71–82.
28. Wang, L.; Hu, C.; He, X.W.; Guo, W.S.; Hou, S.L. A general modelling approach for coated cotton-seeds based on the discrete element method. *Inmateh-Agric. Eng.* **2021**, *63*, 219–228.

agriculture

MDPI

Article

Strip Tillage Improves Productivity of Direct-Seeded Oilseed Rape (*Brassica napus*) in Rice–Oilseed Rape Rotation Systems

Chaosu Li [1,2], Ming Li [2], Tao Xiong [2], Hongkun Yang [1], Xiaoqin Peng [3], Yong Wang [3], Haiyan Qin [4], Haojie Li [2], Yonglu Tang [2] and Gaoqiong Fan [1,*]

1 Crop Ecophysiology and Cultivation Key Laboratory of Sichuan Province, Sichuan Agricultural University, Chengdu 611130, China; 2020101005@stu.sicau.edu.cn (C.L.); 14442@sicau.edu.cn (H.Y.)
2 Crop Research Institute of Sichuan Academy of Agricultural Sciences, Environment-Friendly Crop Germplasm Innovation and Genetic Improvement Key Laboratory of Sichuan Province, Chengdu 610066, China; limimg1005@gmail.com (M.L.); xiongtao27@163.com (T.X.); lhjie@163.com (H.L.); ttyycc88@163.com (Y.T.)
3 Sichuan Academy of Agricultural Machinery Sciences, Chengdu 610066, China; scsnjypxq@163.com (X.P.); luojun0803@126.com (Y.W.)
4 Sichuan Agricultural Technology Extension Station, Chengdu 610041, China; scnj@vip.163.com
* Correspondence: fangaoqiong@sicau.edu.cn; Tel.: +86-28-86290870

Abstract: Oilseed rape (*Brassica napus*) is a crucial global oil crop. It is generally cultivated in rotation with rice in southern China's Yangtze River Basin, where the wet soil and residue retention after rice harvest significantly hinder its seedling establishment. Hence, this study developed a strip-tillage seeder for oilseed rape seeding following rice harvest. Additionally, seedling establishment, soil infiltration and evaporation post-seeding, soil moisture change, oilseed yield, and weed occurrence under strip tillage (ST) were compared with conventional shallow rotary-tillage (SR) and deep rotary-tillage (DR) seeding practices. Compared to SR and DR, the results demonstrated that ST had a higher seeding efficiency and 53.8% and 80.2% lower energy consumption, respectively. ST also enhanced seedling growth and oilseed yield formation more effectively than the competitor tillage treatments, with an oilseed yield increase exceeding 6%. Additionally, ST improved water infiltration and reduced soil water evaporation, resulting in higher topsoil (0–20 cm) moisture during the critical growth stages. Furthermore, ST reduced soil disturbance, significantly decreasing the density of the dominant weed, *Polypogon fugax*. Overall, ST seeding technology has the potential to improve the productivity of oilseed rape in rice–oilseed rape rotation systems, and its yield superiority is mainly due to seedling establishment improvement and soil moisture adjustment.

Keywords: strip tillage; oilseed rape; seedling establishment; yield; soil moisture; weed density

Citation: Li, C.; Li, M.; Xiong, T.; Yang, H.; Peng, X.; Wang, Y.; Qin, H.; Li, H.; Tang, Y.; Fan, G. Strip Tillage Improves Productivity of Direct-Seeded Oilseed Rape (*Brassica napus*) in Rice–Oilseed Rape Rotation Systems. *Agriculture* **2024**, *14*, 1356. https://doi.org/10.3390/agriculture14081356

Academic Editors: Tao Cui, Vito Armando Laudicina, Xiaojun Gao and Qinghui Lai

Received: 20 June 2024
Revised: 31 July 2024
Accepted: 8 August 2024
Published: 14 August 2024

1. Introduction

Oilseed rape (*Brassica napus*) is a vital global oil crop and the largest in China, cultivated on 7.5 million hectares, representing nearly one-fifth of global cultivation and production [1,2]. Despite this, China's significant consumption creates a supply–demand imbalance [1,3]. To address this, the Chinese government has implemented policies to boost domestic production. Nevertheless, mechanization, particularly in sowing and harvesting, remains low, discouraging farmers from planting oilseed rape [4]. Currently, in the Yangtze River Basin, the main cultivation area of oilseed rape in southern China, primary production relies on labor-intensive and inefficient artificial seedling transplanting [2]. Although direct seeding for oilseed rape, compared to traditional manual transplanting, saves labor and cost, the high soil moisture after rice harvest, continuous autumn rainfall, and significant residue retention often result in poor establishment of direct-seeded oilseed rape in this region [5].

Several studies have aimed to improve the establishment of mechanically direct-seeded oilseed rape in high-soil-moisture conditions [6–8]. The main procedure involves soil disturbance and straw mixing, followed by mechanical seeding and fertilization. These steps can be performed separately or simultaneously using a combine seeder. Large clods may be created if the topsoil is too wet when tilled, resulting in high soil roughness affecting subsequent mechanical seeding operations [9]. High moisture levels or excessive straw return can also block mechanical seeding structures, adversely impacting seeding practice and seedling establishment [6,8]. Additionally, in wet clay soils, severe soil disturbance can exacerbate waterlogging for subsequent dryland crops in rice-based systems [5,10].

When exploring alternatives, strip tillage, where rotary tillage occurs only in a narrow strip to facilitate the seeding of the next crop, reduces soil disturbance and straw blockage and adapts well to fields with high soil moisture and residue mulching, particularly for wheat seeding [11]. The tilled soil in the strips contributes to water infiltration and crop root development [12,13]. Removing the residues from tilled strips has a positive effect on mitigating soil temperature changes [14,15]. Moreover, retaining crop residues between tilled strips reduces soil evaporation, allowing increasing moisture storage in the soil profile used by crop roots [14]. In most cases, strip tillage minimizes soil compaction and optimizes the seedbed environments for seed germination and crop seedling growth [16,17]. However, strip tillage adoption is regionally specific, and its positive effect on crop yield depends on multiple factors, such as tillage strip width, soil properties, and climatic conditions [13]. Nevertheless, there is evidence that strip tillage may benefit multiple-cropping production with *graminaceous* crops [13]. Most of the existing strip-tillage practices for oilseed rape production have been conducted in dryland systems, and the yield response varies according to different experimental conditions [18–20]. In contrast, strip tillage under complex conditions with high soil moisture and full residue retention has rarely been reported. Moreover, plowing or rotary tillage has been used as an effective way to control weeds, and strip tillage may increase weed occurrence and thus affect crop yields [21,22]. Therefore, this paper developed a strip-tillage seeder for oilseed rape seeding and conducted a field comparison with conventional shallow and deep rotary-tillage practices. This study aimed to (1) evaluate the seedling establishment of oilseed rape with a strip-tillage seeder; (2) determine the impact of strip tillage on oilseed rape growth and yield; and (3) estimate the effects of strip tillage on soil moisture change and weed occurrence.

2. Materials and Methods

2.1. The Machine Structure and Working Principle of the Strip-Tillage Oilseed Rape Seeder

A design diagram of the innovative strip-tillage oilseed rape seeder is shown in Figure 1. It comprises the following key components: a frame, strip rotary blades, a seed and fertilizer box, a seeding regulation system, a fertilizer distribution system, and a ground wheel. The seeder accommodates 6 or 8 seeding rows, corresponding to 6 or 8 blade groups on the rotary axis. Each group contains 4 blades for preparing the seedbed.

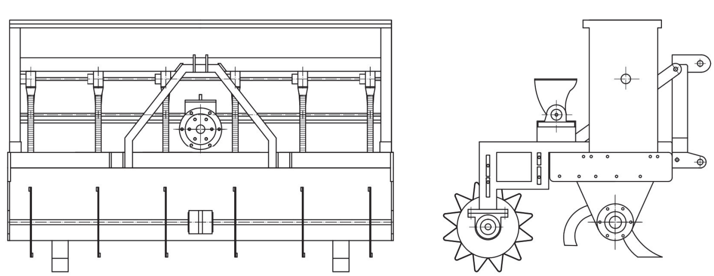

Figure 1. Main view (**left**) and side view (**right**) of the strip-tillage oilseed rape seeder.

The seeder uses a three-wire suspension system connected to the tractor, with the sowing and fertilizer devices driven by the ground wheel behind the seeder. The tractor's movement drives the rotation of the ground wheels, which in turn drive the seeding and fertilizing shafts via a chain. As the blades rotate, the fertilizer dropped in front of them is mixed effectively with soil and straw. Since the seeding tube's pipe mouth is directly opposite the corresponding blade group, the rape seeds fall onto the rotary-tillage belt after the strip rotary-tillage operation. No-tillage soil is maintained between seeding rows to minimize straw blockage. When the tractor stops or the seeder is raised to turn, the ground wheels cease operation, halting seeding and fertilizing automatically. To reduce mud and straw adhesion, the ground wheels behind the seeder are not traditional rollers but two narrow, serrated wheels. This design prevents slippage and minimizes mud accumulation. A picture of the field operation is shown in Figure 2.

Figure 2. Field operation of the strip-tillage oilseed rape seeder.

2.2. Comparison of Different Oilseed Rape Seeding Regimes

2.2.1. Field Trial Design

After developing the above machine, a comparative experiment was conducted under field conditions using conventional rotary-tillage seeding techniques. The experiment took place in Guanghan City, Sichuan Province, located in southwest China during the 2021/2022 and 2022/2023 growing seasons. In 2021/2022, the topsoil (0–20 cm) was sandy loam, while in 2022/2023 it was closer to silty loam. The topsoil moisture before tillage was 52.5% and 45.5% in 2021 and 2022, respectively. The previous crop, rice, was harvested in late September. In 2021, a semi-feed combine harvester was used, leaving straw chopped and dispersed on the soil surface. In 2022, a full-feed combine harvester was employed, and the straw was additionally crushed by a straw crusher before land preparation. The current local rice yield is approximately 10,000 kg ha^{-1} (14% grain moisture content), and the residue amount returned to the field is close to 9000 kg ha^{-1} each year. The seeding dates were 9 October 2021 and 7 October 2022, respectively. In the 2021/2022 season, the experiment included two seeding methods: the innovative seeding practice with the above strip-tillage seeder (ST) and conventional shallow rotary tillage (SR). Each treatment had three replications and was randomly arranged. In the 2022/2023 season, a deep rotary-tillage (DR) seeding practice was added, and three seeding practices were implemented. Each plot covered an area of 120 m^2.

For the ST seeding practice, an 8-row seeder was used in 2021 and a lighter 6-row seeder was used in 2022 under no-tillage and residue-retention conditions. For the SR seeding treatment, an integrated seeding machine performed rotary tillage for land preparation, sowing, and fertilization in one pass under no-tillage conditions, with a till depth of 7–8 cm. The DR seeding practice employed a traditional deep rotary tiller for tillage at a depth of 18–20 cm before seeding, and seeds were sown using the same seeder as in the SR seeding practice.

In the 2021/2022 season, the variety Chuanyou 81 was sown at a rate of 2.9 kg ha^{-1}. In the 2022/2023 season, the variety Chuanyou 83 was used, with seeding rates of 2.6, 2.7, and 2.7 kg ha^{-1} for the ST, SR, and DR treatments, respectively. Throughout the growth period, each treatment received 150 kg nitrogen (N) ha^{-1}, with 60% applied as compound fertilizer

(N-P-K, 15-15-15) during sowing and the remainder as urea at bolting. No irrigation was applied, and diseases and pests were well controlled according to technical requirements. During the 2021/2022 season, given the requirement to investigate the occurrence of weeds, chemical weeding was not conducted during the entire growth stage, while in the 2022/2023 season, chemical weeding was performed. Table 1 reports the temperature and rainfall during the period in which the experiment was conducted.

Table 1. Temperature and rainfall during the experiment.

Year	Factor	October	November	December	January	February	March	April
2021/2022	Mean temperature (°C)	17.3	11.3	8.3	7.7	7.4	17.0	18.3
	Rainfall (mm)	114.8	3.2	1.7	3.1	24.2	18.2	70.7
2022/2023	Mean temperature (°C)	18.3	15.2	7.2	6.6	10.0	14.0	18.9
	Rainfall (mm)	27.6	1.8	0.5	0.1	6.3	21.4	32.3

2.2.2. Sowing Efficiency and Energy Consumption

In the 2022/2023 growing season, the time and fuel consumption for each operation during land preparation and seeding were recorded, including tillage, seeding, fertilization, etc.

2.2.3. Topsoil Disturbance

After seeding in 2022/2023, two representative quadrats were selected in each plot. Each quadrat covered one row and was 35 cm in length. The soil clods in the quadrats were categorized into four groups based on diameter (>20 cm, 10–20 cm, 2–10 cm, and <2 cm). The number of clods and the averaged maximum diameters of the first three groups were measured.

2.2.4. Soil Infiltration and Topsoil Evaporation after Seeding

In 2022/2023, the double-ring method was used to measure soil infiltration after seeding [23]. The rings had a height of 25 cm and diameters of 50 cm (outer) and 25 cm (inner). For the ST treatment, the center of the inner and outer rings was on the midline of the rotary-tilled strip, and for the SR and DR treatments, the topsoil was fully tilled, and the center of the rings was close to the location of the seeds. They were inserted 20 cm into the soil and filled with water using two Mariotte bottles. The water level dropped rapidly in the first 30 min, then the rate slowed down, and data were recorded every 30 min after the slowdown. The water level was consistently maintained at 3 cm in both rings throughout the experiment. A consistent infiltration rate was assumed after three successive measurements showed identical values. The cutting-ring method was used to measure soil evaporation [24]. After seeding, topsoil was excavated using a cutting ring, with a height of 5 cm and a volume of 100 m^2. The ring was sealed with plastic film, and the total weight (soil and cutting ring) was recorded and returned to the sampling position. The cutting rings were removed and weighed after three days to calculate soil evaporation per unit area.

2.2.5. Seedling Emergence

Following seedling emergence, the number of emerged seedlings was assessed. In 2021/2022, six sample sites per plot were randomly investigated. Each site included two rows 2 m in length. In 2022/2023, three quadrats containing three rows 3 m in length were randomly selected to investigate the number of emerged seedlings. The coefficient of variation for the number of seedlings for each plot was also calculated.

2.2.6. Agronomic Characters Measurement at Seedling Stage

At 30 days post-seeding, fifteen representative seedlings were selected from each plot to measure the stem base diameter and the number of green leaves per plant. Then, all seedlings sampled in each plot were mixed and oven-dried at 105 °C for 20 min and then at 75 °C to a constant weight to determine the aboveground dry mass per seedling and the dry mass per m^2. Dry mass per m^2 was the product of dry mass per seedling and the number of seedlings per m^2.

2.2.7. Yield and Yield Components Investigation

Before harvesting at maturity, five and nine representative plants were taken from each plot in the 2021/2022 and 2022/2023 seasons, respectively, and these plants were used to investigate the number of siliques per plant, the number of seeds per silique, and 1000-seed dry weights [25]. At maturity, surviving plants in the center of the plot, undamaged by sampling, were harvested to evaluate the yield. In 2021/2022, the harvested area was 8 m^2 per plot. In 2022/2023, the harvested area encompassed three locations, each with two rows measuring 3 m in length. The number of surviving plants in each quadrat was investigated before harvest. After sun-drying and manual threshing, the seeds were weighed and moisture contents were measured. Seed yield was calculated based on 8% seed moisture.

2.2.8. Weed Occurrence Survey

Weed occurrence was assessed at 90 days post-seeding in the 2021/2022 season. Two quadrats, each 1 m^2, were examined in each plot. The species and stem numbers of weeds in each quadrat were recorded, and weed density per m^2 was calculated.

2.2.9. Soil Moisture Change

In the 2022/2023 season, every 30 days after seeding, soil from the 0–40 cm depth was sampled at three plot locations and divided into layers of 0–10, 10–20, 20–30, and 30–40 cm. The soil from each layer was mixed evenly, and its moisture content was determined by the oven-drying method, where samples were dried at 105 °C to a constant weight.

2.3. Data Analysis

Data were processed using Microsoft Excel 2013. Analysis was conducted using IBM SPSS 22.0 software, and the data were presented as averages. The significant differences among treatments were analyzed using ANOVA, the independent two-sample *t*-test was used to determine the difference between the two treatments in the 2021/2022 season, and Duncan's multiple range test was used to identify the differences among the three treatments in the 2022/2023 season.

3. Results

3.1. Variance Analysis of Seed Yield and Yield Components

The variance analysis revealed that oilseed yield was mainly affected by the seeding practice rather than the year (Table 2). The difference in emerged seedlings per m^2 between the years was noticeable, affecting surviving plant number per m^2. Moreover, the seeding practice mainly affected the number of siliques per plant, while the number of seeds per silique and 1000-grain weights were significantly affected by the year.

Table 2. Variance analysis of oilseed yield, yield components, and benefits under the two experimental years and the different seeding practices.

Factor	Oilseed Yield	Seedling Number per m^2	Surviving Plants per m^2	Number of Siliques per Plant	Number of Seeds per Silique	1000-Seed Dry Weight
Year (Y)	3.1	191.4 **	90.4 **	0.3	42.6 **	10.0 *
Seeding practice (S)	14.9 **	5.5 *	18.0 **	9.7 **	2.0	0.4
Y × S	4.3	7.4 *	26.8 **	0.2	0.002	2.1

The data presented in the table are *F* values. "*" means significantly different ($p < 0.05$); "**" means extremely significantly different ($p < 0.01$).

3.2. Yield and Yield Components

Consistent trends in oilseed yield among seeding treatments were observed across both years, with the ST practice consistently outperforming the other practices (Table 3). In 2021/2022, the ST treatment yielded 6.9% more than SR, though the difference was not significant. In 2022/2023, ST yielded 48.9% and 107.2% more than SR and DR, respectively, and a significant difference was observed among the treatments. The seed yield increase of ST was mainly due to the substantial increase in the number of siliques per plant.

Table 3. Effect of different oilseed rape seeding practices on oilseed yield and yield components.

Year	Seeding Practice	Oilseed Yield (kg ha^{-1})	Surviving Plants per m^2	Number of Siliques per Plant	Number of Seeds per Silique	1000-Seed Dry Weight (g)
2021/2022	ST	2838 ± 168 a	28.9 ± 1.1 b	284.5 ± 27.7 a	13.6 ± 1.6 a	4.22 ± 0.10 a
	SR	2655 ± 496 a	41.1 ± 3.6 a	196.9 ± 69.1 a	12.3 ± 1.0 a	4.13 ± 0.07 a
2022/2023	ST	2899 ± 385 a	24.0 ± 1.1 b	286.6 ± 8.9 a	17.8 ± 0.8 a	3.82 ± 0.09 a
	SR	1947 ± 218 b	24.5 ± 1.0 b	225.0 ± 36.2 ab	16.5 ± 1.1 a	3.99 ± 0.27 a
	DR	1399 ± 211 b	27.2 ± 1.5 a	138.0 ± 67.1 b	17.3 ± 0.7 a	3.84 ± 0.12 a

ST, strip-tillage seeding; SR, shallow rotary-tillage seeding; DR, deep rotary-tillage seeding. Data are presented as means with standard deviations (means ± SDs), and data in the same column from the same year followed by different lowercase letters are significantly different ($p < 0.05$).

3.3. Seeding Efficiency, Energy Consumption, and Soil Disturbance

The efficiency and energy consumption of different seeding methods varied due to differing pre-seeding operations and soil disturbance intensity (Table 4). ST increased seeding efficiency by 28.6% and 62.5% and reduced energy consumption by 53.8% and 80.2% compared to the SR and DR treatments, respectively. Different tillage practices created varied soil clod distributions (Table 4). Clods with extra-large (>20 cm) and large (10–20 cm) diameters dominated in the DR and SR treatments, while the ST treatment mainly produced clods with medium diameters.

Table 4. Effects of different oilseed rape seeding practices on seeding efficiency, energy consumption, and soil clod distributions during the 2022/2023 season.

Seeding Practice	Seeding Efficiency (h ha^{-1})	Fuel Consumption (L ha^{-1})	NCED	ACDED (cm)	NCLD	ACDLD (cm)	NCMD	ACDMD (cm)
ST	3.0	18.7	0 b	-	0 c	-	71.5 ± 8.9 a	5.6 ± 0.5 b
SR	4.2	40.5	1.9 ± 3.3 b	26.2 ± 0.5 a	22.9 ± 5.7 a	15.1 ± 1.8 a	19.0 ± 8.7 b	5.5 ± 1.1 b
DR	8.0	94.5	9.5 ± 3.3 a	27.1 ± 4.5 a	15.2 ± 3.3 b	16.2 ± 2.0 a	3.8 ± 6.6 b	7.5 ± 0.7 a

ST, strip-tillage seeding; SR, shallow rotary-tillage seeding; DR, deep rotary-tillage seeding; NCED, number of clods with extra-large diameters (>20 cm) per m^2; ACDED, average clod diameter for extra-large diameters; NCLD, number of clods with large diameters (10–20 cm) per m^2; ACDLD, average clod diameter for large diameters; NCMD, number of clods with medium diameters (2–10 cm) per m^2; ACDMDA, average clod diameter for medium diameters. Data for soil clods are presented as means with standard deviations (means ± SDs), and data in the same column followed by different lowercase letters are significantly different ($p < 0.05$).

3.4. Seedling Establishments

With nearly the same seeding rates, the difference in seedling number emerged per m^2 between treatments did not reach a significant level in the two experimental years (Table 5). However, the ST treatment exhibited better field distribution uniformity in the 2021/2022 growing season.

Table 5. Effect of different oilseed rape seeding practices on seedling establishments.

Year	Seeding Practice	Seedling Number per m^2	CVSD (%)
2021/2022	ST	47.0 ± 3.0 a	11.1 ± 1.7 b
	SR	56.6 ± 4.0 a	27.0 ± 8.3 a
2022/2023	ST	27.0 ± 2.8 a	11.0 ± 2.0 a
	SR	26.8 ± 2.8 a	11.5 ± 5.8 a
	DR	31.5 ± 2.7 a	10.2 ± 4.9 a

ST, strip-tillage seeding; SR, shallow rotary-tillage seeding; DR, deep rotary-tillage seeding; CVSD, coefficient of variation of seedling distribution. Data are presented as means with standard deviations (means ± SDs), and data in the same column in the same year followed by different lowercase letters are significantly different ($p < 0.05$).

3.5. Agronomic Characters at Seedling Stage

Most agronomic character values for oilseed rape seedlings decreased with the increase in tillage intensity at 30 days post-seeding (Table 6). In 2021/2022, significant differences existed in the main individual parameters between the two seeding practices, while dry mass per m^2 values remained similar. However, in 2022/2023, all tested agronomic parameters were significantly higher under ST compared to SR and DR, and dry mass per m^2 increased by 65.3% and 95.1%, respectively.

Table 6. Effects of different oilseed rape seeding practices on agronomic characters at seedling stage (30 days post-seeding).

Year	Seeding Practice	Diameter of Stem Base (cm)	Number of Green Leaves per Plant	Dry Mass per Plant (g)	Dry Mass per m^2 (g)
2021/2022	ST	4.55 ± 0.12 a	5.93 ± 0.29 a	1.27 ± 0.19 a	60.3 ± 13.1 a
	SR	3.73 ± 0.26 b	5.36 ± 0.23 b	0.88 ± 0.10 b	50.4 ± 8.4 a
2022/2023	ST	4.75 ± 0.36 a	4.92 ± 0.20 a	1.50 ± 0.22 a	40.2 ± 2.4 a
	SR	3.63 ± 0.27 b	4.19 ± 0.20 b	0.92 ± 0.16 b	24.3 ± 3.2 b
	DR	3.45 ± 0.20 b	4.00 ± 0.02 b	0.65 ± 0.08 b	20.6 ± 3.9 b

ST, strip-tillage seeding; SR, shallow rotary-tillage seeding; DR, deep rotary-tillage seeding. Data are presented as means with standard deviations (means ± SDs), and data in the same column in the same year followed by different lowercase letters are significantly different ($p < 0.05$).

3.6. Weed Occurrence

Seeding methods significantly influenced weed occurrence in the field (Table 7). In this study, the dominant weed was *Polypogon fugax.* At 90 days post-seeding with ST, the *Polypogon fuga* densities decreased by 85.2% and 83.7% compared to the SR and DR treatments, respectively.

Table 7. Effects of different oilseed rape seeding practices on field weed density at 90 days post-seeding in the 2021/2022 season.

Seeding Practice	Total Weed Density (Seedlings m^{-2})	*Polypogon Fugax* Density (Seedlings m^{-2})
ST	529 ± 18 b	525 ± 18 b
SR	3560 ± 966 a	3553 ± 967 a
DR	3235 ± 1342 a	3224 ± 1334 a

ST, strip-tillage seeding; SR, shallow rotary-tillage seeding; DR, deep rotary-tillage seeding. Data are presented as means with standard deviations (means ± SDs), and data in the same column followed by different lowercase letters are significantly different ($p < 0.05$).

3.7. Soil Infiltration and Evaporation Post-Seeding

Soil infiltration and evaporation measurements post-seeding showed that the stable infiltration rate in the ST treatment was significantly higher than in the other two treatments, while evaporation was lower (Figure 3). Over three days post-seeding, topsoil evaporation in the ST treatment decreased by 35.1% and 32.7% compared to the SR and DR treatments, respectively.

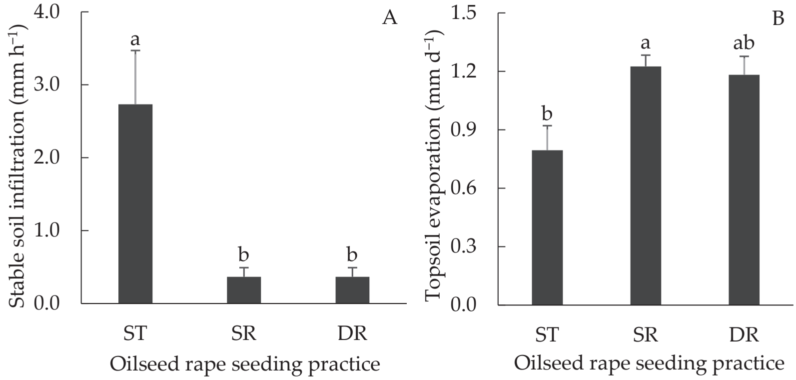

Figure 3. Effects of different oilseed rape seeding practices on stable soil infiltration (**A**) and topsoil evaporation (**B**) post-seeding in the 2022/2023 season. ST, strip-tillage seeding; SR, shallow rotary-tillage seeding; DR, deep rotary-tillage seeding. Bar graphs show the means, and the error bars represent standard deviations. On the bar chart, different lowercase letters indicate significant differences between different oilseed rape seeding practices for each parameter ($p < 0.05$).

3.8. Soil Moisture Change during Oilseed Rape Growth

The ST treatment maintained higher topsoil moisture (0–20 cm) throughout the oilseed rape growth period (Figure 4). The average soil moisture during the whole growth stages at depths of 0–10 cm and 10–20 cm in the ST treatment increased by 11.6% and 24.6% and by 8.0% and 16.6%, respectively, compared to the SR and DR treatments. However, soil moisture differences in deep soil (20–40 cm) between the treatments were reduced.

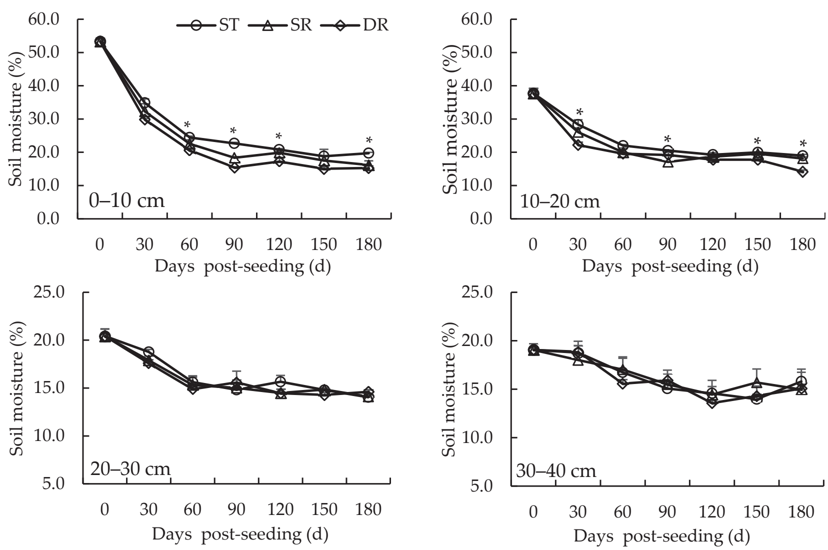

Figure 4. Effects of different oilseed rape seeding practices on soil moisture change during the 2022/2023 season. The moisture data in the figure show the means and the error bars represent standard deviations. ST, strip-tillage seeding; SR, shallow rotary-tillage seeding; DR, deep rotary-tillage seeding. "*" indicates a significant difference in soil moisture among the three treatments at a specific sampling time.

4. Discussion

The low quality of mechanized direct seeding is an important factor limiting oilseed rape yield improvement in rice–oilseed rape rotation systems in southern China [5,6]. This study reveals that, compared with conventional rotary tillage, strip-tillage practices can improve the seedling establishment and yield of oilseed rape. Many studies have confirmed that tillage systems have a pronounced impact on crop yield [26,27]. Strip tillage combines the advantages of no tillage and full tillage and thus positively affects crop yields in most regions, especially increasing dryland system production in cooler temperate areas [13]. This study confirmed that strip tillage positively affects oilseed rape production in subtropical–humid regions.

The positive effects of strip tillage on crop growth and yield are related to improvements in temperature and moisture conditions in seedbeds [12–15]. Some studies have proved that strip tillage in cooler areas can increase seedbed temperature, promoting crop emergence and growth [14,15]. However, the average temperature exceeds 15 °C when oilseed rape is seeded in southern China, and temperature may be not a limiting factor for oilseed rape establishment in this region. In contrast, in this study, the enhancement of seedling establishment and oilseed yield with strip tillage may have been caused by improved seedbed moisture conditions. High soil moisture after rice harvest and continuous rainfall make fields prone to waterlogging [5]. In this study, the soil water infiltration rate with strip tillage was higher than that in the shallow- and deep-tillage systems, which reduced the adverse effects of excessive soil moisture on seed germination and seedling growth. Other studies also supported this result, indicating that reduced tillage preserves soil capillary structure and increases water infiltration [28,29]. In addition, increasing soil surface roughness after intensive tillage leads to rapid topsoil moisture loss, thus affecting water absorption by seeds and seedlings [9]. This study also found that strip tillage with less soil disturbance led to fewer large soil clods and less soil water evaporation, resulting in a relatively ideal soil moisture state in the seedbeds, which positively affected oilseed rape growth. Compared with other conventional tillage practices, the oilseed yield increase with strip tillage in 2021/2022 was lower than that in 2022/2023. The rainfall in the former season was much higher than in the latter, especially in winter and spring, which further confirmed the positive effect of soil moisture retention with strip tillage on oilseed rape yield improvement. Due to the improvement in soil moisture conditions, most agronomic parameters with strip tillage at the oilseed rape seedling stage were superior to those of the competitor tillage regimes, and the number of siliques per plant at maturity was significantly improved. In conclusion, the positive effects of strip tillage on oilseed rape production in southern China are mainly due to soil moisture adjustment, which promotes surface water infiltration to alleviate waterlogging and reduces water evaporation to improve crop drought resistance.

Weeds significantly impact crop growth and yield, yet there is no consensus regarding their occurrence under conservation tillage conditions [30]. This study identified *Polypogon fugax* as the dominant weed species in oilseed rape fields, and its density and total weed density were lower in the strip-tillage treatment than in the other traditional tillage treatments. The occurrence of weeds in the field is influenced by factors including the number and spatial distribution of weed seeds in the soil and the tillage method used for previous crops [31]. In China's Yangtze River Basin, rotary tillage is typically employed before rice transplanting to accommodate transplanting, resulting in most weed seeds being buried deep in the soil. Once the topsoil is disturbed, the weeds rapidly germinate when air and water conditions around the seeds are favorable. In this study, *Polypogon fugax* was primarily found in rotary-tillage belts (Figure 5), contrasting with the relatively uniform distribution of weeds in fully rotary-tilled fields. Therefore, in rice–dryland crop rotation systems, ST seeding practices may potentially reduce weed occurrence during dryland crop growth seasons. In addition, strip tillage reduces fuel consumption in seeding operations by more than 50% (Table 4); thus, coupled with other innovative nutrient managements [32], it will be an option for future oilseed rape sustainable production in rice–oilseed rotation systems.

Figure 5. Weeds mainly occurred in tilled rows under the strip-tillage seeding practice in the oilseed rape fields.

5. Conclusions

Mechanical direct seeding for oilseed rape in rice–oilseed rape rotation systems in southern China faces great challenges due to high soil moisture and residue retention. In this study, the innovative oilseed rape strip-tillage (ST) seeding practice minimized soil disturbance, facilitated efficient seedling establishment, and enhanced seedling growth and seed yield, which was confirmed to benefit oilseed rape production. The seed yield improvement is attributable to the preservation of soil moisture and the suppression of weed germination. ST technology for oilseed rape seeding needs to be evaluated in multiple environments to further improve its adaptability to complex environments following rice harvest.

Author Contributions: Conceptualization, C.L. and G.F.; methodology, C.L., M.L., H.Y., H.Q. and G.F.; investigation, C.L., M.L., T.X. and H.Q.; writing—original draft preparation, C.L.; writing—review and editing, C.L., H.Y., Y.T. and G.F.; visualization, C.L., X.P. and Y.W.; funding acquisition, C.L., Y.T. and H.L. All authors have read and agreed to the published version of the manuscript.

Funding: This research was funded by the Agricultural Technology Collaborative Extension Project of Sichuan Province, China; the Science and Technology Innovation Team of Oilseed Rape of Sichuan Province, China; and the Natural Science Foundation of Sichuan Province (2024NSFSC1223).

Institutional Review Board Statement: Not applicable.

Data Availability Statement: Data are contained within the article.

Acknowledgments: The authors would like to express their gratitude to EditSprings for the expert linguistic services provided.

Conflicts of Interest: The authors declare no conflicts of interest.

References

1. Bonjean, A.P.; Dequidt, C.; Sang, T.; Limagrain, G. Rapeseed in China. *OCL* **2016**, *236*, D605. [CrossRef]
2. Hu, Q.; Hua, W.; Yin, Y.; Zhang, X.; Liu, L.; Shi, J.; Zhao, Y.; Lu, Q.; Chen, C.; Wang, H. Rapeseed research and production in China. *Crop J.* **2017**, *5*, 127–135. [CrossRef]
3. Li, F.; Guo, K.; Liao, X. Risk assessment of china rapeseed supply chain and policy suggestions. *Int. J. Environ. Res. Public Health* **2023**, *20*, 465. [CrossRef] [PubMed]
4. He, A.; Yuan, B.; Jin, Z.; Man, J.; Peng, S.; Zhang, L.; Liu, H.; Nie, L. Comparative study on annual yield, water consumption, irrigation water use efficiency and economic benefits of different rice-oilseed rape rotation systems in Central China. *Agric. Water Manag.* **2021**, *247*, 106741. [CrossRef]
5. Li, L.; Li, J.; Wei, C.; Yang, C.; Zhong, S. Effect of mechanized ridge tillage with rice-rape rotation on paddy soil structure. *Agriculture* **2022**, *12*, 2147. [CrossRef]

6. Liao, Y.; Gao, L.; Liao, Q.; Zhang, Q.; Liu, L.; Fu, Y. Design and test of side deep fertilizing device of combined precision rapeseed seeder. *Trans. Chin. Soc. Agric. Mach.* **2020**, *51*, 65–75. [CrossRef]
7. Wu, M.; Guan, C.; Tang, C.; Chen, S.; Luo, H.; Wang, G.; Xie, F.; Li, X.; Yang, W. Experimental research on 2BYF-6 type no-tillage rape combine seeder in paddy stubble field. *Trans. Chin. Soc. Agric. Eng.* **2007**, *23*, 172–175. [CrossRef]
8. Wei, G.; Zhang, Q.; Liu, L.; Xiao, W.; Sun, W.; Liao, Q. Design and experiment of plowing and rotary tillage buckle device for rapeseed direct seeder. *Trans. Chin. Soc. Agric. Mach.* **2020**, *51*, 38–46. [CrossRef]
9. Keller, T.; Arvidsson, J.; Dexter, A.R. Soil structures produced by tillage as affected by soil water content and the physical quality of soil. *Soil Tillage Res.* **2007**, *92*, 45–52. [CrossRef]
10. Ding, J.; Li, F.; Le, T.; Xu, D.; Zhu, M.; Li, C.; Zhu, X.; Guo, W. Tillage and seeding strategies for wheat optimizing production in harvested rice fields with high soil moisture. *Sci. Rep.* **2021**, *11*, 119. [CrossRef]
11. Li, C.; Tang, Y.; McHugh, A.D.; Wu, X.; Liu, M.; Li, M.; Xiong, T.; Ling, D.; Tang, Q.; Liao, M.; et al. Development and performance evaluation of a wet-resistant strip-till seeder for sowing wheat following rice. *Biosyst. Eng.* **2022**, *220*, 146–158. [CrossRef]
12. Jaskulska, I.; Jaskulski, D. Strip-till one-pass technology in central and eastern Europe: A MZURI pro-til hybrid machine case study. *Agronomy* **2020**, *10*, 925. [CrossRef]
13. Dou, S.; Wang, Z.; Tong, J.; Shang, Z.; Deng, A.; Song, Z.; Zhang, W. Strip tillage promotes crop yield in comparison with no tillage based on a meta-analysis. *Soil Tillage Res.* **2024**, *240*, 106085. [CrossRef]
14. Licht, M.A.; Al-Kaisi, M. Strip-tillage effect on seedbed soil temperature and other soil physical properties. *Soil Tillage Res.* **2005**, *80*, 233–249. [CrossRef]
15. Tabatabaeekoloor, R. Soil characteristics at the in-row and inter-row zones after strip-tillage. *Afr. J. Agric. Res.* **2011**, *6*, 6598–6603. [CrossRef]
16. Chen, Q.; Zhang, X.; Sun, L.; Ren, J.; Yuan, Y.; Zang, S. Influence of tillage on the Mollisols physicochemical properties, seed emergence and yield of maize in northeast China. *Agriculture* **2021**, *11*, 939. [CrossRef]
17. Mikha, M.M.; Hergert, G.W.; Qiao, X.; Maharjan, B. Soil chemical properties after 12 years of tillage and crop rotation. *Agron. J.* **2020**, *112*, 4395–4406. [CrossRef]
18. David, B.; Lucie, B.; Perla, K.; Pavel, C.; Katerina, P.; Vlastimil, M.; Jan, V. Growth and yield of winter oilseed rape under strip-tillage compared to conventional tillage. *Plant Soil Environ.* **2021**, *67*, 85–91. [CrossRef]
19. Saldukaitė, L.; Šarauskis, E.; Zabrodskyi, A.; Adamavičienė, A.; Buragienė, S.; Kriaučiūnienė, Z.; Savickas, D. Assessment of energy saving and GHG reduction of winter oilseed rape production using sustainable strip tillage and direct sowing in three tillage technologies. *Sustain. Energy Technol. Assess.* **2022**, *51*, 101911. [CrossRef]
20. Jankowski, K.J.; Sokólski, M.; Szatkowski, A.; Załuski, D. The effects of tillage systems on the management of agronomic factors in winter oilseed rape cultivation: A case study in North-Eastern Poland. *Agronomy* **2024**, *14*, 437. [CrossRef]
21. Hobbs, P.R.; Sayre, K.; Gupta, R. The role of conservation agriculture in sustainable agriculture. *Philos. Trans. R. Soc. B Biol. Sci.* **2008**, *363*, 543–555. [CrossRef] [PubMed]
22. Hendrix, B.J.; Young, B.G.; Chong, S. Weed management in strip tillage corn. *Agron. J.* **2004**, *96*, 229–235. [CrossRef]
23. Ren, Z.; Zhang, G.; Wang, B.; Shi, Y. Effects of double-ring diameter on soil infiltration rate. *J. Soil Water Conserv.* **2012**, *26*, 94–99.
24. Liu, M.; Wang, S.; Fan, J.; Fu, W.; Du, M. Rapid in-situ determination of soil evaporation with cutting ring method. *Chin. J. Soil Sci.* **2021**, *52*, 55–61.
25. Cai, G.; Yang, Q.; Chen, H.; Yang, Q.; Zhang, C.; Fan, C.; Zhou, Y. Genetic dissection of plant architecture and yield-related traits in *Brassica napus*. *Sci. Rep.* **2016**, *6*, 21625. [CrossRef] [PubMed]
26. Su, Y.; Gabrielle, B.; Makowski, D. A global dataset for crop production under conventional tillage and no tillage systems. *Sci. Data* **2021**, *8*, 33. [CrossRef] [PubMed]
27. Gawęda, D.; Haliniarz, M. Grain yield and quality of winter wheat depending on previous crop and tillage system. *Agriculture* **2021**, *11*, 133. [CrossRef]
28. Li, H.; He, J.; Gao, H.; Chen, Y.; Zhang, Z. The effect of conservation tillage on crop yield in China. *Front. Agric. Sci. Eng.* **2015**, *2*, 179–185. [CrossRef]
29. Wardak, D.L.R.; Padia, F.N.; de Heer, M.I.; Sturrock, C.J.; Mooney, S.J. Zero tillage has important consequences for soil pore architecture and hydraulic transport: A review. *Geoderma* **2022**, *422*, 115927. [CrossRef]
30. Kumar, V.; Mahaja, G.; Dahiya, S.; Chauhan, B.S. Challenges and opportunities for weed management in no-till farming systems. In *No-Till Farming Systems for Sustainable Agriculture*; Dang, Y., Dalal, R., Menzies, N., Eds.; Springer: Berlin/Heidelberg, Germany; Cham, Switzerland, 2020. [CrossRef]
31. Radicetti, E.; Mancinelli, R. Sustainable weed control in the agro-ecosystems. *Sustainability* **2021**, *13*, 8639. [CrossRef]
32. Pramanick, B.; Mahapatra, B.S.; Datta, D.; Dey, P.; Singh, S.P.; Kumar, A.; Paramanik, B.; Awasthi, N. An innovative approach to improve oil production and quality of mustard *(Brassica juncea* L.) with multi-nutrient-rich polyhalite. *Heliyon* **2023**, *9*, e13997. [CrossRef] [PubMed]

agriculture

Article

Improving Sowing Uniformity of a Maize High-Speed Precision Seeder by Incorporating Energy Dissipator

Rui Liu, Guangwei Wu, Jianjun Dong, Bingxin Yan and Zhijun Meng *

Intelligent Equipment Research Center, Beijing Academy of Agriculture and Forestry Sciences, Beijing 100097, China; liur@nercita.org.cn (R.L.); wugw@nercita.org.cn (G.W.); dongjj@nercita.org.cn (J.D.); yanbx@nercita.org.cn (B.Y.)
* Correspondence: lmengzj@nercita.org.cn; Tel.: +86-178-0113-7458

Abstract: To enhance the sowing uniformity of the vacuum seeder in the high-speed working state, a flexible energy-dissipation receiving device was designed. We analyzed the angle and velocity of seed ejection from the seed-metering device. Additionally, we explored the rheological properties of four different sodium alginate (SA) solutions. Combined with high-speed camera technology, the movement characteristics of four kinds of energy dissipators were revealed, and it was determined that the fabrication material of the energy dissipator is colloid with an SA percentage of 10%. The influence of the thickness of the energy dissipator body, impact velocity, and impact angle on the pre- and post-impact velocity difference and end-of-motion transverse displacement value was investigated. The quadratic regression equation between experimental factors and experimental indexes was established, and it was determined that the thickness of the energy dissipator was 7 mm. Field experiment results showed that the working speed was 12~16 km·h^{-1}, the leakage rate was less than 6.83%, the multiple rates were less than 0.97%, the qualified rate was stable at more than 92.4%, and the qualified grain distance variation rate was stable at less than 16.57%. The designed energy-dissipation device is beneficial to improve the overall working performance of high-speed precision seeders. In the future, if the reliability and long-term performance of the energy-dissipation device are further improved, it will be able to meet the requirements for precision seeding under high-speed conditions.

Keywords: maize; high-speed precision; seed transport system; energy dissipation; seeding quality

Citation: Liu, R.; Wu, G.; Dong, J.; Yan, B.; Meng, Z. Improving Sowing Uniformity of a Maize High-Speed Precision Seeder by Incorporating Energy Dissipator. *Agriculture* **2024**, *14*, 1237. https://doi.org/10.3390/agriculture14081237

Academic Editor: Simone Bergonzoli

Received: 9 July 2024
Revised: 22 July 2024
Accepted: 25 July 2024
Published: 26 July 2024

1. Introduction

With the acceleration of China's urbanization process, agricultural production has scaled up significantly. Business entities are now pursuing high-speed and high-efficiency production methods. As a result, high-speed precision seeders have become one of the crucial components in the mechanized production of maize [1–3]. The precision of high-speed maize seeders depends not only on the accuracy of individual key components but also on their ability to work together effectively. Seeds are transported from the seed box to the seed furrow through a series of processes, including filling, carrying, clearing, dropping, and guiding. These processes are conducted sequentially by the vacuum seed-metering device and the seed-guiding device [4–8]. The vacuum seed-metering device picks up the seeds precisely and carries them in a circular motion, while the seed-guiding device restrains the seeds from moving orderly into the seed furrow. The difficulty of cooperation between the two is that the seeds will start from the seed discharge port of the seed-metering device at a certain angle of ejection due to inertia. The position and direction of the seeds entering the seed-guiding device are different with different working speeds. After entering the seed-guiding device, the seeds will collide and bounce. Thus, the seeds cannot continue to enter the seed furrow in a single-seed orderly state, which reduces the sowing accuracy.

In Europe and the USA, high-speed precision planters have the seed-guiding device closely connected to the seed-metering device at the seed discharge port. Additionally, a binding force is applied to guide the seeds smoothly and orderly into the seed-guiding device. The Proesm K precision seeder, developed by [9], transports seeds from the seed box to the seed furrow by vacuum seed-metering device and seed-guiding tube. A vertical, lateral scraper is installed at the seed discharge port of the seed-metering device to force the seeds into the seed-guiding tube in a vertical direction. Chrono 700 high-speed precision seeder, developed by [10], consists of a vacuum seed-metering device and a pneumatic seed-guiding tube. The seed-metering device is inclined at 15 degrees, and the upper part of the seed-guiding tube is positioned close to the seed discharge port. Seeds separated from the seed-metering device enter the seed-guiding tube in a straight line under the action of gravity. The 3505 Planter precision seeder, developed by [11], consists of a vacuum seed-metering device and a belt-type seed-guiding device. Two oppositely rotating seed wheels are installed at the seed discharge port of the seed-metering device, which transfers the seeds to the conveyor belt of the belt-type seed-guiding device. The Tempo R precision planter developed by [12], is equipped with a pneumatic seed-metering device and an air-fed seed-guiding tube, with the help of a pressure-relief wheel and a positive airflow to guide the seed into the seed-guiding tube.

Currently, research in China mainly focuses on either seed-metering devices or seed-guiding devices. Due to the lack of a cooperative theoretical basis and advanced technology, the domestic seed-metering device and seed-guiding tube cannot be closely connected under high-speed working conditions. The difference in seed shape, high vibration frequency of the machine, and variations in seed injection angle into the seed-guiding device cause seeds to easily collide with the inner wall of the seed-guiding device. This prevents the formation of an orderly seed flow, which reduces the seeding uniformity and affects the seeding quality [13,14]. A few researchers in China have added collaborative parts to the seed discharge port of the seed-metering device or the upper part of the seed-guiding tube, which guides the seeds to enter the seed-guiding tube along the same position and direction. The linear seed-pushing device combined with the asymptotic gas-blocking device is only suitable for seed-metering disks with guide grooves, which have a narrow range of applications [15]. The uniformity and stability of seed guidance are poor at high rotational speeds of V-shaped grooved wheels, so it is not suitable for the high-speed working of the seeder [16]. Under the condition of not changing the structure of the seed-metering device or seed-guiding device and not adding a secondary auxiliary seeding device, the technology of stable and orderly seeding is studied to solve the problems of poor uniform grain distance, high leakage, and missed multiple rates caused by collision when seeds enter the seed-guiding device. This is of great significance to realize high-speed and precision seeding.

To eliminate the dynamic energy head that collides with the wall surface of the seed-guiding device and ensure that all seeds can enter the seed-guiding device in an orderly state, therefore improving the uniformity of the sowing of the vacuum seeder in the high-speed working state. A method of realizing the energy dissipation using shear-thinning fluid as the undertaking part was put forward. The dynamic relationship of the seed undertaking process was defined, and the key factors and numerical range affecting the energy-dissipation effect were determined. In addition, the high-speed camera technology was used to analyze the energy-dissipation process, to determine the best working parameters of the energy-dissipation parts. Finally, the feasibility and effectiveness of the energy-dissipation are verified by field experiments.

2. Materials and Methods

2.1. Seed Transport System of High-Speed Vacuum Seeder

As shown in Figure 1, the seed transport system of a high-speed vacuum seeder is mainly composed of a case, upper seed clearing knife, lower clearing knife, seed disk, forced clearing knife, energy-dissipation device, and positive-pressure airflow-assisted blowing seed-guiding device. When the sowing system is working, the single seed can be carried out under the synergistic effect of negative pressure, seed disk, and clearing knife. In the seed-throwing section, a single seed hits the energy-dissipation device under the action of inertia force and gravity. Because the kinetic energy of the seed is absorbed by the energy dissipator, the seed will fall into the barotropic airflow-assisted blow seed-guiding device along the wall or after a slight bounce. When the seed reaches the seed-guiding section, it is accelerated under the airflow blowing and then leaves the seed-guiding device to complete the whole seeding process.

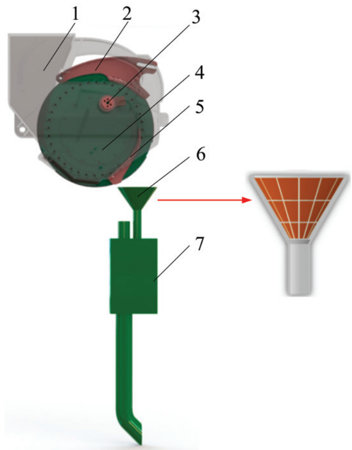

Figure 1. Seed transport system of high-speed vacuum seeder. (1) Case; (2) Upper seed clearing knife; (3) Lower clearing knife; (4) Seed disk; (5) Forced clearing knife; (6) Energy-dissipation device; (7) Positive-pressure airflow-assisted blowing seed-guiding device.

2.2. Effect of Seed-Throwing Process on Qualified Rate of Grain Distance

2.2.1. Motion Analysis in the Initial Stage of Seed-Throwing

As shown in Figure 2, a rectangular coordinate system is established with the horizontal direction as the x-axis and the vertical direction as the y-axis. Because the speed relative to the seed disk is zero when the seeds move circularly with the seed disk at a uniform speed, the instantaneous speed of the seeds leaving the seed-metering disk at the seed discharge port obeys the following Formula (1):

$$\begin{cases} v_{tx1} = 2\pi n r_1 \sin\theta_1 \\ v_{ty1} = 2\pi n r_1 \cos\theta_1 \\ \theta_1 = (k_t - 1)\frac{2\pi}{Z} \\ n = \frac{1\times10^3 v}{3.6LZ} \end{cases} \tag{1}$$

where v is the forward speed of the planter, km·h^{-1}; v_{t1} is the speed of the seed as it leaves the seed disk, m·s^{-1}; L is theoretical grain distance, mm; Z is the number of seed disk holes of the seed disk; n is the rotation speed of seed disk, r·s^{-1}; r is the radius of the circle where the center of the seed disk hole is located, m; θ_1 is the angle of rotation of seeds in the seed discharge area, degree; k_t is the number of seed disk holes that seeds rotate in the seed discharge area.

Simplify Formula (1) to obtain the following Formula (2):

$$v_{tx1} = \frac{1\times10^3\pi v r_1}{1.8LZ}\sin\left(\frac{2\pi k_t - 2\pi}{z}\right) \tag{2}$$

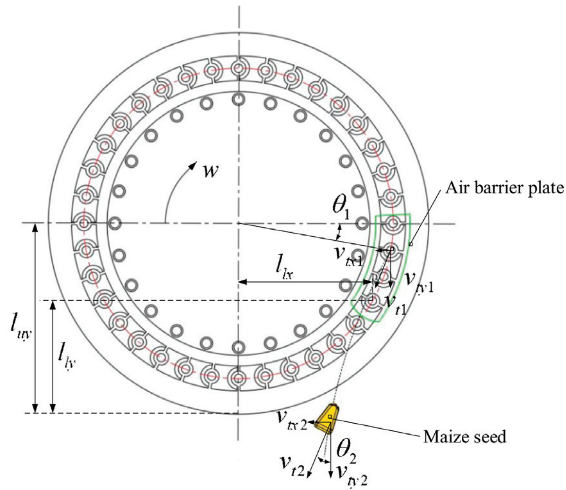

Figure 2. Schematic diagram of motion analysis of seeds after leaving seed disk.

According to the analysis of Formula (2), the horizontal speed of seeds in the initial stage of seed-throwing is related to the forward speed of the seeder, the circle radius of seed disk holes, the number of seed disk holes rotated by seeds in the discharge area, the theoretical grain distance and the number of seed disk holes of seed disk. When the structure of the seed-metering device is determined, the horizontal velocity of the seed at the initial stage of seed-throwing is only positively correlated with the forward speed of the seeder and negatively correlated with the theoretical grain distance. Seeds with a certain initial velocity enter the seed-guiding device with a parabolic trajectory when thrown in an unconstrained state. The higher the speed of the seeder, the higher the horizontal velocity of the seeds, and the greater the transverse displacement, which in turn increases the probability of collision with the wall of the seed-guiding device.

Ideally, the seeds will break away from the seed disk when they reach the upper area of the air barrier plate, but it is impossible for the seeds to break away from the seed disk immediately when the actual working speed is at 8~16 km·h^{-1}. In this study, the upper and lower limit areas of the air barrier plate were taken to calculate the speed of seeds leaving the seed disk and entering the seed-guiding device. Based on Formula (1) and the formula for accelerated motion, when the seeds are detached from the seed disk at the upper and lower limit positions, the speed is $0.183\ \mathrm{m\cdot s^{-1}} \leq v_{t1} \leq 0.321\ \mathrm{m\cdot s^{-1}}$. Subsequently, the seed does parabolic motion with initial velocity v_{t1}. The seed starts to move to the upper part of the seed-guiding device from the upper limit position (flush with the lower end surface of the seed disk), ignoring air resistance, the combined velocity of the seed at the end of the motion is $1.84\ \mathrm{m\cdot s^{-1}} \leq v_{t2} \leq 1.98\ \mathrm{m\cdot s^{-1}}$; according to the displacement formula, we can obtain l_{ux} = 0 m, l_{uy} = 0.14 m. By the formula of the sine function, we can obtain that the angle θ_t of the seed entering the seed-guiding device is 0 degrees.

Similarly, it can be obtained that when the seed moves from the lower limit position, the combined velocity of the seed at the end of the motion is $1.01\ \mathrm{m\cdot s^{-1}} \leq v_{t2} \leq 1.055\ \mathrm{m\cdot s^{-1}}$, the displacement of seed movement is $0.00796\ \mathrm{m} \leq l_{lx} \leq 0.0125\ \mathrm{m}$, l_{ly} = 0.07 m, the angle θ_2 of seed entering the seed-guiding device is 6.5~10.1 degrees. The angle value of the seed entering the seed-guiding device under actual working conditions cannot be the same as the theoretical value, so it is necessary to expand the width of the experimental value to investigate the motion law of the seed energy-dissipation process. Based on the above analysis, the angle of seeds entering the seed-guiding device $\theta_2 \in [0^\circ, 30^\circ]$ and the speed of seeds entering the seed-guiding device $1\ \mathrm{m\cdot s^{-1}} \leq v_{t2} \leq 3\ \mathrm{m\cdot s^{-1}}$ were selected for experimental study.

2.2.2. Analysis of Seed Collision Motion

Maize seeds can be classified as horse-tooth shape, spheroid shape, and ellipsoid shape according to their geometrical shapes, as shown in Figure 3. Due to the irregular shape of the seed, different parts of the seed impact the wall of the seed-guiding device, the direction of rotation in the seed guide tube is different, and the seed collision equation of motion obeys the following Formula [17–20]:

$$\begin{cases} m\frac{d^2x}{dt^2} = F_n + F_\tau + G \\ I\frac{dw_p}{dt} = F_n b\cos\psi - F_\tau b\sin\psi \\ F_n = \frac{4}{3}Y^* R^{1/2}\xi_n^{3/2} \\ F_\tau = -S_\tau\xi_\tau \\ G = mg \end{cases} \tag{3}$$

where F_n is the normal contact force, N; F_τ is the tangential contact force, N; G is the weight of the seed, N; I is the moment of inertia of the seed, kg·m^2; w_p is the angular velocity of the seed rotation, rad·s^{-1}; b is the length of the long axis of the seed, m; ψ is the angle between the collision position of the seed and the long axis, degree; x is the displacement of the seed center, m; Y^* is the equivalent Young's modulus of the seed, Pa; R is the equivalent radius of the seed, m; ζ_n is the normal coincidence, m; ζ_τ is the tangential coincidence, m.

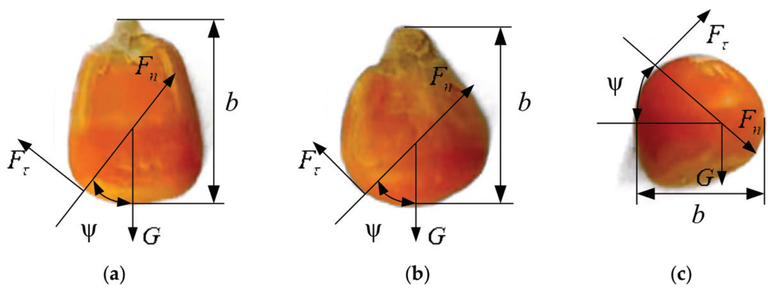

Figure 3. Maize seeds of different shapes. (**a**) Horse-tooth shape; (**b**) Spheroid shape; (**c**) Ellipsoid shape.

When the seed collides with the wall of the seed-guiding device, energy is absorbed by the deformation of the seed [21]; therefore, the kinetic energy equation after the collision is shown in Formula (4):

$$E = \frac{1}{2}mv_p^2 - \int_0^q F_n v_n dq \tag{4}$$

where v_p is the velocity before the seed impacts the wall surface, m·s^{-1}; q is the normal momentum when the seed recovers deformation, N·s v_n is the normal relative velocity between particles at the collision point, m·s^{-1}.

Combined with Formulae (3) and (4), it can be seen that the irregular shape of seeds, inconsistent collision points, different rotational movements, and different kinetic energy losses after seeds bounce up result in different trajectories for seed bounce movements. To evaluate the order of seeds entering the seed-guiding device, it is necessary to analyze the changes in seed velocity and movement after collision.

2.3. Design of Energy-Dissipation Device and Principle of Seed Energy Dissipation

2.3.1. Design of Energy-Dissipation Device

Viscous fluid dampers are highly sensitive to velocity changes and can effectively absorb vibration and impact energy. They have been successfully used in bridges, engineering machinery, and rolling stock to absorb vibration shock energy and reduce equipment damage caused by shock [22–25]. The results of the study show that when the relative motion speed of the viscous fluid due to external excitation is small, the energy dissipated by the shear-thinning fluid is much larger than that dissipated by the shear-thickening fluid. Conversely, when the relative motion speed of the viscous fluid due to external excitation is large, the energy dissipated by the shear-thickening fluid is greater than that dissipated by the shear-thinning fluid [26]. Because the theoretical velocity of seeds entering the seed-guiding device is small, the external excitation to viscous fluid is also small. Therefore, the energy-dissipation characteristics of different types of viscous fluid are comprehensively compared and analyzed. Based on this analysis, we choose shear-thinning fluid as the material of energy-dissipation parts in this study.

The energy-dissipation device consists of a funnel and an energy dissipator. To facilitate the impacted seeds to quickly fall to the seed-guiding device, the inclination angle of the funnel is determined to be 70 degrees. The outlet of the funnel is directly connected to the air intake chamber of the seed-guiding device, so their diameters are identical. Since the energy-dissipation material is a viscoelastic fluid, grid strips are arranged on the inner wall of the funnel to prevent deformation under bumpy conditions. The energy-dissipation materials are laid in blocks within the grid.

2.3.2. Theoretical Model of Seed Energy Dissipation

The process of the seed impacting the energy-dissipation material after departure from the seed disk is a decelerating motion. As a viscous fluid, the shear-thinning fluid provides resistance to the seeds. From the initial moment of impact to the point of lowest velocity, the resistance experienced by the seeds is primarily due to liquid drag force and viscous shear stress [27,28]. Taking maize seeds as the analysis object, Formula (5) can be obtained according to the momentum theorem.

$$\begin{cases} mv_{t2} - mv_{t3} = \int_0^{t_e} F_e + F_{vis} \\ F_e = \dfrac{1}{2}\rho_l C_e A_e v_{t2}^2 \\ F_{vis} = f_l A_l \\ A_l = 2\pi a_e x_l \\ f_l = \dfrac{\eta_a v_{t2}}{x} \end{cases} \tag{5}$$

where v_{t2} is the velocity of the seed impacting the flexible material, m·s^{-1}; v_{t3} is the minimum velocity of the seed after impacting the flexible material, m·s^{-1}; t_e is the time of the seed impacting the flexible material, s; F_e and F_{vis} are the fluid drag force and viscous force exerted by the fluid on the seed, respectively, N; ρ_l is the density of the fluid, kg·m^{-3}; C_e is the coefficient of resistance; A_e is the characteristic area, i.e., the seed entering the flexible material part of the horizontal projection, m^2; f_l is the shear stress exerted by the seed on the flexible body, N·m^{-2}; A_l is the characteristic area of f_l acting on the surface of the seed, m^2; a_e is the equivalent radius of the seed, m; x is the length of the seed entering into the flexible material, m.

Simplify Formula (5) to obtain the following Formula (6):

$$v_{t3} = v_{t2} - \frac{\rho_l C_e A_e t_e v_{t2}^2 + 4\pi a_e t_e \eta_a v_{t2}}{2m} \tag{6}$$

Formula (6) represents the energy-dissipation equation after the seed impacts the flexible material. We can clearly find that the velocity after the seed impacts the flexible material is negatively correlated with the velocity of the seed impacting the flexible material and the viscosity of the fluid, respectively, i.e., the larger the velocity of the impact, the larger the value of the viscosity of the fluid and the larger the kinetic energy dissipated by the seed. The kinetic energy dissipated by the seed is related to the horizontal projection area of the seed entering flexible materials. Because maize seeds are irregular objects, the attitude of the seed impacting flexible materials will also affect the energy dissipation of the seed.

2.4. Preparation of Experimental Materials

Sodium alginate (SA) dissolves in water to form a viscous colloid with good softness and uniformity. The viscosity of its aqueous solution increases with the increase in SA concentration [29,30]. Therefore, SA is selected as dispersed phase particles and deionized water as a dispersed medium to prepare shear-thinning fluid. A certain amount of SA (Shanghai Macklin Biochemical Co., Ltd., Shanghai, China) is dissolved in deionized water at 25 °C and then stirred in a magnetic stirring water bath (Spring instrument. Co., Ltd., Changzhou, China) until the SA was uniformly distributed. Under the same experimental conditions, the solutions were prepared with SA mass shares of 5%, 10%, 15% and 20%, respectively.

2.5. Test Bench

To study the feasibility of using SA to make an energy-dissipation effect, experiments were carried out on a self-made impact device test bench, as shown in Figure 4. The test equipment mainly consists of an L-PRI 1000 high-speed camera (produced by AOS Technologies AG, with a frame rate of 100 frames per second during the test), bracket, energy dissipator, and computer. During the test, the high-speed camera's frame rate is set to 100 frames per second. Each experiment records the movement of the seeds with the high-speed camera, saves the video in. raw4 format, and imports it into the motion analysis software TEMA Classic 2021. The first step is to select the marker tracking point and set the algorithm and parameters for the point. The second step is to select the seed motion segment to identify and interpret the tracking point. The third step is to calibrate the seed motion segment in two dimensions. The fourth step is to display the tracking data and obtain the 2D-pixel coordinates of the maize seed in the image sequence. Finally, the speed, displacement and acceleration of the seeds were calculated by TEMA Classic software.

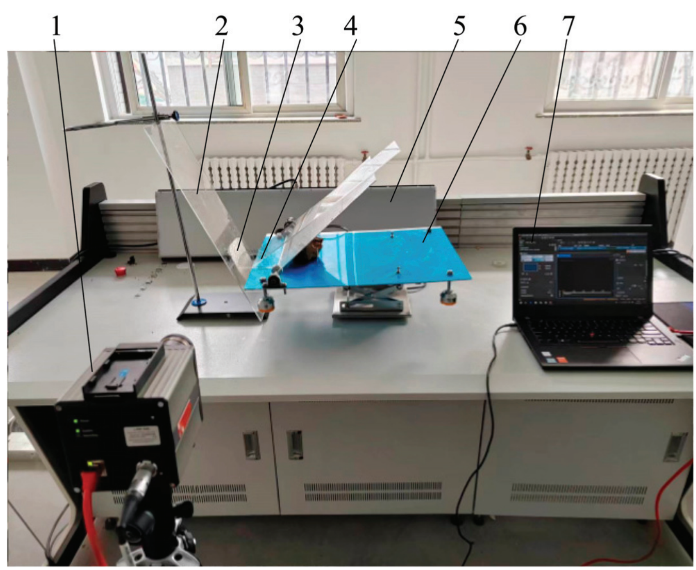

Figure 4. Impact test bench. (1) L-PRI 1000 high-speed camera; (2) Acrylic plate bracket; (3) Energy dissipator; (4) Protractor; (5) Fill light; (6) Adjusting bracket; (7) Computer.

Under natural conditions, SA aqueous solution loses water, which directly affects its viscosity and elasticity if water loss is excessive. Therefore, for the test, the SA solution is made into an energy dissipator with dimensions of 150 × 150 × 2 mm and wrapped with 0.02 mm thick polyethylene material. (which meets the requirements of GB/T1040.3-2006 [31]). In practical applications, the energy-dissipation material is laid on a funnel with a fixed inclination angle, forming an energy-dissipation device. The inclination angle of the fixed energy-dissipation material bracket on the impact test bench is set to match that of the funnel, which is 70 degrees. In the test, the maize seeds are released manually by adjusting the height. The seeds slid down a smooth acrylic plate to achieve the desired impact speed. The movement angle of the seeds is changed by rotating the adjusting bracket. Zhengdan 958 maize seeds are selected, with a moisture content of 13% and a thousand-grain mass of 375 g.

2.6. Field Experiments

To further verify the effect of the energy dissipator on sowing quality enhancement under high-speed conditions, the 2BQX-6J maize/soybean high-speed vacuum precision seeder, with and without an energy-dissipation device, was used as the test carrier. The field test was carried out at the Beijing Agricultural Machinery Experimental Station. The supporting power for the test was provided by a John Deere 1654 tractor (power 165 hp). The fan of the seed-metering device was driven by a hydraulic motor, with the fan pressure set at 4.5 kPa with an error of 0.5 kPa. The theoretical grain distance was set to 25 cm, and the soil type of the test site was sandy loam. Ungraded Zhengdan 958 maize seed was used in the test, and the field test site is shown in Figure 5. The length of the test area was set to 100 m, with the middle 20 m designated as the data collection area. The working speeds were set to 12 km·h^{-1}, 14 km·h^{-1}, and 16 km·h^{-1}, respectively.

Figure 5. Field experiments.

2.7. Experimental Scheme and Evaluation Index

2.7.1. Evaluation Index

The pre-and post-impact velocity difference and the end-of-motion transverse displacement value are used as the bench test indexes. The average value of 20 seeds in each group is taken to evaluate the test results. The calculation method of the experiment index is shown in Formula (7):

$$\begin{cases} y_1 = \dfrac{\sum\limits_{j=1}^{n} (v_{cj} - v_{mj})}{n} \\ y_2 = \dfrac{\sum\limits_{j=1}^{n} x_z}{n} \end{cases} \tag{7}$$

where y_1 is the pre- and post-impact velocity difference, m·s^{-1}; y_2 is the value of transverse displacement at the end of the movement, mm; v_{cj} is the maximum velocity before the seed impacts the flexible body, m·s^{-1}; v_{mj} is the minimum velocity after the seed impacts the flexible body, m·s^{-1}; x_z is the horizontal position of the end of the seed movement (about to touch the tabletop), mm.

According to the requirements of JB/T10293-2013 [32] Technical Conditions for Single-Seed (Precision) Seeder, the field experiment was carried out with qualified rate, leakage rate, multiple rate, and qualified grain distance variation rate as experimental indexes. The calculation method of the experiment index is shown in Formula (8):

$$\begin{cases} y_3 = \frac{n_1}{N} \times 100\% \\ y_4 = \frac{n_2}{N} \times 100\% \\ y_5 = \frac{n_0}{N} \times 100\% \\ y_6 = \sqrt{\frac{\sum n_i X_i}{n'_2} - \overline{X^2}} \times 100\% \end{cases} \tag{8}$$

Specifically,

$$\begin{cases} X_i = \frac{x_m}{x_t} \\ n'_1 = \sum n_i (X_i \in \{0 \sim 0.5\}) \\ n'_2 = \sum n_i (X_i \in \{> 0.5 \sim \leq 1.5\}) \\ n'_3 = \sum n_i (X_i \in \{> 1.5 \sim \leq 2.5\}) \\ n'_4 = \sum n_i (X_i \in \{> 2.5 \sim \leq 3.5\}) \\ n'_5 = \sum n_i (X_i \in \{> 3.5 \sim +\infty\}) \\ n_2 = n'_1 \\ n_1 = n'_1 + n'_2 + n'_3 + n'_4 + n'_5 - 2n_2 \\ n_0 = n'_3 + 2n'_4 + 3n'_5 \\ N = n'_2 + 2n'_3 + 3n'_4 + 4n'_5 \end{cases} \tag{9}$$

where y_3 is the qualified rate, %; y_4 is the multiple rate, %; y_5 is the leakage rate, %; y_6 is the qualified grain distance variation rate,%; X_i is the scale value, x_m is measured seed spacing, mm; x_t is theoretical seed spacing, mm; n_i is the frequency.

2.7.2. One Factor and Multifactor Experimental Design

To study the rheological behavior of SA solution in a steady shear flow field, we used a DHR-2 rheometer (TA Instrument Co., Ltd., New Castle, DE, USA) to obtain the macroscopic response characteristics of SA solution under stress or strain conditions. To investigate the changes in the fluid under dynamic shear, time was taken as the independent variable, while the energy storage modulus and energy-dissipation modulus were taken as the dependent variables. Oscillatory tests were performed using the rheometer, setting the low shear rate to 0.1/s and the high shear rate to 100/s, with each time period lasting 20 s. The mass fractions of SA in the dispersed phase were 5%, 10%, 15% and 20%.

Based on the theoretical analysis of seed energy dissipation, the mass fraction of dispersed phase in the fluid, impact velocity, and impact angle are selected as experiment factors. The pre-and post-impact velocity difference and the transverse displacement at the end of the movement are selected as experiment indexes. A single-factor experimental study on the process of seed energy dissipation is carried out. The level codes of experimental factors are shown in Table 1.

Table 1. Factor level of single-factor experiment.

Level	Factors		
	Mass Fraction of Dispersed Phase in Fluid/%	**Impact Velocity/m·s^{-1}**	**Impact Angle/°**
1	10	1	0
2	15	2	15
3		3	30

2.7.3. Orthogonal Experimental Design

To improve the energy-dissipation effect of seed, it is necessary to optimize the structure of the energy-dissipation body. Based on the single-factor experiment, the thickness of the energy dissipator, impact velocity and impact angle are selected as experimental factors to carry out a quadratic regression orthogonal experiment with three factors and three levels. The level codes of experimental factors are shown in Table 2.

Table 2. Factor level of quadratic regression orthogonal experiment.

Level	Factors		
	Thickness of Energy Dissipator ***E*/mm**	**Impact Velocity** ***F*/m·s^{-1}**	**Impact Angle *W*/°**
−1	4	1	0
0	6	2	15
1	8	3	30

3. Results and Discussion

3.1. Analysis of Rheological Property of Shear-Thinning Fluid

Figure 6 shows the variation curves of fluid viscosity values with the shear rate for different SA mass fractions. It can be seen from the figure that when the mass fraction of SA is fixed value in the test level, the viscosity of fluid decreases with the increase of shear rate, which shows a continuous shear-thinning phenomenon. When the mass fraction of SA is less than 10%, and the shear rate is greater than 10/s, the fluid's viscosity is very low, indicating a low critical shear rate. At a shear rate of 0.1/s, the viscosity values are 1003.3 Pa·s and 2257.5 Pa·s for SA mass fractions of 15% and 20%, respectively. The viscosity decreases significantly when the shear rate is increased to 100/s, indicating that a proper increase in SA is beneficial to increase the fluid's critical shear rate.

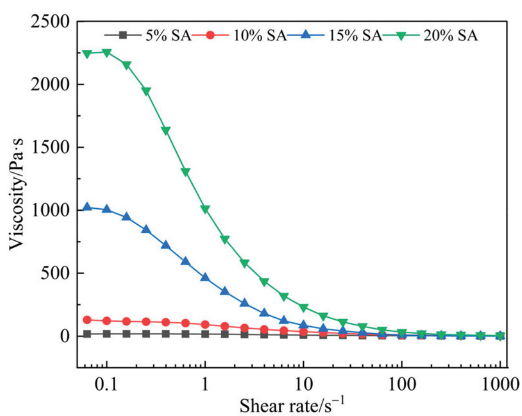

Figure 6. Rheological curves of fluid under different mass fractions.

The SA solution is a viscoelastic fluid, making the study of its viscoelasticity particularly important. According to the theory of viscoelasticity, elasticity represents the solid behavior of the system, while viscosity represents the liquid behavior. The elastic and viscous strengths of the system are expressed by the storage modulus (G′) and the dissipation modulus (G″), respectively [33]. When maize seeds impact on energy-dissipation parts made of SA solution at a certain velocity, the fluid movement process can be roughly divided into three stages under the action of shear force: the no-collision period under low shear rate, the collision period under high shear rate and recovery period under low shear rate.

Figure 7a–d record the values of energy storage modulus (G') and energy-dissipation modulus (G'') for fluids with SA mass fractions of 5%, 10%, 15%, and 20%, respectively, across the three stages. As can be seen from the figure, the values of energy storage modulus and energy-dissipation modulus increase with the increase of the mass fraction of SA in the four sets of tests. Specifically, the values of G' and G'' for 5% SA fluid are smaller, and the energy storage modulus of the fluid is smaller than the energy-dissipation modulus in the three time periods. Please note that G'' is larger than G' during both the collision and recovery stages in the same set of tests, which indicates that the 5% SA fluid exhibits liquid-like behavior and has poor shape retention. For 10% SA fluid, the energy storage modulus is smaller than the energy-dissipation modulus throughout all three stages, but the values of G' and G'' increase significantly, indicating enhanced viscous and elastic properties. Therefore, it demonstrates that the 10% SA fluid can absorb energy and recover from deformation. For 15% SA fluid, the energy storage modulus is larger than the energy consumption modulus in the time period of 0~20 s and 40~60 s, which indicates that the fluid is a kind of solid and has a certain shape-retaining ability without shear action. The energy consumption modulus is larger than the energy storage modulus in the time period of 20~40 s, which indicates that the fluid mainly exhibits viscous characteristics when it is subjected to shear force. Thus, it proves that 15% SA fluid mainly consumes energy. The value of G' for 15% SA fluid is approximately equal to three times 10% SA fluid, and the value of G'' for 15% SA fluid is approximately equal to twice 10% SA fluid for the collision-free period at a low shear rate. In the recovery period at a low shear rate, the value of G' for 15% SA fluid is approximately equal to two times 10% SA fluid, and the difference between the two G'' values is very small, which indicates that the ability of 15% SA fluid to recover deformation in the absence of shear is slightly better than that of 10% SA fluid. The values of G' and G'' are approximately equal for 15%SA fluid and 10% SA fluid for the collision period at a high shear rate. A comprehensive analysis of the rheological properties of the 10% SA and 15% SA fluids shows that the energy-dissipation modulus of both is approximately equal from the shear stage to the recovery stage, but there is a difference in specific rheological properties of both during the recovery stage. The G' and G'' variation rules of 20% SA fluid and 15% SA fluid are the same in all three time periods, but the energy storage modulus of 20% SA fluid in the absence of shear is significantly increased, which indicates that the elastic properties of the fluid are better.

When seeds come into contact with the energy-dissipation body, the fluid flows under the influence of shear force, resulting in a damping force that dissipates external energy. In this paper, the shear-thinning fluid is used as the energy-dissipation material, which is laid in the middle of the seed-guiding device and the seed-metering device. In the ideal state, the seeds lose all their kinetic energy upon impact with the fluid, the fluid does not deform after impact, and the fluid exhibits excellent shape retention, which ensures that the seeds enter the seed-guiding device along the vertical direction. Fluid needs to have an appropriate balance of viscosity and elasticity. If the elasticity of the fluid is too low, the ability to recover from deformation is poor, which can easily cause sticking. Conversely, if the fluid's elasticity is too high, it can cause the seeds to rebound, failing to meet the requirements for energy dissipation. In addition, the analysis shows that the 5% SA fluid is mainly in a liquid-like state, with a large amount of subsidence after seed impact, which makes it impossible to maintain the shape of the energy dissipator. Conversely, the 20% SA fluid is more elastic, with a sharp rebound after seed impact. Therefore, 5% SA and 20% SA fluids are not suitable as materials for energy-dissipation devices. Thus, 10% SA and 15% SA fluids will be selected for experimental studies on seed energy dissipation.

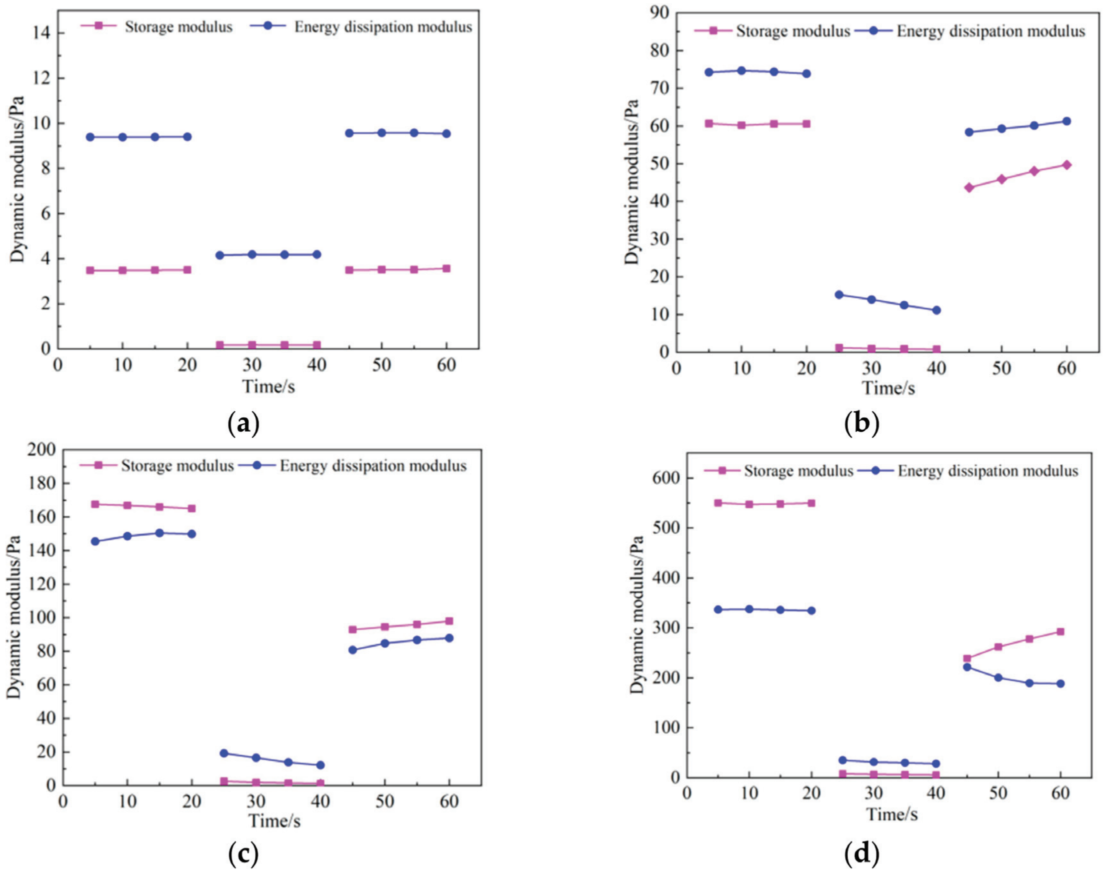

Figure 7. Viscoelasticity of fluid under different mass fractions. (**a**) 5% SA; (**b**) 10% SA; (**c**) 15% SA; (**d**) 20% SA.

3.2. Analysis of the Seed Energy-Dissipation Process

3.2.1. Feasibility of the Seed Energy Dissipation

When the mass fraction of SA in the dispersed phase is 10%, the impact velocity is 2 m·s^{-1} and the impact angle is 30 degrees, maize seeds might impact flexible material in four postures: the largest side in the plane of seed contacts flexible material (broad-side impact), the tip of seed contacts flexible material (tip impact), the side of seed contacts flexible material (side impact) and the tail of seeds contacts flexible materials (bottom impact), as shown in Figure 8a–d in turn. Additionally, the movement posture of seeds changes obviously after impacting the energy-dissipation material. The movement of seeds after contact with flexible material is different, with different postures of seeds impacting flexible materials. This phenomenon is consistent with the theoretical analysis of the seed energy-dissipation equation.

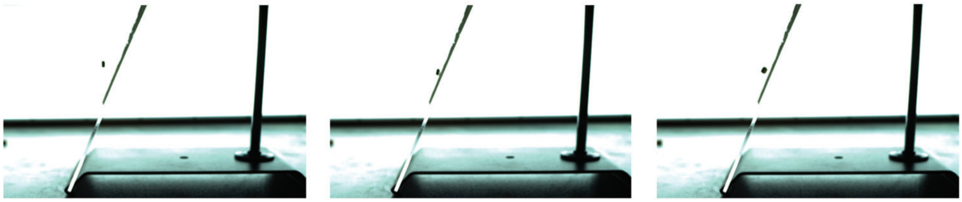

(**a**)

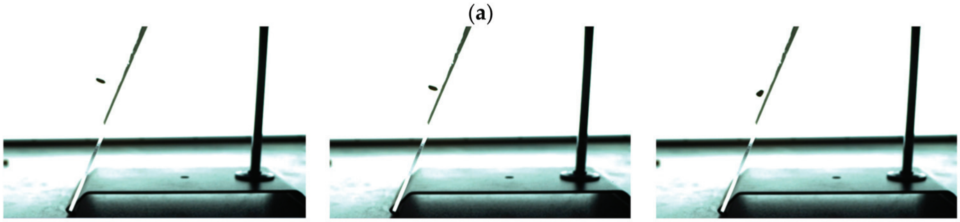

(**b**)

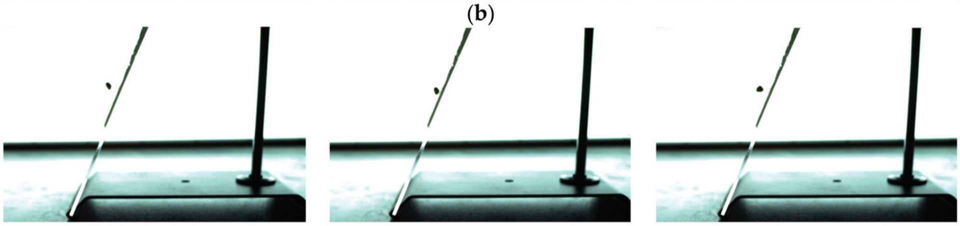

(**c**)

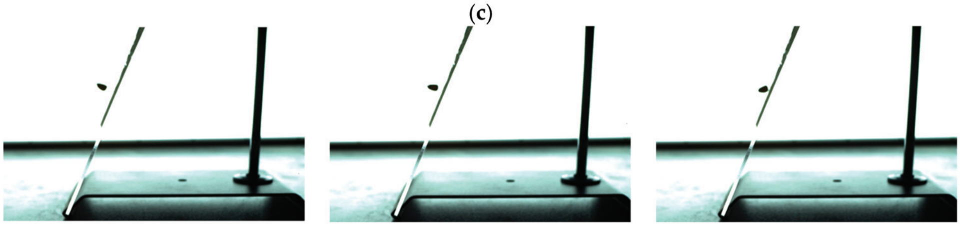

Figure 8. Different postures of seeds impacting the energy dissipator. (**a**) Broad-side impact; (**b**) Tip impact; (**c**) Side impact (**d**) Bottom impact.

The velocity and transverse displacement of the seed under four impact postures as a function of time are shown in Figures 9–12.

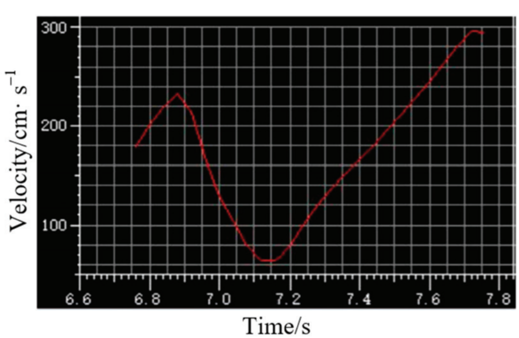

(**a**)

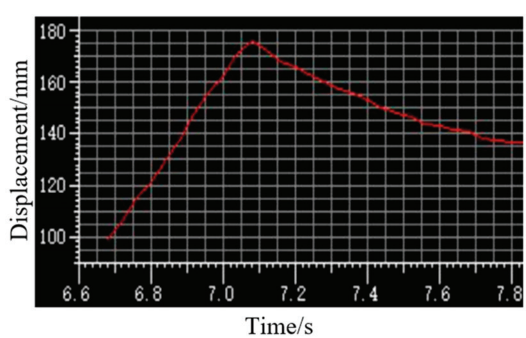

(**b**)

Figure 9. Motion analysis of broad-side impact. (**a**) Time-velocity curve; (**b**) Time-transverse position curve.

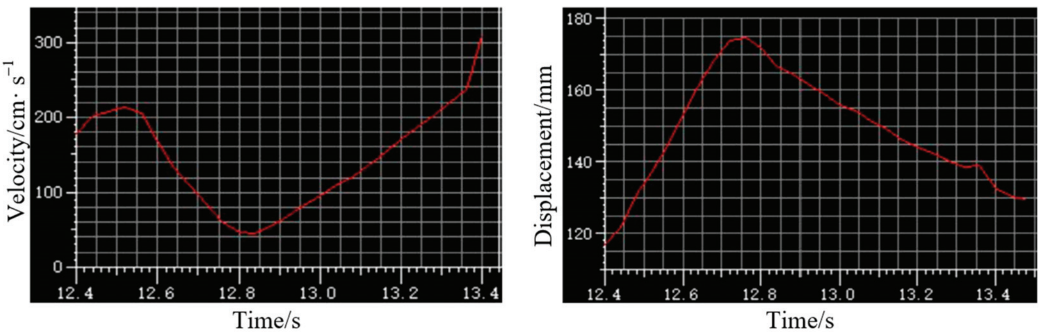

(a) (b)

Figure 10. Motion analysis of tip impact. (**a**) Time-velocity curve; (**b**) Time-transverse position.

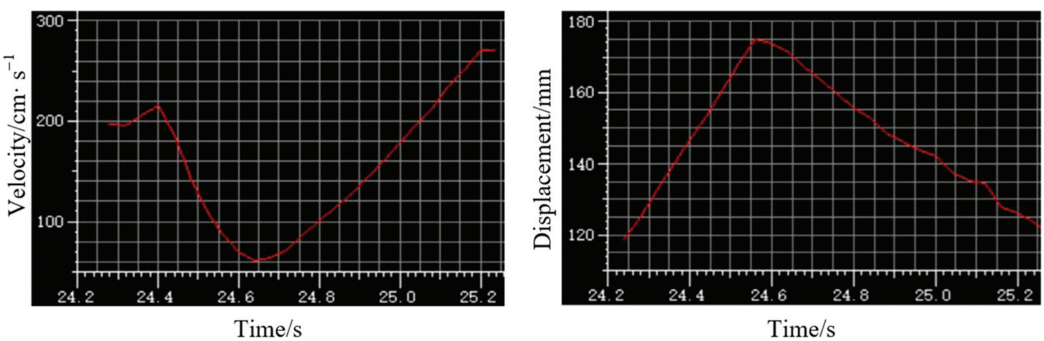

(a) (b)

Figure 11. Motion analysis of side impact. (**a**) Time-velocity curve; (**b**) Time-transverse position curve.

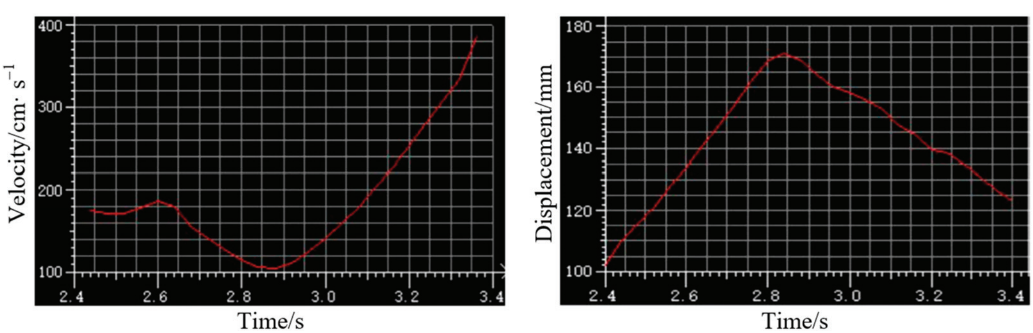

(a) (b)

Figure 12. Motion analysis of bottom impact. (**a**) Time-velocity curve; (**b**) Time-transverse position curve.

By analyzing the time-velocity curves in Figures 9–12, it can be seen that before and after the seeds hit the flexible materials, the seed velocity experienced three stages: acceleration, deceleration, and re-acceleration over time. Before the seeds contact the flexible material, due to the small height of the flexible material, the seed velocity increases slightly under gravity. After the seed comes into contact with the flexible material, the shear force is exerted on the flexible material, causing the material to flow and rapidly dissipate the seed's kinetic energy of the seed, resulting in the seed's velocity rapidly decreasing to a minimum. When the seed separates from the flexible material, it accelerates under the action of gravity, causing its velocity to increase. The seed's velocity in the second stage is greatly reduced, which proves that the flexible materials designed in this paper effectively reduce the seed's velocity. It also can be found that the reduction in kinetic energy varies with different impact postures. Specifically, the seed's velocity decreased from 2.32 $m \cdot s^{-1}$ to 0.63 $m \cdot s^{-1}$ for broad-side impact, from 2.18 $m \cdot s^{-1}$ to 0.41 $m \cdot s^{-1}$ for tip impact, from 2.11 $m \cdot s^{-1}$ to 0.60 $m \cdot s^{-1}$ for side impact, and from 1.92 $m \cdot s^{-1}$ to 1.01 $m \cdot s^{-1}$ for bottom impact. The greater the pre- and post-impact velocity difference, the more effective the energy absorption of the energy dissipator. The seed velocity curve rapidly changes from a minimum in the second stage to continuous growth in the third stage, indicating that the seeds are not stuck in the flexible material.

By analyzing the time-transverse position curves in Figures 9–12, it can be seen that before and after the seed impacts the flexible material, the seed's transverse displacement goes through two stages: an increase followed by a decrease over time. Due to the horizontal impact velocity, the seed's transverse displacement gradually increases before contacting the material. After the seed contacts the flexible material, the seed has a reverse horizontal velocity, and its transverse displacement gradually decreases, indicating the elasticity of the flexible material, which ensures that the seed quickly separates from the flexible material after impact. In the experiment, the energy-dissipation material bracket is fixed. Considering the arrangement position of the test device, it can be seen that the greater the transverse displacement of the seed's moving end, the smaller the distance between the seed and the bracket's end face, indicating a smaller bounce amplitude after impact. The transverse displacement of the seed's moving end is the largest for broad-side impact, resulting in the smallest bounce amplitude. The transverse displacement values of the moving end of seeds are different under the four impact postures, but the difference is very small, which shows that seeds can enter the seed-guiding device along the same position. The above analysis verified the feasibility of using an SA solution to make an energy-dissipation device.

3.2.2. Influence of Experimental Factors on Energy-Dissipation Process

The influence of different mass fractions of fluid dispersed phase on the pre-and post-impact velocity difference is shown in Figure 13. When the impact angle is a fixed value in the test range, the energy dissipator can effectively dissipate the seed's kinetic energy at each velocity level. The 10% SA fluid has a better kinetic energy-dissipation ability than the 15% SA fluid because the 10% SA fluid exhibits stronger flow performance under the same shear force, producing a larger damping force and thus dissipating more energy. At the same impact velocity, the pre- and post-impact velocity difference is smallest at an impact angle of 0 degrees and largest at an impact angle of 30 degrees. This may be because maize seeds are irregular objects; a larger impact angle increases the contact area with the energy dissipator during oblique motion, resulting in a larger trailing force from the fluid and greater kinetic energy dissipation.

The influence of different mass fractions of fluid dispersed phase on the transverse displacement values at the end of the seed movement is shown in Figure 14. At the same impact velocity and angle, the transverse displacement values of seeds impacting the 10% SA fluid are larger than those impacting the 15% SA fluid, further supporting the good energy absorption effect of the 10% SA fluid. Based on the above experimental results, 10% SA fluid is determined to be the fabrication material for the energy dissipator. However, within the test range, although the velocity difference of seeds after impacting the energy dissipator is significantly reduced, the post-impact seed velocity remains high. For example, when the impact velocity is 3 $m \cdot s^{-1}$ and the impact angle is 0 degrees, the pre-and post-impact velocity is 1.14 $m \cdot s^{-1}$, indicating the need to further optimize the energy dissipator's structure.

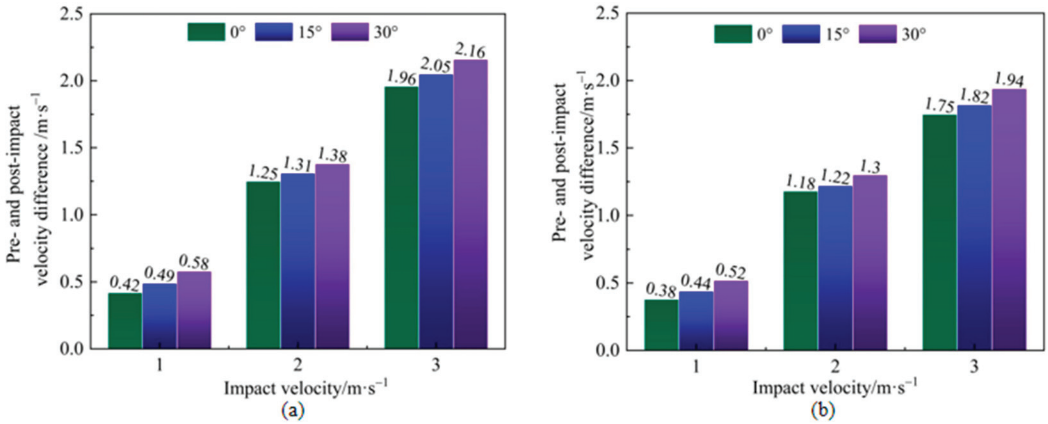

Figure 13. Influence of different mass fractions of fluid dispersed phase on the pre- and post-impact velocity difference. (**a**) 10% SA; (**b**) 15% SA.

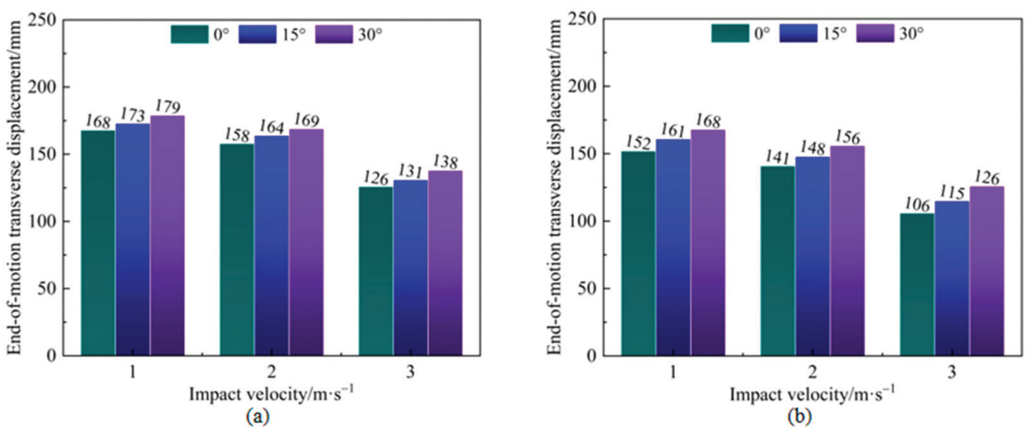

Figure 14. Influence of different mass fractions of fluid dispersed phase on the transverse displacement. (**a**) 10% SA; (**b**) 15% SA.

3.3. Optimization of Energy Dissipator

To further reduce the bounce degree of seeds after impacting the energy dissipator, based on the previous test and analysis results, a regression orthogonal test design was carried out according to Box-Behnken central combination test design theory. The test scheme and results are shown in Table 3.

3.3.1. Analysis of Variance and Establishment of Regression Model

Using Design-Expert 10 software (Stat-Ease Ltd., Godward St NE, Minneapolis, MN, USA) to carry out regression analysis on the experiment data in Table 3, the regression equations between the pre- and post-impact velocity difference y_1, end-of-motion transverse displacement value y_2, energy dissipator thickness E, impact velocity F, and impact angle W as shown in Formula (10).

$$\begin{cases} y_1 = 1.8 + 0.23E + 0.078F + 0.81W + 0.045EF - 0.15E^2 - 0.15F^2 - 0.057W^2 \\ y_2 = 170.06 + 2.5E - 18.75F + 6.25W - 8.18F^2 + 4.83W^2 \end{cases} \quad (10)$$

Table 3. Design and results of the orthogonal experiment.

Number	Thickness of Energy Dissipator E/(mm)	Impact Velocity F/(m·s^{-1})	Impact Angle W/(degree)	Pre- and Post-Impact Velocity Difference y_1/(m·s^{-1})	Value of Transverse Displacement at the End of the Movement y_2/(mm)
1	−1	0	−1	1.44	167
2	−1	0	1	1.62	178
3	1	1	0	2.45	145
4	1	0	1	1.73	185
5	−1	1	0	2.18	141
6	0	1	−1	2.33	142
7	0	0	0	1.78	169
8	0	0	0	1.86	172
9	0	−1	−1	0.68	180
10	−1	−1	0	0.65	179
11	0	0	0	1.81	166
12	0	1	1	2.47	156
13	1	−1	0	0.74	184
14	0	0	0	1.82	175
15	0	0	0	1.74	171
16	0	−1	1	0.91	191
17	1	0	−1	1.59	171

The results of the variance analysis of the regression equation are shown in Table 4. The models of pre- and post-impact velocity difference and end-of-motion transverse displacement value are extremely significant. However, the lack of fit of regression equations is insignificant. The determination coefficients R^2 of y_1 and y_2 are 0.9469 and 0.8574, respectively, which indicates that the predicted value of the regression equation has an excellent correlation with the actual value. The primary and secondary factors affecting the pre- and post-impact velocity difference and end-of-motion transverse displacement value are impact velocity F, impact angle W, and energy dissipator thickness E, in turn.

Table 4. Variance analysis of regression equations.

Source of Variation	y_1/(m·s^{-1})				y_1/(mm)			
	SS	*DF*	*F*	*P*	*SS*	*DF*	*F*	*P*
Model	5.54	9.00	441.51	<0.0001 **	3453.24	9.00	57.70	<0.0001 **
E	0.05	1.00	34.48	0.0006 **	50.00	1.00	7.34	0.03 *
F	5.20	1.00	3731.64	<0.0001 **	2812.50	1.00	412.74	<0.0001 **
W	0.06	1.00	42.71	0.0003 **	312.50	1.00	45.86	0.0003 **
EF	8.1×10^{-3}	1.00	5.81	0.00467 **	0.25	1.00	0.03	0.8535
EW	4.0×10^{-4}	1.00	0.29	0.608	2.25	1.00	0.33	0.5835
FW	2.0×10^{-3}	1.00	1.45	0.267	2.25	1.00	0.33	0.5835
E^2	0.09	1.00	67.75	<0.0001 **	0.13	1.00	0.33	0.8945
F^2	0.09	1.00	65.51	<0.0001 **	281.39	1.00	0.02	0.0004 **
W^2	0.01	1.00	9.9	0.0162 *	98.02	1.00	41.29	0.0068 **
Lack of fit	1.67×10^{-3}	3.00	0.28	0.84	2.50	3.00	14.39	0.971
Pure error	8.1×10^{-3}	4.00	441.51	<0.0001				
Total	5.55	16.00						

Note: * indicates significance at 0.05 level; ** denotes significance at 0.01 level.

3.3.2. Analysis of the Influence Effect of Energy Dissipator Thickness

To analyze the relationship between the energy dissipator thickness and the energy-dissipation effect, contour plots between the elements and the indicators were obtained using the Design-Expert 10 software, as shown in Figure 15. At the same velocity level, the pre-and post-impact velocity difference increases with the energy dissipator thickness. However, when the energy dissipator increases from 6 mm to 8 mm, the growth rate of the pre-and post-impact velocity difference decreases. This may be because the seed's impact velocity is small. The applied shear force cannot make the energy dissipator flow and then cannot dissipate more kinetic energy. Therefore, within the range of experimental values, there is an optimal thickness of the energy dissipator, which can dissipate the kinetic energy of seeds to the maximum extent. At a fixed impact velocity, the interaction between the thickness of the energy dissipator and the impact angle has a minimal effect on the pre-and post-impact velocity difference. When the impact angle or impact velocity is fixed, the end-of-motion transverse displacement is positively correlated with the energy dissipator thickness.

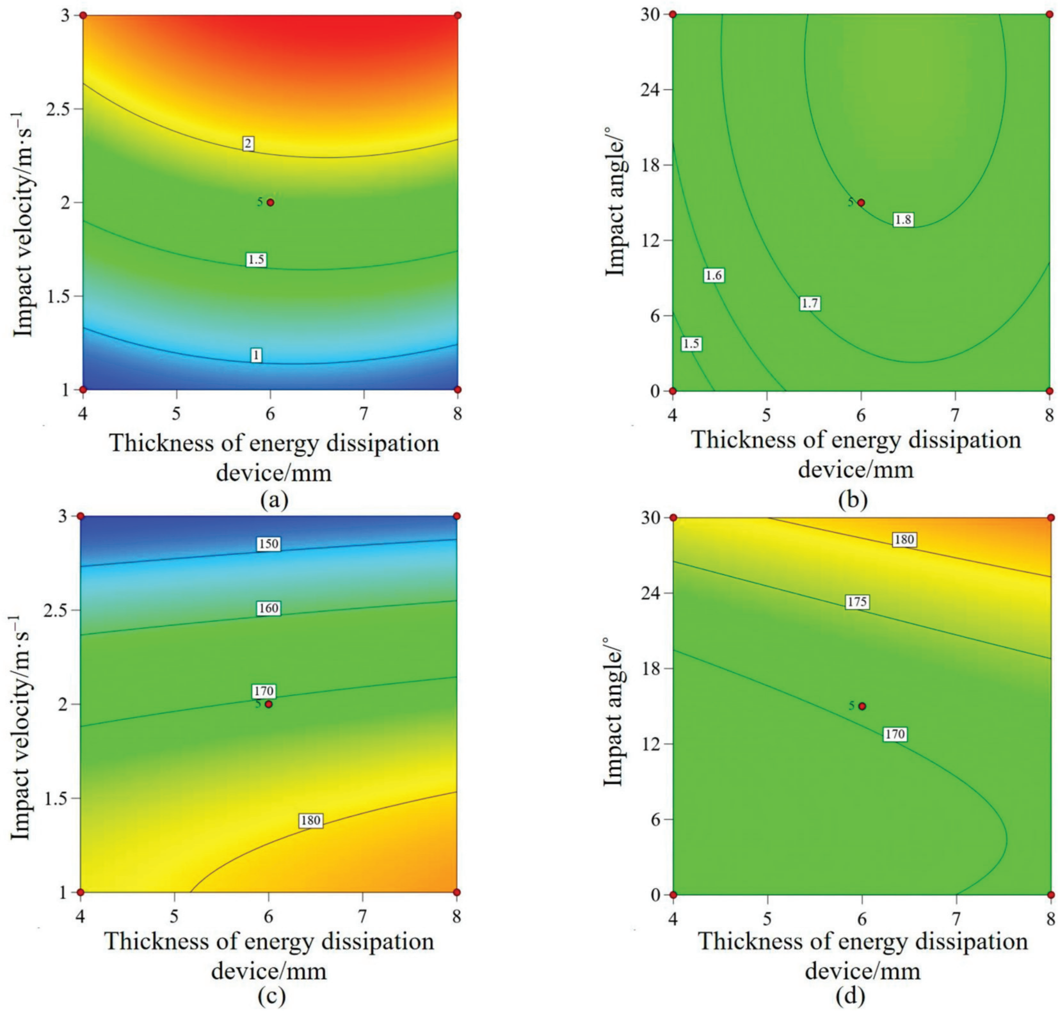

Figure 15. Influence effect of two-factor interaction on evaluation index. (**a**) Influence effect of impact velocity and thickness on pre- and post-impact velocity difference; (**b**) Influence effect of impact angle and thickness on pre- and post-impact velocity difference; (**c**) Influence effect of impact velocity and thickness on end-of-motion transverse displacement; (**d**) Influence effect of impact angle and thickness on end-of-motion transverse displacement.

3.3.3. Parameter Optimization and Experimental Validation

To determine the optimal thickness of the energy-dissipation flexible bearing body, the maximum pre-and post-impact velocity difference and end-of-motion transverse displacement are used as the evaluation index. The regression model is solved by multi-objective optimization, and the optimization objective function and constraint conditions are shown in Formula (11).

$$\begin{cases} max y_1(E, F,\ W) \begin{cases} 4 \le E \le 8 \\ 1 \le F \le 3 \\ 0 \le W \le 30 \end{cases} \\ max y_2(E,\ F,\ W) \begin{cases} 4 \le E \le 8 \\ 1 \le F \le 3 \\ 0 \le W \le 30 \end{cases} \end{cases} \tag{11}$$

Combined with the test results, it is observed that at each level of impact velocity, the pre-and post-impact velocity difference and end-of-motion transverse displacement are the smallest at an impact angle of zero. Therefore, the optimization calculation module of Design-Expert is used to determine the optimum thickness of the energy-dissipation flexible bearing body at three speeds when the impact angle is zero, as shown in Table 5. The optimal thickness of the energy-dissipation flexible bearing body for the optimized range of impact velocities is 6.3~6.9 mm. Because the thickness of the energy-dissipation flexible bearing body needs to meet the minimum bounce of the seed at all impact velocities, the predicted value at the maximum impact velocity was chosen as the optimal value. Considering the production difficulty, the thickness of the energy-dissipation flexible bearing body is determined to be 7 mm.

Table 5. Parameter optimization and experimental validation results.

Impact Velocity/(m·s^{-1})	Impact Angle/(°)	Thickness/(mm)		y_1/(m·s^{-1})		y_2/(mm)	
		Predicted Value	Measured Value	Predicted Value	Measured Value	Predicted Value	Measured Value
1	0	6.3	7.0	0.68	0.71	180.8	173.0
2	0	6.6	7.0	1.46	1.48	169.7	164.0
3	0	6.9	7.0	2.36	2.41	142.1	137.0

Verification tests were carried out to verify the accuracy of the optimization results, as shown in Table 5. The results showed that when the impact velocity was 1~3 m·s^{-1}, the pre-and post-impact velocity difference was 0.71~2.41 m·s^{-1}, with a seed velocity absorption ratio of 71~80.3%, indicating a better energy-dissipation effect. The difference between the predicted value and the actual value of the pre-and post-impact velocity difference is small. For the end-of-motion transverse displacement, the actual value is less than the predicted value, with an error of less than 8 mm. The main reason is that maize seeds are irregular in shape, and the postures of the seeds at the end of the movement are different. During image processing, the center of the seeds is taken as the measuring point, so the displacement values are different.

3.4. Analysis of Field Experiment Results

Comparative test results are shown in Figure 16. According to the field test results at different working speeds, the data analysis showed that the numerical differences for the same test index were very small at the same working speed level, which indicated that the seed transport system of the high-speed vacuum seeder could work continuously and stably. At all speed levels, the leakage rate was less than 6.83%, the multiple rate was less than 0.97%, the qualified rate was stable at more than 92.4%, and the qualified grain distance variation rate was stable at less than 16.57%. When working parameters were the same, the grain spacing uniformity was significantly better than the planter without the energy-dissipation device. For example, at a working speed of 14.13 km·h^{-1}, the leakage rate decreased by 2.4%, the multiple rates decreased by 0.4%, the qualified index increased by 2.8%, and the qualified grain distance variation rate decreased by 3.63%. The results showed the same tendency with Li's research [34]. This proves that the energy-dissipation device designed in this paper is beneficial for improving the overall working performance of high-speed precision seeders.

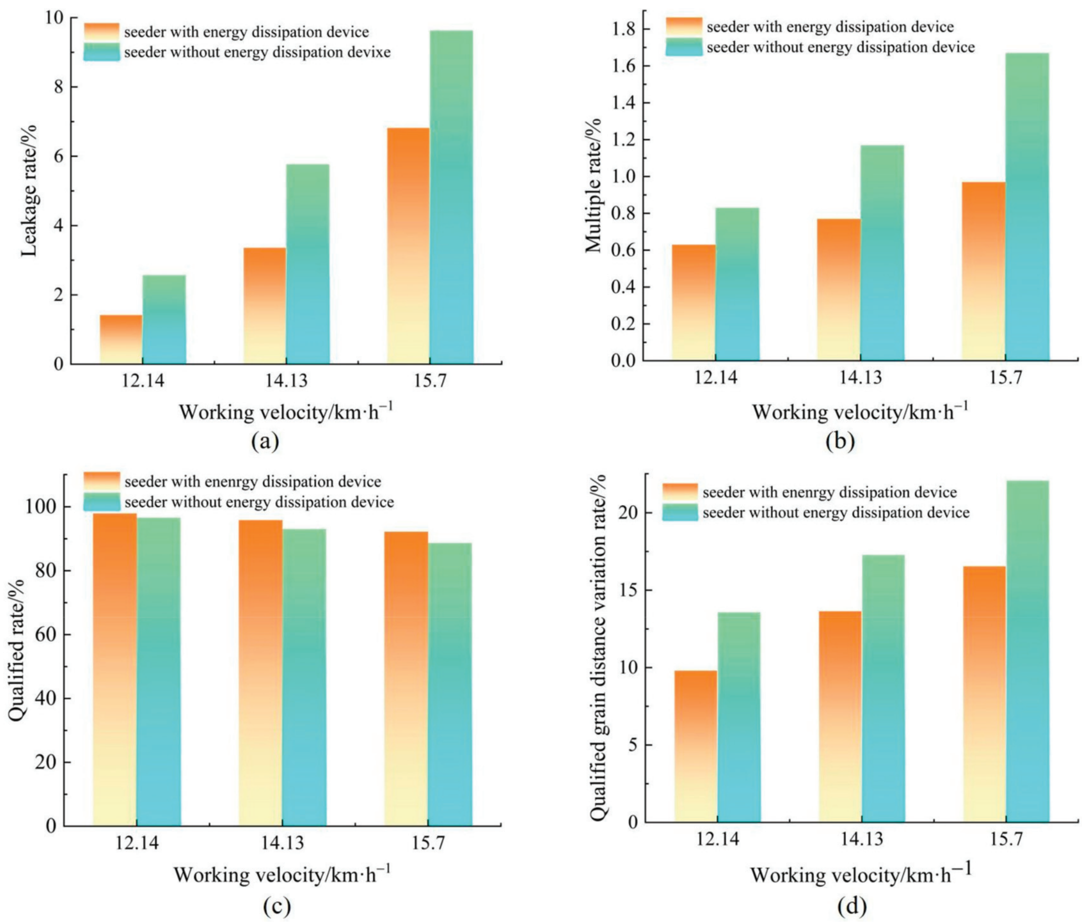

Figure 16. Comparative test results. (**a**) Leakage rate at different velocities; (**b**) Multiple rates at different velocity; (**c**) Qualified rate at different velocities; (**d**) Qualified grain distance variation rate at different velocities.

4. Conclusions

(1) Seed-throwing in an unconstrained state and seed impact with the wall of the seed-guiding device results in poor sowing uniformity of the seeder under high-speed working.

(2) The mass fraction of the fluid dispersed phase significantly influenced the energy dissipation and flexible undertaking. The results of rheological performance experiments show that the rheological properties of 10% SA and 15% SA fluids are similar. Both fluids exhibit good energy absorption and strong deformation recovery ability.

(3) The motion posture, velocity, and displacement of the seed energy-dissipation process are evaluated, and it is determined that the material of the energy dissipator is the colloid with an SA percentage of 10%.
(4) The thickness of the energy dissipator was determined to be 7 mm through regression orthogonal experiments and parameter optimization. The results of the validation experiments show that when the impact velocity was 1~3 $m \cdot s^{-1}$, the pre-and post-impact velocity difference was 0.71~2.41 $m \cdot s^{-1}$, the absorption ratio of seed velocity was 71~80.3%, indicating a better energy-dissipation effect.
(5) The field experiment results prove that the high-speed vacuum seed transport system could work continuously and stably. When the working speed was 12~16 $km \cdot h^{-1}$, the leakage rate was less than 6.83%, the multiple rate was less than 0.97%, the qualified rate was stable at more than 92.40%, and the qualified grain distance variation rate was stable at less than 16.57%, which proves that the energy-dissipation device is beneficial for improving the overall working performance of high-speed precision seeder. In the future, the dynamics of seed movement, as they fall into the seed furrow, will be studied in detail, with the aim of enhancing the application of the energy-dissipation device in practical agricultural production.

Author Contributions: Conceptualization, G.W.; methodology, R.L.; software, R.L.; validation, Z.M.; formal analysis, R.L.; investigation, B.Y. and R.L.; resources, B.Y. and Z.M.; data curation, R.L.; writing—original draft preparation, R.L.; writing—review and editing, Z.M and G.W.; visualization, J.D. and R.L.; supervision, G.W.; project administration, J.D.; funding acquisition, Z.M. All authors have read and agreed to the published version of the manuscript.

Funding: This research was funded by the National Key Research and Development Program of China (2021YFD2000402) National Natural Science Foundation (32301705).

Institutional Review Board Statement: Not applicable.

Data Availability Statement: Data are contained within the article. The data presented in this study can be requested from the authors.

Conflicts of Interest: The authors declare no conflicts of interest.

References

1. Kus, E. Evaluation of some operational parameters of a vacuum single-seed planter in maize sowing. *J. Agric. Sci. Tarim Bilim. Derg.* **2021**, *27*, 327–334.
2. Yatskul, A.L.; Lemiere, J.P. Establishing the conveying parameters required for the air-seeders. *Biosyst. Eng.* **2018**, *166*, 1–12. [CrossRef]
3. Yang, L.; He, X.T.; Tao, C.; Zhang, D.X.; Song, S.; Rui, Z.; Mantao, W. Development of mechatronic driving system for seed meters equipped on conventional precision corn planter. *Int. J. Agric. Biol. Eng.* **2015**, *8*, 1–9.
4. Ding, Y.Q.; He, X.T.; Yang, L.; Zhang, D.X.; Cui, T.; Li, Y.H.; Zhong, X.J.; Xie, C.J.; Du, Z.H.; Yu, T.C. Low-cost turn compensation control system for conserving seeds and increasing yields from maize precision planters. *Comput. Electron. Agric.* **2022**, *199*, 107118. [CrossRef]
5. Han, D.; Zhang, D.; Jing, H.; Yang, L.; Cui, T.; Ding, Y.; Wang, Z.; Wang, Y.; Zhang, T. DEM-CFD coupling simulation and optimization of an inside-filling air-blowing maize precision seed-metering device. *Comput. Electron. Agric.* **2018**, *150*, 426–438. [CrossRef]
6. Pareek, C.M.; Tewari, V.K.; Machavaram, R. Multi-objective optimization of seeding performance of a pneumatic precision seed metering device using integrated ANN-MOPSO approach. *Eng. Appl. Artif. Intell.* **2023**, *117*, 105559. [CrossRef]
7. Liu, Q.W.; He, X.T.; Yang, L.; Zhang, D.X.; Cui, T.; Qu, Z.; Yan, B.X.; Wang, M.T.; Zhang, T.L. Effect of travel speed on seed spacing uniformity of corn seed meter. *Int. J. Agric. Biol. Eng.* **2017**, *10*, 98–106.
8. Shi, S.; Zhou, J.; Liu, H.; Fang, H.; Jian, S.; Zhang, R. Design and experiment of pneumatic precision seed-metering device with guided assistant seed-filling. *Trans. Chin. Soc. Agric. Mach.* **2019**, *50*, 61–70. (In Chinese with English Abstract)
9. Sola. Proesm-K. Available online: https://solagrupo.com/es/pr/sembradoras-monograno/prosem-k-variant-manual-fija-Prosem%20K%20Variant%20manual%20fija-11 (accessed on 21 June 2024).
10. Maschio. Chrono700. Available online: https://www.maschio.com/en/web/international/chrono-700 (accessed on 21 June 2024).
11. Kinze. 3505Planter. Available online: https://www.kinze.com/planters/3505-planter/ (accessed on 21 June 2024).

12. Vaderstad. TempoR. Available online: https://www.vaderstad.com/ca-en/planting/tempo-planter/powershoot/ (accessed on 21 June 2024).
13. Liu, R.; Liu, L.J.; Li, Y.J.; Liu, Z.J.; Zhao, J.H.; Liu, Y.Q.; Zhang, X.D. Numerical simulation of seed-movement characteristics in new maize delivery device. *Agriculture* **2022**, *12*, 1944. [CrossRef]
14. Liu, R.; Liu, L.J.; Li, Y.J.; Liu, Z.J.; Zhao, J.H.; Liu, Y.Q.; Zhang, X.D. Design and experiment of corn high speed air suction seed metering device with disturbance assisted seed-filling. *Trans. Chin. Soc. Agric. Mach.* **2022**, *53*, 50–59. (In Chinese with English Abstract)
15. Li, Y.; Yang, L.; Zhang, D.; Cui, T.; Zhang, K.; Xie, C.; Yang, R. Analysis and test of linear seeding process of maize high speed precision metering device with air suction. *Trans. Chin. Soc. Agric. Eng.* **2020**, *36*, 26–35. (In Chinese with English Abstract)
16. Zhao, S.; Chen, J.; Wang, J.; Chen, J.; Yang, C.; Yang, Y. Design and Experiment on V-groove dialing round type guiding-seed device. *Trans. Chin. Soc. Agric. Mach.* **2018**, *49*, 146–158. (In Chinese with English Abstract)
17. Gao, Z.; Lu, C.Y.; Li, H.W.; He, J.; Wang, Q.J.; Huang, S.H.; Li, Y.X.; Zhan, H.M. Measurement method of collision restitution coefficient between corn seed and soil based on the collision dynamics theory of mass point and fixed surface. *Agriculture* **2023**, *12*, 1611. [CrossRef]
18. Li, H.; Li, Y.; Tang, Z.; Xu, L.; Zhao, Z. Numerical simulation and analysis of vibration screening based on EDEM. *Trans. Chin. Soc. Agric. Eng.* **2011**, *27*, 117–121. (In Chinese with English Abstract)
19. Li, X.P.; Zhang, W.T.; Xu, S.D.; Ma, F.L.; Du, Z.; Ma, Y.D.; Liu, J. Calibration of collision recovery coefficient of corn seeds based on high-speed photography and sound waveform analysis. *Agriculture* **2023**, *13*, 1677. [CrossRef]
20. Wojtkowski, M.; Pecen, J.; Horabik, J.; Molenda, M. Rapeseed impact against a flat surface: Physical testing and DEM simulation with two contact models. *Powder Technol.* **2010**, *198*, 61–68. [CrossRef]
21. Li, J.; Su, N.; Hu, J.; Yang, Z.; Sheng, L.; Zhang, X. Numerical analysis and experiment of abrasive flow machining microhole structure based on CFD-DEM coupling. *Trans. Chin. Soc. Agric. Eng.* **2018**, *34*, 80–88. (In Chinese with English Abstract)
22. Chen, Y.; Geng, R.; Ma, L. Design and selection of fluid viscous devices for shock control of bridges. *China Civ. Eng. J.* **2007**, *40*, 55–61. (In Chinese with English Abstract)
23. Elsinawi, A.H.; Jhemi, A.; Alhamaydeh, M. Adaptive seismic isolation of structures using MR-fluid dampers. In Proceedings of the 2013 5th International Conference on Modeling, Simulation and Applied Optimization, ICMSAO 2013, Hammamet, Tunisia, 28–30 April 2013.
24. Jia, J.; Shen, X.; Du, J.; Wang, Y.; Hua, H. Design and experimental research on fluid viscous dampers. *Chin. J. Mech. Eng.* **2008**, *44*, 194–198. (In Chinese with English Abstract) [CrossRef]
25. Park, B.; Lee, Y.; Park, M.; Ju, Y.K. Vibration control of a structure by a tuned liquid column damper with embossments. *Eng. Struct.* **2018**, *168*, 290–299. [CrossRef]
26. Zhang, C.-H.; Wang, Y.; Du, J.-Y.; Wen, Z.-D. Effect of power-law fluid damping in a shock isolation system. *J. Ship Mech.* **2015**, *19*, 975–981. (In Chinese with English Abstract)
27. Ma, J.; Liu, D.; Chen, X. Experimental study of oblique impact between dry spheres and liquid layers. *Phys. Rev. E Stat. Nonlinear Soft Matter Phys.* **2013**, *88*, 033018. [CrossRef] [PubMed]
28. Ma, J.; Liu, D.; Chen, Z.; Chen, X. Agglomeration characteristics during fluidized bed combustion of salty wastewater. *Powder Technol.* **2014**, *253*, 537–547. [CrossRef]
29. Lee, K.Y.; Mooney, D.J. Alginate: Properties and biomedical applications. *Prog. Polym. Sci.* **2012**, *37*, 106–126. [CrossRef]
30. Zhu, J.; Marchant, R.E. Design properties of hydrogel tissue-engineering scaffolds. *Expert Rev. Med. Devices* **2011**, *8*, 607–626. [CrossRef]
31. Li, W.C.; Qiao, K.; Zheng, Y.D.; Yan, Y.; Xie, Y.J.; Liu, Y.; Ren, H.M. Preparation, mechanical properties, fatigue and tribological behavior of duble crosslinked high strength hydrogel. *J. Mech. Behav. Biomed. Mater.* **2022**, *126*, 105009. [CrossRef] [PubMed]
32. Ling, L.; Wu, G.W.; Wen, C.K.; Xiao, Y.J.; Fu, W.Q.; Dong, J.J.; Ding, J.H.; Meng, Z.J.; Yan, B.X. Influence of speed measurement method on performance of an electric-drive maize precision planter. *Biosyst. Engineering.* **2024**, *238*, 175–187. [CrossRef]
33. Wittmer, J.P.; Xu, H.; Benzerara, O.; Baschnagel, J. Fluctuation-dissipation relation between shear stress relaxation modulus and shear stress autocorrelation function revisited. *Mol. Phys.* **2015**, *113*, 2881–2893. [CrossRef]
34. Li, Y.; Yang, L.; Zhang, D.; Cui, T.; He, X.; Du, Z.; Wang, D. Performance analysis and structure optimization of the maize precision metering device with air suction at high-speed condition. *Trans. Chin. Soc. Agric. Eng.* **2022**, *38*, 1–11.

agriculture

MDPI

Article

Design and Experiment of the Profiling Header of River Dike Mower

Mingsheng Li [1,*], Yulin Yan [1], Lin Tian [2], Xingzheng Chen [1] and Fanyi Liu [1]

[1] College of Engineering and Technology, Southwest University, Chongqing 400715, China; yanyulin2023@email.swu.edu.cn (Y.Y.); chenxzh@swu.edu.cn (X.C.); liufanyi2018@swu.edu.cn (F.L.)
[2] College of Engineering, China Agricultural University, Beijing 100091, China; tianlin2022@126.com
* Correspondence: lms040709321@swu.edu.cn

Abstract: Drawing upon advancements in profiling technology, this paper presents an innovative lateral profiling mechanism for the header to improve mowing efficiency and the ability to adapt to terrain for river dike mowers. It delves into the imitation principle and forced situations. Furthermore, a novel lawn protection boot design has been introduced, capable of adjusting mowing heights with swift transitions. The structural integrity of this boot has been optimized through rigorous finite element analysis. Meanwhile, the rolling shaft and cutter have been carefully selected and designed, with a mechanical model of the cutter established to examine its motion and force characteristics. In addition, hydraulic circuits tailored to fulfill the required functions of the header have been devised, and key hydraulic components have been appropriately selected. Key components are subjected to finite element analysis by using ANSYS to verify and optimize their structural strength. Prototype testing and field trials are subsequently conducted, revealing that the mower can achieve a mowing speed of 0.85 m/s on flat ground and a 25-degree slope, thereby fulfilling the design requirements for mowing speed. The imitation mechanism adapts to different embankment terrains. Notably, the lawn protection boots offer adjustable mowing heights of 10.4 cm, 12 cm, and 14 cm, respectively, with a height adjustment range of approximately 2 cm for each position, meeting the requirement for adjusting mowing heights. In addition, the transition time between different positions of the lawn protection boots is less than 5 min, achieving rapid switching and operational efficiency. Furthermore, a mowing uniformity test is conducted by using a header equipped with profiling functionality. The results reveal that the mowing effect of the profiling header meets design requirements, demonstrating its effectiveness and reliability in agricultural applications.

Keywords: mower; profiling header; lawn protection boot; simulation analysis; experiment

Citation: Li, M.; Yan, Y.; Tian, L.; Chen, X.; Liu, F. Design and Experiment of the Profiling Header of River Dike Mower. *Agriculture* **2024**, *14*, 1188. https://doi.org/10.3390/agriculture14071188

Academic Editor: Xiaojun Gao

Received: 20 June 2024
Revised: 15 July 2024
Accepted: 16 July 2024
Published: 19 July 2024

1. Introduction

China, renowned for its extensive river networks, attributes substantial investments dedicated to river flood control annually, particularly in the field of embankment construction and reinforcement [1,2]. The total length of these constructed embankments in China stands at an impressive 413,676 km, among which a significant portion of these embankments, specifically those rated at Grade 5 or higher, spans an outstanding 275,495 km. Thus, the rigorous management and construction of these river embankments play a pivotal role in effectively mitigating the risks of flooding disasters and embankment breaches, therefore fostering national economic development and safeguarding lives and properties of the populace [3].

Notably, research has demonstrated the crucial role of vegetation in stabilizing river embankments [4]. To mitigate the deleterious effects of rainfall erosion and subsequent damage to embankments, grass-covering techniques have traditionally been the frontline approach for embankment preservation [5–8]. Nevertheless, if vegetation becomes overly tall and dense, it can hinder the timely identification of seepage, rodent burrows, ant nests, and breaches, thereby posing serious threats to flood prevention efforts. Consequently, the implementation of regular maintenance and lawn care practices has been paramount [9]. However, the existence of challenges such as excessive embankment slopes, loose soil, and uneven terrain has posed significant difficulties in maintaining the integrity of these vegetable barriers [10].

Therefore, the embankment mower, a specialized type of mower characterized by large header dimensions, long cutting width, and high mowing efficiency, can serve as a useful tool for embankment maintenance. Although the range of available mowers is diverse, few have met the stringent requirements for embankment mowing with imitation capabilities [11–14]. Furthermore, existing mowers have often struggled with issues such as sluggish height adjustments, cumbersome operational processes, inconvenient replacement of lawn protection boots, and damage to embankment lawns during mowing operations [15–18]. As for the application of imitation technology in mowers, researchers are mainly attracted by two distinct types: mechanical structure imitation and hydraulic imitation. On the one hand, mechanical structure imitation primarily relies on sliding panels, mechanical lifting devices, and special mechanical structures to achieve imitation. For one thing, the imitation of sliding panels falls under the category of passive imitation, employing a straightforward structure that adjusts the distance between the cutter and the ground by swapping out sliding panels. As an example, the R0212 mower, designed by the German company Neumeister, incorporates sleeve wrenches and threaded rods to precisely adjust the height of the cutting unit, thereby fulfilling the imitation goal of altering the distance from the sliding panel [19]. For another, the imitation through lifting devices involves elevating the components of the mower to achieve the desired imitation. Many of these products rely on the balancing effect of springs to achieve floating imitation. Wu et al., for instance, have developed a small, self-propelled mower trimmer that utilizes the deformation of profiling springs to achieve floating imitation on uneven terrain [20]. Hydraulic profiling, on the other hand, represents an active profiling method, leveraging hydraulic mechanisms to lift the cutting device and achieve profiling.

The present paper is dedicated to addressing the challenges posed by embankment mowers, which suffer from inadequacy in profiling capability, incompetence in adjusting mowing heights, incapability in lawn protection boot switching, and dilemmas in embankment lawns. The study, with a focus on enhancing operational efficiency, proposes an innovative imitation solution alongside an optimized design for lawn protection boots to ensure the cleanliness of embankment lawns, elevate the imitation capabilities of river dike mowers, and safeguard embankment safety. Thorough optimization has been conducted on various components, including the header bracket, cutters, and transmission components, leading to the creation of a profiling-capable header and the implementation of adjustable mowing heights. Therefore, these advancements culminate in the successful prototyping of the entire machine. To further validate the effectiveness of the novel design, extensive field experiments have been conducted on the embankments of the Yellow River. These tests concentrate on evaluating the imitation capabilities, precision of mowing height adjustment, and protection of the lawn by the optimized header. The ultimate objective of this research is to provide both technical support and a robust theoretical framework that can be leveraged to further advance the field of mower imitation technology.

2. Materials and Methods

2.1. Machine Structure and Operational Fundamentals

The river dike mower is composed primarily of four distinct components: the walking chassis, the header support, the profiling mechanism, and the mowing device, as depicted in Figure 1. Firstly, the tracked chassis serves as the foundation, supporting the weight of the entire machine and facilitating the movement of the header for grass cutting. Secondly, the header support, in conjunction with the lifting hydraulic cylinder, allows for precise adjustment of the header's elevation, ensuring optimal cutting performance. Thirdly, the profiling capabilities of the mower are categorized into lateral and longitudinal profiling.

Noticeably, lateral profiling is primarily achieved through a meticulously designed mechanical structure, while longitudinal profiling is facilitated by the controlled movement of the lifting hydraulic cylinder. Fourthly, the mowing device, situated on the header, is the heart of the mowing process, with internal blades rotating at high speeds to shear the grass through centrifugal force. In this study, we also focus on the development and application of "Lawn Protection Boots," a specialized footwear designed to minimize damage to grass surfaces during maintenance and other activities on turf areas. Finally, the lawn protection boots serve as a crucial interface between the mower's header and the lawn surface, which not only protects the integrity of the lawn but also allows for fine-tuning of the mowing height. The engine chosen for this mower is a water-cooled, four-stroke, three-cylinder model known as the 3TNV88, manufactured by Yanmar Engine (Qingdao, China) Co. Table 1 summarizes the key structural parameters that govern the performance and functionality of this agricultural machinery.

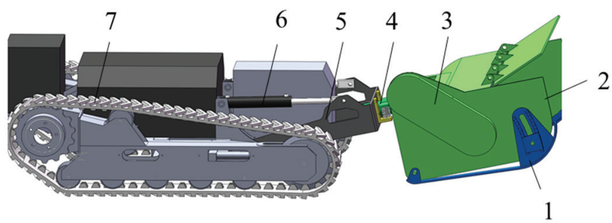

Figure 1. The overall structure of the river dike mower: 1. Lawn protection boots; 2. Mowing device; 3. Hydraulic motor; 4. Profiling mechanism; 5. Header support; 6. Lifting hydraulic cylinder; 7. Crawler chassis.

Table 1. Key structural parameters of river dike mowers.

Parameter Name	Parameter Value
Engine type	Yanmar 3TNV88
Engine power (kW)	20
Dimensions length/width/height (mm)	2900/1570/1000
Mass (kg)	880
Number of cutter circumferences (blade)	4
Number of cutter axes (blade)	9
Mowing range (mm)	1300
Hydraulic motor type	BMR50

2.2. Design of Key Components

2.2.1. Design of Lifting Mechanism

The lifting mechanism of the header incorporates three components: the base, the hydraulic cylinder, and the header support. The function of this mechanism lies in its ability to efficiently raise and lower the header. Notably, during the lifting and lowering process, the mower does not perform mowing operations. During mowing, the hydraulic cylinder incorporates a strategic amount of float, thus enabling longitudinal profiling and enhancing mowing precision. This structure is clearly depicted in Figure 2a.

Let us consider the geometric relationships within this mechanism by assuming that the angle between the header support AC and the horizontal direction is a, and the angle between the hydraulic cylinder BC and the vertical direction is a_2. Furthermore, when the piston rod of the hydraulic cylinder is fully retracted, the length of BC is L_{BC0}. Additionally, let L_{BC0} be the length at which the piston rod starts to extend from the inner end of the hydraulic cylinder. Based on these geometric relationships, a comprehensive geometric model is constructed, as illustrated in Figure 2b.

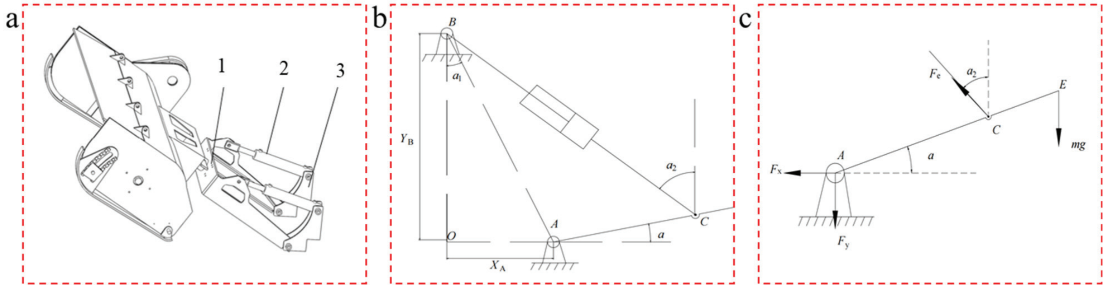

Figure 2. Design of the header lifting mechanism: (**a**) Structure configuration of the header lifting mechanism: 1. Header support, 2. Lifting hydraulic cylinder, 3. Base; (**b**) Sketch map of the header lifting mechanism; (**c**) Force analysis diagram of the header support.

In triangle ABC, there exists the following:

$$\begin{cases} (L_{BC0} + x) \cdot \sin\alpha_2 = L_{AB} \cdot \sin\alpha_1 + L_{AC} \cdot \cos\alpha \\ L_{AB} \cdot \cos\alpha_1 = (L_{BC0} + x) \cdot \cos\alpha_2 + L_{AC} \cdot \sin\alpha \end{cases} \tag{1}$$

The following can be derived from Formula (2):

$$\alpha = \arcsin\frac{(L_{BC0} + x)^2 - {L_{AB}}^2 - {L_{AC}}^2}{2L_{AB} \cdot L_{AC}} + \alpha_1 = f(x) \tag{2}$$

in the following formula: $L_{AB} = \sqrt{x_A^2 + y_B^2}$, $\alpha_1 = \arctan\frac{x_B}{y_B}$.

L_{AB} is the distance between the upper and lower articulation points on the support, L_{AC} is the distance between the lower articulation point on the base and the articulation point on the header support, α_2 is the angle between the line connecting the upper articulation point on the base as well as the lower articulation point on the hydraulic cylinder and the vertical direction, and $f(x)$ is the function of the hydraulic cylinder's extension displacement x.

The force situation of the header support in the vertical direction is elaborated in Figure 2c. The force and moment equilibrium equations of the header support are as follows:

$$\begin{cases} F_e \cdot \cos\alpha_2 - mg - F_y = 0 \\ F_e \cdot \sin\alpha_2 - F_x = 0 \\ F_e \cdot L_{AC} \cdot \cos(\alpha_2 - \alpha) - L_{AD} \cdot mg \cdot \cos\alpha = 0 \end{cases} \tag{3}$$

In the formula, F_x is the horizontal force at the articulation point between the header support and the base, F_y is the vertical force at the articulation point, m is the mass of the header, F_e is the force exerted by the hydraulic cylinder, L_{AC} is the distance between the articulation point of the header support and the base and the articulation point on the hydraulic cylinder, and L_{AD} is the distance between the articulation point of the header support and the base and the connection point between the support and the header.

2.2.2. Design of Mowing Device

The Y-type swing blade stands out due to its diverse and notable characteristics, which includes its exceptional impact resistance, double-sided blade, wear resistance, formidable crushing ability, and uniform force distribution. This blade type has found widespread application in a range of mowers. Given its distinguished performance profile, the Y-type cutter, depicted in Figure 3a, has been selected as the primary blade for this study.

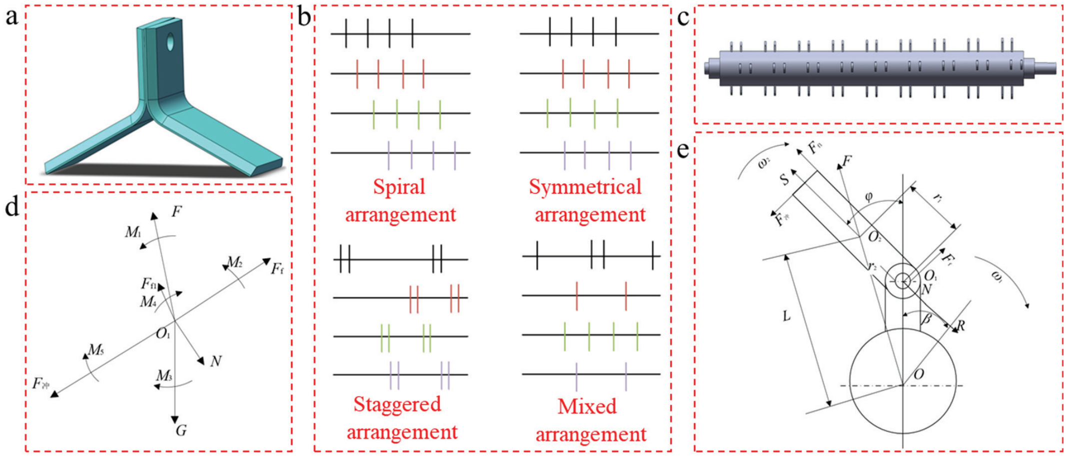

Figure 3. Design of the mowing device: (**a**) Schematic diagram of cutter structure; (**b**) Arrangement of cutters; (**c**) Structure of the rollers; (**d**) Torque diagram of the cutter; (**e**) Force diagram of the cutter.

When configuring the blade arrangement on the roller, it is imperative to ensure that no cuts are missed during the mowing process and that there is no potential for blockages or interference among the blades. The typical blade arrangements include spiral, symmetrical, staggered, and symmetrical staggered configurations, as exemplified in Figure 3b. Among these four arrangements, the symmetrical layout offers uniformity in blade spacing, resulting in even stress distribution across the roller during rotation. Additionally, this arrangement simplifies the assembly process. Consequently, the roller of this mower has been designed with a symmetrical blade arrangement.

To determine the optimal number of cutters, it is of great significance to take careful consideration of the roller's length and arrangement. An insufficient number of cutters can lead to missed cuts, compromising mowing efficiency. Conversely, an excess of blades can increase the torque and startup power of the roller, potentially resulting in blockages and entanglement issues. Hence, the number of cutters needs to be designed rationally [21]. Typically, the number of cutters is calculated using the following formula:

$$n = L_T \delta \tag{4}$$

In the formula, n is the total number of cutters (piece), δ is the cutter density (piece/mm), straight blades are generally taken as 0.05 to 0.07 piece/mm, T-shaped blades are generally taken as 0.01 piece/mm, and L_T is the distribution length of cutters on the roller, mm.

By substituting L_T = 1400 mm into the equation, the number of cutters can be calculated as n = 36 pieces. The result is exhibited in Figure 3c.

The roller speed is a crucial parameter in the performance of the mower. Once the roller speed attains an optimal level, the cutters can execute an efficient cutting process [22]. Furthermore, the roller speed is intricately linked to the determination of the appropriate speed for the power mechanism, thereby emphasizing the necessity for a judicious choice of the roller speed [23]. Generally, the roller speed can be accurately determined through the application of Equation (5).

$$n_1 = \frac{30(v_a + v_m)}{\pi R_s} \tag{5}$$

In the formula, v_a is the cutting speed of the blade (m/s), v_m is the operating speed of the mower (m/s), and R_s is the rotational radius of the cutter root edge (m).

Research has embodied that to achieve effective cutting, the minimum linear velocity at the cutter root edge should not be less than 10 m/s, while the cutting speed of the cutter edge generally ranges from 20 to 50 m/s [23]. Take v_a = 25 m/s as an example. In this case, the forward speed of the mower is taken as v_m = 0.8 m/s, and the rotational radius at the root is R_s = 120 mm. Substituting these values into Equation (5), we obtain n_1 = 2054 r/min. Thus, the speed of the shaft is taken as 2100 r/min.

During the operational phrase, a force analysis of the cutter's motion state has been conducted, as illustrated in Figure 3d,e. The forces acting on the cutter mainly consist of the gravitational force G of the cutter, the centripetal force S generated by the rotation of the cutter around the pin axis, the centripetal force F generated by the rotation of the cutter around the central axis, the normal pressure force N exerted on the connection point between the pin axis and the cutter, as well as the impact force F_t exerted by vegetation and soil on the front of the cutter during collision cutting and the frictional force F_{f1} between vegetation and the cutter. The formulas for quantifying the impact force and frictional force, particularly when contaminants such as weeds and soil collide with and rub against the cutter, are as follows:

$$F_t t = M \Delta v \tag{6}$$

$$F_1 = \mu F_t \tag{7}$$

In the formula, M is the weight of impurities at the time of colliding (kg), Δv is the linear velocity difference at the time of colliding (m/s), t is the colliding time (s), and μ is the coefficient of friction between the cutter and the impurities.

At the rotational center point O_1 of the cutter, the following exists:

$$m_1 r_1 R \omega_1^2 \sin\phi + F_f r_2 - m_1 g \sin(\omega_1 t + \phi) - F_t t - \frac{1}{2} F_{f_1} \beta = 0 \tag{8}$$

The critical angle at which the cutter is relatively stationary to the center O_1 of the pinhole is $\varphi \approx 1.4^\circ$. By substituting the various parameters of the cutter into Equation (8) we can accurately determine the precise pressure applied by the pin on the cutter, along with other pertinent values, at any specific moment in time.

2.2.3. Design of the Profiling Mechanism

The lateral profiling mechanism and its primary operational process are outlined in Figure 4a–c. When both ends of the header encounter minor bumps or pits in the terrain, the imbalance between the header and the ground surface triggers a rotational movement around the pivot axis. This rotational stability is maintained by a pair of springs, one in compression and the other in tension, jointly maintaining the overall equilibrium of the header. Specifically, if the left end of the header encounters a minor protrusion as the pivot axis rotates, the left spring assumes a tensile state, while the right spring compresses. Similarly, when the right end of the header encounters a bump or depression, the profiling mechanism responds with the corresponding lateral adjustment. This adaptive profiling is achieved through the concurrent stretching and compression of the springs at both ends, along with the rotational movement of the pivot axis, effectively delivering lateral profiling functionality at both extremities of the header.

The longitudinal profiling mechanism and its primary operational process are visualized in Figure 4d–f. As the mower traverses terrain with significant elevation, the hydraulic cylinder initiates a retraction action. Conversely, when the mower encounters a deep depression in the soil, the hydraulic cylinder extends outward, thereby enabling profiling functionality in the longitudinal direction. This adaptive behavior ensures that the mower maintains optimal contact with the ground, regardless of the terrain's irregularities.

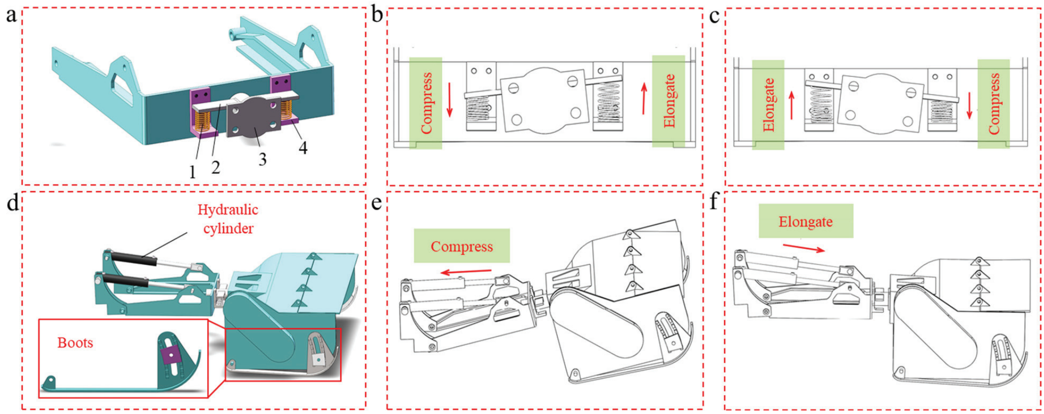

Figure 4. Design of the profiling mechanism: (**a**) Schematic diagram of the transverse profiling mechanism: 1. Spring, 2. Upper guard plate, 3. Header connecting plate, 4. Lower support; (**b**,**c**) Operational status of the transverse profiling mechanism; (**d**) Schematic diagram of longitudinal profiling mechanism; (**e**,**f**) Operational status of the longitudinal profiling mechanism.

2.2.4. Design of Hydraulic System

The design principle of hydraulic system for controlling the header lifting is illustrated in Figure 5. Initially, the electromagnetic valves 5 and 6 are set in their appropriate positions. As the header encounters a raised road surface, the hydraulic cylinder piston rod retracts. This retraction triggers a sequence of events: the oil flows through the appropriate side of electromagnetic valve 5, then passes through check valve 8, and ultimately returns to the oil tank through the hydraulic cylinder. Conversely, upon encountering a depressed road surface, the piston rod extends. At this point, oil pumped from the hydraulic cylinder passes through throttle valve 7, then flows through the right position of the electromagnetic valve 6, and finally returns to the oil tank. These two circuits are pivotal in achieving the longitudinal profiling functionality required for traversing embankment terrain. When it becomes necessary to lift the header, electromagnetic valve 5 is actuated to the left position. This allows the oil to flow from the hydraulic pump 2, through electromagnetic valve 5, then through check valve 8, and into the hydraulic cylinder. Once the oil passes through the cylinder, it returns to the oil tank. Conversely, for lowering the header, triggered by the activation of the stroke switch, electromagnetic valve 6 is shifted to its left position, facilitating their respective limit positions. This ensures that the lifting or lowering of the header is precisely controlled and halted at the desired heights.

The principal hydraulic components of the lawn mower comprise hydraulic motors dedicated to propulsion and cutter rotation, a hydraulic pump, cylinders, a reservoir, and valves, of which the meticulous calculation and selection of these components are paramount to ensure optimal performance [24].

When it comes to hydraulic motors, the mower features both a traveling hydraulic motor and a blade rotation hydraulic motor. While the selection and calculation for the motor that rotates the cutter have already been addressed in a prior section, the focus now shifts to the selection and calculation of the propulsion hydraulic motor [25,26].

The torque required for the crawler drive is precisely known to be 1963.5 N·m, with a reduction ratio of 6 for the crawler section. As a result, the output torque of the hydraulic motor only needs to exceed M_k = 327.25 N·m to fulfill the power requirements. The displacement V of the traveling hydraulic motor can typically be determined using the following standard formula:

$$V = \frac{2\pi M_k}{p\eta} \tag{9}$$

In the formula, p is the working pressure of the mower's hydraulic system, and we assume it to be 20 MPa, and η is the volumetric efficiency of the high-speed hydraulic motor and we adopt a value of 0.9.

The maximum speed of the hydraulic motor is generally calculated by the following formula:

$$v_{max} = 2\pi r_d n_{max} \cdot 60 \tag{10}$$

In the formula, v_{max} is the maximum speed of the mower, and we assume it to be 12 km/h, n_{max} is the rated maximum speed of the hydraulic motor (r/min), and r_d is the selected drive radius of the crawler, and we set it to be 160 mm.

Put each value into the calculation to obtain $V \approx 120$ mL/r, and $n_{max} \approx 200$ r/min. Both the selected hydraulic motor displacements should meet 120 mL/r; and the maximum rated speed is 200 r/min. Based on various parameters of the mower's movement, the hydraulic motor model BMR50 is selected as the traveling hydraulic motor.

Furthermore, other types of hydraulic components, including pumps, tanks, and valve components, are selected according to the required functionalities and parameters. This selection is made according to comprehensive operational analysis, considering both the practicality and cost-effectiveness of the various options. The detailed breakdown of the selection process for the various hydraulic components can be found in Table 2.

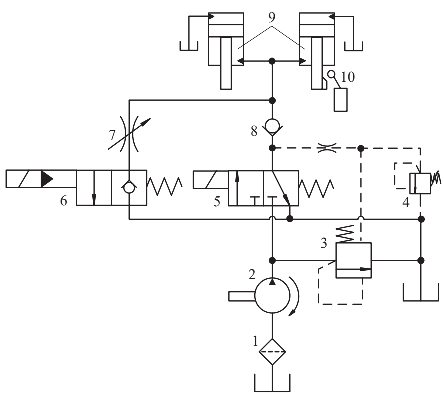

Figure 5. Design of hydraulic system for header elevation control: 1. Oil filter; 2. Positive displacement hydraulic pump; 3. Differential pressure relief valve; 4. Safety valve; 5. Two-position three-way solenoid directional valve; 6. Two-position two-way solenoid directional valve; 7. Throttle valve; 8. Check valve; 9. Header lifting hydraulic cylinder; 10. Stroke switch.

Table 2. Main hydraulic components selection of mower.

Hydraulic Components	Parameters
The cutter rotation hydraulic motor	M4MF37-32 series axial piston hydraulic motor
The walking hydraulic motor	BMR50 series hydraulic motor
Hydraulic pump	Closed-loop triple gear pump: M4PV28-28S228AR3BJR-557 + 2 HMPZA12RTXGSGAPMM1
Check valve	DIF-L20H1
Oil tank	250L

2.3. Experiment Scheme

2.3.1. Simulation Experiment

As the lawn protection boot serves as the principal component responsible for transmitting forces between the header and the ground, this present study employs the software

ANSYS2020 Workbench to perform a rigorous static analysis and optimization of the key structures of the boot. The mesh size is set to 2.437 mm. Furthermore, the material properties utilized in the study are outlined in Table 3.

Table 3. Material property settings.

Type of Material	Density P/kg·m^{-3}	Modulus of Elasticity E/MPa	Poisson's Ratio	Strength of Yield σ_s/MPa
Q235	7850	200,000	0.3	235

To access the dynamic behavior of the mower, which is the pivotal working unit, motion simulation analysis is conducted using the software ADAMS2020 [27]. Specifically, the roller shaft is configured with a rotational constraint, simulating a rotational speed of 2600 rpm, equivalent to the nominal operating speed of the mower. The simulation duration is set to 0.01 s, with a total of 5000 steps, ensuring a detailed and accurate representation of the mower's operational dynamics.

2.3.2. Field Experiment

The experiment site is located on the river dike of the Yellow River, specifically in Mengjin County, Luoyang City, Henan Province, China, positioned at 34 degrees north latitude and 112 degrees east longitude. The experiment was performed beneath a clear sky. The river dike, an artificially constructed embankment, exhibits a slope ranging from 10 to 30 degrees and boasts a width of 3 to 5 m. The grass species within this locale are mainly composed of ryegrass, carpet grass, bermudagrass, and step grass, maintaining an average height of 23.2 cm and an average diameter of 40 mm.

- Test contents: The specific experiments include verifying the mower's mowing speed [28], validating mowing productivity [29], testing the uniformity of mowing with and without profiling conditions, and analyzing the effect of the lawn protection boot at three different height adjustment positions during mowing.
- Test equipment: The key component is the prototype mower, other vital equipment includes a smartphone, a tape measure for accurate measurements (DELI with a range of 10 m and precision markings at the millimeter level), an angle gauge for assessing slopes (SOUTHERN JZC-B2 and measuring accuracy 1 Degree), a stopwatch for timing (CASIO HS-70W accurate to 1/100 s), and a marker bar for designation.
- Test methods: For the conduct of the experiment, a five-point sampling technique, also recognized as the diagonal method, is employed. This technique involves the selection of a uniformly spaced grassy area along the bank and the subsequent division of this area into five small rectangular sections arranged diagonally. The centers of four sample points are positioned equidistant from the center point on each diagonal. Each designated sample point encompasses an area of 0.25 square meters. The experiments are conducted on flat terrain and on slopes of 25 degrees, and the duration required for mowing each sample point is meticulously recorded [30,31]. The following is about validation test design:

(1) The experimental design for the mowing speed and productivity:

Mowing speed and productivity are fundamental performance indicators of the mower during normal operational conditions. Only when these two parameters meet the design requirements can the mower be considered as compliant with the required performance criteria. Consequently, it is necessary to conduct experimental verification and analysis on both parameters.

(2) The experimental design for a mowing height test in three gears of a lawn protection boots:

To ascertain the optimal mowing height for each gear, three distinct sections of embankment grassland are selected, ensuring similar terrain conditions and uniform grass height density across all test sites. The lawn protection boots are installed at gears one, two, and three, respectively, for mowing tests. After every two meters of mowing, the remaining stubble height is measured five times to ensure accurate data collection. The collected data are then organized into a comparative chart, allowing for a visual analysis of the remaining stubble heights across the three lawn protection boot positions.

(3) The experimental design for comparing the uniformity of mowing with and without contour-following conditions on the header:

Two embankment grasslands, each 10 m in length and exhibiting slight unevenness, are selected as test sites. Both grasslands possess identical grass density, height, and other relevant parameters, facilitating a fair comparison between the two conditions. Initially, the mower without the profiling mechanism is tested on Grassland One. Following the mowing process, the stubble height is measured at 2-m intervals, totaling 5 sampling points. The same procedure is repeated with a mower equipped with the profiling mechanism on Grassland Two, with the stubble height at 2-m intervals to obtain another set of data.

3. Results and Discussion

3.1. Analysis of Simulation Results

The header exhibits a gravity load of 160 kg, bearing a lawn protection boot force of 1600 N. Given the structural characteristics of the lawn protection boots, one end has borne 1000 N while the other has borne 600 N, as manifest in Figure 6a. As illustrated in Figure 6b,c, the maximum stress on the sliding boots has reached 137.57 MPa, accompanied by a maximum deformation of 0.35 mm, indicating notable regions of stress concentration. To alleviate stress concentration and streamline the design, a thorough optimization of the lawn protection boot's structure is required. A range of optimization methods, including shape optimization, structural topology optimization, and dimension optimization, are available. For this specific optimization, dimension optimization and shape optimization are chosen. The optimization process involves making strategic modifications to the design. Small blocks are excised from the locking points of the lawn protection boots and replaced with three pairs of locking holes. This approach reduces the weight and overall dimensions of the lawn protection boots, thereby simplifying the installation process. The simulation analysis of the optimized lawn protection boot structure reveals intriguing results. As presented in Figure 6d–i, the highest stress points consistently occur at the juncture between the bottom support plate and the base plate of the boots across gears one, two, and three. In gears one and two, the maximum deformation occurs at the apex of the upper support plate, while in gear three, the point of maximum deformation shifts to the highest point of the boot base. As the gear levels progress, both the maximum stress and total deformation exhibit a decreasing trend. Across all three gear levels, the peak stress recorded is 44.52 MPa. This value falls well within the yield strength of the material Q235 used for the lawn protection boots, which is rated at 235 MPa. Thus, the optimized design meets the required standards, ensuring durability and reliability in agricultural applications.

After enhancing the design of the lawn protection boots, a substantial reduction in stress and deformation is observed. According to the comparison of stress and deformation cloud maps before and after the improvements [32], the maximum stress exerted on the boots decreases significantly, from 135.57 MPa to 44.52 MPa, representing a notable drop of 91.05 MPa. Similarly, the maximum deformation also decreases markedly, dropping from 0.35 mm to 0.11 mm, a momentous reduction of 0.24 mm. These findings clearly indicate that the stress concentration within the lawn protection boots has been significantly mitigated, highlighting the effectiveness of the enhancements made.

The kinematic simulation model of the mower device is depicted in Figure 7a. As evident in Figure 7b–d, the mower undergoes a start-up phase ranging from 0 to 0.005 s, during which there are significant fluctuations in the blade speed. Subsequently, the blade speed gradually stabilizes and eventually converges to approximately 2600 rpm, closely matching the roller speed. Similarly, the highest and lowest points of the blade exhibit comparable fluctuations. Although the trajectory of the blade tip initially appears irregular, it ultimately stabilizes into a circular motion centered around the roll axis. This observation suggests that the cutters on the roller are arranged and distributed in a uniform and reasonable manner, fulfilling the requirements for high-speed mower operation.

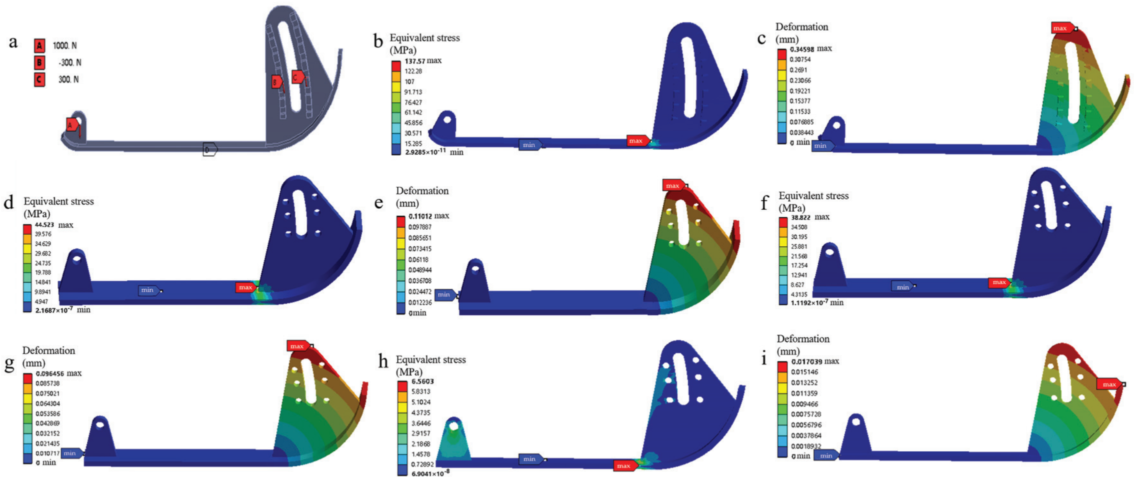

Figure 6. Static analysis of the lawn protection boots: (**a**) Load and constraint settings of the lawn protection boot; (**b**,**c**) Equivalent stress and deformation contour plots of the lawn protection boot; (**d**–**i**) Equivalent stress and deformation contour plots of the optimized lawn protection boot in gears one through three.

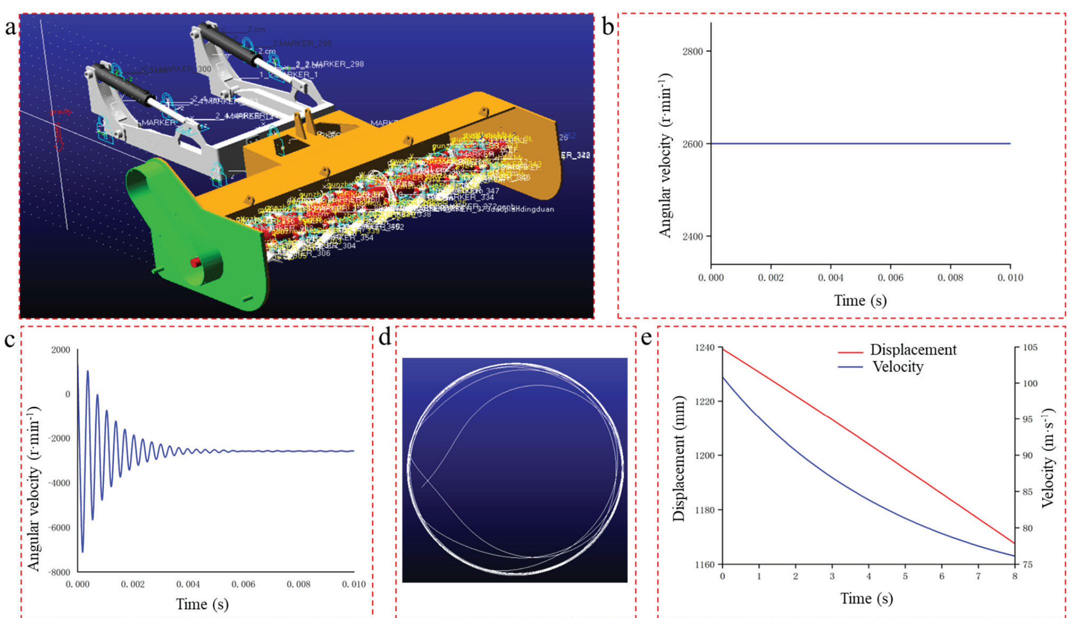

Figure 7. Kinematic simulation analysis of the header: (**a**) Results of simulation model construction; (**b**) Variation of roller shaft angular velocity; (**c**) Variation of the cutter center angular velocity; (**d**) Motion trajectory curve of blade tip; (**e**) Velocity and displacement curves at the centroid of the header.

To further validate the rationality of the mower lifting mechanism design, a simulation analysis of the mower lifting mechanism can be conducted [33]. This simulation thoroughly examines the motion characteristics of the header during the lifting process, thereby verifying the functionality of the lifting mechanism. The simulation modeling process involves importing the model by adding constraints, kinematic subs, and drivers. Drawing upon the findings of previous conclusion, which indicate that the hydraulic cylinder stroke is 160 mm, and the lifting time should not exceed 10 s, we assume a lifting speed of 20 mm/s for the hydraulic cylinder every 20 mm of upward movement. Consequently, the simulation is executed for a duration of 8 s, divided into 200 discrete steps. By observing the lifting situation of the header, as presented in Figure 7e, we can deduce that during the lifting process, the maximum speed reached is 100.8 mm/s, while the minimum speed is 76.1 mm/s. This comprehensive simulation analysis confirms that the design and parameter selection of the header lifting mechanism align with the intended working conditions and satisfy the designated design requirements.

3.2. Analysis of Field Experiment Results

3.2.1. Mower Mowing Speed and Productivity Experiment Verification

Experimental principle: The operational speed of the mower is calculated according to the following formula, and the average of five measurements is taken at the end:

$$v = \frac{\sum L}{\sum t} \tag{11}$$

In the formula, v is the machine working speed (m/s), $\sum L$ is the total length of the area, which is determined by the experiment (m), and $\sum t$ is time spent (s).

Specific steps: Five 10-m sites are selected on flat ground with a 25° slope. Under normal mower operating conditions, the time taken for mowing is recorded at each sample point. Finally, the speed values of the five sample points on flat ground and the 25° slope are calculated using Formula (11), as presented in Table 4.

Table 4. Mower mowing speed on flat ground and a 25° slope.

Samples	1	2	3	4	5
Level mowing speed/m·s^{-1}	0.63	0.77	0.83	1	0.91
25° slope mowing speed/m·s^{-1}	0.67	0.83	1	1	0.83

The mowing productivity of a mower serves as a key parameter for assessing the effectiveness of its header design, which in turn serves as an indirect indicator of the success of the mower's profiling. The following outlines the methodology for verifying the mowing productivity of a mower:

Experimental principle of mowing productivity of mower:

$$p = \frac{A}{t} \tag{12}$$

In the formula, p is mowing productivity (m^2/s), A is Area of mowing (m^2), and t is mowing time (s).

Specific steps: Five plots of land are selected, including flat ground and featuring a 25° slope, as depicted in Figure 8d. Each plot measures 10 m in length and width, facilitating the conduct of precise mowing experiments. During these experiments, the width of the mower's cutting swath is measured, and the time taken for each mowing session is recorded. These data are then utilized to compute the mowing productivity by using the Formula (12).

The measured width of the mower's cutting swath is determined to be 1.3 m. By substituting these values into Formula (12), the mowing productivity on flat ground and the 25° slope is calculated, respectively, as presented in Table 5.

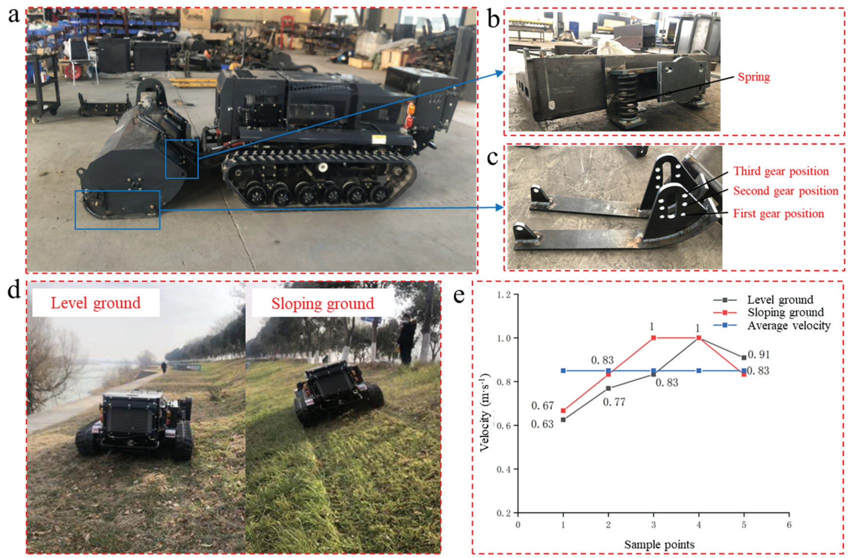

Figure 8. Machine prototype and field experiment: (**a**) Overall machine structural configuration; (**b**) Lateral profiling mechanism; (**c**) Lawn protection boot; (**d**) Flat and sloping ground tests; (**e**) Mowing speed analysis.

Table 5. Mowing productivity of the mower on flat ground and a 25° slope.

Samples	1	2	3	4	5
Flat mowing productivity/$m^2 \cdot h^{-1}$	2925	3600	3900	4680	4255
25° slope mowing productivity/$m^2 \cdot h^{-1}$	3120	4680	4680	4680	3900

The results of the processed prototype mower are presented in Figure 8a–c. Its operating efficiency is evaluated on both flat ground and a 25° slope. The experiment area and the corresponding results are depicted in Figure 8d,e. Notably, the average working speed of the mower on both flat ground and slopes is recorded as 0.85 m/s. This speed falls squarely within the designed mowing speed range of 0.27 m/s to 2.7 m/s, thus fulfilling the designated requirements.

A comparative graph of mowing speeds derives from speed curve graphs plotted for mowing on flat ground with a 25° slope. This is clearly manifested in Figure 8e. From the graph, it can be observed that under normal operating conditions, the mower exhibits nearly identical mowing speed on both flat and sloped terrain. Notably, the speed stabilizes at 0.85 m/s. This speed falls within the predefined mowing speed range of 1 km/h to 10 km/h, thus fulfilling the established design criteria.

The values presented in Table 5 reveal an average mowing productivity of 3872 m^2/h on flat ground and an even higher rate of 4212 m^2/h on a 25° slope. Notably, both of these averages exceed the minimum stipulated requirement of 3000 m^2/h for the mower's designated mowing productivity. Therefore, it can be confidently concluded that the header effectively meets the established design requirements for mowing operations.

The mower's productivity when mowing on a 25° slope is higher compared to flat ground. This is primarily because of its ability to adjust to changes in the terrain's elevation, allowing it to maintain a consistent cutting effect. Additionally, the force of gravity on the slope provides the mower with extra power, resulting in more efficient mowing on sloped surfaces.

3.2.2. Experiment Verification of a Mowing Height Test in Three Gears of Lawn Protection Boots

To assess the functional efficiency of the lawn protection boots, extensive tests have been conducted at three different gear positions, each tailored to varying cutter heights relative to the ground: gear position 1 set at a cutter height of 6 cm, gear position 2 at 8 cm, and gear position 3 at 10 cm.

The results of these tests are depicted in Figure 9a,b. It is observed that the differences in mowing height among the three gears increase at almost the same rate. Specifically, the average stubble height for Gear 1 is recorded as 10.4 cm, Gear 2 exhibited 12 cm, and Gear 3 yielded 14 cm. Notably, the height disparities among the three gears are approximately 2 cm, and the total time required for gear adjustments does not exceed 5 min, thus meeting the design requirement for gear modulation in the boots.

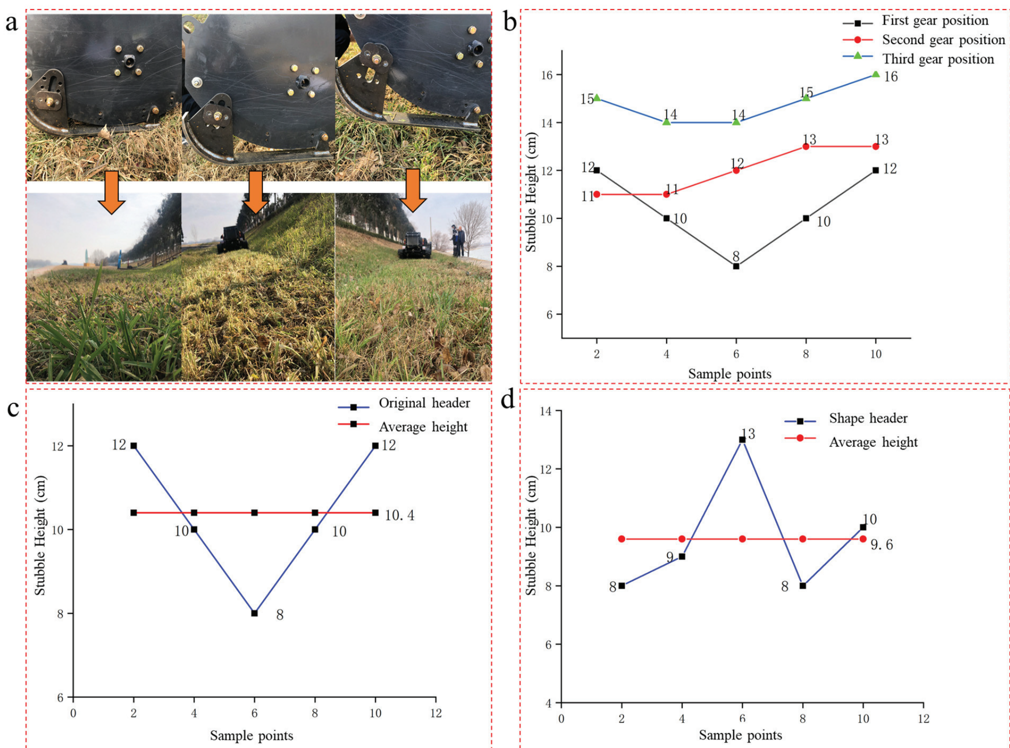

Figure 9. Comprehensive performance experiment of header: (**a**) Effect of three-speed change experiment of lawn protection boot; (**b**) Stubble height after three-speed change of lawn protection boot; (**c**) Stubble height of conventional header operation; (**d**) Stubble height for profiling header operation.

3.2.3. Comparison Experiment of Mowing Uniformity with and without Profiling of the Header

Furthermore, to evaluate the operational effectiveness of the profiling header, a comparative analysis is conducted between a traditional header and the profiling header, as manifested in Figure 9c,d. The stubble heights for platforms devoid of profiling and those equipped with profiling are calculated using Equation (13), yielding values of μ_N = 10.4 cm and μ_Y = 9.6 cm, respectively. In this case, '*N*' and '*Y*' serve as abbreviations, representing platforms without a profiling header and with a profiling header, respectively.

$$\mu = \frac{\sum_{i=1}^{n} x_i}{n} \tag{13}$$

In the formula, μ is the mean stubble height; $\sum_{i=1}^{n} x_i$ is the sum of stubble height; and n is the number of sampled data points.

Then, utilizing the variance calculation Formula (14), we can compute the variance to obtain a value of σ_N^2 = 2.24, and σ_Y^2 = 3.34.

$$\sigma^2 = \frac{\sum_{i=1}^{n} (x_i - \mu)^2}{n} \tag{14}$$

Here, σ^2 is the variance; $\sum_{i=1}^{n}(\mathrm{x_i} - \mathrm{\mu})^2$ is the sum of squares of the differences between each data point and the mean value; and n is the number of sampled data points. Then, using Formula (15), we can obtain the standard deviation of σ_N = 1.497 and σ_Y = 1.828. Finally, we employ the coefficient of variation using Formula (16), and then acquire CV_N = 14.39% and CV_Y = 19.04%. Here, σ is standard deviation; and CV is coefficient of variation.

$$\sigma = \sqrt{\frac{\sum_{i=1}^{n} (x_i - \mu)^2}{n}} = \sqrt{\sigma^2} \tag{15}$$

$$CV = \frac{\sigma}{\mu} \times 100\% \tag{16}$$

After the comparison between the performance data of the profiling headers and non-profiling (traditional) headers, it is evident that the profiling header exhibits a slightly higher standard deviation of 1.828 compared to 1.497 for the non-profiling header. In addition, the coefficient of variation of the profiling header, standing at 19.04%, is also slightly higher than that of the 14.39% of the non-profiling header. These findings indicate that during the mowing process, the performance of the profiling header exhibits relatively greater fluctuations and variability.

A higher standard deviation signifies that the profiling header demonstrates greater variance in the measured data. This may reflect pronounced differences in its performance across diverse conditions or at various times. Moreover, the elevated coefficient of variation further corroborates the relatively unstable performance of the profiling header, which can be attributed to a range of factors, including variations in terrain, crop type, or operating parameters.

The performance data of the profiling header exhibits certain fluctuations; however, it remains within the design specifications for crucial indicators such as mowing height. The fact that the deviation amount remained within the permissible range underscores the overall reliability and practicality of the system.

4. Conclusions

(1) This simulation verifies the functionality of the lifting mechanism by closely analyzing the motion characteristics of the header during the lifting process. Based on this information, we can deduce that the lifting process achieved a peak velocity of 100.8 mm/s and a minimum velocity of 76.1 mm/s. This comprehensive simulation analysis confirms that the design and parameter selections of the header lifting mechanism satisfy the specified design requirements and align with the intended working conditions.

(2) Significantly, the mower maintains a consistent operating speed of 0.85 m/s on both flat and sloping terrain. This velocity falls precisely within the designated range of 0.27 m/s to 2.7 m/s, which is the intended speed for mowing. The findings indicated a significantly greater rate of 4212 m^2/h on a 25° incline, while the average mowing efficiency on flat terrain was 3872 m^2/h. Notably, both of these averages exceed the

minimum stipulated requirement of 3000 m^2/h for the mower's designated mowing productivity, thus fulfilling the designated requirements.

(3) An experiment was conducted to determine the maximum level of gear adjustment for the lawn protection boots. Notably, the height differences between the three gears are only about 2 cm, which meets the design requirement for gear modulation in the boots. When assessing the uniformity of mowing with and without a profiling header, the validation indicates that the former exhibits a slightly greater standard deviation (1.828) compared to the latter (1.497). Essentially, the profiling header adapts to the transformation of river dikes within an acceptable range of variation and meets the design criteria for important factors such as the evenness of mowing.

Author Contributions: Conceptualization, M.L.; methodology, M.L.; software, M.L. and Y.Y.; validation, M.L. and Y.Y.; formal analysis, M.L. and Y.Y.; investigation, M.L., Y.Y. and L.T.; resources, M.L. and L.T.; data curation, M.L.; writing—original draft preparation, M.L., Y.Y. and L.T.; writing—review and editing, X.C. and F.L.; visualization, M.L. and L.T.; supervision, X.C., F.L. and M.L.; project administration, M.L. All authors have read and agreed to the published version of the manuscript.

Funding: This research has been funded by the Chongqing Special Key Project for Technological Innovation and Application Development, under the grant number cstc2021jscx-gksb0003.

Institutional Review Board Statement: Not applicable.

Data Availability Statement: The datasets used and/or analyzed during the current study are available from the corresponding author upon reasonable request.

Conflicts of Interest: The authors declare that they have no conflicts of interest pertaining to the content, execution, or publication of this research.

References

1. *GB 50286-2013*; Code for Design of Embankment Slope Engineering. Ministry of Water Resources of the People's Republic of China: Beijing, China, 2013.
2. *2019 National Water Conservancy Development Statistics Bulletin*; Ministry of Water Resources of the People's Republic of China: Beijing, China, 2019.
3. Bátori, Z.; Kiss, P.J.; Tölgyesi, C.; Deák, B.; Valkó, O.; Török, P.; Erdős, L.; Tóthmérész, B.; Kelemen, A. River embankments mitigate the loss of grassland biodiversity in agricultural landscapes. *River Res. Appl.* **2020**, *36*, 1160–1170. [CrossRef]
4. Löbmann, M.T.; Geitner, C.; Wellstein, C.; Zerbe, S. The influence of herbaceous vegetation on slope stability—A review. *Earth-Sci. Rev.* **2020**, *209*, 103328. [CrossRef]
5. Cole, L.J.; Stockan, J.; Helliwell, R. Managing riparian buffer strips to optimise ecosystem services: A review. *Agric. Ecosyst. Environ.* **2020**, *296*, 106891. [CrossRef]
6. Vannoppen, W.; Poesen, J.; Peeters, P.; De Baets, S.; Vandevoorde, B. Root properties of vegetation communities and their impact on the erosion resistance of river dikes. *Earth Surf. Process. Landf.* **2016**, *41*, 2038–2046. [CrossRef]
7. Scheres, B.; Schüttrumpf, H. Investigating the erosion resistance of different vegetated surfaces for ecological enhancement of sea dikes. *J. Mar. Sci. Eng.* **2020**, *8*, 519. [CrossRef]
8. van den Hoven, K.; Grashof-Bokdam, C.J.; Slim, P.A.; Wentholt, L.; Peeters, P.; Depreiter, D.; Koelewijn, A.R.; Stoorvogel, M.M.; van den Berg, M.; Kroeze, C.; et al. Greening the dike revetment with historic sod transplantation technique in a living lab. *J. Flood Risk Manag.* **2024**, *17*, e12968. [CrossRef]
9. Zanetti, C.; Macia, J.; Liency, N.; Vennetier, M.; Mériaux, P.; Provensal, M. Roles of the riparian vegetation: The antagonism between flooding risk and the protection of environments. In Proceedings of the 3rd European Conference on Flood Risk Management FLOODrisk, Lyon, France, 17–21 October 2016; Volume 7, p. 13015.
10. van der Meer, J.; Steendam, G.J.; Mosca, C.A.; Guzzo, L.B.; Takata, K.; Cheong, N.S.; Eng, C.K.; Lj, L.A.; Ling, G.P.; Siang, C.W.; et al. Wave overtopping tests to determine tropical grass species and topsoils for polder dikes in a tropical country. *Coast. Eng. Proc.* **2020**, *36*, 31. [CrossRef]
11. Orlyanskaya, I.A.; Jhalnin, E.V.; Orlyansky, A.V.; Petenev, A.N.; Kulaev, E.V. Comparative efficiency of segment-finger and rotary mowers for grass cutting. In Proceedings of the AIP Conference Proceedings, Stavropol, Russia, 27–30 September 2021; Volume 2661, p. 070002.
12. Nishimura, Y.; Yamaguchi, T. Grass Cutting Robot for Inclined Surfaces in Hilly and Mountainous Areas. *Sensors* **2023**, *23*, 528. [CrossRef] [PubMed]
13. Liao, J.C.; Chen, S.H.; Zhuang, Z.Y.; Wu, B.W.; Chen, Y.J. Designing and Manufacturing of Automatic Robotic Lawn Mower. *Processes* **2021**, *9*, 358. [CrossRef]

14. Xiao, M.H.; Zhao, Y.; Wang, H.; Xu, X.; Bartos, P.; Zhu, Y. Design and Test of Hydraulic Driving System for Undercarriage of Paddy Field Weeder. *Agriculture* **2024**, *14*, 595. [CrossRef]
15. Kang, C.Q.; Ng, P.K.; Liew, K.W. The Conceptual Synthesis and Development of a Multifunctional Lawnmower. *Inventions* **2021**, *6*, 38. [CrossRef]
16. Khodke, K.R.; Kukreja, H.; Kotekar, S. Literature Review of Grass Cutter Machine. *Int. J. Emerg. Technol. Eng. Res.* **2018**, *6*, 97–101.
17. Diwakaran, S.; Kumar, M.D.V.; Mohanreddy, P.S.; Rishika, C.; Sreenivasulu, P.; Sivasubramanian, M. Design of an Autonomous Mower with Height Adjustable Cutting Motor. In Proceedings of the 2023 4th International Conference on Signal Processing and Communication (ICSPC), Coimbatore, India, 23–24 March 2023; pp. 348–352.
18. Kang, C.Q.; Ng, P.K.; Liew, K.W. A TRIZ-Integrated Conceptual Design Process of a Smart Lawnmower for Uneven Grassland. *Agronomy* **2022**, *12*, 2728. [CrossRef]
19. Lei, X.H.; Qi, Y.N.; Zeng, J.; Yuan, Q.C.; Chang, Y.H.; Lyu, X. Development of unilateral obstacle-avoiding mower for Y-trellis pear orchard. *Int. J. Agric. Biol. Eng.* **2022**, *15*, 71–78. [CrossRef]
20. Wu, B.; Wang, D.; Wang, G.; Fu, Z.; Guo, Z.; Gong, Z.; Li, T. Design and Simulation of the Copying Spring of Selfpropelled Mowers. In Proceedings of the 2015 ASABE Annual International Meeting, New Orleans, LA, USA, 26–29 July 2015; p. 152188918.
21. Zhang, Y.; Tian, L.; Cao, C.; Zhu, C.; Qin, K.; Ge, J. Optimization and validation of blade parameters for inter-row weeding wheel in paddy fields. *Front. Plant Sci.* **2022**, *13*, 1003471. [CrossRef] [PubMed]
22. Sheng, Y.Y.; Tian, C.Y.; Xiao, M.H.; Yao, W.Q.; Wang, Q.Q.; Shi, X.Y. Design and Analysis of a Portable Greenhouse Weeding Machine. *J. Comput. Methods Sci. Eng.* **2019**, *19*, 229–241. [CrossRef]
23. Tian, F.; Xia, K.; Wang, J.; Song, Z.; Yan, Y.; Li, F.; Wang, F. Design and experiment of self-propelled straw forage crop harvester. *Adv. Mech. Eng.* **2021**, *13*, 16878140211024455. [CrossRef]
24. Nkakini, S.; Branly, Y. Design, Fabrication and Evaluation of a Spiral Blade lawn mower. *Eur. Int. J. Sci. Technol.* **2014**, *3*, 165–172.
25. Zhao, L.; Wang, J.; Zhang, Z.W. Research on Parameter Design of Multi-axis Hydrostatic Transmission Vehicle. *MATEC Web Conf.* **2017**, *139*, 00215. [CrossRef]
26. Cao, L.; Miao, S. Design of Chinese Cabbage Harvester. In Proceedings of the 2020 IEEE International Conference on Mechatronics and Automation (ICMA), Beijing, China, 13–16 October 2020; pp. 243–248.
27. Guan, P.; Yang, J. Design and test of a new type of coupling weeder. *Int. J. Mech.* **2023**, *17*, 16–24. [CrossRef]
28. Zhang, L.; Yao, C.; Ying, W.; Luo, S.; Ying, F. Theoretical analysis and design of roller mower straight blade. *J. Mech. Sci. Technol.* **2024**, *38*, 3597–3606. [CrossRef]
29. Pirchio, M.; Fontanelli, M.; Frasconi, C.; Martelloni, L.; Raffaelli, M.; Peruzzi, A.; Gaetani, M.; Magni, S.; Caturegli, L.; Volterrani, M.; et al. Autonomous Mower vs. Rotary Mower: Effects on Turf Quality and Weed Control in Tall Fescue Lawn. *Agronomy* **2018**, *8*, 15. [CrossRef]
30. Iwano, Y.; Hasegawa, T.; Tanaka, A.; Iizuka, K. Development of the trimmer-type mowing system against a slope. In Proceedings of the 2016 International Conference on Advanced Mechatronic Systems (ICAMechS), Melbourne, VIC, Australia, 16 January 2017; pp. 23–28.
31. Fontanelli, M.; Chiaro, N.D.; Gagliardi, L.; Frasconi, C.; Raffaelli, M.; Peruzzi, A.; Luglio, S.M. Measuring the operative performance of autonomous mowers on slopes. In Proceedings of the 2023 IEEE International Workshop on Metrology for Agriculture and Forestry (MetroAgriFor), Pisa, Italy, 6–8 November 2023; pp. 404–408.
32. Yan, J.; Gao, L.; Wang, L.; Gong, X. Design, finite element analysis and utility of automatic weeder for port. *Coast. Res.* **2019**, *93*, 901–904. [CrossRef]
33. Peigang, J.; Yinnan, L.; Yang, L. Design and Simulation Analysis of Weeding Machine Chassis Based on CATIA and ADAMS. In Proceedings of the 2023 International Conference on Electronics and Devices, Computational Science (ICEDCS), Marseille, France, 22–24 September 2023; pp. 158–162.

agriculture

MDPI

Article

Analysis of Vibration Characteristics of Tractor–Rotary Cultivator Combination Based on Time Domain and Frequency Domain

Yuanyuan Gao [1,2], Yifei Yang [1], Shuai Fu [3], Kangyao Feng [1], Xing Han [1], Yongyue Hu [1], Qingzhen Zhu [1,2] and Xinhua Wei [1,2,*]

[1] School of Agricultural Engineering, Jiangsu University, Zhenjiang 212013, China; gaoyy0910@ujs.edu.cn (Y.G.); yyfjsdxyx@stmail.ujs.edu.cn (Y.Y.); kangyaofeng@stmail.ujs.edu.cn (K.F.); hanx1010@stmail.ujs.edu.cn (X.H.); hy_0512@stmail.ujs.edu.cn (Y.H.); qingzhen_zhu@ujs.edu.cn (Q.Z.)
[2] Key Laboratory of Modern Agricultural Equipment and Technology, Ministry of Education, Zhenjiang 212013, China
[3] Weichai Lovol Intelligent Agricultural Technology Co., Ltd., Weifang 261200, China; fushuai@lovol.com
* Correspondence: 1000003563@ujs.edu.cn

Abstract: A good planting bed is a prerequisite for improving planting quality, while complex ground excitation often leads to machine bouncing and operation vibration, which then affects the operation effect. In order to improve the quality of rotary tillage operations, it is necessary to study the effects of various vibration excitations on the unit during tractor rotary tillage operations and analyze the vibration interaction relationship among the tractor, the three-point suspension mechanism, and the rotary tiller. For this purpose, multiple three-way acceleration sensors were installed at different positions on the rotary tiller unit of a Lexing LS1004 tractor(Lexing Agricultural Equipment Co. Ltd., Qingdao, China) to collect vibration data at different operating speeds and conduct vibration characteristic analysis between different components. The test results showed that when the unit moved forward at 2.1 km/h, 3.6 km/h, and 4.5 km/h, respectively, the vibration acceleration of the tractor, the three-point suspension mechanism, and the rotary tiller increased with the increase in speed, and there was indeed interaction between them. The vertical acceleration change during the test in the three-point suspension mechanism was the most significant (5.914 m/s^2) and was related to the increase in the speed of the vehicle and the vibration transfer of the rotary tiller. Meanwhile, the vertical vibration acceleration of the tractor's symmetrical structure was not similar, suggesting the existence of structural assembly problems. From the perspective of frequency domain analysis, the resonant frequency at the cab of the tractor was reduced in a vertical vibration environment, with relatively low frequencies (0~80 Hz) and small magnitudes, which might be beneficial to the driver's health. The rotary tillage group resonated around 350 Hz, and this characteristic can be used to appropriately increase the vibration of the rotary tiller to reduce resistance. The tractor cab resonated around 280 Hz, which must be avoided during field operations to ensure driver health and reduce machine wear. The research results can provide a reference for reducing vibration and resistance during tractor rotary tillage operations, as well as optimizing and improving the structure of rotary tillers and tractors.

Keywords: seed bed preparation; tractor rotary tillage; ground excitation; vibration interaction relationship; time–frequency characteristics; power spectral density

Citation: Gao, Y.; Yang, Y.; Fu, S.; Feng, K.; Han, X.; Hu, Y.; Zhu, Q.; Wei, X. Analysis of Vibration Characteristics of Tractor–Rotary Cultivator Combination Based on Time Domain and Frequency Domain. *Agriculture* **2024**, *14*, 1139. https://doi.org/10.3390/agriculture14071139

Academic Editors: Xiaojun Gao, Qinghui Lai and Tao Cui

Received: 13 June 2024
Revised: 10 July 2024
Accepted: 11 July 2024
Published: 13 July 2024

1. Introduction

In agricultural production, land preparation is a key point. Through land preparation operations, the soil in the field can be made more suitable for the growth of crops. Traditional farming machinery, such as disc harrows and share plows, require greater tractor traction. In contrast, tractor rotary tillage units have become the main method for land preparation due to their wide range of applicable operations and lower power load requirements. Therefore, the research on the operation performance of a rotary tiller will help to improve the final operation quality and crop yield [1–3].

Due to the complex field operating environment, agricultural machinery often faces severe vibrations caused by multisource excitations during operation, which reduces the reliability of the machinery and leads to a decline in work quality [4,5]. However, the appropriate vibration can help reduce the resistance of rotary tillage operations and tractor power consumption. For this reason, it is necessary to understand the vibration characteristics of the tractor during rotary tillage operations. At present, there have been a large number of studies on the working quality of tractors and rotary tillers at home and abroad. In terms of tractors, Han et al. designed a coordinated control system between engine load characteristics and plowing depth to stabilize the engine load by adjusting the plowing depth, allowing the tractor to work within the range of high power and low fuel consumption [6]. An approach that combines multi-objective particle swarm optimization (MOPSO) and wavelet decomposition algorithms has been used to collect input vibration signals efficiently, making it extremely convenient for tractor bumping tests [7]. Watanabe et al. established a three-degree-of-freedom nonlinear tractor dynamics model and used a delayed feedback (DF) control algorithm to eliminate complex vibrations in tractor motion [8]. Singh et al. implemented the online transmission of raw acceleration data in all directions of the tractor cab seat and driver's head based on the Internet of Things module and obtained its power spectral density (PSD) [9]. In addition to tractors, the mounted machine directly affects the quality of operation. Therefore, some scholars have studied the vibration characteristics of land preparation machinery [10,11]. For example, Lai et al. used EDEM 2017, ADAMS 2013, and other simulation software to derive the load model of the rotary tiller gearbox and then carried out stress–strain analysis to find out the design defects of the gearbox [12]. Guo et al. studied the vibration acceleration signals of the hood and handrails of the micro-tiller under four conditions and found that the anisotropic vibration of the hood and handrails was less than that of the static conditions when the engine was running at high speed, because the blades cutting the soil increased the damping of the whole machine [13]. Then, the soil's absorption of certain frequency energies caused the tiller to experience violent vibrations in the handle due to unbalanced inertial force, providing a reference for reducing resistance and energy consumption during rotary tillage operations. Du et al. considered the influence of tractor wheel subsidence and structural deformation of rotary tiller unit on tillage depth and designed a system that could realize the automatic monitoring of the tillage depth of a suspended rotary tiller, which would allow for a comprehensive evaluation of the quality of tillage depth [14]. Chen took the micro-tiller as their research object, tested the vibration of each structure of the micro-tiller under eight working conditions, and analyzed the time domain and frequency domain, thereby reducing the work resistance of the micro-tiller [15]. She then verified the established dynamic model of the whole machine through modal analysis and other means and proposed optimization measures. In the field of the effectiveness of land leveling technology, laser-controlled leveling and GNSS-controlled leveling technologies have been used to enhance the practical benefits of land leveling, contributing valuable research ideas for the future direction of reducing mechanical energy loss during leveling technology [16].

It can be seen from the studies above that research on the vibration characteristics of tillage and land preparation equipment has mostly focused on the tractor, and there is a lack of research on the analysis of the vibration characteristics of the tractor and rotary tiller combination during the operation [17–19]. Since rotary tillers and tractors are related to each other when working in the field, they are stimulated to vibrate and affect each other's vibration [20]. To this end, this paper takes a rotary tiller, a tractor, and the three-point suspension mechanism used to fixedly connect the two as the research objects, collecting and analyzing the vibration conditions of the tractor, three-point suspension mechanism, and rotary tiller, exploring the possible interaction between the units at a stable speed and studying the impact of vibration on the normal operation of the unit, in order to provide a basis for improving the reliability of tractors and rotary tiller, as well as improving and optimizing the structure of the implements to reduce vibration and resistance from soil.

2. Materials and Methods

2.1. Tractor and Rotary Tiller Structure

In this test, a Lexing LS1004 tractor (Lexing Agricultural Equipment Co. Ltd., Qingdao, China) was used to pull the rotary tiller. Its main performance parameters are shown in Table 1. The Dongfanghong 1GQN-250G rotary tiller (YTO GROUP CORPORATION, Luoyang, China) was selected for plowing operations, as shown in Figure 1, and it was connected to the tractor with a three-point suspension mechanism. Its main performance parameters are shown in Table 2 [21].

Table 1. Main performance parameters of tractor.

Rotating Speed/rpm	PTO/rpm	Overall Size/mm
2100	540/750/1000	4540 × 2000 × 2650

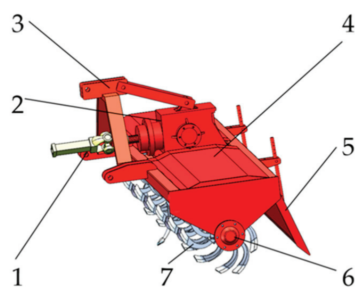

Figure 1. Main structure of rotary tiller: (1) Transmission system, (2) Gear box, (3) Linkage frame, (4) Cover, (5) Soil leveling board, (6) Rotary tiller shaft, (7) Rotary tiller blade.

Table 2. Main performance parameters of rotary tiller.

Matching Horsepower/Hp	Cultivated Width/cm	Cultivation Depth/cm	PTO/rpm
90~105	250	2~16	720/540

The rotary tiller is mainly composed of a transmission system, a gear box, a linkage frame, a cover, a flat soil support plate, a rotary tiller shaft, and a rotary tiller blade. The tractor power was inputted into the gear box through the universal joint of the transmission system, driving the cutter shaft to rotate and the rotary tillage blade to perform soil plowing and soil crushing operations. The soil leveling board was used to prevent soil from splashing and further breaking up the soil during the operations.

2.2. Analysis of the Main Vibration Sources of the Unit

The Dongfanghong 1GQN-250G rotary tiller adopts an intermediate bevel gear transmission. The power of the tractor's power output shaft was transmitted to the intermediate gearbox through the universal joint transmission shaft. The specific transmission path is shown in Figure 2, and the direction of power transmission has been marked with red arrows in the figure. It can be seen from the figure that when a tractor-mounted rotary tiller was operating, in addition to the tractor engine and the possible uneven field surface, its main vibration sources included the rotary tiller gear box, the rotary tiller blade shaft, and the impact load generated by the rotary tiller blade cutting the soil [22].

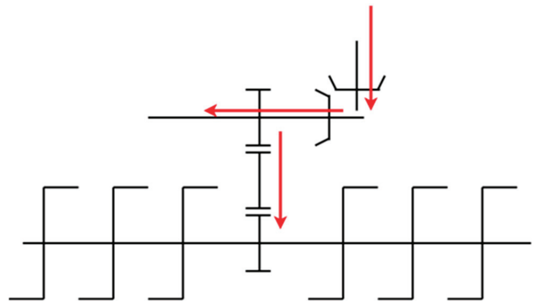

Figure 2. Rotary tiller power transmission route.

When the unit was performing rotary tillage operations, we set the tractor's power take off (PTO) speed to 540 r/min. At this time, the theoretical engine speed was about 1680 r/min. In the test, the first-stage bevel gear transmission ratio of the rotary tiller gearbox was 15:22, and the theoretical rotation speed of the rotary tiller's cutter shaft was 252 r/min [23]. The theoretical vibration frequency of the engine can be obtained according to Equation (1), and the theoretical vibration frequency of PTO and rotary blade shaft can be obtained according to Equation (2) [24]. The theoretical vibration frequencies of each vibration source are shown in Table 3.

$$f_1 = \frac{2}{60c} n_i i \tag{1}$$

where f_1 is the theoretical vibration frequency of the engine, Hz; c is the number of engine strokes; n_i is the theoretical engine speed, r/min; i represents the number of cylinders.

$$f = \frac{n}{60} \tag{2}$$

where f is the theoretical vibration frequency of PTO and rotary blade shaft, Hz; n is the theoretical speed of the kinematic mechanism, r/min.

Table 3. Theoretical vibration frequency of the main vibration source of the unit.

Vibration Source	Theoretical Vibration Frequency/Hz
PTO	8~10
Tractor engine	54~58
Rotary tiller shaft	4~5

2.3. Laboratory Equipment

The vibration acceleration acquisition and analysis system of the tractor rotary tillage unit mainly consists of a dynamic signal analyzer, three-way acceleration sensors, post-processing software, a voltage inverter, a 12 V DC power supply and a laptop, as shown in Figure 3. Among them, the Spider-80Xi analyzer (Crystal Instruments Company, Santa Clara, CA, USA) has 32 input channels and is powered by a DC power supply with a voltage of 10 V to 22 V; the three-way acceleration sensor model is BWJ13533, and the sensitivity of each sensor is shown in Table 4. The inverter model is BOKAI 3000 WDC/AC (Zhongshan Xinyihao E-commerce Co. Ltd, Zhongshan, China) inverter, which was used to convert 12 V DC power into 220 V AC power to power the dynamic signal analyzer.

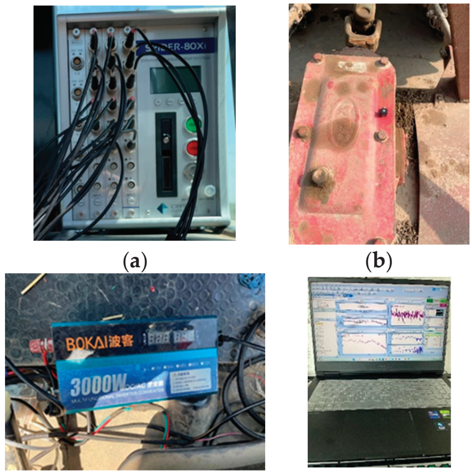

(**a**) (**b**) (**c**) (**d**)

Figure 3. Collection and analysis system: (**a**) Spider-80Xi analyzer, (**b**) Three-way acceleration sensor (at the rotary tiller), (**c**) Inverter, (**d**) Upper computer interface.

Table 4. Sensor sensitivity in all directions.

Sensor Number	**Sensitivity in All Directions/mV·g^{-1}**		
	X	**Y**	**Z**
1	50.24	50.39	50.53
2	49.64	50.27	50.16
3	49.10	49.88	49.60
4	49.35	50.41	51.05
5	49.21	50.33	49.62
6	49.86	50.05	49.28
7	48.82	50.14	50.26
8	49.40	48.66	49.01

In order to facilitate subsequent test data processing, during the test process, the unit's traveling direction was set as the X direction, the vertical forward direction as the Y direction, and the vertical direction to the ground as the Z direction. In this way, the vibration test data at different positions of the unit were uniformly divided into three directions, X, Y, and Z.

2.4. Experimental Program

During the tractor rotary tillage operations, the vibration signals of the rotary tiller, tractor, and linkage were collected by the three-way acceleration sensors and transmitted to the road spectrum test and analysis system through the Spider-80Xi dynamic signal analyzer. Then, the characteristic values (RMS) of the acceleration signal were extracted, and the time domain analysis and PSD analysis were carried out to obtain the sequence of effects of the main excitation sources on the vibration magnitude of the unit components [25].

The experiment was conducted in a rice stubble field. Since the ground of the paddy field was relatively flat after beating and drying, the influence of uneven ground on the vibration of the machine was considered as a minor factor in this experiment. In order to reduce the impact of the tractor engine on the collected signals, sensors were arranged at different positions of the unit as a blank control in the experiment. As shown in Figure 4, three-way acceleration sensors were installed on the rotary tiller, tractor, and three-point suspension mechanism to obtain vibration data. The installation position should be as close as possible to the excitation source to obtain accurate measurement data [26].

For this purpose, the position of each measuring point was set as follows: measuring point 1 (center of the rotary cultivator), measuring point 2 (suspended lower left pull rod), measuring point 3 (suspended right lower pull rod), measuring point 4 (tractor left rear wheel), measuring point 5 (tractor right rear wheel), measurement point 6 (tractor cab), measurement point 7 (tractor left front wheel), and measurement point 8 (tractor right front wheel). Finally, a total of 8 measurement points and 3 working conditions were used to conduct vibration characteristics test experiments. Among them, measuring points 4, 5, 7, and 8 were all arranged on the front and rear axles of the tractor chassis. The three working conditions were, respectively, the operating status of the rotary tiller unit when traveling at speeds of 2.1 km/h, 3.6 km/h, and 4.5 km/h. In addition, in order to reduce the influence of external factors on the test results [27], the vibration characteristic parameters of the rotary tiller and tractor cab with zero speed were collected. Meanwhile, the operating parameters of the rotary tiller were kept unchanged during the experiment to test the effect of working speed and soil excitation on the vibration characteristics of the machine.

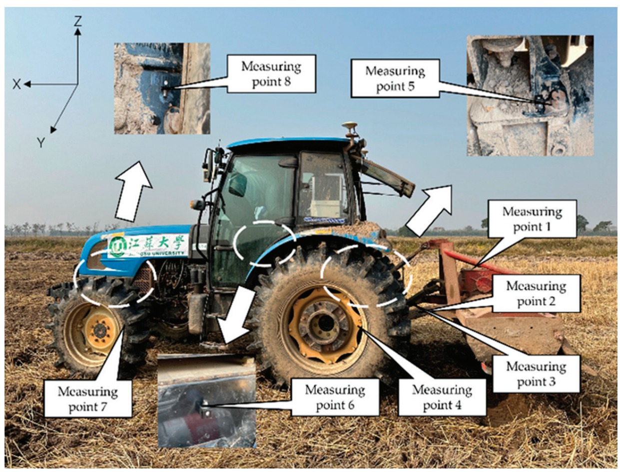

Figure 4. Installation location of each sensor.

2.5. *Signal Acquisition and Analysis*

According to the above-mentioned measurement requirements, the sensors were first installed in a specific position and their three-axis orientations were recorded. They were then connected to the dynamic signal analyzer via a wire harness to check whether the individual channel data were normal. Meanwhile, in order to ensure the accuracy of the experimental waveform, the sampling frequency should be at least twice the frequency of the analyzed signal [28]. Before the experiment, the Spider-80Xi dynamic signal analyzer sampling rate was set to 2560 Hz, continuous sampling mode was performed, and 24 input channels were turned on. After the settings were completed, the vibration signal collection test was performed. While the three working speeds were stable, the vibration acceleration data was collected. Under stable working conditions, the sampling time of each group was 40 s. Based on the acceleration data obtained under stable sampling time, the vibration characteristics of the tractor rotary tillage operation were analyzed.

2.5.1. Time Domain Analysis

The root mean square (RMS) is often used to measure the fluctuation of random signal near the mean value, which can directly reflect the strength of the signal [29]. Therefore, the vibration signal data were processed, and the RMS was calculated to provide a basis for subsequent vibration analysis. The calculation formula of the RMS is shown in Equation (3).

$$RMS = \sqrt{\frac{1}{N}\sum_{k=1}^{N} x_k^2} = \sqrt{\frac{x_1^2 + x_2^2 + x_3^2 + \cdots + x_k^2}{N}} \tag{3}$$

where x_k is the vibration acceleration value, m/s^2; N is the number of signals collected.

With a view to reduce the impact of the location distribution of measuring points on the measurement results and obtain more accurate measurement data, the sensors fixed on the unit components were arranged symmetrically along the center line of the unit. Among the 8 measuring points, measuring points 2 and 3 were symmetrical about the center line of the unit; measuring points 4 and 5 on the tractor's rear axle were symmetrical about the tractor's center line; and measuring points 7 and 8 on the tractor's front axle were symmetrical about the tractor's center line. The measurement data of measuring point 1 and measuring point 6 were not additionally processed.

2.5.2. Frequency Domain Analysis

In order to further analyze the vibration signal, the time domain signal is generally converted into the frequency domain signal through Fast Fourier Transformation (FFT) [30]. This method is often used to analyze the signal spectrum in digital signal processing. The PSD of the rotary tiller and the tractor can be obtained by analyzing their frequency domain data [31]. PSD is a measure of the mean square value of random variables. It eliminates the impact of frequency resolution on the amplitude of the spectral function and represents the distribution of signal power at each frequency point. For any random signal, the PSD expression can be determined through Equation (4) [32].

$$\lim_{T\to\infty}\frac{1}{T}\int_0^T |\sigma(t)|^2 dt = \lim_{T\to\infty}\frac{1}{T}\int_{-\infty}^{+\infty} |F_\sigma(\omega)|^2 df = \int_{-\infty}^{+\infty} S_\sigma(f)df \tag{4}$$

where $\sigma(t)$ is a random signal; $F_\sigma(\omega)$ is $\sigma(t)$ after Fourier transform; $S_\sigma(f)$ represents the distribution of signal average power spectrum in frequency domain.

For the purpose of studying the influence of vehicle speed on the vibration characteristics of the rotary tillers and tractors, the vibration acceleration data of measuring point 1 on the rotary tiller and measuring point 6 on the tractor under three working conditions were processed. We then obtained the power spectrum peak value and corresponding peak frequency of each working condition of the two points.

3. Results and Discussion

3.1. Time Domain Analysis of Rotary Tillage Unit

The vertical RMS values of the rotary tiller and tractor with zero speed are listed in Table 5. The RMS values of the vertical vibration acceleration at different positions of the unit under the three working conditions are shown in Table 6, and the RMS values of the vertical acceleration on both sides of the rotary tillage unit are shown in Table 7.

Table 5. Vertical vibration acceleration of the cab of rotary tiller and tractor under no-load condition.

The Location of the Measurement Point	RMS/m·s^{-2}
Rotary tiller	20.865
Cab	1.201

Table 6. RMS of vertical vibration acceleration at different positions of the rotary tillage unit under three working conditions.

Speed/ km·h^{-1}	RMS of Vertical Vibration Acceleration at Different Positions of the Unit/m·s^{-2}				
	Rotary Tiller	**Three-Point Suspension Mechanism**	**Tractor Rear Wheels**	**Cab**	**Tractor Front Wheels**
2.1	21.532	12.507	2.104	1.218	6.500
3.6	24.950	20.594	4.820	1.333	4.884
4.5	26.399	24.026	5.306	1.346	7.726
Average value	24.294	19.042	4.077	1.299	6.370
Standard deviation	2.499	5.914	1.726	0.070	1.425

Table 7. RMS of vertical acceleration on both sides of the rotary tillage unit under three working conditions.

Speed/ km·h^{-1}	RMS of Vertical Acceleration on Both Sides of the Rotary Tillage Unit/m·s^{-2}					
	Linkage Left Lower Tie Rod	**Linkage Right Lower Tie Rod**	**Tractor Left Rear Wheel**	**Tractor Right Rear Wheel**	**Tractor Left Front Wheel**	**Tractor Right Front Wheel**
2.1	20.382	4.632	4.129	0.078	10.973	2.018
3.6	24.463	16.725	9.566	0.074	7.192	2.575
4.5	27.509	20.543	10.529	0.082	12.848	2.603
Average value	24.118	13.967	8.075	0.078	10.338	2.399
Standard deviation	3.576	8.306	3.451	0.004	2.881	0.330

The following can be seen from the data in Tables 5–7:

(1) The vertical amplitude of the rotary tiller and tractor cab in the working state was higher than in the no-load state, and the amplitude increased with the speed, indicating that the unit had other excitation sources besides the rotary tiller. However, this change would be obvious at a higher speed. When the vehicle speed was 2.1 km/h, the amplitude increased by only 0.667 m/s^2 and 0.017 m/s^2, respectively, compared with zero speed, while the amplitude increase was 5.534 m/s^2 and 0.145 m/s^2, respectively, at the speed of 4.5 km/h. During the tractor rotary tillage operations, the average vertical acceleration generated by the rotary tiller at different vehicle speeds was 24.294 m/s^2, and the average vertical acceleration generated by the three-point suspension mechanism was 19.042 m/s^2, which was much larger than the vertical acceleration everywhere of the tractor. This showed that the rotary tiller was the most important excitation source in the unit. In addition, an analysis of the vibration conditions at different positions of the tractor showed that the vertical vibration of the front wheel (6.370 m/s^2) was greater than the tractor's rear wheel (4.077 m/s^2) and the cab (1.299 m/s^2). In addition to the different distances from the rotary tiller, the reason might also be related to the front and rear wheel load, stubble thickness, front and rear wheel vibration amplitude, and other factors.

(2) Investigating the changes in the vertical vibration acceleration of the different parts, it could be seen that the influence of working speed on each measurement part from large to small was as follows: three-point suspension mechanism > rotary tiller > tractor rear wheels > tractor front wheels > cab. Among them, the standard deviation of the three-point suspension mechanism (5.914 m/s^2) was much larger than that of other parts, indicating that speed changes had the greatest impact on the three-point suspension mechanism. The reason may be that the three-point suspension mechanism, the tractor, and the rotary tiller used pins and other movable connections, so it was greatly affected by inertia. The vertical vibration change in the rotary tiller (2.499 m/s^2) was second only to the three-point suspension mechanism, indicating that the vehicle speed was an important factor in the vibration changes in the rotary

tiller operation, which, in turn, affected the quality of the rotary tillage operation. While the cab's vertical vibration acceleration changed the least (0.070 m/s^2), presumably because the tractor's vibration damping device had good vibration damping performance near the cab.

(3) The vertical vibration amplitude and vibration acceleration standard deviation of the rotary tiller and the three-point suspension mechanism were much larger than those of the tractor components, indicating that the biggest excitation source for the two came from their interaction, which meant their interaction led to a severe vibration. The vertical acceleration amplitude of the rear wheels of the tractor (4.077 m/s^2) was generally smaller than that of the front wheels (6.370 m/s^2), which was related to the fact that the mass of the rear wheel was greater than that of the front wheel. However, the acceleration changes in the rear wheels (1.726 m/s^2) were greater than those in the front wheel (1.425 m/s^2). It was speculated that the rear wheels were affected by the violent vibration of the three-point suspension device, which accelerated the change in its own vibration amplitude.

(4) From working condition 1 to working condition 3, the overall vertical vibration acceleration of the rotary tiller and tractor increased, but the growth rate slowed down. The vibration acceleration of each part of the tractor increased as the vehicle sped up as a whole but the vibration acceleration of the tractor's front wheel decreased by 1.616 m/s^2 from 2.1 km/h to 3.6 km/h, and then increased again when it reached 4.5 km/h. It was speculated that when the vehicle speed was 3.6 km/h, the load distribution of the tractor changed, and the load on the left front wheel became smaller.

(5) The durability of agricultural machinery could be detected using vibration signals [33]. The vibration of the symmetrical structure of the wheeled tractor should be similar, but the vibration acceleration on the left side of each measured part in Table 5 was greater than that of the right side. This might have been caused by problems with the tractor parts and structural assembly, which, in turn, led to abnormal vibration transmission paths of the front and rear wheels and the three-point suspension mechanism symmetry point [34]. The vibration acceleration of the tractor's front left wheel only decreased by 3.781 m/s^2 when the speed was 3.6 km/h, resulting in a decrease in the vibration acceleration of the tractor's front wheel, as in Table 7. At this time, the tractor's vibration damping mechanism could not achieve a more balanced vibration suppression effect on the left and right sides, and further inspection of the quality of the tractor's assembly and parts was required.

(6) During the experiment, the three-point suspension mechanism produced the maximum amplitude, influencing the rotary tiller and tractor connected to its axle pin to produce greater vibration, which, in turn, affected the operation of the unit. For the tractor, the vibration was transmitted from the rear axle to the cab, causing a higher vibration of the seat, resulting in reduced comfort of the tractor seat, which was not conducive to the driver's long-term operation of the tractor. At the same time, appropriately increasing the amplitude of the rotary tiller could reduce the cutting resistance of the rotary tiller blade into the soil, which is conducive to improving the quality of rotary tillage operation [35], but excessive vibration may also aggravate blade fatigue damage. For this reason, the resonance frequency of the rotary tiller should be avoided as much as possible.

(7) Judging from the results of time domain analysis alone, higher speed means larger amplitude for each component, but this inference still needs further verification.

3.2. Frequency Domain Analysis of Rotary Tillage Unit

In order to obtain the change in the energy occupied by the center of mass vibration signal of the rotary cultivator and tractor in the unit frequency band along with the frequency, the collected time domain data was processed. Since measuring point 6 was installed in the cab, the vibration it measured could also reflect the vibration characteristics to the operator to a certain extent. For this reason, FFT transformation was performed on the vertical vibration data of measuring point 6 at three speeds, and the frequency domain data in the range of 0~80 Hz were obtained, as shown in Figure 5. The power spectrum peaks and corresponding peak frequencies at the center of mass of the rotary tiller and tractor under different working conditions are shown in Table 8, and the PSD is shown in Figure 6. For non-stationary random signals, the above processing could not reflect the characteristics of the signal frequency changing with time. In order to process non-stationary random signals, it was necessary to jointly represent the time domain and frequency domain of the signal in two dimensions, which means, time–frequency analysis. The signal analyzer in Matlab 2022a could be used to perform time–frequency analysis on the original time domain data collected. The local time–frequency analysis of the gearbox and cab under working condition 1 is shown in Figure 7.

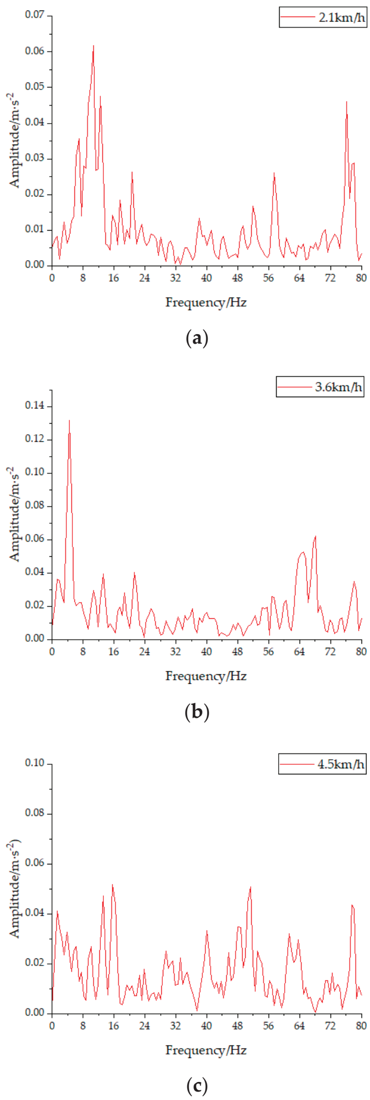

Figure 5. Vertical FFT diagrams of the cab in the low frequency range (0−80 Hz): (**a**) The speed at 2.1 km/h, (**b**) The speed at 3.6 km/h, (**c**) The speed at 4.5 km/h.

Table 8. Peak power spectrum of center of mass of rotary tiller and tractor.

Measuring Point Location	Rotary Tiller Gearbox			Tractor Cab		
Speed/km·h^{-1}	2.1	3.6	4.5	2.1	3.6	4.5
Peak axial	X	Y	Y	X	X	X
Peak/(m·s^{-2})^2	15.728	7.213	7.958	0.216	0.115	0.794
Frequency/Hz	351	466	548	270	275	274

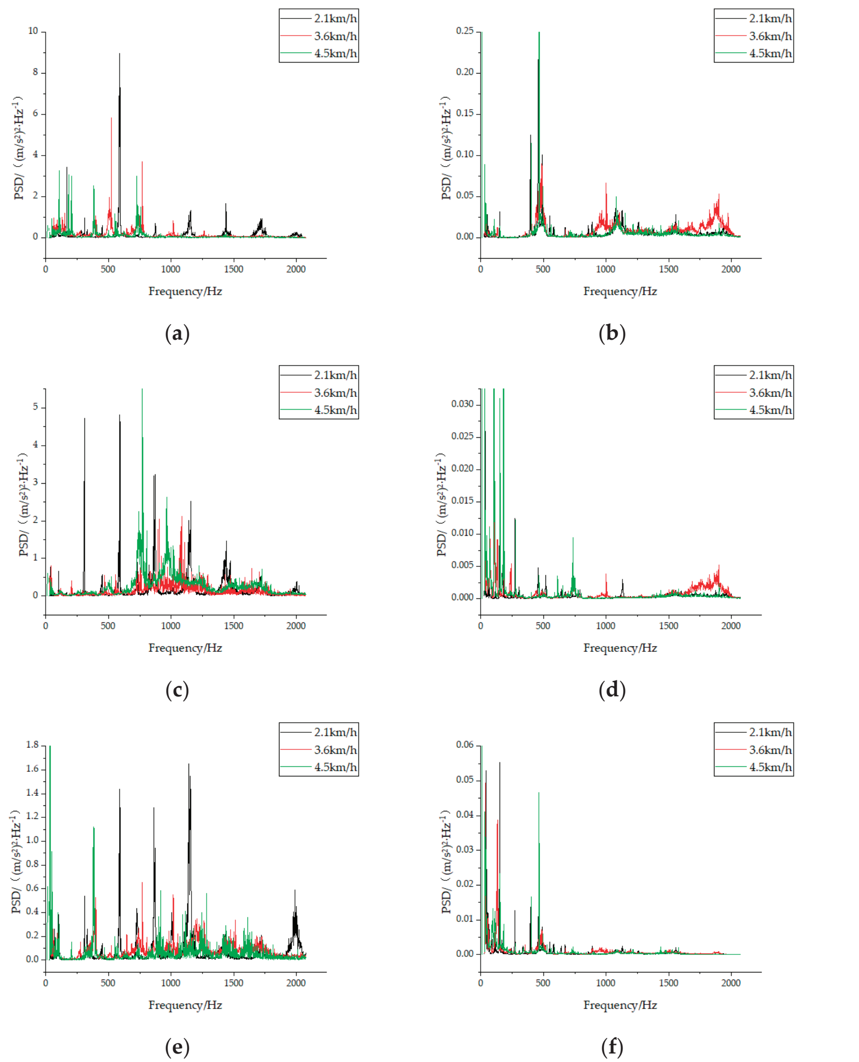

Figure 6. PSD drawings of gearbox and cab in various directions: (**a**) Gearbox, X direction, (**b**) Cab, X direction, (**c**) Gearbox, Y direction, (**d**) Cab, Y direction, (**e**) Gearbox, Z direction, (**f**) Cab, Z direction.

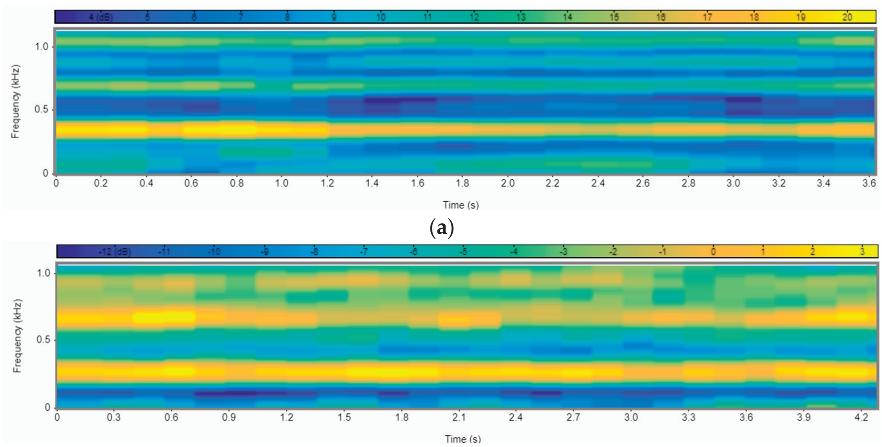

(**a**)

(**b**)

Figure 7. Local time−frequency analysis of working condition 1: (**a**) Gearbox and (**b**) Cab.

Based on the data charts above, the relationship between vibration acceleration and frequency changes near the gearbox (rotary tiller) and tractor cab (tractor) was analyzed, and the following conclusions were drawn:

(1) At the three working speeds, the amplitude of the tractor cab appeared as small peaks in the frequency range of 0~8 Hz, and with the increase in working speed, the peak frequency of the amplitude reduced from 6.8 Hz to 4.9 Hz. As the human body is more sensitive to vertical vibration frequencies in the range of 4–8 Hz, it would not be appropriate to work for a long time in that environment. The change in the peak frequency of the seat vibration in the low frequency range (1~16 Hz) was consistent with the content in the literature [36]. Therefore, maintaining high-speed operation of the unit in actual operation may avoid the sensitive frequency interval of the human body and maintain human health.

(2) For the tractor, the peaks of vibration energy first occurred intensively in the low-frequency range of 0~100 Hz. Under the three working speeds, the power spectrum density in the X, Y, and Z directions all produced the first peak near 33 Hz. Regardless of the speed and direction, in the frequency range of 30~50 Hz, the energy occupied by the tractor's vibration signal began to gather significantly, especially at the highest speed, indicating that the first-order natural frequency of the tractor may exist in the continuous range of 30~50 Hz. In the wide range of 100~500 Hz, the power spectrum density values of the tractor in each direction varied, and the overall vibration energy density was higher. Combined with the corresponding frequency of the power spectrum peak of the rotary tiller in Table 8, it could be seen that the tractor had a resonance band of a certain width in this range. Unlike the tractor, the vibration signal power distribution of the rotary tiller in the range of 0~100 Hz was not significant, and the vibration energy in all directions was less than in the range above 250 Hz. Considering that its design purpose was to loosen the topsoil, it is beneficial for the rotary tiller to have much greater vibration energy than the tractor cab when working.

(3) For the movement of the rotary tiller in the X direction, the peak power spectrum of working condition 1 (15.728 $(m/s^2)^2$) was much larger than that of working conditions 2 and 3. Figure 7a is the time–frequency diagram of the X-direction vibration of the rotary tiller gearbox under working condition 1. After processing with the band stop filter, it could be seen that there was a relatively obvious vibration energy distribution at various frequencies, among which the energy distribution at a frequency of about 350 Hz was the most significant, and the energy concentration did not change over

time. More concentrated energy distributions could also be seen when the frequencies were near 700 Hz, 1050 Hz, and 1400 Hz (that was, integer multiples of 350 Hz). In the short period, the other frequency components except 350 Hz were not significant, indicating that the energy of the rotary tiller under working condition 1 was the most concentrated at the frequency of 350 Hz. This was consistent with the frequency corresponding to the gearbox vibration peak in Table 8 (351 Hz). It was inferred that the center of mass of the rotary cultivator resonated near the frequency of 350 Hz.

(4) Figure 7b is a time–frequency diagram of the vibration of the tractor cab in the X direction under working condition 1. The figure showed that the frequency corresponded to the maximum vibration at about 280 Hz, and the energy there remained unchanged during the sampling time. In Table 8, the tractor centroid power spectrum peak at a frequency of 274 Hz under working condition 3 increased significantly (0.794 $(m/s^2)^2$), and the peak frequencies under the three working conditions were all in the 270–280 Hz range. Therefore, it can be speculated that there was a resonance frequency in this interval.

(5) The X-direction resonance frequency of the rotary tiller was around 350 Hz, which was higher than the X-direction resonance frequency of the tractor cab (280 Hz). For tractors, people would want to avoid resonance, but this is different for rotary tillers. For the entire unit, improving operating efficiency is to better perform the rotary tillage operations. Since increasing the vibration of the rotary tiller can reduce the adhesion of soil to the rotary tiller blades [37], the operating speed can be increased to increase the amplitude of the rotary tiller operation, thereby reducing the resistance of the soil to the rotary tiller operation and improving operating efficiency and quality.

(6) For the movement of the gearbox in the Y direction, the PSD diagram showed that its vibration energy was concentrated in the high-frequency range of 750~1000 Hz, which was much higher than the resonance frequencies in the X and Z directions. Therefore, when considering avoiding resonance of the rotary cultivator, only the vibration in the X and Z directions need to be considered. The tractor cab in the Y direction generated a large vibration acceleration near 78 Hz. The vibration energy was concentrated in the lower frequency range of 75~135 Hz under various working conditions, but the overall vibration acceleration of the Y-axis was low, causing little impact.

(7) The Z-direction rotary tiller gearbox had a wide frequency range of violent vibrations, and large vibrations occurred between 430 and 1200 Hz under three working conditions. It was speculated that this was related to the fact that the rotary tiller would jump up and down in the vertical direction due to the rotary tiller blade encountering resistance when entering the soil and the vibration acceleration of the blade axis changing more obviously in the Z direction. The maximum vibration acceleration frequencies generated by the tractor in the Z direction were 66 Hz, 78 Hz, and 272 Hz, respectively, which were more concentrated than those in the X and Y directions.

(8) The results of the frequency domain analysis showed that high speed did not always lead to high amplitude. Sometimes, the PSD values of the rotary tiller in each direction at low speed were higher than those at high speed. In the low-frequency range relevant to human health, the low-speed amplitude was also greater than the high-speed amplitude.

(9) When using the signal analyzer in Matlab 2022a for the time–frequency analysis shown in Figure 7, a band-stop filter was also used to preprocess the original signal data, and the frequency components of the resulting time–frequency diagram were still relatively complex. In order to obtain a time–frequency diagram with clearer vibration energy distribution and better time–frequency aggregation, the next step could be to use continuous wavelet transform and other analysis methods with good time–frequency resolution to extract the characteristics of the vibration signal.

4. Conclusions

This paper took the rotary tiller, tractor, and three-point suspension mechanism as research objects and explored the interaction between the units at different speeds through vibration characteristic analysis. Based on the results of the vibration test experiments of the rotary tillage unit under three working speed conditions, combined with time domain and frequency domain analysis, the following conclusions can be drawn:

(1) The vibration amplitude of the rotary tiller needs to be appropriately increased to reduce the resistance to soil penetration, but the interaction between the tractor and the rotary tiller causes the vibration to be transmitted to the tractor synchronously, which is harmful to the tractor. Therefore, while the tractor is mounted with a rotary tiller and operates at high speed and efficiency, the vibration reduction capacity of the tractor also needs to be optimized to achieve higher quality of work and more stable operation.

(2) Generally speaking, the vibration acceleration at each measurement point increased with the increase in working speed, but this was not necessarily the case in certain frequency domain intervals. In some frequency domain intervals, the amplitude did not always increase with increasing speed. It might be that the low-frequency range is less affected at low speed, while the amplitude change in the high-frequency range at higher speeds still needs to be tested.

(3) The reason for why the vibration amplitude of the unit increased with the tractor speed might be related to the more violent collision between the unit and the stubble surface caused by the increase in speed. However, in the low-frequency and low-amplitude range, which has an important impact on human health, the vertical resonance frequency of the cab seat decreased with the increase in amplitude (from 6.8 Hz to 4.9 Hz). In the future, the change law of the vertical amplitude of the seat under high-speed operation of the unit can be studied to help the driver operate the tractor more healthily.

This paper obtained the interaction relationship among the components of the unit by collecting and analyzing the vibration data of the tractor, three-point suspension mechanism, and rotary tiller under different working conditions, and it also speculated on the possible structural assembly problems of the tractor within the experiment. The vibration data analysis method used in this paper can be further used to explore the interaction relationship and vibration characteristics between the tractor and the suspension agricultural implement system. In the future, the vibration analysis method can be further used to study the influence of factors such as field surface flatness and of PTO speed on the combined operation effect of the tractor and rotary tiller.

Author Contributions: Conceptualization, Y.G. and X.W.; methodology, Y.G., Y.Y. and S.F.; software, Y.Y. and K.F.; validation, Y.Y.; formal analysis, X.H. and S.F.; investigation, Y.Y. and K.F.; resources, Y.G. and X.W.; data curation, Y.Y.; writing—original draft preparation, Y.Y. and S.F.; writing—review and editing, Y.G. and Y.Y.; visualization, Y.H. and Q.Z.; supervision, S.F.; project administration, Y.G. All authors have read and agreed to the published version of the manuscript.

Funding: This study was financially supported by Jiangsu Provincial Natural Science Foundation (Grant No. BK20210776), the National Natural Science Foundation of China (Grant No. 32201672), the Priority Academic Program Development of Jiangsu Higher Education Institutions (Grant No. PAPD-2023-87), and Jiangsu Province and Education Ministry Co-sponsored Synergistic Innovation Center of Modern Agricultural Equipment (Grant No. XTCX1002).

Institutional Review Board Statement: Our studies did not involve humans or animals.

Data Availability Statement: The data presented in this study are available on request from the corresponding author.

Conflicts of Interest: Author Shuai Fu was employed by the company Weichai Lovol Intelligent Agricultural Technology Co., Ltd. The remaining authors declare that the research was conducted in the absence of any commercial or financial relationships that could be construed as a potential conflict of interest.

References

1. Qin, J.W. Current status and suggestions for the use of tillage machinery standards. *Agric. Mach. Qual. Superv.* **2020**, *01*, 20–21.
2. Chen, W.X. Discussion on the technical characteristics of rotary tiller and land preparation technology. *Guangxi Agric. Mech.* **2022**, *05*, 22–25.
3. Wang, Z.; Zhou, J.; Wang, X. Research on Energy Management Model for Extended-range Electric Rotary-tilling Tractor. *Trans. Chin. Soc. Agric. Mach.* **2023**, *54*, 428–438. [CrossRef]
4. Chen, S.R.; Zhou, Y.P.; Tang, Z.; Lu, S.N. Modal vibration response of rice combine harvester frame under multi-source excitation. *Biosyst. Eng.* **2020**, *194*, 177–195. [CrossRef]
5. Zhai, C.; Long, J.; Taylor, R.; Weckler, P.; Wang, N. Field scale row unit vibration affecting planting quality. *Precis. Agric.* **2020**, *21*, 589–602. [CrossRef]
6. Han, J.Y.; Yan, X.X.; Tang, H. Method of controlling tillage depth for agricultural tractors considering engine load characteristics. *Biosyst. Eng.* **2023**, *227*, 95–106. [CrossRef]
7. Sun, L.; Liu, M.; Wang, Z.; Wang, C.; Luo, F. Research on Load Spectrum Reconstruction Method of Exhaust System Mounting Bracket of a Hybrid Tractor Based on MOPSO-Wavelet Decomposition Technique. *Agriculture* **2023**, *13*, 1919. [CrossRef]
8. Watanabe, M.; Sakai, K. Delayed feedback control for chaotic vibration in nonlinear impact dynamics of bouncing agricultural tractor. *Sci. Rep.* **2023**, *13*, 10695. [CrossRef]
9. Singh, A.; Nawayseh, N.; Samuel, S.; Dhabi, Y.K.; Singh, H. Real-time vibration monitoring and analysis of agricultural tractor drivers using an IoT-based system. *J. Field Robot.* **2023**, *40*, 1723–1738. [CrossRef]
10. Sun, Y.; Ke, S.; Wang, G.; Liu, Z. Control Strategy Simulation Analysis of a New Micro-cultivator MR Elastomer Vibration Isolation System. *Adv. Eng. Sci.* **2020**, *52*, 218–225. [CrossRef]
11. Liao, Y.T.; Qi, T.X.; Liao, Q.X.; Zeng, R.; Li, C.L.; Gao, L.P. Vibration characteristics of pneumatic combined precision rapeseed seeder and its effect on seeding performance. *J. Jilin Univ. (Eng. Technol. Ed.)* **2022**, *52*, 1184–1196. [CrossRef]
12. Lai, Q.H.; Yu, Q.X.; Dong, J.Y. Dynamic analysis of rotary tiller gearbox based on EDEM, ADAMS and ANSYS. *J. Intell. Fuzzy Syst.* **2019**, *36*, 1153–1160. [CrossRef]
13. Guo, L.; Jian, C.; Xie, H.J.; Wang, S.M. Vibration test and analysis of mini-tiller. *Int. J. Agric. Biol. Eng.* **2016**, *9*, 97–103. [CrossRef]
14. Du, X.W.; Yang, X.L.; Pang, J.; Ji, J.T.; Jin, X.; Chen, L. Design and Test of Tillage Depth Monitoring System for Suspended Rotary Tiller. *Trans. Chin. Soc. Agric. Mach.* **2019**, *50*, 43–51. [CrossRef]
15. Chen, Y. Random Vibration Characteristics Analysis and Experimental Research of Self-Propelled Micro Tillage Machine. Ph.D. Thesis, Chongqing University of Technology, Chongqing, China, 2017.
16. Chen, G.; Hu, L.; Luo, X.; Wang, P.; He, J.; Huang, P.; Zhao, R.; Feng, D.; Tu, T. A review of global precision land-leveling technologies and implements: Current status, challenges and future trends. *Comput. Electron. Agric.* **2024**, *220*, 108901. [CrossRef]
17. Shao, X.D.; Yang, Z.H.; Song, Z.H.; Liu, J.H.; Yuan, W. Analysis of influence of tractor rotary tillage load on power take-off driveline. *Trans. Chin. Soc. Agric. Mach.* **2022**, *53*, 332–339. [CrossRef]
18. Liu, W.; Zheng, E.L.; Zhou, Y.Q.; Yao, H.P.; Zhu, Y. Vibration characteristics analysis of wheeled tractor/implement system under plough operation condition. *J. Nanjing Agric. Univ.* **2021**, *44*, 1002–1012. [CrossRef]
19. Zhu, S.H.; Xu, G.; Yuan, J.Q.; Ma, J.F.; Yi, L.; Li, K. Influence of implement's mass on vibration characteristics of tractor-implement system. *Trans. Chin. Soc. Agric. Eng.* **2014**, *30*, 30–37. [CrossRef]
20. Hu, H.B.; Li, Z.Y. Discussion on the working status and efficiency of tractor rotary tillage unit. *Trans. Chin. Soc. Agric. Mach.* **1989**, *03*, 96–99.
21. Liu, B.J.; Geng, Y.F. Research & development on dongfanghong 1gqn series rotary tiller. *Shandong Agric. Mach.* **2002**, *8*, 5–9. [CrossRef]
22. Lin, J.X.; Liao, Q.X.; Zhang, Q.S.; Zhang, Q.S.; Kang, Y.; Zhang, J.Q. Vibration characteristics analysis and structural improvement of the shovel type seedbed preparation machine suitable for rapeseed mechanical direct seeding. *Trans. Chin. Soc. Agric. Eng.* **2023**, *39*, 39–48. [CrossRef]
23. Wei, J.B.; Wang, Y.; Zhang, C.L.; Jiang, Y.B.; Guan, L. Application analysis of matching tractor PTO shaft and agricultural ma-chinery. *China South. Agric. Mach.* **2023**, *54*, 45–48. [CrossRef]
24. Wang, J.X.; Shuai, S.J. *Automotive Engine Fundamentals*, 2nd ed.; Tsinghua University Press: Beijing, China, 2011; 128p.
25. Pang, J.; Li, Y.M.; Ji, J.T.; Xu, L.Z. Vibration excitation identification and control of the cutter of a combine harvester using triaxial accelerometers and partial coherence sorting. *Biosyst. Eng.* **2019**, *185*, 25–34. [CrossRef]
26. Gao, Z.P.; Xu, L.Z.; Li, Y.M.; Wang, Y.D.; Sun, P.P. Vibration measure and analysis of crawler-type rice and wheat combine harvester in field harvesting condition. *Trans. Chin. Soc. Agric. Eng.* **2017**, *33*, 48–55. [CrossRef]
27. Qian, P.; Lu, T.; Shen, C.; Chen, S. Influence of vibration on the grain flow sensor during the harvest and the difference elimination method. *Int. J. Agric. Biol. Eng.* **2021**, *14*, 149–162. [CrossRef]
28. Yao, Y.C.; Song, Z.H.; Du, Y.F.; Zhao, Y.X.; Mao, E.R.; Liu, F. Analysis of vibration characteristics and its major influenced factors of header for corn combine harvesting machine. *Trans. Chin. Soc. Agric. Eng.* **2017**, *33*, 40–49. [CrossRef]

29. Yan, J. Study on Vibration Characteristics of Tractor Based on Excitation of Agricultural Terrain Roughness. Ph.D. Dissertation, Inner Mongolia Agricultural University, Hohhot, China, 2020.
30. Wu, X. Application of fast fourier transform in signal processing. *Inf. Rec. Mater.* **2021**, *22*, 184–186. [CrossRef]
31. Zhang, H.Q.; Wang, C.; Cui, Y. Comparative analysis study of conventional time-frequency analysis methods. *Chang. Inf. Commun.* **2020**, *08*, 55–56.
32. Geng, L.X.; Li, K.; Pang, J.; Jin, X.; Ji, J.T. Test and analysis of vibration characteristics of transplanting machine based on time frequency and power spectral density. *Trans. Chin. Soc. Agric. Eng.* **2021**, *37*, 23–30. [CrossRef]
33. Ma, Z.; Zhang, Z.L.; Zhang, Z.H.; Song, Z.Q.; Liu, Y.B.; Li, Y.M.; Xu, L.Z. Durable Testing and Analysis of a Cleaning Sieve Based on Vibration and Strain Signals. *Agriculture* **2023**, *13*, 2232. [CrossRef]
34. Zhang, M.J.; Jin, J.F.; Chen, Y.Y.; Chen, Y.K. Vibration symmetry characteristics of wheeled tractor structure. *J. Jilin Univ. (Eng. Technol. Ed.)* **2023**, *53*, 2136–2142. [CrossRef]
35. Wang, W.M.; Wang, T.Y.; Guo, B.; Chen, X.; Zhou, F.J. Design and test of key components of rotary cultivator based on vibration drag reduction principle. *Trans. Chin. Soc. Agric. Mach.* **2019**, *50*, 35–45. [CrossRef]
36. Zhou, Z.; Griffin, M.J. Response of the seated human body to whole-body vertical vibration: Biodynamic responses to sinusoidal and random vibration. *Ergonomics* **2014**, *57*, 693–713. [CrossRef] [PubMed]
37. Liu, G.; Xia, J.; Zheng, K.; Cheng, J.; Wang, K.; Zeng, R.; Wang, H.; Liu, Z. Effects of vibration parameters on the interfacial adhesion system between soil and metal surface. *Soil Till. Res.* **2022**, *218*, 105294. [CrossRef]

agriculture

Article

Experimental and Numerical Analysis of Straw Motion under the Action of an Anti-Blocking Mechanism for a No-Till Maize Planter

Qingyi Zhang [1,2,3], Huimin Fang [1,2,3,*], Gaowei Xu [4], Mengmeng Niu [5] and Jinyu Li [1]

1 School of Agricultural Engineering, Jiangsu University, Zhenjiang 212013, China; zhangqingyi@ujs.edu.cn (Q.Z.); 2212316040@stmail.ujs.edu.cn (J.L.)
2 Key Laboratory for Theory and Technology of Intelligent Agricultural Machinery and Equipment, Jiangsu University, Zhenjiang 212013, China
3 Jiangsu Province and Education Ministry Co-Sponsored Synergistic Innovation Center of Modern Agricultural Equipment, Zhenjiang 212013, China
4 Department of Automotive Engineering, Shandong Jiaotong University, Jinan 250357, China; 202107@sdjtu.edu.cn
5 Field Operation Technology and Equipment Innovation Center, Shandong Academy of Agricultural Machinery Sciences, Jinan 250100, China; moonniu@126.com
* Correspondence: fanghuimin@ujs.edu.cn; Tel.: +86-155-0860-2886

Abstract: To address the low clearance rate issue of the anti-blocking mechanism for maize no-till planters in the Huang-Huai-Hai Plain of China, experiments and simulations were conducted to analyze the individual and collective movements of straw under the action of the round roller-claw anti-blocking mechanism. A tracer-based measurement method for straw displacement was applied firstly. Experimental results showed that the straw forward displacement could be characterized by the average horizontal displacements of longitudinal and lateral tracers, while the straw side displacement could be characterized by the lateral displacement of the longitudinal tracer. The straw forward displacement was 58.95% greater than the side displacement. Forward, side, and total displacements of straw increased as the mechanism's forward speed increased from 3 km/h to 7 km/h, with corresponding rates of increase at 233.98%, 43.20%, and 162.47%, respectively. Furthermore, a model of straw–soil–mechanism interaction was constructed in EDEM 2022 software. The relative error between experimental and simulated straw clearance rates was 11.20%, confirming the applicability of the simulation model for studying straw–soil–mechanism interaction. Based on the simulation model, three straw tracers of different lengths were selected to study the motion behavior of straw. It was inferred that despite differences in straw length, the movement behaviors of the three straw tracers under the influence of the anti-blocking mechanism were similar. Additionally, longer straws exhibited greater displacements in all directions. This paper serves as a reference for studying straw motion behavior influenced by anti-blocking mechanisms.

Keywords: no-till planting; anti-blocking mechanism; straw displacement; tracer technology; discrete element method; straw clearance rate; straw motion behavior

Citation: Zhang, Q.; Fang, H.; Xu, G.; Niu, M.; Li, J. Experimental and Numerical Analysis of Straw Motion under the Action of an Anti-Blocking Mechanism for a No-Till Maize Planter. *Agriculture* **2024**, *14*, 1001. https://doi.org/10.3390/agriculture14071001

Academic Editors: Xiaojun Gao, Qinghui Lai and Tao Cui

Received: 15 May 2024
Revised: 19 June 2024
Accepted: 23 June 2024
Published: 26 June 2024

1. Introduction

The Huang-Huai-Hai Plain in China is characterized by semi-arid and semi-humid climates, with the predominant agricultural practice being the rotation of winter wheat and summer maize crops. With the continuous improvement in crop yields in recent years, there has been a corresponding increase in the production of straw [1]. However, an increasing amount of straw is being either discarded or openly burned, leading to significant resource wastage and a range of associated issues such as atmospheric pollution and traffic disruptions [2].

Incorporating crop residue cover, as a fundamental tenet of conservation agriculture, offers multifaceted benefits. It not only enhances straw utilization efficiency and mitigates pollution [3] but also mitigates soil erosion [4], enhances the physico-chemical properties of soil [5], and boosts crop yield [6]. However, the presence of straw residue covers poses challenges to maize planting in the Huang-Huai-Hai Plain. Maize planters are prone to blockages, leading to poor planting possibility and sowing quality [7]. Anti-blocking maize planters play a crucial role in ensuring efficient seeding and high sowing quality [8]. An effective anti-blocking mechanism is essential for mitigating straw blockages and enhancing the sowing reliability of maize planters.

Various types of anti-blocking mechanisms are designed to perform tasks such as chopping residues ahead and along the planting path, pushing residues sideways, or burying residues in a strip ahead of furrow opening. Recent developments in anti-blocking mechanisms include an oblique anti-blocking device [9], a round roller-claw anti-blocking mechanism [10], a spiral discharge anti-blocking and row-sorting device [11], a bionic shifting and diffluence straw anti-blocking device [12], and a combined stubble burying and anti-blocking device [13]. These anti-blocking mechanisms find applications in rapeseed direct planting as well as corn no-tillage planting. Theoretical [14,15], experimental [16,17], and numerical [18,19] methods are employed to assess the performance of anti-blocking mechanisms in terms of soil disturbance and straw cleaning rate. For instance, Li et al. [14] analyzed the performance of symmetrical spiral row-sorting of the straw device with a theoretical method, Jiang et al. [16] tested the performance of a seedbed preparation machine before transplanting of rapeseed with a combined transplanter in the field, and Zhu et al. [18] optimized the structural parameters of the bionic shifting and diffluence straw anti-blocking mechanism via EDEM 2022 software. However, these studies focused on the design and optimization of the anti-blocking mechanism. There is a lack of attention to the interaction between straw and the anti-blocking mechanism.

The interaction between straw and agricultural implements is crucial for developing effective anti-blocking mechanisms, and the interaction is usually characterized by straw movement [20]. Researchers employ various methods to analyze straw movement, including theoretical analysis, advanced testing, numerical simulations, and experiments. Gu et al. [21] demonstrated the effectiveness of the "laminar flow splitter" due to its property of round-flow. Gao et al. [22] designed an anti-blocking mechanism, combining a driven divider with a passive residue separating device based on the theory of the boundary layer in fluid mechanics. Liao et al. [23] tracked the movement and throwing trajectory of straws, cut down by the saw-tooth anti-blocking mechanism of a no-tillage planter, with the help of high-speed photography. Niu et al. [15] studied individual and group straw movement numerically. Fang et al. [20] evaluated anti-blocking devices through experiments and simulations. Some studies utilized high-speed cameras [9] and tracer technology [10] to observe straw movement but lacked detailed explanations. Understanding straw motion requires clarity on how anti-blocking devices control and guide it, an aspect currently under-researched in straw–soil–mechanism interaction studies.

In order to address the dilemma of our unclear understanding of straw motion under the influence of anti-blocking mechanisms, a controlled soil bin experiment and discrete element simulation were conducted to achieve the following objectives: (i) propose a measurement method for straw displacement and investigate the effects of working parameters of the anti-blocking mechanism on straw displacement via an experiment; (ii) validate the simulation model of straw–soil–mechanism interaction, and analyze the motion behavior of straw based on simulation.

2. Materials and Methods

2.1. Description of Anti-Blocking Mechanism

The anti-blocking furrow opener, depicted in Figure 1a, is constructed from steel and affixed to a maize planter, specifically tailored for no-tillage sowing in the Huang-Huai-Hai Plain. A pivotal component of this furrow opener is the round roller-claw anti-blocking mechanism, illustrated in Figure 1b. This mechanism has the capability to rotate horizontally under power while advancing alongside the anti-blocking furrow opener. The geometrical characteristics of the anti-blocking mechanism, as outlined in Table 1, were employed for its shape and design.

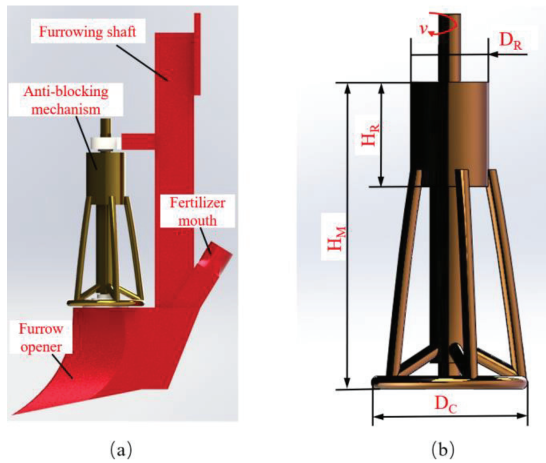

Figure 1. Experimental mechanism: (**a**) furrow opener; (**b**) anti-blocking mechanism.

Table 1. Characteristics of a round roller-claw anti-blocking mechanism.

Parameters	Values
Height of whole mechanism H_M/(mm)	234
Height of round roller H_R/(mm)	80
Biggest diameter of claw D_C/(mm)	120
Diameter of round roller D_R/(mm)	60

2.2. Experimental Design

2.2.1. Description of Soil Bin Experiment

The indoor experiments, depicted in Figure 2, were carried out in the soil bin at the Shandong Academy of Agricultural Machinery Sciences, located in Shandong Province, People's Republic of China (China). The dimensions of soil bin are 60 m × 2.5 m × 1 m (length × width × depth) and it is filled with sufficient soil, enabling the testing of the maize planter. The maize planter was propelled by a PTO shaft of the soil bin tester, while two sets of gear reducers facilitated the rotational motion of the anti-blocking mechanism. The soil density was managed at 1.70 g/cm^3 with the average moisture content of the 0–5 cm soil layer as 10.07%, and 13.51% for the next 5 cm soil depth. The soil hardness was 0.96 MPa.

The straw was uniformly distributed across the soil surface, creating a coverage area of straw measuring 1 m in width and 20 m in length, ensuring that the anti-blocking mechanism moved forward in the middle of the straw row. The wheat straw used in the experiments was harvested from fields in Shandong Province, China, with an average mulching quantity of 610 kg/mu.

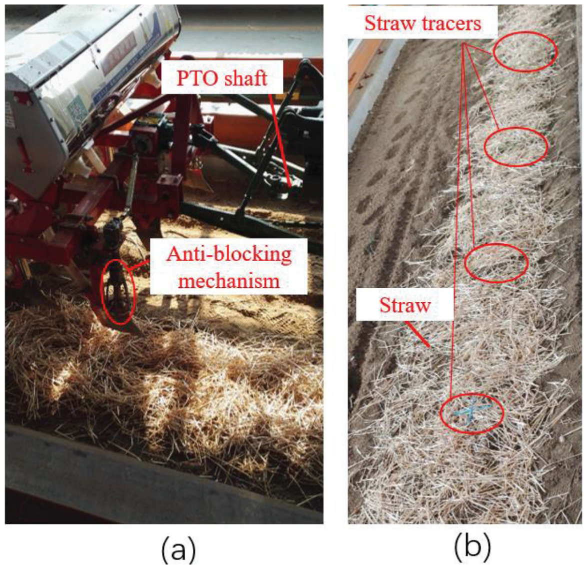

Figure 2. Experimental site in soil bin: (**a**) experimental equipment; (**b**) straw distribution.

2.2.2. Description of Straw Tracer

Five groups of straw tracers were positioned in the test sample area, which were painted purple, blue, red, green, and black, respectively. Each group of straw tracers was spaced 1 m apart to avoid motion interference. Two straw tracers with same color were utilized, with one aligned parallel to the forward motion of the anti-blocking mechanism, termed the longitudinal straw tracer. The other straw tracer, placed perpendicular to it, was called the lateral straw tracer. Every set of longitudinal and lateral straw tracers shared the same color, where the lateral straw tracers were distinguished by special markings at both ends. Three sets of straw tracers (purple, red, and black) were positioned along the forward trajectory of the anti-blocking mechanism, while the remaining two sets (blue and green) were placed laterally, offset by 30 mm from the forward path. The arrangement of the straw tracers is illustrated in Figure 3.

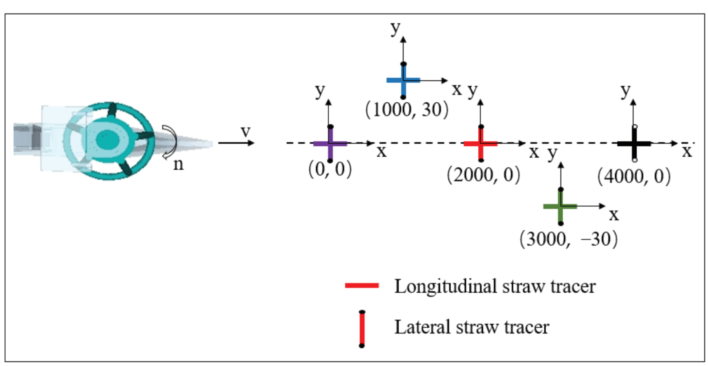

Figure 3. Schematic view of straw tracer placements. Note: v represents the forward velocity, km/h; n represents the rotational speed of the anti-blocking mechanism, r/min.

2.2.3. Measurement

(A) Straw displacement

Straw displacement refers to the movement of straw in both horizontal and lateral directions. It is determined by calculating the absolute difference between the initial and final positions of straw tracers.

(B) Straw clearance rate

The straw clearance rate quantifies the change in the quantity of straw within a 60 mm range on either side of the anti-blocking mechanism forward path. It is calculated as the ratio of the difference in straw weight before and after the anti-blocking mechanism's operation to the initial straw weight within this specified range.

2.3. Simulation Design

2.3.1. Description of Simulation Model

The simulation model of straw–soil-mechanism interaction was developed using EDEM 2022 (Version 8.0.0, Altair Engineering, Inc., Troy, MI, United States). Hard spheres of 5 mm radius were used to represent soil particles, and the contact model between soil particles was based on the Hertz–Mindlin bonding model. Hard spheres with a radius of 3 mm were used to represent straw particles, with a space of 5 mm separating adjacent straw particles.

Considering the actual length of the straw in the field and the size of the straw particles, three lengths of 36, 76, and 116 mm, respectively, were used to model the straw in this study. The 7, 15, and 23 spheres, respectively, were connected to form the 36, 76, and 116 mm straw, respectively. There were 60,000 soil particles and 2400 straw particles, with three lengths of 36 mm, 76 mm, and 116 mm, respectively, generated randomly. According to the previous work [10], the material properties and interaction parameters used in this simulation were as detailed in Table 2. Figure 4 illustrates this simulation model.

Table 2. Simulation parameters.

Parameters	Values
Density of soil/(gm^{-3})	1.85
Density of straw/(gm^{-3})	0.24
Density of steel/(gm^{-3})	7.87
Poisson ratio of soil	0.38
Poisson ratio of straw	0.4
Poisson ratio of steel	0.3
Shear modules of soil/(Pa)	1×10^6
Shear modules of straw/(Pa)	1×10^6
Shear modules of steel/(Pa)	7.9×10^{10}
Recovery coefficient of soil–soil	0.6
Recovery coefficient of soil–steel	0.6
Recovery coefficient of straw–steel	0.3
Static fiction coefficient of soil–soil	0.6
Static fiction coefficient of soil–steel	0.6
Static fiction coefficient of straw–steel	0.3
Rolling fiction coefficient of soil–soil	0.4
Rolling fiction coefficient of soil–steel	0.05
Rolling fiction coefficient of straw–steel	0.01

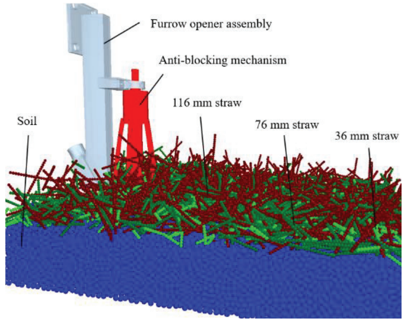

Figure 4. Simulation model of straw–soil-mechanism interaction.

2.3.2. Description of Straw Tracer

In the simulation, 2400 straw particles were randomly generated on the soil surface. Straws of different lengths were chosen as the straw tracer to assess and analyze the displacement of a single piece of straw by monitoring its movement. As straw was randomly distributed on the soil surface, it was essential to compare the differences in the motion behavior of straw at the same location. There are two principles for selecting the three straw tracers. Firstly, tracers should align closely with the forward path of the anti-blocking mechanism, maintaining consistency in the X coordinate values. Secondly, maintaining consistent relative heights of the tracers ensures uniformity in the Y coordinate values, that is, the Y coordinate values are as consistent as possible. Based on these principles, the selected straw tracers and their relative positions in the anti-blocking mechanism are as shown in Figure 5.

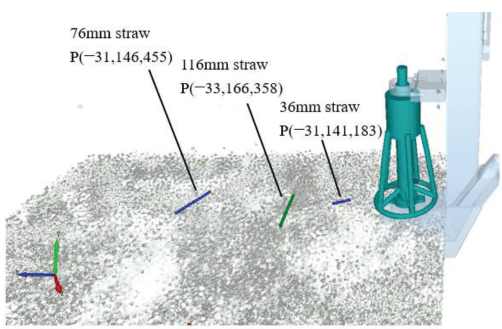

Figure 5. The straw tracers in the simulation and their positions.

2.3.3. Measurement

(A) Straw movement

The positions of three straw tracers were continuously monitored at every instance, utilizing the established model for full coverage of straw distribution. Straw movement refers to the positional changes in straw in both horizontal and lateral directions. The simulation characterizes straw movement by observing the fluctuations in tracer positions over time.

(B) Straw clearance rate

We chose a 60 mm span on either side of the anti-blocking mechanism as the designated area for analyzing straw clearance in the simulation. The straw clearance rate is defined as the ratio of the difference in the straw quantity before and after simulation to the initial straw quantity.

2.4. Experimental and Numerical Treatment Design

Three sets of experiments and simulation were designed and conducted in this study. In the first group of experiments, the orientation and position of the straw tracers were evaluated to determine their impact on straw displacement based on the soil bin test. Additionally, the method for measuring straw displacement was established. Subsequently, the effect of the operational parameters of the anti-blocking mechanism (forward and rotational speed) on straw displacement (forward, side, and total displacement) was investigated using the established measurement technique. This experimental set included three sets of forward speeds (3, 5, and 7 km/h) and four sets of rotational speeds (260, 400, 530, and 740 r/min).

The second experiment focused on using the straw clearance rate to characterize straw side movement. The verification of the simulation model was assessed by comparing the difference in the straw clearance rate between simulation and experimental results. This experiment involved five sets of forward speeds (3, 5, 7, 8, and 9 km/h) while maintaining a constant rotational speed of 400 r/min.

In the simulation, three different straw lengths (36 mm, 76 mm, and 116 mm) positioned approximately at the same location were chosen for motion tracking based on the simulation model. This numerical treatment aimed to analyze the motion behavior of straw under constant conditions of rotational speed (400 r/min) and forward speed (7 km/h).

2.5. Statistical Analysis

Detection of significant differences among the results was performed through analysis of variance using SPSS ver.23 [24]. A significance level of 0.05 in a Duncan test was adopted in this study [25].

3. Results and Discussions

3.1. Measurement Method of Straw Displacement

3.1.1. Effect of Tracer Orientations on Straw Displacement

Longitudinal and lateral orientations were observed for all straw tracers during the experiment. Forward and side straw displacements, measured using longitudinal and lateral tracers, are depicted in Figure 6. The round roller-claw anti-blocking mechanism was tested at rotational speeds of 260, 400, 530, and 740 r/min, respectively, along with three forward speeds of 3, 5, and 7 km/h.

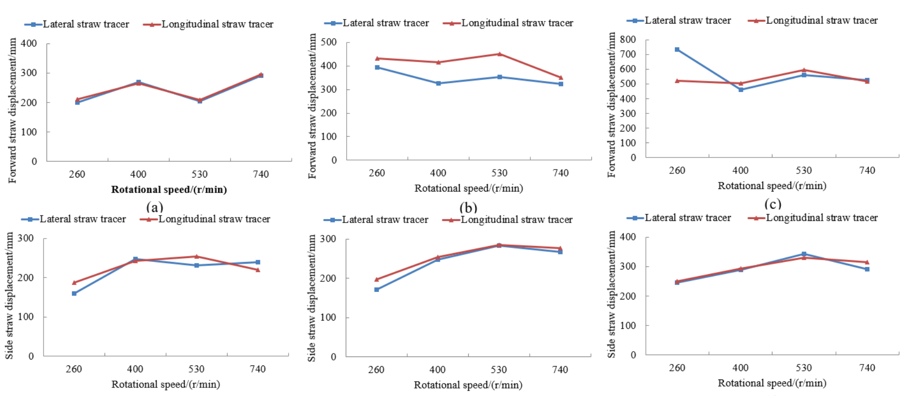

Figure 6. Straw displacements measured with longitudinal and lateral straw tracers: (**a**,**d**) straw forward and side displacements under forward speeds of 3 km/h; (**b**,**e**) straw forward and side displacements under forward speeds of 5 km/h; (**c**,**f**) straw forward and side displacements under forward speeds of 7 km/h.

Figure 6a–c depicts the forward displacement of straw measured by tracers placed both longitudinally and laterally under varying operational conditions. The discrepancy between the measurements was minimal at a forward speed of 3 km/h (Figure 6a), exhibiting an average absolute difference of 6.2 mm and an average relative difference of 2.8%. However, at a forward speed of 5 km/h (Figure 6b), the disparity peaked, with an average absolute difference of 63.1 mm and an average relative difference of 18.3%. Notably, at a forward speed of 7 km/h, a notable difference emerged only when the anti-blocking mechanism operated at a rotational speed of 260 rpm, resulting in an absolute difference of 212 mm, possibly attributable to considerable error induced by straw dragging [26]. Additionally, the average absolute error under varying operating parameters was 29.22 mm, with a relative error of 5.83%. The side displacement of straw, as depicted in Figure 6d–f, was measured using tracers positioned both longitudinally and laterally across various operational settings. The comparison revealed a slight disparity between the measurements obtained from the two placement strategies, showing an average absolute difference of 13.93 mm and a relative difference of 5.83%.

The analysis suggested that tracers employing the two placement strategies manifest noteworthy errors in assessing forward displacement, which ought to be the mean of both. Nonetheless, the discrepancy in side displacement measurement was insignificant. Hence, longitudinal straw tracers are recommended for side displacement measurement, aligning with the findings of Fang et al. [26], that is, when studying the straw displacement under the action of a rotating component, the straw forward displacement can be obtained by considering the average horizontal displacements of longitudinal and lateral tracers, and the straw side displacement can be obtained by considering the lateral displacement of the longitudinal tracer.

3.1.2. Effect of Tracer Positions on Straw Displacement

Using straw tracers positioned variably to measure both forward and side displacements of straw, the effects of the tracer position on straw displacements were ascertained, as depicted in Figure 7.

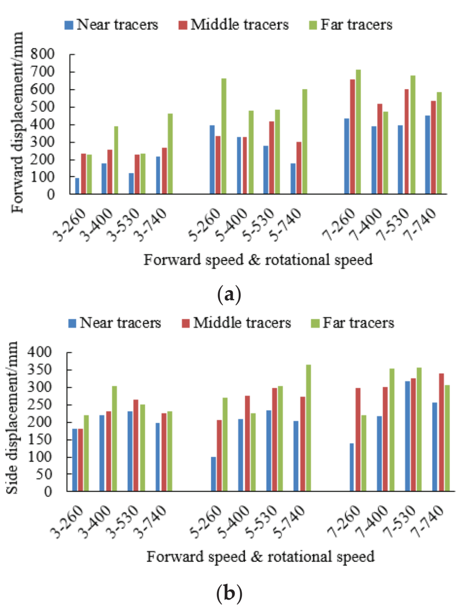

Figure 7. Straw displacements measured with straw tracers at different positions: (**a**) the forward straw displacement measured with straw tracers at different positions; (**b**) the side straw displacement measured with straw tracers at different positions.

The anti-blocking mechanism induces horizontal movement in straw as it advances. Additionally, the rotating mechanism throws straw tangentially, resulting in a combined motion in both horizontal and lateral directions. A comparison of straw displacements in the horizontal and lateral directions reveals that lower forward and rotational speeds of the anti-blocking mechanism result in smaller side displacements of the nearby straw tracer. Furthermore, the side displacement of straw was generally less than the forward displacement, aligning with previous research findings [27]. This phenomenon primarily occurs due to the straw's low side component velocity upon being thrown tangentially by the mechanism, coupled with constraints from surrounding straw.

Straw tracers placed at various positions experience distinct forces from the anti-blocking mechanism and surrounding straw, leading to variations in straw displacement. Both forward and side displacements followed a consistent trend, where the straw tracer at the distant position showed the highest displacement, followed by the middle position, and finally, the nearby position had the smallest displacement. This is attributed to the motion of straw under the influence of the anti-blocking mechanism resembling fluid flow; hence, straw at distant positions experiences larger displacements as it is situated at the periphery of the fluid. Using the displacement measured by the middle-position straw tracer as the control, the average forward displacement of the distant-position straw tracer exceeded that of the middle position by 28.37%, while the middle-position tracer's displacement was 25.75% higher than the nearby tracer. In the lateral direction, the side displacement measured by the straw tracer at the distant position was 5.95% higher than that measured by the straw tracer at the middle position, and the side displacement of the middle-position tracer was 22.07% higher than that of the nearby tracer. Concerning various forward speeds of the anti-blocking mechanism, the forward displacements measured by the distant-position straw tracer were 34.03%, 61.94%, and 5.98% higher than those of the middle position, while the middle-position tracer's displacements were 37.66%, 14.18%, and 27.59% higher than those of the nearby tracer at forward speeds of 3, 5, and 7 km/h. In terms of side displacement, the straw tracer in the middle position showed displacements 8.26%, 28.89%, and 26.26% higher than those of the nearby tracer, respectively, at forward speeds of 3, 5, and 7 km/h. Side displacements measured by the distant-position straw tracer were 11.34% and 10.79% higher than those measured by the middle-position straw tracer at forward speeds of 3 and 5 km/h, respectively. At a forward speed of 7 km/h, the distant position straw tracer's displacements were marginally (1.94%) less than those of the middle-position straw tracer.

Furthermore, upon comparing the average displacements of the straw tracers at distant and nearby positions with the displacement obtained by the straw tracer in the middle position, it was found that the relative errors in forward and side displacements under various operating parameters of the anti-blocking mechanism were 21.25% and 12.35%, respectively. At a forward speed of 3 km/h for the anti-blocking mechanism, the difference in forward displacement between them exhibited no discernible pattern with variations in the rotational speed of the anti-blocking mechanism. This observation was consistent for side displacement as well, with relative errors in forward and side displacements at 23.06% and 9.75%, respectively. When the forward speed of the anti-blocking mechanism was 5 km/h, the mean forward displacement of the straw tracers at distant and nearby positions was 29.95% higher than that of the straw tracer in the middle position, while the mean side displacement was 11.14% lower than that of the straw tracer in the middle position. At a forward speed of 7 km/h for the anti-blocking mechanism, the average forward displacement of the straw tracers at distant and nearby positions was 10.73% less than that of the straw tracer in the middle position. Moreover, the side displacement of the two exhibited no apparent correlation with alterations in the rotational speed of the anti-blocking mechanism, with a relative error of 16.16%.

Hence, to comprehensively account for the impact of straw tracers at distinct positions on straw displacement and to better reflect the actual dynamics of straw movement, this research adopted the mean displacements of straw tracers at varied positions as representative values for straw displacement. The straw tracers were generally not placed in different positions in previous studies [26,27], and this study provides a straw displacement measurement method to reduce measurement errors caused by the position of straw tracers. Specifically, the mean forward displacement of straw tracers at distant, middle, and nearby positions will serve as the horizontal displacement metric for straw, while the mean side displacement of straw tracers in the same positions will function as the corresponding side displacement metric.

3.2. Straw Displacement Influenced by the Working Parameters of the Mechanism

Following the harvest of the wheat crop, the straw is distributed across the field, after which maize seeding is conducted directly. If the straw cannot be pushed ahead and sideways, the maize planter is prone to blockages. Assessing the impact of operational parameters on straw displacement is crucial for evaluating the effectiveness of the anti-blocking mechanism [10]. Figure 8 displays the forward, side, and total straw displacement under various rotational speeds (260, 400, 530, and 740 rpm) and forward speeds (3, 5, and 7 km/h) of the anti-blocking mechanism. Apart from instances where the straw forward displacement was marginally less than the side displacement at a forward speed of 3 km/h and a rotational speed of 530 rpm, the forward displacement consistently exceeded the side displacement across all operational parameters of the anti-blocking mechanism. The average absolute value of displacement was 155 mm, with a relative difference of 58.95%.

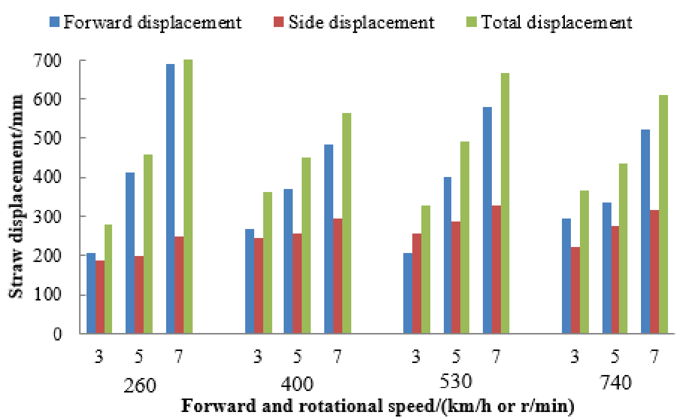

Figure 8. The forward straw displacement measured in different forward and rotational speed conditions.

Forward displacement of straw increased with the forward speed of the mechanism, which maintained consistency across all four rotational speeds of the anti-blocking mechanism. a lower rotational speed of the anti-blocking mechanism correlated with a higher increase in the straw forward displacement rate. At a rotational speed of 260 rpm, the forward displacement increased by 100.49% when the forward speed changed from 3 km/h to 5 km/h, and by 233.98% when the forward speed increased from 3 km/h to 7 km/h. Nevertheless, no consistent pattern emerged in the straw forward displacement variations with rotational speed at a constant forward speed of the mechanism.

Regarding side displacement, straw displacement increased with forward speed, consistent across all four rotational speeds of the anti-blocking mechanism. A higher rotational speed of the anti-blocking mechanism correlated with a greater increase in straw side displacement rate. At a rotational speed of 740 rpm, side displacement increased by 25.38% as the forward speed changed from 3 km/h to 5 km/h, and by 43.20% as the forward speed increased from 3 km/h to 7 km/h. Nevertheless, no consistent pattern emerged in straw side displacement variations with rotational speed at a constant forward speed of the mechanism.

Concerning total displacement, straw displacement rose with an increasing forward speed of the mechanism at constant rotational speeds of the anti-blocking mechanism, consistent across all four rotational speeds. Since forward displacement of straw consistently exceeded side displacement, the trend in total straw displacement mirrored that of forward displacement. Thus, a lower rotational speed of the anti-blocking mechanism resulted in a higher rate of increase in total straw displacement. At a rotational speed of 260 rpm, total displacement increased by 64.23% as the forward speed changed from 3 km/h to 5 km/h, and forward displacement increased by 162.47% as the forward speed increased from 3 km/h to 7 km/h. Nevertheless, there was no discernible pattern in the variations in total straw displacement with rotational speed at a constant forward speed of the mechanism.

3.3. Verification of the Numerical Model and Straw Motion Analysis

3.3.1. Verification of the Simulation Model Based on the Straw Clearance Rate

The straw clearance rate might be more suitable to describe straw side movement because it represents the movement behavior of a group of pieces of straw in a defined specific area, while the straw side displacement was measured only by specific straw tracers. The experimental and simulation results of straw clearance rates with different forward speeds are shown in Figure 9, where the rotational speed of the anti-blocking mechanism is 740 rpm.

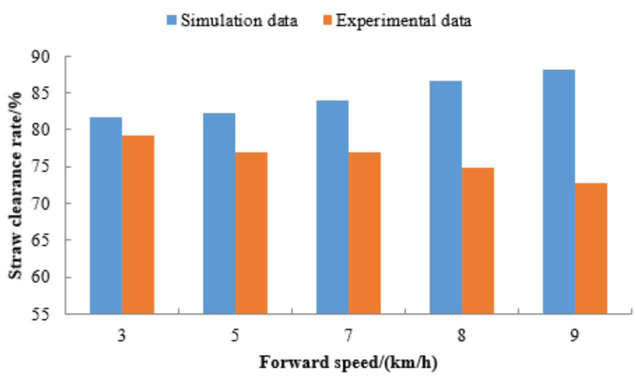

Figure 9. Comparison of straw clearance rates between simulation and experimental results.

The straw clearance rate decreased with the increase in the forward speed of the anti-blocking mechanism in the experiment. The forward speed was too fast for the straw to be ejected from the furrow in time when it moved outward with the anti-blocking mechanism. This also indicated that the straw would remain in the furrow when the ratio of circumferential velocity to forward velocity was large. However, the decrease in the proportion of straw clearance rate with the increase in the forward speed of the mechanism was not significant; the straw clearance rate only increased by 8.17% when the forward speed increased from 3 km/h to 9 km/h.

In the simulation, the straw clearance rate increased with the increase in the forward speed of the anti-blocking mechanism. Additionally, the straw clearance rate only increased by a small margin (7.84%) when the forward speed increased from 3 km/h to 9 km/h. There was a different trend in straw clearance rate variation between the simulation and experimental results, which might be because the straw in the simulation was rigid and did not intertwine and clump together while moving with the anti-blocking mechanism. But during the experiment, where the straw could become entangled and compressed when the forward speed was high, this phenomenon made the straw difficult to eject. The difference in straw clearance rates the between simulation and experimental results might indicate that rigid straw was ejected more easily.

Although the simulation straw clearance rates under various operating parameters were higher than the experimental data, the discrepancies were relatively minor. The average relative error between the experimental and simulation straw clearance rates was 11.20%, with the minimum error (2.99%) occurring at a forward speed of 3 km/h for the anti-blocking mechanism, and the maximum error (20.95%) occurring at a forward speed of 9 km/h. The relative error increased with the increase in the forward speed of the mechanism, indicating that the assumption of rigid straw in the simulation had a greater impact when the forward speed of the mechanism was high. However, the small differences in their values also indicated that the simulation model was suitable for studying the interaction between straw and the anti-blocking mechanism, especially at a lower forward speed (less than 7 km/h, where the error is 9.11%). Therefore, subsequent simulations of straw motion were based on a forward speed of 7 km/h for the anti-blocking mechanism.

3.3.2. Analysis of Individual Straw Movement Behaviors

Three straw tracers, each of different lengths, were selected to track their motion during the simulation. At the beginning of the simulation, all three straws were stationary and were located on the ground in front of the anti-blocking mechanism. Subsequently, under the combined effect of the anti-blocking mechanism and the surrounding straw, they ascended along the rotation direction of the mechanism at a certain speed. Afterwards, the straws were ejected under the increasing centrifugal force and decreasing support force of the straw bed. The changes in the position of the straw in the side, forward, and vertical directions are shown in Figure 10. From the figure, it is evident that although the lengths of the straws are different, their motion behaviors under the action of the anti-blocking mechanism are similar.

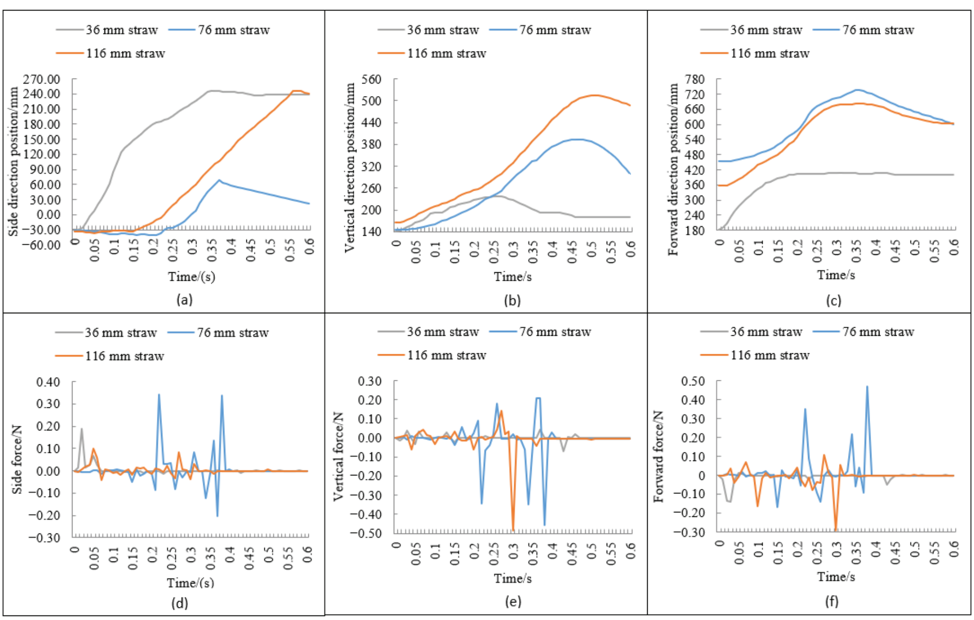

Figure 10. The movement and force of selected straws: (**a**–**c**) the movement trajectory of straw in the side, vertical, and forward directions over time; (**d**–**f**) the force exerted on straw in the side, vertical, and forward directions over time.

In the side direction, the straws moved along the rotation direction of the anti-blocking mechanism and were subsequently ejected. This phenomenon was similar to the motion behavior of straw under the action of rotating mechanisms [27]. The side displacements of the longer and shorter straws were similar, while that of the medium-length straw was the smallest. The shortest straw (36 mm) rapidly moved approximately 280 mm laterally under the influence of the anti-blocking mechanism and then remained nearly stationary thereafter. The longest straw (116 mm) did not exhibit as drastic a movement as the shortest straw (36 mm) but had approximately equal side displacements. The smallest side displacement of the medium-length straw might be due to the inhibiting effect of the surrounding dense straw.

In the vertical direction, the straws exhibited climbing behavior under the influence of the anti-blocking mechanism. This proved that the mechanism with a small-diameter upper and large-diameter lower structure would lift the straw during rotation [15]. Moreover, the climbing behavior was more pronounced and the climbing duration longer for the longer straw. The shortest straw only climbed approximately 95 mm before descending, while the medium-length and the longest straw climbed 248 mm and 348 mm, respectively. The vertical motion of the straw tracers confirmed the functionality of the anti-blocking mechanism in guiding the straw to climb.

In the horizontal direction, the straw moved forward under the influence of the anti-blocking mechanism. All straws of different lengths moved forward under the push of the mechanism initially. Subsequently, the medium-length straw and the longest straw exhibited backward behavior after losing the guiding effect of the mechanism. The continuous backward movement behavior indicated that the straw formed a smooth flow under the action of the mechanism. Additionally, the longer the straw, the greater the distance it travelled; for example, the 116 mm straw moved 325 mm in the forward direction.

4. Conclusions

A tracer-based measurement method was applied to investigate the impact of operational parameters of the anti-blocking mechanism on straw displacement. Then, a straw–soil-mechanism interaction model was developed using EDEM 2022 software. The model's feasibility was confirmed from the perspective of straw clearance rates. Furthermore, the model was used to study the individual motion behavior of straw over time under the influence of the anti-blocking mechanism. The research results showed that the tracer method could be used to study the straw displacement under the action of the anti-blocking mechanism. The experimental results also indicated that the forward displacement, side displacement, and total displacement of the straw increased with the increase in the forward speed of the mechanism at a constant speed of rotation. The straw–soil–mechanism interaction model could be used to study the motion behavior of straw. Straws in different positions had similar movement behaviors under the action of the anti-blocking mechanism. The motion behavior of straw under the anti-blocking mechanism offers insights into the interactions among straw, soil, and anti-blocking mechanisms.

Author Contributions: Conceptualization, Q.Z. and H.F.; methodology, Q.Z. and M.N.; software, Q.Z. and H.F.; validation, Q.Z., H.F. and G.X.; formal analysis, M.N. and J.L.; investigation, Q.Z., H.F., G.X. and M.N.; resources, H.F.; data curation, H.F.; writing—original draft preparation, Q.Z. and J.L.; writing—review and editing, H.F., G.X. and M.N.; visualization, Q.Z.; supervision, H.F.; project administration, H.F.; funding acquisition, H.F. All authors have read and agreed to the published version of the manuscript.

Funding: This research was funded by the China Postdoctoral Science Foundation, grant number 2023M741433, the Research Foundation for Talented Scholars of Jiangsu University, grant number 22JDG041, the Priority Academic Program Development of Jiangsu Higher Education Institutions, grant number PAPD-2023-87, and the Jiangsu University Agricultural Engineering Department Project, grant number NGXBTD20240307.

Institutional Review Board Statement: Not applicable.

Data Availability Statement: The analyzed datasets are available from the corresponding author on reasonable request.

Conflicts of Interest: The authors declare no conflicts of interest.

References

1. Li, W.; Zhang, C.; Ma, T.; Li, W. Estimation of summer maize biomass based on a crop growth model. *Emir. J. Food Agric.* **2021**, *33*, 742–750. [CrossRef]
2. Memon, M.S.; Chen, S.; Niu, Y.; Zhou, W.; Elsherbiny, O.; Liang, R.; Du, Z.; Guo, X. Evaluating the efficacy of sentinel-2B and landsat-8 for estimating and mapping wheat straw cover in rice-wheat fields. *Agronomy* **2023**, *13*, 2691. [CrossRef]
3. Guo, Y.; Cui, M.; Xu, Z. Spatial characteristics of transfer plots and conservation tillage technology adoption: Evidence from a survey of four provinces in China. *Agriculture* **2023**, *13*, 1601. [CrossRef]
4. Melland, A.R.; Antille, D.L.; Dang, Y.P. Effects of strategic tillage on short-term erosion, nutrient loss in runoff and greenhouse gas emissions. *Soil Res.* **2016**, *55*, 201–214. [CrossRef]
5. Tunio, M.H.; Gao, J.; Talpur, M.A.; Lakhiar, I.A.; Chandio, F.A.; Shaikh, S.A.; Solangi, K.A. Effects of different irrigation frequencies and incorporation of rice straw on yield and water productivity of wheat crop. *Int. J. Agric. Biol. Eng.* **2020**, *13*, 138–145. [CrossRef]
6. Khan, I.; Iqbal, B.; Khan, A.A.; Inamullah; Rehman, A.; Fayyaz, A.; Shakoor, A.; Farooq, T.H.; Wang, L. The interactive impact of straw mulch and biochar application positively enhanced the growth indexes of maize (*Zea mays* L.) crop. *Agronomy* **2022**, *12*, 2584. [CrossRef]
7. Ahmad, F.; Adeel, M.; Qiu, B.; Ma, J.; Shoaib, M.; Shakoor, A.; Chandio, F.A. Sowing uniformity of bed-type pneumatic maize planter at various seedbed preparation levels and machine travel speeds. *Int. J. Agric. Biol. Eng.* **2021**, *14*, 165–171. [CrossRef]
8. Zhang, X.; Li, H.; Du, R.; Ma, S.; He, J.; Wang, Q.; Chen, W.; Zheng, Z.; Zhang, Z. Effects of key design parameters of tine furrow opener on soil seedbed properties. *Int. J. Agric. Biol. Eng.* **2016**, *9*, 67–80.
9. Yao, W.; Diao, P.; Miao, H.; Li, S. Design and experiment of anti-blocking components for shallow stubble clearing based on soil bin test. *Agriculture* **2022**, *12*, 1728. [CrossRef]
10. Fang, H.; Niu, M.; Zhu, Z.; Zhang, Q. Experimental and numerical investigations of the impacts of separating board and anti-blocking mechanism on maize seeding. *J. Agric. Eng.* **2022**, *LIII*, 1273.
11. Li, Y.; Lu, C.; Li, H.; He, J.; Wang, Q.; Huang, S.; Gao, Z.; Yuan, P.; Wei, X.; Zhan, H. Design and experiment of spiral discharge anti-blocking and row-sorting device of wheat no-till planter. *Agriculture* **2022**, *12*, 468. [CrossRef]
12. Zhu, H.; Zhang, X.; Hong, Y.; Bai, L.; Zhao, H.; Ma, S. Design and experiment of bionic shifting and diffluence straw anti-blocking device. *Agric. Res. Arid Areas* **2023**, *41*, 318–328.
13. Du, W.; Zhou, G.; Zhang, Q.; Bian, Q.; Liao, Q.; Liao, Y. Design and experiment of the anti-blocking device combined stubble burying for rapeseed direct seeding. *Trans. Chin. Soc. Agric. Eng.* **2024**, *40*, 60–70.
14. Li, Y.; Lu, C.; Li, H.; Wang, Z.; Gao, Z.; Wei, X.; He, D. Design and experiment of symmetrical spiral row-sorting of the straw device based on kinematics analysis. *Agriculture* **2022**, *12*, 896. [CrossRef]
15. Niu, M.; Fang, H.; Chandio, F.A.; Shi, S.; Xue, Y.; Liu, H. Design and experiment of separating guiding anti-blocking mechanism for no-tillage maize planter. *Trans. Chin. Soc. Agric. Mach.* **2019**, *50*, 52–58.
16. Jiang, L.; Tang, Q.; Wu, J.; Yu, W.; Zhang, M.; Jiang, D.; Wei, D. Design and test of seedbed preparation machine before transplanting of rapeseed combined transplanter. *Agriculture* **2022**, *12*, 1427. [CrossRef]
17. Yao, W.; Zhao, D.; Miao, H.; Cui, P.; Wei, M.; Diao, P. Design and experiment of oblique anti-blocking device for no-tillage planter with shallow plowing stubble clearing. *Trans. Chin. Soc. Agric. Mach.* **2022**, *53*, 42–52.
18. Zhu, H.; Wu, X.; Qian, C.; Bai, L.; Ma, S.; Zhao, H.; Zhang, X.; Li, H. Design and experimental study of a bi-directional rotating stubble-cutting no-tillage planter. *Agriculture* **2022**, *12*, 1637. [CrossRef]
19. Wang, L.; Bian, O.; Liao, Q.; Wang, B.; Liao, Y.; Zhang, O. Burying stubble and anti-blocking deep fertilization composite device for rapeseed direct planting in high stubble and heavy soil rice stubble field. *Trans. Chin. Soc. Agric. Mach.* **2023**, *54*, 83–94.
20. Fang, H.; Shi, S.; Qiao, L.; Niu, M.; Xu, G.; Jian, S. Numerical and experimental study of working performance of round roller claw type anti-blocking mechanism. *J. Chin. Agric. Mech.* **2018**, *39*, 1–9.
21. Gu, Y.; Zhang, Y.; Song, J. A study on "laminar flow splitter" as blocking proofing device for mulching no-tillage planters. *Trans. Chin. Soc. Agric. Mach.* **1994**, *25*, 46–51.
22. Gao, N.; Zhang, D.; Yang, L.; Cui, T. Design of anti-blocking mechanism combined driven divider with passive residue separating device. *Trans. Chin. Soc. Agric. Mach.* **2014**, *45*, 85–91.
23. Liao, Q. Analysis on the saw-tooth anti-blocking mechanism for no-tillage planter by the high-speed photograph technology. *Trans. Chin. Soc. Agric. Mach.* **2005**, *26*, 46–49.
24. George, D.; Mallery, P. *IBM SPSS Statistics 23 Step by Step: A Simple Guide and Reference*, 14th ed.; Routledge, Taylor & Francis Group: London, UK, 2016; pp. 169–176.
25. Fang, H.; Niu, M.; Wang, X.; Zhang, Q. Effects of reduced chemical application by mechanical-chemical synergistic weeding on maize growth and yield in East China. *Front. Plant Sci.* **2022**, *13*, 1024249. [CrossRef]

26. Fang, H.; Zhang, Q.; Chandio, F.A.; Guo, J.; Sattar, A.; Arslan, C.; Ji, C. Effect of straw length and rotavator kinematic parameter on soil and straw movement by a rotary blade. *Eng. Agric. Environ. Food* **2016**, *9*, 235–241. [CrossRef]
27. Fang, H.; Ji, C.; Ahmed, A.T.; Zhang, Q.; Guo, J. Simulation analysis of straw movement in straw-soil-rotary blade system. *Trans. Chin. Soc. Agric. Mach.* **2016**, *47*, 60–67.

agriculture

MDPI

Article

Design and Experimentation of Rice Seedling Throwing Apparatus Mounted on Unmanned Aerial Vehicle

Peichao Yuan [1], Youfu Yang [1], Youhao Wei [1], Wenyi Zhang [2,*] and Yao Ji [1,*]

[1] Nanjing Institute of Agricultural Mechanization, Ministry of Agriculture and Rural Affairs, Nanjing 210014, China; 82101212127@caas.cn (P.Y.); 82101215527@caas.cn (Y.Y.); 82101225605@caas.cn (Y.W.)
[2] Graduate School of Chinese Academy of Agricultural Sciences, Beijing 100083, China
* Correspondence: zhangwenyi@caas.cn (W.Z.); jiyao@caas.cn (Y.J.)

Abstract: In order to further exploit the production advantages of rice throwing, this paper proposes a systematically designed throwing device suitable for integration with unmanned aerial vehicles (UAVs). The device primarily comprises a seedling carrying and connection system, a seedling pushing mechanism, and a seedling guiding device. The operational principles and workflow of the device are initially elucidated. Subsequently, an analysis of factors influencing rice throwing effectiveness is conducted, with throwing height, working speed, and the bottom diameter of the seedling guide tube identified as key factors. Seedling spacing uniformity and seedling uprightness are designated as performance indicators. A three-factor, three-level response surface experiment is conducted, yielding regression models for the experimental indicators. Through an analysis of the response surface, the optimal parameter combination is determined to be a throwing height of 142.79 cm, a working speed of 55.38 r/min, and a bottom diameter of the seedling guide tube of 43.51 mm. At these parameters, the model predicts a seedling spacing uniformity of 88.43% and a seedling uprightness of 88.12%. Field experiments validate the accuracy of the optimized model results. Experimental data indicate that under the optimal operational parameters calculated by the regression model, the seedling spacing uniformity is 86.7%, and the seedling uprightness is 84.2%. The experimental results meet the design requirements, providing valuable insights for UAV rice-throwing operations.

Keywords: agricultural machinery; unmanned aerial vehicle; transplanting device; experiment

Citation: Yuan, P.; Yang, Y.; Wei, Y.; Zhang, W.; Ji, Y. Design and Experimentation of Rice Seedling Throwing Apparatus Mounted on Unmanned Aerial Vehicle. *Agriculture* **2024**, *14*, 847. https://doi.org/10.3390/agriculture14060847

Academic Editors: Dainius Steponavičius and Caiyun Lu

Received: 16 April 2024
Revised: 21 May 2024
Accepted: 27 May 2024
Published: 28 May 2024

1. Introduction

Rice constitutes a primary staple crop in China. Rice seedlings transplanted through the process of seedling throwing exhibit growth advantages such as rapid growth and prolific tillering. This practice contributes to the enhancement of rice yield, demonstrating considerable potential for further development [1–4]. To further exploit the advantages of rice throwing, mechanized rice transplanters have rapidly evolved from disorderly to orderly operations [5]. Domestically, orderly rice transplanters mainly include the following three methods: pneumatic, roller-type, and clamping, which transfer seedlings into the field through seedling guides. Pneumatic transplanters occasionally encounter issues with nozzle failure, resulting in unstable operation. Roller-type transplanters may cause damage to seedlings. Clamping transplanters are prone to drift issues and require higher field preparation standards [6–8]. Additionally, the terrain in hilly and mountainous areas is characterized by small agricultural plots and steep slopes. Ground machinery operation is challenging, and field-to-field transitions pose difficulties. The mechanization level of rice cultivation in domestic hilly areas is less than 10% [9–11].

To address these issues, this study aims to leverage the advantages of UAVs for seedling throwing operations. UAV operations are characterized by rapid execution speed and excellent maneuverability [12]. Using UAVs allows for liberation from the structural constraints inherent in ground-based machinery. This facilitates the adjustment of seedling throwing height, thereby enhancing planting effectiveness. In hilly and mountainous terrain, UAVs experience lesser influence from topography. This is another advantage that distinguishes it from ground-based machinery.

Research on agricultural UAVs includes aspects such as agricultural monitoring and disaster assessment using remote sensing technology [13–16]. In terms of UAV operations, applications such as fertilization, pesticide spraying, and seeding have been explored [17–20]. There has been limited research on UAV rice throwing. Therefore, investigating the application of UAVs for solid material handling is of significant reference value to this study [21,22]. In the fertilization stage of UAV operations, flight altitude and spreading speed significantly affect fertilization effectiveness [23–25]. In the seeding stage, agricultural UAVs mainly employ the following two forms of seeding: disorderly broadcasting and orderly row broadcasting [26]. Orderly row broadcasting typically requires guiding channels to control the seed distribution. Song Cancan et al. [27] have studied the wind distribution around multi-rotor UAVs and designed a pneumatic rice seeding device. This device is regulated by a groove wheel to control the amount of seed discharge. The high-speed airflow generated by the fan accelerates the expulsion of rice seeds. Subsequently, the rice seeds are dispersed through separate and independent diversion channels. This method enhances the controllability and uniformity of rice seed sowing. Liu Wei et al. [28] studied the stability of the displacement of a sowing device under a fixed sowing speed condition. He developed a rice seeding device capable of simultaneously sowing five rows. The seeding rate of this device can be adjusted according to the operational requirements.

In conclusion, operational speed, flight altitude, and guiding devices are important factors influencing the orderly operation of UAVs. In recent years, domestic agricultural UAVs have seen rapid development, with continuous expansion of their operational capabilities and significant enhancement of their performance. With the increasing market ownership of UAVs, a deep material technology foundation has been laid for orderly seedling-throwing by UAVs. This paper presents the design of a UAV-mounted sequential rice seedling throwing apparatus. The operational parameters of this device were optimized through bench testing. The validation of the device was conducted through field trials. The aim is to provide design references for expanding the production applications of UAVs and complement existing seedling-throwing machinery types.

2. Materials and Methods

2.1. Overall Structure and Workflow

The UAV-mounted rice-throwing device comprises the seedling carrying and connection system, the seedling pushing mechanism, and the seedling guiding mechanism, as illustrated in Figure 1. The MG-1P agricultural UAV is chosen as the power platform. This UAV is manufactured by DJI, located in Shenzhen, China. It has a rated payload of 10 kg and a maximum flight time of approximately 9 min when fully loaded. The seedling carrying and connection system is placed on a specially designed landing gear, with the seedling pushing mechanism mounted at the bottom of the seedling carrying and connection system. The seedling guiding mechanism is installed beneath the seedling carrying and connection system and the seedling pushing mechanism. The devices that the UAV needs to suspend are all manufactured using 3D printing technology (manufactured by Wenext, headquartered in Shenzhen, China). Their total mass is approximately 5.2 kg, and when fully loaded with seedlings, the overall weight does not exceed 9.8 kg.

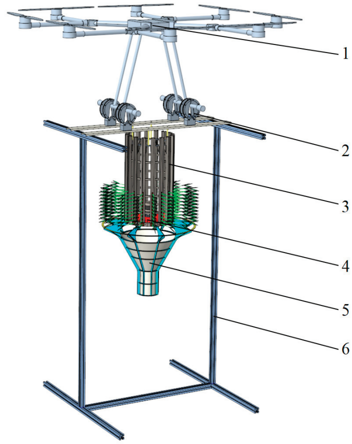

Figure 1. Overall structure of UAV transplanting system: 1. unmanned aerial vehicle; 2. connection mechanism; 3. seedling carrying box; 4. seedling pushing mechanism; 5. seedling guiding device; 6. docking frame.

Based on the operational status during UAV operation, the process can be divided into four stages. First, during the preparation stage, well-nurtured rice bowl seedlings are preloaded into the seedling carrying mechanism before UAV operation. The entire device is then placed on the docking frame. Second, during the seedling retrieval stage, the UAV is remotely controlled to fly above the rice seedling carrying and connection system, hover at an appropriate altitude, and then connect with the UAV using specific mechanical claws. Third, during the operation stage, the UAV suspends the rice seedling throwing apparatus and flies to the designated field. The UAV flies at a constant speed along the planned route. Simultaneously, the remote-controlled seedling-pushing mechanism starts operating. When the first seedling in the seedling slot is ejected, the remaining seedlings fall successively with the assistance of counterweight blocks. Rice seedlings are continuously pushed into the seedling guiding device at a constant speed. Subsequently, the seedlings fall into the field under the combined influence of their own gravity and the airflow generated by the UAV's rotors. The planting process is illustrated in Figure 2. Finally, after the seedling throwing is completed, the UAV flies back above the docking frame. Simultaneously, using a remote control, it opens the mechanical claw to detach from the seedling throwing apparatus. Afterward, the UAV flies toward another seedling-loaded throwing apparatus, repeating the above process in a cycle.

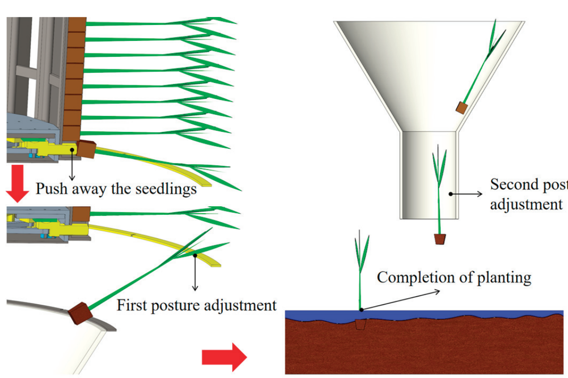

Figure 2. Process of planting seedlings.

2.2. *Working Principle*

2.2.1. Rice Seedling Carrying and Connection System

The seedling carrying and connection system is employed for both loading seedlings and connecting to the UAV. As shown in Figure 3, it consists of two main parts as follows: the seedling carrying box and the connection mechanism. In this study, the traditional tray-in-a-box approach was abandoned, and a ring-stacked seedling carrying box was introduced to facilitate the installation of the UAV. The height of the seedling carrying box is 900 mm. It consists of 16 seedling slots and can carry up to 960 rice seedlings. To avoid the entanglement of leaves, the seedling slots are evenly distributed on a circle with a diameter of 300 mm. The advantage of the circular distribution is that the consistent position of the seedlings can be easily adjusted. Even if the seedlings are pushed out at different positions, there is no cumulative positional error. At the bottom of each seedling tank, there is a 12 mm diameter hole for the push rod and a seedling outlet, and a top cover is installed on the top of the seedling carrying box. It serves to improve the overall structural strength and provides a mounting position for the connecting mechanism. The connection mechanism comprises four specially designed claws arranged in a rectangular distribution and two cantilever beams. The specialized clamp utilizes a parrot-beak-like comb-shaped claw, altering the force distribution of the clamp. It transforms the lateral clamping force acting on the mechanical claw into longitudinal pressure on the "parrot beak" structure. This pressure further differentiates into shear force on the bolts connecting the claws, ensuring the stability of the connection. The connection mechanism is connected to the top cover of the seedling carrying box via four copper screws.

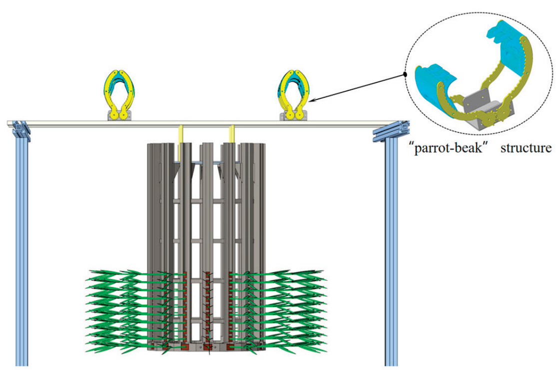

Figure 3. Rice seedling carrying and connection system.

2.2.2. Seedling Pushing Mechanism

The seedling pushing mechanism is utilized to sequentially push rice seedlings out of the seedling carrying box in a predetermined order. Its internal structure is illustrated in Figure 4. The motor base is mounted on the back of the chassis. Within the recess of the chassis, there are 16 identical-sized push rods and connecting rods installed. The push rods are secured onto sliders (MGN7C, manufactured by HIWIN, headquartered in Taiwan, China), ensuring linear movement. At the end face of each push rod, there is a layer of elastic material adhered to prevent damage to the rice bowl substrate during seedling pushing. The distance between the follower crankshaft and the primary crankshaft remains constant. While the length of the connecting rods maintains a fixed proportion to the center distance of the primary crankshaft. The disk is the core component of the seedling-pushing mechanism. It is connected to the follower crankshaft at the bottom, connected to the connecting rods at the top, and linked to the primary crankshaft in the middle section. The motor (42GA775, manufactured by Vantel, headquartered in Jiangsu, China) is connected to the center of the chassis via a primary crankshaft. When the motor drives the main crankshaft to rotate one full circle, it sequentially pushes out 16 rice seedlings.

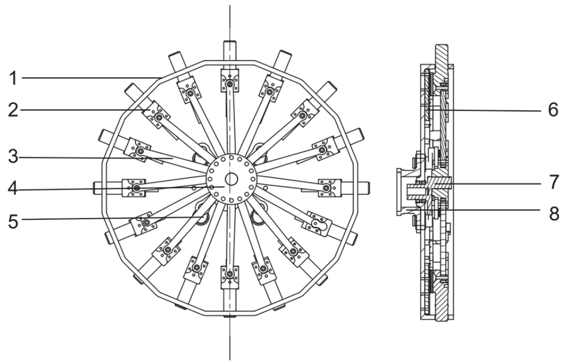

Figure 4. Composition of the Pushing Seedling Institution section: 1. seedling pushing chassis; 2. push rod; 3. connecting rod; 4. disk; 5. follower crankshaft; 6. slide; 7. primary crankshaft; 8. motor base.

The seedling pushing mechanism consists of two types of four-bar linkages combined. The primary crankshaft, follower crankshaft, and disk form a double-crank mechanism. The disk, connecting rod, and push rod form a crank-slider mechanism. In the double-crank mechanism, the motion of each point on the disk follows a circular trajectory consistent with the end of the primary crankshaft. Thus, this point and the center of the hidden trajectory can serve as the crank in the crank-slider mechanism. With this design approach, it is possible to achieve a single motor input and multiple pushrod outputs.

Taking the end actuator of the seedling pushing mechanism as the research subject, the schematic diagram of its mechanism motion is illustrated in Figure 5, where a Cartesian coordinate system is established. The rotated center of the primary crankshaft after translation is the origin *O*. The direction of the push rod axis is the x-axis and the vertical direction is the y-axis. Here, *ab* represents the primary crankshaft, with *a* length of l_1, and *bc* represents the connecting rod with a length of l_2. When the primary crankshaft rotates at an angle α, the angle between the push rod axis and the connecting rod is β, at which point the distance of the slider from the rotation center is *L*.

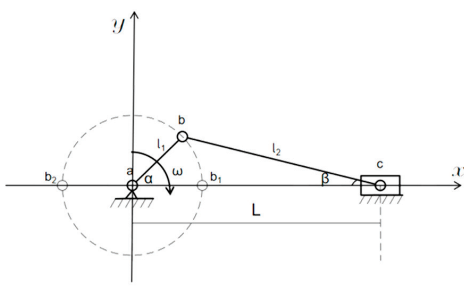

Figure 5. Sketch of the actuating end mechanism of the rice-pushing mechanism.

During the crank rotation, the primary crankshaft and connecting rod are twice in the same straight line, the crank positions are ab_1 and ab_2, which correspond exactly to the two limit positions of the slider, and their distances from the center of rotation are $L_{\max}$ and $L_{\min}$, respectively, which can be computed to derive the push rod strokes as follows:

$$s = L_{\max} - L_{\min} = 2 \times l_1 \quad (1)$$

The height of the rice seedling bowl used in this article is 18 mm. To ensure that the rice seedlings can be fully pushed out, according to Equation (1), the length of the main shaft should be at least 9 mm. Without affecting the working performance, and to ensure a more compact coordination of each part, the dimensions of each component are finally determined. The center distance between the primary crankshaft and the follower crankshaft is 12 mm. The length of the connecting rod is 72 mm. The diameter of the push rod is 12 mm. The diameter of the disk is 50 mm. The diameter of the outer circle of the seedling pushing chassis is 254 mm.

The closed vector equation of the mechanism is as follows:

$$\begin{cases} \vec{L}_1 + \vec{L}_2 = \vec{L} \\ l_1 e^{-i\alpha} + l_2 e^{i\beta} = L \end{cases} \tag{2}$$

Expanding Equation (2) using Euler's formula as follows:

$$\begin{cases} L = l_1 \cos\alpha + l_2 \cos\beta \\ l_1 \sin\alpha - l_2 \sin\beta = 0 \end{cases} \tag{3}$$

Differentiating Equation (2) yields the velocity equation for the slider L as follows:

$$-l_1\omega_1 i e^{-i\alpha} + l_2\omega_2 i e^{i\beta} = V_l \tag{4}$$

Expanding Equation (4) using Euler's formula as follows:

$$\begin{cases} -l_1\omega_1 i \cos\alpha + l_1\omega_1 \sin\alpha + l_2\omega_2 i \cos\beta - l_2\omega_2 \sin\beta = V_l \\ V_l = l_1\omega_1 \sin\alpha - l_2\omega_2 \sin\beta \end{cases} \tag{5}$$

where L represents the distance from the slider to the center of rotation; l_1 denotes the distance from the crankshaft center; l_2 stands for the length of the connecting rod; α represents the angle turned by the crankshaft; β indicates the angle of the connecting rod; ω_1 represents the angular velocity of the crankshaft; and ω_2 represents the angular velocity of the connecting rod.

From Equation (3), it can be observed that when the end displacement of the push rod is maximal, $\alpha = 0°$ and $\beta = 180°$, or when the end displacement of the push rod is minimal, $\alpha = 180°$ and $\beta = 0°$. Substituting these values into Equation (3) reveals that the velocity of the push rod at these points is zero. This reduces the risk of damaging the seedling matrix. Additionally, the positions of the push rod at any two symmetric locations within the transplanting mechanism are identical, but their trends of variation are opposite. Within the 180° division, the values of α and β for any given phase of the push rod are unequal. It indicates that the motion states of the push rod correspond differently to each phase. This validates the feasibility of gradual transplanting.

The operation process of a single push rod is illustrated in Figure 6a, which depicts the following three sequential positions: the origin, midpoint, and apex positions. These positions correspond to the beginning, middle, and end stages of seedling transplantation, respectively, indicating the relative positions of the seedlings and the transplanting mechanism. As depicted in Figure 6b, the origin position aligns with the bottom end face of the seedling trough, while the apex position aligns with the seedling ejection point. Building upon this foundation, sixteen push rods initiate reciprocating motions in the same sequential order, as shown in Figure 6c. When push rod 1 reaches the apex position, the seedling is completely ejected from the trough, marking the completion of the seedling pushing process. Meanwhile, push rod 2 reaches the midpoint position with its velocity directed outward along the axis, indicating that the seedling is about to be ejected. Conversely, push rod 16, the last push rod in the rotation direction, also reaches the midpoint position with its velocity directed inward along the axis. This indicates that the seedlings have been pushed out before push rod 1.

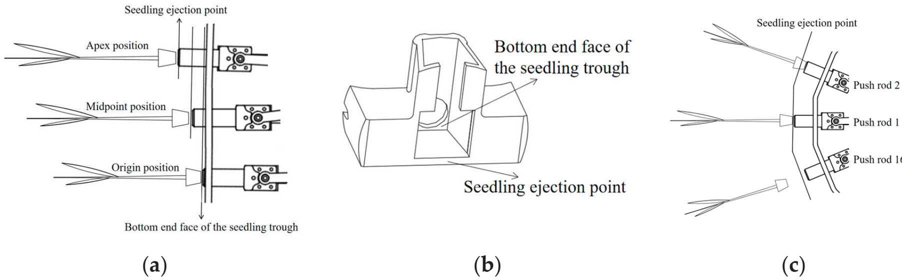

Figure 6. Timing diagram of pushing rice planting movement: (**a**) different timing positions for the same putter; (**b**) position interpretation; (**c**) same timing position for different putters.

2.2.3. Seedling Guiding Device

The seedling guiding apparatus is utilized to adjust the posture of rice seedlings during transplantation, ensuring that the root portion of the seedlings faces downward and descends in an upright manner, as depicted in Figure 7. The blocking ring structure restricts the movement of the seedling tip, facilitating the seedling bowl to drop first. The conical section of the seedling guide pipe concentrates the landing position of rice seedling bowls. The cylindrical narrowing section of the guide pipe enhances the uprightness of the seedlings. In order to reduce the overall weight of the device, it comprises an external framework and internal seedling guide pipe. The external framework is securely fastened to the seedling carrier frame using bolts. The internal seedling guide pipe is positioned within the external framework, enabling adjustment of the rice seedling drop channel. Since the external framework bears the primary load, the internal seedling guide pipe can be made as thin as possible. By maintaining seedling guidance functionality, the overall weight of the guide tube can be significantly decreased.

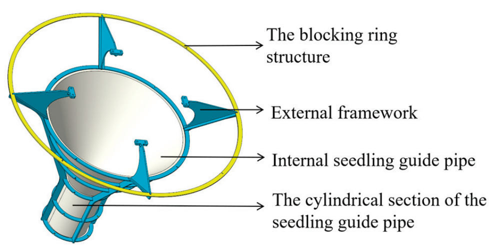

Figure 7. Seedling Guiding Device.

3. Working Performance Test

3.1. Platform Test

The platform test in this study utilized a square soil trough provided by the Nanjing Agricultural Mechanization Research Institute of the Ministry of Agriculture and Rural Affairs. The dimensions of the trough are 500 cm $\times$ 100 cm $\times$ 30 cm. According to the requirements for rice seedling throwing, the soil in the trough needs to undergo soaking, pulping, and settling treatment. Rice seedlings selected for throwing should be at the three-leaf stage, with the height of the seedlings ranging between 160 and 180 mm. The experimental platform is depicted in Figure 8. The UAV was securely fastened to the platform and rotated at idle speed during the experiments. The seedling throwing apparatus could be directly placed on the square frame. A motor was used to drive a synchronous belt for moving the platform.

Figure 8. Test stand.

3.1.1. Test Conditions

To investigate the effects of seedling throwing height, primary crankshaft working speed, and bottom diameter of the seedling guide tube on the rice seedling throwing performance. These factors were chosen as the three variables in the experiment. The spacing pass rate and the uprightness pass rate were selected as the evaluation criteria. The expressions for each criterion are as follows:

$$U = \frac{V_0}{V} \times 100\% \tag{6}$$

$$I = \frac{M_0}{V} \times 100\% \tag{7}$$

where U represents the spacing pass rate; I denotes the qualified rate of rice seedling uprightness; V_0 stands for the number of qualified seedlings with appropriate plant spacing within the measured area; M_0 represents the number of upright seedlings counted within the measured area; and V represents the total number of seedlings measured within the measured area.

In this experiment, the standard plant spacing for transplanting is 150 mm. To maintain stable plant spacing, the rotational speed of the main shaft is kept in linkage with the flight speed of the UAV. Each rotation of the primary crankshaft will push out 16 rice seedlings. The flight speed of the UAV at this point is shown in Equation (8). Design-Expert 10 was utilized to design a three-factor, three-level quadratic orthogonal experimental design. After verification, it was determined that the throwing height should be selected between 120 and 160 cm; the primary crankshaft working speed should range from 45 to 75 r/min; and the bottom diameter of the seedling guide tube should be between 40 and 60 mm. Table 1 presents the influencing factors and their levels.

$$v = \frac{16qn}{60} \tag{8}$$

where v represents the flight speed of the UAV, m/s; q represents the standard plant spacing, m; and n represents the rotational speed of the primary crankshaft, rpm.

Table 1. Factor and level design.

Level	Height X_1/cm	Working Speed X_2 (r/min)	Diameter X_3/mm
−1	120	45	40
0	140	60	50
1	160	75	60

3.1.2. Results and Discussion

The experimental results are presented in Table 2. Using Design-Expert 10 software, a multivariate regression fitting analysis was conducted to establish quadratic polynomial regression models for the spacing pass rate, Y_1, and the uprightness pass rate, Y_2, as shown in Equations (9) and (10). Subsequently, variance analysis was performed on the regression equations, with results detailed in Table 3.

$$\begin{aligned} Y_1 = {} & 87.92 - 0.42X_1 - 1.24X_2 - 2.76X_3 + 0.4X_1X_2 - 0.15X_1X_3 - 0.57X_2X_3 \\ & -0.9{X_1}^2 - 1.42{X_2}^2 - 3.17{X_3}^2 \end{aligned} \tag{9}$$

$$\begin{aligned} Y_2 = {} & 87.84 - 0.93X_1 - 0.28X_2 - 1.58X_3 - 0.025X_1X_2 - 0.13X_1X_3 + 0.22X_2X_3 \\ & -2.16{X_1}^2 - 1.46{X_2}^2 - 1.36{X_3}^2 \end{aligned} \tag{10}$$

Table 2. Test results.

Test Number	X_1	X_2	X_3	Spacing Pass Rate Y_1/%	Uprightness Pass Rate Y_2/%
1	1	1	1	80.6	82.2
2	1	−1	0	86.6	83.2
3	−1	1	0	83.8	85.3
4	0	1	0	88.4	88.2
5	0	1	−1	86.1	86.2
6	−1	1	1	82.2	83.7
7	−1	−1	0	87.8	85.6
8	0	1	0	87.6	87.2
9	0	1	1	78.8	83.1
10	1	1	0	84.2	82.8
11	0	1	0	88.2	87.8
12	0	−1	−1	86.7	87.4
13	0	1	0	88.2	87.4
14	1	1	−1	85.8	85.2
15	−1	1	−1	86.8	86.2
16	0	−1	1	81.7	83.4
17	0	1	0	87.2	88.6

Table 3. Analysis of variance for the qualified rates of plant spacing and seedling uprightness.

Variance Source	Degree of Freedom	Sum of Squares		Mean Square		F Value		*p* Value	
		Y_1	Y_2	Y_1	Y_2	Y_1	Y_2	Y_1	Y_2
Model	9	135.47	67.87	15.05	7.54	32.47	21.7	<0.0001	0.0003
X_1	1	1.44	6.85	1.44	6.85	3.12	19.7	0.1208	0.003
X_2	1	12.25	0.61	12.25	0.61	26.42	1.74	0.0013	0.2285
X_3	1	61.05	19.85	61.05	19.85	131.68	57.12	<0.0001	0.0001
X_1X_2	1	0.64	0.0025	0.64	0.0025	1.38	0.0072	0.2785	0.9348
X_1X_3	1	0.09	0.063	0.09	0.063	0.19	0.18	0.6728	0.6842
X_2X_3	1	1.32	0.2	1.32	0.2	2.85	0.58	0.1351	0.4701
${X_1}^2$	1	3.39	19.6	3.39	19.6	7.32	56.41	0.0304	0.0001
${X_2}^2$	1	8.52	8.94	8.52	8.94	18.38	25.74	0.0036	0.0014
${X_3}^2$	1	42.38	7.76	42.38	7.76	91.4	22.33	<0.0001	0.0021
Residual	7	3.25	2.43	0.46	0.35				
Lack of fit	3	2.24	1.12	0.75	0.37	2.96	1.14	0.1609	0.4346
Pure terror	4	1.01	1.31	0.25	0.33	0.41			
Cor total	16	138.72	70.3						

X_1, X_2, and X_3 represent the levels of throwing height, working speed, and bottom diameter of the seedling guide tube, respectively. Y_1 denotes the spacing pass rate, while Y_2 represents the uprightness pass rate.

As shown in Table 3, the significance levels in both regression models are highly significant; all lack-of-fit terms are greater than 0.05, indicating a high degree of fit for the regression models. Therefore, the working parameters of the transplanting device can be optimized using this model.

From the analysis of Table 3, it is evident that the working speed of the throwing mechanism and the diameter of the seedling guide tube have the most significant impact on the spacing pass rate in the model, with their interaction also being highly significant. Similarly, for the uprightness pass rate, the throwing height and the diameter of the seedling guide tube have the most significant impact on the model, with their interaction also being highly significant. To further analyze the interactive effects of throwing height, the working speed of the throwing mechanism, and the bottom diameter of the seedling guide tube on the spacing pass rate and the uprightness pass rate, response surface plots were generated using Design-Expert 10 software, as depicted in Figure 9.

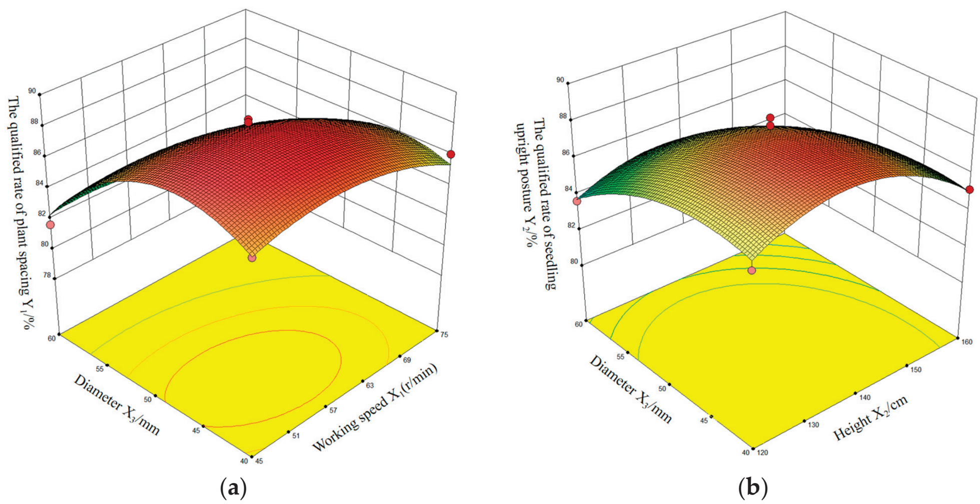

Figure 9. Response surface analysis: (**a**) response surface of the spacing pass rate under different working speeds and bottom diameters of the seedling guide tube; (**b**) response surface of the uprightness pass rate under different throwing heights and bottom diameters of the seedling guide tube.

To achieve the best transplanting effect and obtain the optimal working parameters for each influencing factor, Design-Expert 10 software was utilized to optimize and solve for the throwing height, working speed, and diameter of the bottom opening of the seedling guide tube. The constraint conditions are as shown in Equation (11). When the throwing height is 142.79 cm, the working speed is 55.38 r/min, and the diameter of the seedling guide tube is 43.51 mm, the spacing pass rate is 88.43%, and the uprightness pass rate is 88.12%.

$$\left\{ \begin{array}{l} \left\{ \begin{array}{l} \max Y_1(X_1, X_2, X_3) \\ \max Y_2(X_1, X_2, X_3) \end{array} \right. \\ s.t. \left\{ \begin{array}{l} 120 < X_1 < 160 \\ 45 < X_2 < 75 \\ 40 < X_3 < 60 \end{array} \right. \end{array} \right. \quad (11)$$

3.2. Field Test

To validate the actual planting effect of the UAV orderly throwing device, field experiments were conducted in rice fields at the Baima Experimental Base in Nanjing City, Jiangsu Province. Based on the optimal operating parameters obtained from the platform test, the UAV flight speed was set to 2.2 m/s, the seedling throwing height was set to 143 cm, the primary crankshaft working speed was 55 r/min, and the bottom diameter of the seedling guide tube was 44 mm. The experimental process is depicted in Figure 10.

(**a**) (**b**) (**c**)

Figure 10. Test procedure: (**a**) disengagement from the docking frame; (**b**) flight toward the operating area; (**c**) transplanting effectiveness.

Through experimentation, the spacing pass rate was determined to be 86.7%, while the uprightness pass rate was 84.2%. The experimental findings align with the anticipated design objectives, albeit marginally lower than the optimized model's predictions. This variance is attributed to disparities between the laboratory settings and the field environment. In practical rice paddy operational settings, the effectiveness of throwing seedlings is subject to the influence of environmental wind conditions. Furthermore, distinctions in soil composition between the laboratory and the experimental field contribute to non-uniform soil hardness and varying water depths across different areas of the experimental site. These factors collectively contribute to a slight decrease in the compliance rate observed.

4. Discussion

The basic principle of the seedling throwing machine is to allow rice seedlings to fall into the field relying on their own gravity. During this process, the posture of the seedlings and the speed at which they enter the mud have a significant impact on the planting effect. Currently, most rice seedling throwing machines use the chassis of transplanters, which greatly limits the throwing height. In actual operation, insufficient speed when entering the mud leads to the problem of seedling drifting. Therefore, pneumatic seedling throwing machines have been developed to increase the speed of seedlings entering the mud. Due to the different principles of seedling throwing, the methods for adjusting the posture of different seedling-throwing machines also vary. However, they all aim to ensure a better upright posture of the seedlings. In addition, ground-based seedling throwing machines are inconvenient in complex terrain environments such as hilly areas with steep slopes.

This study employs UAV as the platform for seedling throwing. UAVs can navigate away from the ground, thus exhibiting better adaptability to different plots. UAVs can also easily control height and are almost unrestricted within an effective throwing height. Based on the above advantages, there is a need for more in-depth research on the effect of seedling throwing using UAVs.

From the response surface of the spacing pass rate, it can be observed that an increase in working speed and an enlargement diameter of the seedling guide tube will lead to a decrease in the spacing pass rate. The spacing pass rate is higher when the working speed is between 50 and 70 r/min and the diameter of the seedling guide tube is between 45 and 55 mm. This is because a higher working speed results in a greater throughput of seedlings per second within the seedling guide tube, increasing the risk of seedling jamming and leading to significant variations in plant spacing. A decrease in the diameter of the seedling guide tube causes seedlings to be closer to the central axis of the bottom opening, thereby reducing the degree of variation in plant spacing. However, when the diameter of the seedling guide tube is too small, it may lead to poor seedling dropping, resulting in a decrease in the spacing pass rate.

From the response surface of the uprightness pass rate, it can be seen that an increase in the diameter of the seedling guide tube and an increase in throwing height will result in a decrease in the uprightness pass rate. The best seedling uprightness is achieved when the diameter of the seedling guide tube is between 40 and 55 mm and the throwing height is between 130 and 150 cm. This is because a smaller diameter of the seedling guide tube allows for better adjustment of seedling posture. Lower throwing heights increase the risk of seedling tilting, while higher throwing heights result in greater variability in seedling posture in the air, affecting seedling uprightness.

Within the above parameters, although the UAV operates quickly in a single line, the overall efficiency is limited. For example, when the primary crankshaft speed is 60 r/min, the UAV's flight speed is 2.4 m/s. Without considering the replacement of seedling trays, the theoretical operational efficiency is approximately 0.25 hm^2/h. This efficiency gap compared to ground machinery is significant. To improve efficiency, future research will focus on the following:

1. Investigating multi-row seedling throwing operations by UAVs. Within the limits of payload and flight stability, adding more rows significantly improves the efficiency of seedling throwing;
2. Researching rapid seedling loading methods for UAVs. Although this study proposed a design for a quick-change seedling box, it still requires the manual loading of seedlings into the box. Currently, there is a lack of automated row-wise seedling loading systems to enhance loading efficiency. In the future, efforts can be made to further supplement logistical equipment for UAV operations, gradually improving the completeness of UAV throwing systems;
3. Studying uneven rotor airflow distribution in multi-row operations. After UAVs implement multi-row seedling throwing, the airflow distribution from the rotors beneath the UAV varies. This results in inconsistent wind conditions affecting different parts of the throwing devices. To ensure uniform transplanting, further research is needed on the distribution of rotor airflow in multi-row UAV operations.

5. Conclusions

This paper, based on analyzing the current situation of seedling throwing, presents a novel seedling-throwing scheme design and experimental analysis. The following conclusions have been drawn:

1. In response to the challenges of difficult terrain in hilly areas for ground-based agricultural machinery and suboptimal rice throwing effects, a UAV-based orderly seedling throwing apparatus was designed. The main structural components and operational procedures of the device are introduced. The working principles of key components, such as the seedling carrying and connection system, seedling pushing mechanism, and seedling guiding device, are analyzed;
2. To further enhance the operational performance of the seedling throwing apparatus, an analysis of factors affecting rice throwing effectiveness was conducted. The throwing height, working speed, and diameter of the seedling guide tube outlet were considered as influencing factors. Performance indicators, including the spacing pass rate and the uprightness pass rate, were used. A three-factor, three-level response surface experimental design was employed, and a regression model for the experimental indicators was obtained. An analysis of the response surface results identified the optimal parameter combination as follows: a throwing height of 142.79 cm, a working speed of 55.38 r/min, and a bottom diameter of the seedling guide tube of 43.51 mm. At these optimal parameters, the model predicted a seedling spacing compliance rate of 88.43% and a seedling erectness compliance rate of 88.12%;
3. To validate the accuracy of the model optimization results, field experiments were conducted. Experimental data showed that under the optimal operating parameters calculated using the regression model, the spacing pass rate was 86.7%, and the uprightness pass rate was 84.2%. The experimental results met the design requirements, providing valuable insights for UAV-based rice seedling throwing.

Author Contributions: Conceptualization, P.Y. and Y.J.; methodology, P.Y., Y.Y. and Y.J.; software, P.Y. and Y.W.; validation, W.Z. and P.Y.; formal analysis, P.Y., Y.J. and W.Z.; investigation, P.Y. and

W.Z.; resources, P.Y., Y.J., Y.Y. and W.Z.; data curation, P.Y., Y.Y. and Y.W.; writing—original draft preparation, P.Y.; writing—review and editing, P.Y. and Y.Y.; visualization, P.Y. and Y.W.; supervision, W.Z. and Y.J.; project administration, W.Z. and Y.J.; funding acquisition, W.Z. and Y.J. All authors have read and agreed to the published version of the manuscript.

Funding: This research was funded by the Science and Technology Innovation Project of the Chinese Academy of Agricultural Sciences (Grant No. CAAS-SAE-202301).

Institutional Review Board Statement: Not applicable.

Informed Consent Statement: Not applicable.

Data Availability Statement: The data presented in this study are available in the article.

Acknowledgments: The authors thank the editor and anonymous reviewers for providing helpful suggestions for improving the quality of this manuscript.

Conflicts of Interest: The authors declare no conflicts of interest.

References

1. Zhang, H.; Hu, Y.; Yang, J.; Dai, Q.; Huo, Z.; Xu, K.; Wei, H.; Gao, H.; Guo, B.; Xing, Z.; et al. Development and Prospect of Rice Cultivation in China. *Sci. Agric. Sin.* **2021**, *54*, 1301–1321.
2. Tian, X.; Qin, F.; Li, M. Empirical analysis of the difference of rice production costs in China. *Trans. CSAE* **2005**, *21*, 247–250.
3. Wu, G.; Yu, G.; Xiang, X.; Wang, L. Design and test of rice potted-seedling transplanting mechanism with three transplanting arms. *Trans. CSAE* **2017**, *33*, 15–22.
4. Xia, Q.; Zhang, W.; Ji, Y.; Li, K. Research status and trend of mechanical throwing seedling technology and equipment in China. *J. Chin. Agric. Mech.* **2019**, *40*, 201–208.
5. Li, Z.; Ma, X.; Li, X.; Chen, L.; Li, H.; Yuan, Z. Research Progress of Rice Transplanting Mechanization. *Trans. CSAM* **2018**, *49*, 1–20.
6. Tang, Y.; Wang, Y.; Zhang, D.; Luo, X. Research on Four-Wheel Drive Pneumatic Throwing Transplanter of Paddy Seedling. *J. Chin. Agric. Mech.* **2009**, *3*, 72–75.
7. Wang, L.; Wang, P.; Li, Y.; Song, J. Experiment Study on 2ZPY-H530 Rice Potted-seedling Transplant. *J. China Agric. Univ.* **2002**, *7*, 21–24.
8. Qian, M.; Yu, G.; Jiang, C.; Zhao, Y. Work Principle and Parameter Optimization of Rice-seedling Transplanter with Non-circular Gears. *Trans. CSAM* **2014**, *45*, 64–69.
9. Li, Y.; Xu, J.; Wang, M.; Liu, D.; Sun, H.; Wang, X. Development of autonomous driving transfer trolley on field roads and its visual navigation system for hilly areas. *Trans. CSAE* **2019**, *35*, 52–61.
10. Gong, X.; Fu, Q.; Sun, A.; Guan, Y.; Wang, B.; Li, M. Rice planting potential in plain-hill-wetland area estimated by nature-society water cycle model. *Trans. CSAE* **2019**, *35*, 138–147.
11. Jiang, Y.; Sun, Z.; Wang, R.; Xia, C.; Ye, Q.; Guo, Y. Design and performance test of the omnidirectional leveling system for crawler work machine in hilly areas. *Trans. CSAE* **2023**, *39*, 64–73.
12. Liu, W.; Zhou, Z.; Xu, X.; Gu, X.; Zou, S.; He, W.; Luo, X.; Huang, J.; Lin, J.; Jiang, R. Evaluation method of rowing performance and its optimization for UAV-based shot seeding device on rice sowing. *Comput. Electron. Agric.* **2023**, *207*, 107718. [CrossRef]
13. Ni, J.; Yao, L.; Zhang, J.; Cao, W.; Zhu, Y.; Tai, X. Development of an unmanned aerial vehicle-borne crop-growth monitoring system. *Sensors* **2017**, *17*, 502. [CrossRef]
14. Li, J.; Lan, Y.; Zhou, Z.; Zeng, S.; Huang, C.; Yao, W.; Zhang, Y.; Zhu, Q. Design and test of operation parameters for rice air broadcasting by unmanned aerial vehicle. *Int. J. Agric. Biol. Eng.* **2016**, *9*, 24–32.
15. Yeh, J.; Lin, K.; Yuan, L.; Hsu, J. Automatic counting and location labeling of rice seedlings from unmanned aerial vehicle images. *Electronics* **2024**, *13*, 273. [CrossRef]
16. Amarasingam, N.; Gonzalez, F.; Salgadoe, A.S.A.; Sandino, J.; Powell, K. Detection of White Leaf Disease in Sugarcane Crops Using UAV-Derived RGB Imagery with Existing Deep Learning Models. *Remote Sens.* **2022**, *14*, 6137. [CrossRef]
17. Li, J.; Lan, Y.; Shi, Y. Research progress on airflow characteristics and field pesticide application system of rotary-wing UAV. *Trans. CSAE* **2018**, *34*, 104–118.
18. Gao, X.; You, Z.; Wu, H.; Wang, S.; Cao, M. Design and Experiment of Green Manure Seed Broadcast Device Based on Unmanned Aerial Vehicle Platform. *Trans. CSAM* **2022**, *53*, 76–85.
19. Zhang, Q.; Zhang, K.; Liao, Q.; Liao, Y.; Wang, L.; Shu, C. Design and experiment of rapeseed aerial seeding device used for UAV. *Trans. CSAE* **2020**, *36*, 138–147.
20. Zhang, H.; Lan, Y.; Wen, S.; Chen, C.; Xu, T.; Chen, S. Modelling approach of spray retention on rice in plant protection using unmanned aerial vehicle. *Trans. CSAE* **2022**, *38*, 40–50.
21. Villette, S.; Piron, E.; Miclet, D. Hybrid centrifugal spreading model to study the fertiliser spatial distribution and its assessment using the transverse coefficient of variation. *Comput. Electron. Agric.* **2017**, *137*, 115–129. [CrossRef]
22. Chojnacki, J.; Berner, B. The influence of air stream generated by drone rotors on transverse distribution pattern of sown seeds. *J. Res. Appl. Agric. Eng.* **2018**, *63*, 9–12.

23. Tang, Y.; Fu, Y.; Guo, Q.; Huang, H.; Tan, Z.; Luo, S. Numerical simulation of the spatial and temporal distributions of the downwash airflow and spray field of a co-axial eight-rotor plant protection UAV in hover. *Comput. Electron. Agric.* **2023**, *206*, 107634. [CrossRef]
24. Song, C.; Liu, L.; Wang, G.; Han, J.; Zhang, T.; Lan, Y. Particle deposition distribution of multi-rotor UAV-based fertilizer spreader under different height and speed parameters. *Drones* **2023**, *7*, 425. [CrossRef]
25. Song, C.; Zhou, Z.; Zang, Y.; Zhao, L.; Yang, W.; Luo, X.; Jiang, R.; Ming, R.; Zang, Y.; Zi, L.; et al. Variable-rate control system for UAV-based granular fertilizer spreader. *Comput. Electron. Agric.* **2020**, *180*, 105832. [CrossRef]
26. Xiao, H.; Li, Y.; Yuan, L.; Zhang, Z. Application and Prospect of China Agricultural Unmanned Aerial Vehicle in Rice Production. *J. Guangxi Agric. Sci.* **2021**, *48*, 139–147.
27. Song, C.; Zhou, Z.; Jiang, R.; Luo, X.; He, X.; Ming, R. Design and parameter optimization of pneumatic rice sowing device for unmanned aerial vehicle. *Trans. CSAE* **2018**, *34*, 80–88.
28. Liu, W.; Zou, S.; Xu, X.; Gu, Q.; He, W.; Huang, J.; Huang, J.; Lyu, Z.; Lin, J.; Zhou, Z.; et al. Development of UAV-based shot seeding device for rice planting. *Int. J. Agric. Biol. Eng.* **2022**, *15*, 1–7. [CrossRef]

agriculture

MDPI

Article

Research on a Multi-Lens Multispectral Camera for Identifying Haploid Maize Seeds

Xiantao He [1,2], Jinting Zhu [1], Pinxuan Li [1], Dongxing Zhang [1,2], Li Yang [1,2,*], Tao Cui [1,2], Kailiang Zhang [1,2] and Xiaolong Lin [1]

[1] College of Engineering, China Agricultural University, Beijing 100083, China
[2] Key Laboratory of Soil-Machine-Plant System Technology of Ministry of Agriculture, Beijing 100083, China
[*] Correspondence: yl_hb68@126.com; Tel.: +86-010-6273-7765

Abstract: Haploid breeding can shorten the breeding period of new maize varieties and is an important means to increase maize yield. In the breeding program, a large number of haploid seeds need to be screened, and this step is mainly achieved manually, which hinders the industrialization of haploid maize breeding. This article aims to develop a multispectral camera to identify the haploid seeds automatically. The camera was manufactured by replacing narrow-band filters of the ordinary CCD camera, and the RGB, 405 nm, 980 nm and 1050 nm images of haploid or diploid seeds were simultaneously captured (the characteristic wavelengths were determined according to color and high-oil markers of maize). The performance was tested using four maize varieties with the two genetic markers. The results show that the developed multispectral camera significantly improved the recognition accuracy of haploid maize seeds to 92.33%, 97.33%, 97% and 93.33% for the TYD1903, TYD1904, TYD1907 and TYD1908 varieties, respectively. The cameras in the near-infrared region (wavelengths of 980 nm and 1050 nm) achieved better performance for the varieties of high-oil marker, with an increase of 0.84% and 1.5%, respectively. These results demonstrate the strong potential of the multispectral imaging technology in the haploid seed identification of maize.

Keywords: maize; haploid seed identification; multispectral imaging; AlexNet-based model

Citation: He, X.; Zhu, J.; Li, P.; Zhang, D.; Yang, L.; Cui, T.; Zhang, K.; Lin, X. Research on a Multi-Lens Multispectral Camera for Identifying Haploid Maize Seeds. *Agriculture* **2024**, *14*, 800. https://doi.org/10.3390/agriculture14060800

Academic Editor: Bruno Bernardi

Received: 4 April 2024
Revised: 16 May 2024
Accepted: 18 May 2024
Published: 22 May 2024

1. Introduction

Maize (*Zea mays* L., also commonly known as corn) is one of the important food crops in the world, and its output has a significant influence on global food security [1–3]. The world population is gradually growing, while arable land is limited, resulting in an increasing demand for maize yield [4]. The cultivation of new varieties of maize is the key means to boost per-unit yield. There are many breeding methods to obtain new maize varieties [5]. Compared with other breeding methods, the haploid breeding technique has the following advantages: (1) shortening the breeding period; (2) overcoming the incompatibility of distant hybridization; (3) reducing land and labor use; (4) improving breeding efficiency, etc. [6,7]. However, the proportion of haploid seeds is low in haploid breeding, and only about 10% of the required haploid seeds can be gained in a single breeding cycle [8]. It is difficult to identify haploid seeds in mixed maize seeds (haploid and diploid), which restricts the engineering of haploid breeding of maize. Therefore, it is of great significance to develop automatic detection technology of haploid seeds.

Morphological identification (MI), cyto-anotomy identification (CI) and gene marking (GM) are the three main technologies to identify haploid maize seeds [9]. MI refers to judging whether maize is haploid or not by observing the morphological structure of maize at the seedling stage. Although this method is intuitive and effective, the detection cycle is long and the cost is high. CI is complicated and extremely destructive, and haploid seeds are identified by dissecting all seeds. GM is the most widely used and effective haploid identification method at present [10]. It marks the haploid and diploid seeds with different genotypes and phenotypes, and a large number of haploid corn seeds can be selected manually. The advantages of this method are that haploid seeds can be identified at the seed stage, and it is easier to achieve automatic haploid screening. Color marker and high-oil marker are two commonly used gene markers. Color marker uses the R1-nj gene to induce pigment differences in maize seeds, so that diploid embryos have purple marks, while haploid embryos do not [11]. The color difference in seed embryos enables human beings to intuitively identify haploid and diploid corn seeds. However, the expression of R1-nj varies greatly among different varieties of maize, resulting in a high recognition error rate by the human eye when the color difference of the embryo is faint. Haploid maize seeds can also be identified by high-oil marker, and the oil content of induced diploid embryos is significantly higher than that of haploid embryos [12]. However, some varieties exhibit overlapping oil content in haploid and diploid seeds, making it difficult to distinguish. The simultaneous use of color marker and high-oil marker is an effective means to improve the recognition accuracy of haploid seeds [13]. In practice, the haploid corn seeds marked by these two methods are mainly identified by artificial means, which takes a lot of manpower and time, and also cannot meet the needs of the breeding industry. Therefore, there is an urgent need to develop a rapid and non-destructive haploid seed identification and screening method.

Some detection techniques based on gene markers have been used for the automatic identification of haploid maize seeds, including RGB image, nuclear magnetic resonance (NMR), near-infrared spectroscopy (NIR), hyper-spectral imaging (HSI) and multispectral imaging (MSI). RGB image uses the RGB camera to capture the color marker of the seed embryo, and this method has not been satisfactory for haploid seeds with a small color difference [14–19]. NMR separates haploids based on oil marker, but NMR is cumbersome in operation, slow in sorting and costly in manufacturing [8,20–23]. NIR is widely used for the quantitative detection of liquids and powders, such as the contents of protein, oil, sugar and pigment, but the accuracy is easily affected by the size and shape of seeds when identifying haploid maize seeds [24–29]. Compared with NIR, HSI technology can obtain the external characteristics of seeds, such as color, size and texture, as well as the internal chemical composition distribution of the seeds with spectral and image information, which counteracts the effects of the size and shape of the seeds on the spectral information [30–34]. However, the data acquisition of HIS is slow and its cost is high. MSI is similar to HSI, and the key difference is that MSI only obtains spectral images under characteristic wavelengths [35–38]. The acquisition is fast, and the cost is greatly reduced. However, MSI needs to be customized according to the application scenario. At present, there is no report on MSI technology applied to the detection of haploid seeds of maize.

The main objectives of this study are as follows: (1) To design a four-channel multi-lens MSI camera, which can collect the information of color marking and high-oil marking of maize seeds simultaneously; (2) To research the preprocessing algorithm of the MSI image of haploid seeds, to establish the classification model of haploid seeds based on convolutional deep neural network, and to realize the identification of haploid seeds with color marking and high-oil marking; (3) To establish a detection system of haploid seeds of maize and to provide technical support for the following automatic sorting of haploid seeds.

2. Materials and Methods

2.1. The Design of Multispectral Camera for Haploid Maize Identification

The developed MSI camera is shown in Figure 1a, including an RGB camera and cameras with wavelengths of 405 nm, 980 nm and 1050 nm. The RGB camera can capture the shape and color of seeds. The 405 nm camera is in the range of 380 nm~470 nm of the violet light, which can strengthen the image of purple marks on the embryo. The 980 nm and 1050 nm cameras are in the band range of near-infrared, and their wavelengths are the strong absorption peaks of the C-H functional groups characterizing the oil contents, so as to achieve the identification of haploid seeds with high-oil marker. In this way, 4 MSI images of haploid seeds can be captured simultaneously. The manufacturing scheme of the MSI camera is shown in Figure 1b. The optical filter of the ordinary CCD camera (manufactured by Xingkai Security Technology Company (Shenzhen, China), camera diameter 15 mm, resolution 1280 × 720, signal-to-noise ratio ≥48 dB, frames 30 f/s, 5 V powered by the image processor) was removed and replaced with a narrow-band filter in front of the camera. It was successively replaced by the filter with a wavelength at 405 nm, 980 nm and 1050 nm (manufactured by Fuzhe Laser Technology Company (Shenzhen, China), with a diameter of 14–15 mm and a thickness of 1–1.2 mm). When the camera operates, the spectral information of the seed first passes through the lens, then reaches the filter. The filter blocks all spectra except for the characteristic wavelengths, and finally, the CCD sensor perceives the seed image information at the characteristic wavelengths. Consequently, the four images at RGB, 405 nm, 980 nm and 1050 nm are obtained and transmitted to the image processor via USB.

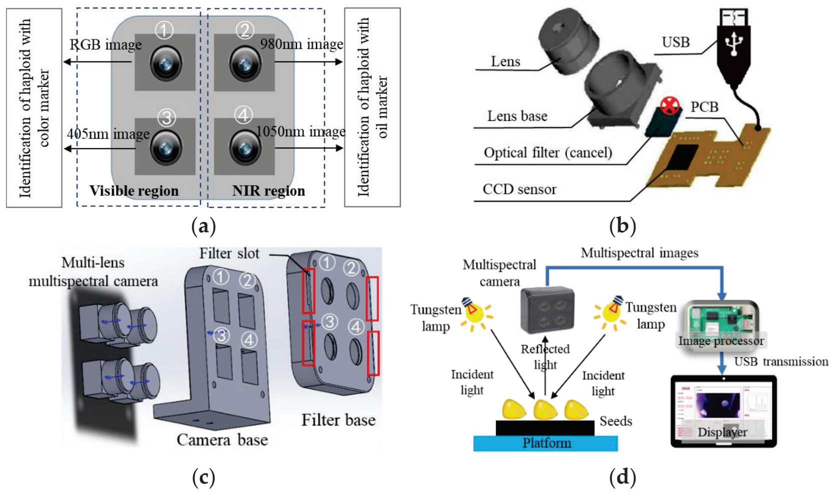

Figure 1. The design of muti-lens MSI camera for haploid seed identification. (**a**) Wavelength selection for MSI camera; (**b**) Manufacturing method of spectral camera based on CCD camera; (**c**) Fixing device of MSI camera; (**d**) Identification system of haploid seeds.

The designed fixing device of camera is shown in Figure 1c, including a camera base and a filter base. The filters were inserted and fixed through the slots on the side of the filter base. The diameter of the circular hole for fixing filter is 12 nm, which is good to install and replace the filter. The detection system of haploid seeds is shown in Figure 1d, which includes seed placement platform, light source, MSI camera, image processor (Raspberry PI 4b, Raspberry PI, Cambridge, UK) and displayer. The light source uses two symmetrically placed tungsten lamps (12 V, 20 W). When working, the tungsten lamp shines the light on maize seed; then, the light is reflected to the MSI camera. The MSI camera transmits the multispectral images to the image processor; then, the processor discriminates haploid and diploid seeds and sends the identification results on the display. The image processor uses the Rasberry Pi 4b, which has four USB ports to connect four cameras and facilitates the sequential capture of images via USB connections.

2.2. Samples and Sample Preparation

Maize samples were divided into two categories: color-marker section and high-oil-marker section. All samples were provided by a breeding company (China National Tree Seed Group Co., Ltd., Beijing, China). In the first section, two varieties (TYD1903 and TYD1904) were obtained using the traditional color inducer CAU5 as the paternal line. The embryo and endosperm of the diploid seeds were both labeled purple, while only the endosperm of the haploid seeds was marked purple. In the second section, the high-oil inducer material CHOI3 was used as the paternal line to produce two other varieties (TYD1907 and TYD1908). These varieties generated haploid and diploid seeds with both oil content and color markers. Specifically, the diploid seeds not only had a purple embryo marker but also a higher oil content compared to the haploid seeds. The total sample size was 400 seeds, with 100 seeds in each category.

2.3. Chemical Composition Determination

The pH-differential method was used for the determination of the anthocyanin content (AC, mg·L^{-1}). Three seeds from each haploid and diploid group of every variety were randomly chosen from the four maize varieties for AC determination. Cyanidin-3-O-glucoside (CAS No.: 7084-24-4) was employed as the standard sample, with a molar absorptivity (ε) of 26,900 $M^{-1}cm^{-1}$ and a molar mass (MW) of 432 Da. Then, the AC value was determined using the formula $AC = a \cdot b/(\varepsilon \cdot l) \times MW \times 10^3$, where a represents the difference in absorptivity between two pH solutions, b denotes the dilution rate and l signifies the path length of the colorimetric vessel (cm). During testing, the values of b and l were established as 24 and 1 cm, respectively. The oil content rate (OCR, %) of haploid and diploid seeds was determined by the NMR-based oil testing instrument NM120-015V-I (Shanghai Newman Electronic Technology Co., Ltd., Shanghai, China).

2.4. Multispectral Image Collection

The detection system of haploid seeds (Figure 2) was established, and the MSI camera was pointed at the seed embryo, and its height was adjusted to ensure that the four cameras could collect seed images at the same time. The distance between the MSI camera and the acquisition platform was determined to be 150 mm. The focus of each camera was adjusted to obtain clear images. The black platform was use to acquire MSI images with clean background. The fixed rod of tungsten lamp on left and right side was at 60 degrees with the vertical rod of the holder, and the distance between the halogen tungsten lamp and the vertical rod was 280 mm. The MSI images of maize seeds were collected one by one, and 4 images of each were obtained at the same time. The images were stored by category for the subsequent establishment of identification model of haploid seeds.

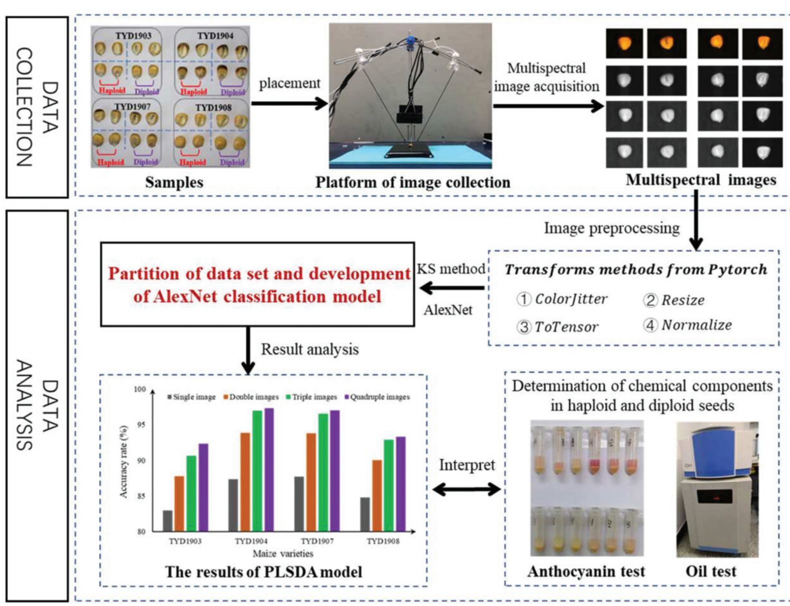

Figure 2. Schematic flow of the image collection and the haploid identification.

2.5. Image Preprocessing

Pytorch was applied to preprocess the obtained images of the maize seeds (100 images each variety). The process includes the following: (1) Transforms.Resize was used to scale the image sizes in proportion to AlexNet's input size of 224 × 224. (2) Transforms.ColorJitter was used to adjust the brightness, contrast, saturation and tone of the images with value of 0.1, thus obtaining an expanded 400 image sets for each variety. Considering that the position of seeds might affect haploid recognition, the rotation (90 degrees in one step) and translation (50 up, down, left and right) of image were conducted to obtain an expanded 800 image sets with orientation changed. Thus, additional 1200 images were obtained. (3) Transforms.ToTensor and Transforms.Normalize were used to normalize images. This process can reduce the occurrence of gradient explosion and gradient disappearance and accelerate the convergence of the model. KS method was used to divide the data set. For 1300 sets of each category, 700 sets were used as the model training and the other 600 sets were used as the model testing.

2.6. Classification Model of Haploid Seeds

AlexNet was applied to establish the classification models of haploid and diploid seeds. It is a classical convolutional neural network, whose network structure consists of 5 convolutional layers and three fully connected layers (i.e., 2 fully connected hidden layers and 1 fully connected output layer) [39]. Each convolution layer contains convolution kernel, bias term, activation function, and local response normalization (LRN) module. The first, second, and fifth convolutional layers are followed by a maximum pooling layer, and the last three layers are fully connected layers. The final output layer, softmax, converts the network output into probability values that are used to predict the category of the image. The nonlinear activation function, modified linear unit (ReLU), is used in the AlexNet. Compared with traditional activation functions (sigmoid and tanh), ReLU can effectively solve the problem of gradient disappearance while maintaining the fast computation speed, thus making training more efficient. LRN was used to suppress the response of neighboring neurons and avoid overfitting, and this can improve the generalization ability of the network.

$$b_{x,y}^{i} = \frac{a_{x,y}^{i}}{\left(\mathrm{k} + \alpha \sum_{j=\max(0,i-\frac{n}{2})}^{\min(N-1,\, i+\frac{n}{2})} \left(a_{x,y}^{j}\right)^{2}\right)^{\beta}} \tag{1}$$

where $b_{x,y}^{i}$ is the normalized value of the ith feature map at position (x, y), $a_{x,y}^{i}$ is the original value of the ith feature map at position (x, y), n is the neighborhood size, N is the number of feature maps, and k, α and β are hyperparameters with values of 2, 10^{-4} and 0.75, respectively.

3. Results and Discussion

3.1. Analysis of Seed Multispectral Images

The results depicted in Figure 3 illustrate the outcomes of analyzing both haploid and diploid seeds across color-marked and oil-marked varieties. In general, diploid seeds exhibited higher AC values compared to haploid seeds across all four maize varieties. This distinction can be attributed to the utilization of the R1-nj pigment gene during maize seed induction, resulting in the presence of a purple marker in diploid embryos, whereas haploid embryos lack this marker. Notably, TYD1904 demonstrated the highest AC, with the greatest disparity between haploid and diploid seeds. Conversely, TYD1908 exhibited the lowest AC, while TYD1903 displayed the smallest difference between haploid and diploid AC values. Distinct OCRs were noted between haploid and diploid seeds for TYD1907 and TYD1908, whereas TYD1903 and TYD1904 showed significant overlaps. This suggests that distinguishing between haploid and diploid seeds based on oil content alone is challenging for color-marked varieties. Furthermore, the average OCRs of diploid samples for TYD1907 and TYD1908 were noticeably higher than those of haploid samples.

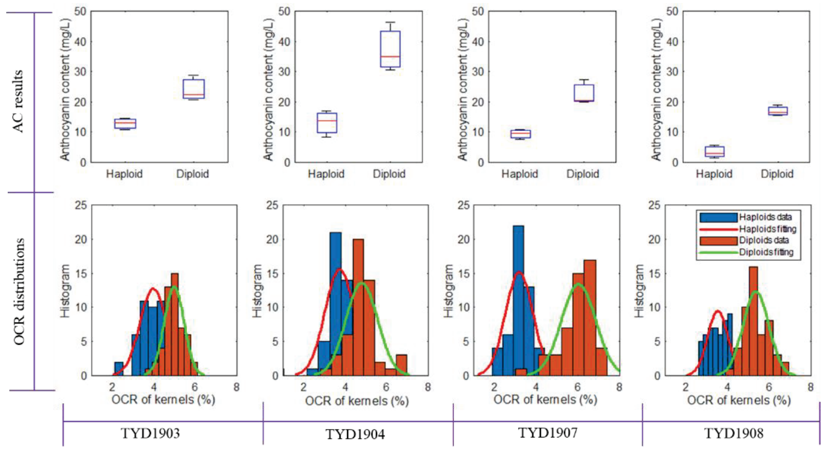

Figure 3. The result of anthocyanin and oil measurement of four maize varieties. AC: anthocyanin content; OCR: oil content rate.

The images of haploid and diploid seeds of four varieties in different wavelengths are shown in Figure 4. For the RGB images of all varieties, it can be observed that the embryo purple of TYD1904 is the deepest, while that of TYD1908 is the lightest, consistent with the measured anthocyanin content results. The anthocyanin content of TYD1903 and TYD1907 is roughly the same, but in the RGB images, the embryo purple of TYD1907 is more pronounced than that of TYD1903. This is because more anthocyanins of TYD1903 are distributed inside the seeds. For the 405 nm images, it can be seen that the embryo purple was enhanced, especially in the varieties of TYD1904 and TYD1907. Compared to the RGB and 405 nm images, the 980 nm and 1050 nm images contain the smaller purple difference between haploid and diploid seeds, but the differences from TYD1907 and TYD1908 are greater than that from TYD1903 and TYD1904. Overall, there are differences between the images of haploid and diploid seeds, which is the basis for identifying the haploid seeds from diploid seeds.

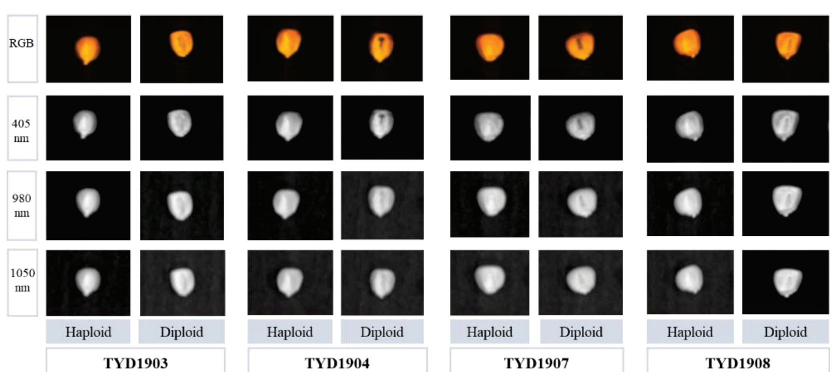

Figure 4. The images of haploid and diploid seeds at different wavelengths.

3.2. The Performance of AlexNet-Based Model

The recognition accuracy of haploid seeds of each variety under a single wavelength is shown in Table 1. The RGB camera had the highest recognition accuracy for haploid seeds with an average of 93.58%, followed by the 405 nm camera with an average of 92.42%. The performance of the 980 nm camera and the 1050 nm camera was comparatively poorer, ranging from 77.25% to 79.63%. Moreover, the performance of the 1050 nm camera was worse compared to the 980 nm camera. The reason for this is that as the wavelength of the filter increases, the intensity of the transmitted wavelength decreases under the same light source, leading to a weaker image signal at the wavelength of 1050 nm. The RGB and 405 nm cameras had significantly higher recognition accuracy for the varieties with an obvious purple marker (TYD1904 and TYD1907), reaching over 95%. The 980 nm and 1050 nm cameras had higher recognition accuracy for the varieties with a high-oil marker (TYD1907 and TYD1908) compared to the varieties with only a color marker (TYD1903 and TYD1904), reaching accuracies of 87.75% and 84.79%, respectively. This is because the 980 nm and 1050 nm cameras are in the near-infrared region and can identify both the anthocyanin difference and the oil difference between haploid and diploid seeds.

Table 1. Results of the AlexNet-based model for identifying haploid seeds with single image.

Varieties	RGB (%)	405 nm (%)	980 nm (%)	1050 nm (%)	Average (%)
TYD1903	90.33	88.00	78.00	75.67	83.00
TYD1904	96.67	95.83	79.83	77.00	87.33
TYD1907	95.83	95.00	81.17	79.00	87.75
TYD1908	91.50	90.83	79.50	77.33	84.79
Average (%)	93.58	92.42	79.63	77.25	85.72

The recognition accuracy of the four varieties under different combinations of cameras are shown in Figure 5 and Table 2. It can be observed that the accuracy of the combination of two cameras ranged from 78.67% to 97%, while the accuracy of the combination of three cameras ranged from 89% to 97.33%. The full combination of four cameras yielded the best performance with an accuracy range of 92.33% to 97.33%. It was evident that the recognition accuracy of the combination of multiple cameras was higher than that of a single camera, and with an increase in the number of cameras, the recognition accuracy increased (Figure 6).

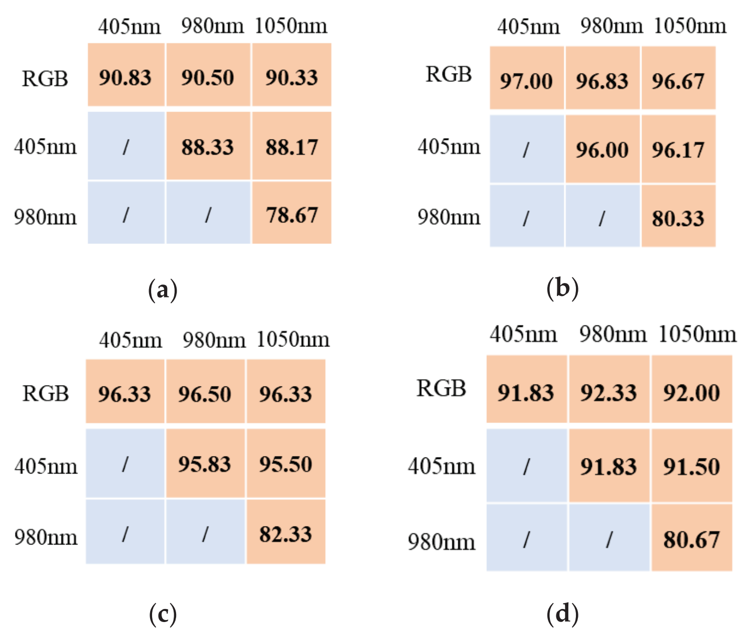

Figure 5. Results of the AlexNet-based model for identifying haploid seeds with two cameras. (**a**) TYD1903; (**b**) TYD1904; (**c**) TYD1907; (**d**) TYD1908.

Table 2. Results of the AlexNet-based model for identifying haploid seeds with three or four cameras.

Varieties	RGB-405 nm–980 nm (%)	RGB-405 nm–1050 nm (%)	RGB-980 nm–1050 nm (%)	405 nm–980 nm–1050 nm (%)	RGB-405 nm–980 nm–1050 nm (%)
TYD1903	91.50	91.17	90.83	89.00	92.33
TYD1904	97.33	97.17	97.00	96.33	97.33
TYD1907	96.50	96.50	96.67	96.33	97.00
TYD1908	92.83	93.17	93.00	92.50	93.33

The presented analysis indicates that combinations with the RGB camera performed better than those without the RGB camera. For instance, the combination of the RGB camera and 980 nm camera for the TYD1903 variety achieved 90.5%, which was higher than the 88.33% achieved by the combination of the 405 nm camera and the 980 nm camera. The reason for this result is that the RGB camera captured images with three channels (i.e., R, G and B channels), resulting in higher image clarity. Additionally, the color differences among the four varieties are more pronounced than the differences in oil content.

For varieties with a clear color marker, the accuracy of the RGB camera was already high. Adding other cameras could further improve recognition accuracy, but the improvement margin was limited. For example, the recognition accuracy for TYD1904 using the RGB camera was 96.67%, and it increased to 97.33% when other cameras were added, resulting in a marginal increase of 0.66%. However, for varieties with a light color marker, it is essential to combine other cameras with the RGB camera. For TYD1903, the recognition accuracy with the RGB camera alone was 90.33%, which increased to 92.33% when three other cameras were added, resulting in an increase of 2%.

Moreover, the 980 nm and 1050 nm cameras performed better for varieties with a high oil content. For instance, the accuracy of the combination of the RGB, 980 nm and 1050 nm cameras for TYD1907 and TYD1908 increased by 0.84% and 1.5%, respectively, while for TYD1903 and TYD1904, the accuracy increased only by 0.5% and 0.33%, respectively. This indicates that adding cameras in the near-infrared region can improve the recognition accuracy of haploid seeds, especially for the varieties with a high-oil marker.

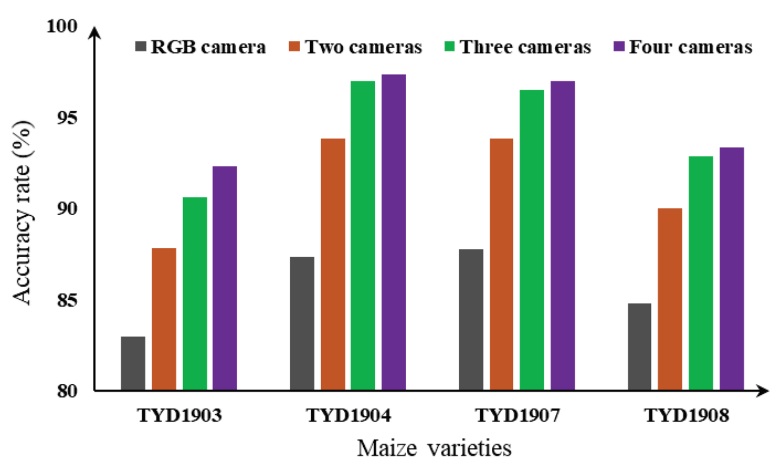

Figure 6. The results of identifying haploid seeds under different varieties and multispectral images.

3.3. Comprehensive Analysis

Through the above analysis, it is evident that the developed MSI camera has significant performance advantages in identifying haploid maize seeds compared to a single camera. Furthermore, it exhibits clear cost advantages in comparison to existing MSI cameras on the market. As shown in Table 3, the CCD camera costs USD 14.6, while the filters for 405 nm, 980 nm, and 1050 nm cost USD 16.7, USD 13.9 and USD 38.9, respectively. The total cost of the MSI camera is only USD 139.1, making it relatively affordable compared to market-available MSI cameras (which typically cost more than USD 1000).

Table 3. The price list of components used in the MSI camera.

Component Name	Number	Unit price (USD)	Total (USD)
CCD camera	4	14.6	139.1
Filter 405 nm	1	16.7	
Filter 980 nm	1	13.9	
Filter 1050 nm	1	38.9	
Fixing device	1	11.2	

Compared to the HSI camera and NIR and NMR spectrometers, MSI has significant advantages in real-time seed detection systems (Table 4). However, existing MSI cameras on the market usually have fixed wavelengths and are often mounted on drones for the acquisition of normalized difference vegetation index (e.g., NDVI), making them difficult to directly apply to the identification of haploid maize seeds. The wavelengths of the images captured by the developed multispectral camera were selected based on the characteristics of haploid maize seeds, and the filters can be easily replaced through the slots on the side of the filter base for expanding detection purposes in the future. In addition, the image augmentation technique was utilized in this study to expand the data set and construct an AlexNet-based model. To mitigate the potential for overfitting, we plan to acquire data sets from a broader variety of maize breeds in future studies. This proactive approach will serve to enhance the robustness of the model, particularly in its ability to accurately identify haploid seeds across a range of maize varieties.

Table 4. The comparison with different devices for detecting haploid seeds.

Detection Device	Price	Detection Speed	Accuracy	Remarks
MSI camera	Low	High	Medium	Images are associated with the characteristic wavelengths.
HSI camera	High	Slow	High	Slow data acquisition and processing speed.
NIR spectrometer	Medium	High	Medium	Generally used for detection of homogeneous liquids or powders
NMR spectrometer	High	Medium	Medium	The cost is very high, commonly used in medical fields

4. Conclusions

This study developed a multi-lens MSI camera for the identification of haploid maize seeds, and the performance was tested using four maize varieties with two different genetic markers. The conclusions of the research can be drawn as follows:

(1) Compared to the conventional RGB camera, the developed MSI camera significantly improved the recognition accuracy of haploid maize seeds. The accuracy of the MSI camera for identifying haploid seeds of four maize varieties (TYD1903, TYD1904, TYD1907 and TYD1908) was 92.33%, 97.33%, 97% and 93.33%, respectively, while the accuracy of the RGB camera was 90.33%, 96.67%, 95.83% and 91.5%, respectively. These results demonstrate the strong potential of MSI technology in haploid maize seed identification.

(2) The cameras in the NIR region (wavelengths of 980 nm and 1050 nm) showed better identification performance for the varieties with a high-oil marker. The accuracy of

the combination of the RGB, 980 nm and 1050 nm cameras for TYD1907 and TYD1908 increased by 0.84% and 1.5%, respectively, while for TYD1903 and TYD1904, the accuracy increased only by 0.5% and 0.33%, respectively. Therefore, adding cameras in the NIR region can improve the recognition accuracy of haploid seeds, especially for the varieties with a high-oil marker.

(3) The MSI camera was manufactured based on the ordinary CCD camera, and the overall cost was much lower than for existing MSI cameras on the market. Furthermore, the developed MSI camera is specifically tailored for the identification of haploid maize seeds, making it easier for this MSI camera to be widely applied in haploid maize breeding.

Author Contributions: Conceptualization, X.H., D.Z. and L.Y.; methodology, X.H., J.Z. and P.L.; software, X.H., J.Z. and P.L.; validation, X.H., J.Z. and T.C.; formal analysis, J.Z., P.L. and K.Z.; investigation, X.H. and J.Z.; resources, X.H. and J.Z.; data curation, X.H., J.Z. and P.L.; writing—original draft preparation, X.H., J.Z., X.L. and L.Y.; writing—review and editing, X.H., J.Z., P.L., X.L. and L.Y.; visualization, D.Z. and T.C.; supervision, L.Y. and K.Z.; project administration, X.H.; funding acquisition, X.H. and T.C. All authors have read and agreed to the published version of the manuscript.

Funding: This research was supported by The National Key Research and Development Program of China (2021YFD2000402, 2021YFD2000404) and the earmarked fund for CARS-02.

Institutional Review Board Statement: Not applicable.

Data Availability Statement: The data used in this study were self-tested and self-collected. As the control method designed in this paper is still being further improved, data cannot be shared at present.

Acknowledgments: We acknowledge the China National Tree Seed Group Corporation Limited for providing the samples for our study.

Conflicts of Interest: The authors declare no conflict of interest.

References

1. Erenstein, O.; Jaleta, M.; Sonder, K.; Mottaleb, K.; Prasanna, B.M. Global Maize Production, Consumption and Trade: Trends and R&D Implications. *Food Secur.* **2022**, *14*, 1295–1319. [CrossRef]
2. Ranum, P.; Peña-Rosas, J.P.; Garcia-Casal, M.N. Global Maize Production, Utilization, and Consumption. *Ann. N. Y. Acad. Sci.* **2014**, *1312*, 105–112. [CrossRef] [PubMed]
3. Rouf Shah, T.; Prasad, K.; Kumar, P. Maize—A Potential Source of Human Nutrition and Health: A Review. *Cogent Food Agric.* **2016**, *2*, 1166995. [CrossRef]
4. Tian, X.; Engel, B.A.; Qian, H.; Hua, E.; Sun, S.; Wang, Y. Will Reaching the Maximum Achievable Yield Potential Meet Future Global Food Demand? *J. Clean. Prod.* **2021**, *294*, 126285. [CrossRef]
5. Li, R.; Zhang, G.; Liu, G.; Wang, K.; Xie, R.; Hou, P.; Ming, B.; Wang, Z.; Li, S. Improving the Yield Potential in Maize by Constructing the Ideal Plant Type and Optimizing the Maize Canopy Structure. *Food Energy Secur.* **2021**, *10*, e312. [CrossRef]
6. Takele, M. Review on Haploid and Double Haploid Maize (*Zea mays*) Breeding Technology. *Int. J. Agric. Sci. Food Technol.* **2022**, *8*, 052–058. [CrossRef]
7. Meng, D.; Liu, C.; Chen, S.; Jin, W. Haploid Induction and Its Application in Maize Breeding. *Mol. Breed.* **2021**, *41*, 20. [CrossRef] [PubMed]
8. Melchinger, A.E.; Schipprack, W.; Würschum, T.; Chen, S.; Technow, F. Rapid and Accurate Identification of in Vivo-Induced Haploid Seeds Based on Oil Content in Maize. *Sci. Rep.* **2013**, *3*, 2129. [CrossRef]
9. De Oliveira Couto, E.G.; Davide, L.M.C.; de Oliveira Bustamante, F.; von Pinho, R.G.; Silva, T.N. Identificação de Milho Haploide Por Citometria de Fluxo, Marcadores Morfológicos e Moleculares. *Cienc. Agrotecnol.* **2013**, *37*, 25–31. [CrossRef]
10. Wang, Y.; Lv, Y.; Liu, H.; Wei, Y.; Zhang, J.; An, D.; Wu, J. Identification of Maize Haploid Kernels Based on Hyperspectral Imaging Technology. *Comput. Electron. Agric.* **2018**, *153*, 188–195. [CrossRef]
11. Chaikam, V.; Nair, S.K.; Babu, R.; Martinez, L.; Tejomurtula, J.; Boddupalli, P.M. Analysis of Effectiveness of R1-Nj Anthocyanin Marker for in Vivo Haploid Identification in Maize and Molecular Markers for Predicting the Inhibition of R1-Nj Expression. *Theor. Appl. Genet.* **2015**, *128*, 159–171. [CrossRef]
12. Liu, C.; Li, J.; Chen, M.; Li, W.; Zhong, Y.; Dong, X.; Xu, X.; Chen, C.; Tian, X.; Chen, S. Development of High-Oil Maize Haploid Inducer with a Novel Phenotyping Strategy. *Crop J.* **2022**, *10*, 524–531. [CrossRef]

13. Chaikam, V.; Molenaar, W.; Melchinger, A.E.; Boddupalli, P.M. Doubled Haploid Technology for Line Development in Maize: Technical Advances and Prospects. *Theor. Appl. Genet.* **2019**, *132*, 3227–3243. [CrossRef] [PubMed]
14. Zhang, J.; Wu, Z.; Song, P.; Li, W.; Chen, S.; Liu, J. Embryo Feature Extraction and Dynamic Recognition Method for Maize Haploid Seeds. *Nongye Gongcheng Xuebao/Trans. Chin. Soc. Agric. Eng.* **2013**, *29*, 199–203.
15. Altuntaş, Y.; Kocamaz, A.F.; Cömert, Z.; Cengiz, R.; Esmeray, M. Identification of Haploid Maize Seeds Using Gray Level Co-Occurrence Matrix and Machine Learning Techniques. In Proceedings of the 2018 International Conference on Artificial Intelligence and Data Processing (IDAP), Malatya, Turkey, 28–30 September 2018; pp. 8–12. [CrossRef]
16. Veeramani, B.; Raymond, J.W.; Chanda, P. DeepSort: Deep Convolutional Networks for Sorting Haploid Maize Seeds. *BMC Bioinform.* **2018**, *19*, 289. [CrossRef]
17. Song, P.; Zhang, H.; Wang, C.; Luo, B.; Zhang, J.X. Design and Experiment of a Sorting System for Haploid Maize Kernel. *Int. J. Pattern Recognit. Artif. Intell.* **2018**, *32*, 1855002. [CrossRef]
18. Altuntaş, Y.; Cömert, Z.; Kocamaz, A.F. Identification of Haploid and Diploid Maize Seeds Using Convolutional Neural Networks and a Transfer Learning Approach. *Comput. Electron. Agric.* **2019**, *163*, 104874. [CrossRef]
19. Sabadin, F.; Galli, G.; Borsato, R.; Gevartosky, R.; Campos, G.R.; Fritsche-Neto, R. Improving the Identification of Haploid Maize Seeds Using Convolutional Neural Networks. *Crop Sci.* **2021**, *61*, 2387–2397. [CrossRef]
20. Wang, H.; Liu, J.; Xu, X.; Huang, Q.; Chen, S.; Yang, P.; Chen, S.; Song, Y. Fully-Automated High-Throughput NMR System for Screening of Haploid Kernels of Maize (Corn) by Measurement of Oil Content. *PLoS ONE* **2016**, *11*, e0159444. [CrossRef]
21. Li, H.; Qu, Y.; Yang, J.; Cui, L.; Mao, X.; Liu, Z. Analysis on Single Kernel Weight and Oil Content of Different Grain Types in Maize Based on NMR. *Trans. Chin. Soc. Agric. Eng.* **2018**, *34*, 183–188. [CrossRef]
22. Ge, W.; Li, J.; Wang, Y.; Yu, X.; An, D.; Chen, S. Maize Haploid Recognition Study Based on Nuclear Magnetic Resonance Spectrum and Manifold Learning. *Comput. Electron. Agric.* **2020**, *170*, 105219. [CrossRef]
23. Qu, Y.; Liu, Z.; Zhang, Y.; Yang, J.; Li, H. Improving the Sorting Efficiency of Maize Haploid Kernels Using an NMR-Based Method with Oil Content Double Thresholds. *Plant Methods* **2021**, *17*, 2. [CrossRef] [PubMed]
24. Sendin, K.; Manley, M.; Williams, P.J. Classification of White Maize Defects with Multispectral Imaging. *Food Chem.* **2018**, *243*, 311–318. [CrossRef] [PubMed]
25. Li, W.; Li, J.; Li, W.; Liu, L.; Li, H.; Chen, C.; Chen, S. Near Infrared Spectroscopy Analysis Based Machine Learning to Identify Haploids in Maize. *Spectrosc. Spectr. Anal.* **2018**, *38*, 2763–2769. [CrossRef]
26. Cui, Y.; Ge, W.; Li, J.; Zhang, J.; An, D.; Wei, Y. Screening of Maize Haploid Kernels Based on near Infrared Spectroscopy Quantitative Analysis. *Comput. Electron. Agric.* **2019**, *158*, 358–368. [CrossRef]
27. Shen, F.; Huang, Y.; Jiang, X.; Fang, Y.; Li, P.; Liu, Q.; Hu, Q.; Liu, X. On-Line Prediction of Hazardous Fungal Contamination in Stored Maize by Integrating Vis/NIR Spectroscopy and Computer Vision. *Spectrochim. Acta-Part A Mol. Biomol. Spectrosc.* **2020**, *229*, 118012. [CrossRef]
28. Sendin, K.; Manley, M.; Marini, F.; Williams, P.J. Hierarchical Classification Pathway for White Maize, Defect and Foreign Material Classification Using Spectral Imaging. *Microchem. J.* **2021**, *162*, 105824. [CrossRef]
29. Chavez, R.A.; Cheng, X.; Herrman, T.J.; Stasiewicz, M.J. Single Kernel Aflatoxin and Fumonisin Contamination Distribution and Spectral Classification in Commercial Corn. *Food Control* **2022**, *131*, 108393. [CrossRef]
30. Golhani, K.; Balasundram, S.K.; Vadamalai, G.; Pradhan, B. A Review of Neural Networks in Plant Disease Detection Using Hyperspectral Data. *Inf. Process. Agric.* **2018**, *5*, 354–371. [CrossRef]
31. Weng, H.; Lv, J.; Cen, H.; He, M.; Zeng, Y.; Hua, S.; Li, H.; Meng, Y.; Fang, H.; He, Y. Hyperspectral Reflectance Imaging Combined with Carbohydrate Metabolism Analysis for Diagnosis of Citrus Huanglongbing in Different Seasons and Cultivars. *Sens. Actuators B Chem.* **2018**, *275*, 50–60. [CrossRef]
32. Wakholi, C.; Kandpal, L.M.; Lee, H.; Bae, H.; Park, E.; Kim, M.S.; Mo, C.; Lee, W.H.; Cho, B.K. Rapid Assessment of Corn Seed Viability Using Short Wave Infrared Line-Scan Hyperspectral Imaging and Chemometrics. *Sens. Actuators B Chem.* **2018**, *255*, 498–507. [CrossRef]
33. Kimuli, D.; Wang, W.; Wang, W.; Jiang, H.; Zhao, X.; Chu, X. Application of SWIR Hyperspectral Imaging and Chemometrics for Identification of Aflatoxin B1 Contaminated Maize Kernels. *Infrared Phys. Technol.* **2018**, *89*, 351–362. [CrossRef]
34. Kimuli, D.; Wang, W.; Lawrence, K.C.; Yoon, S.C.; Ni, X.; Heitschmidt, G.W. Utilisation of Visible/near-Infrared Hyperspectral Images to Classify Aflatoxin B1 Contaminated Maize Kernels. *Biosyst. Eng.* **2018**, *166*, 150–160. [CrossRef]
35. Yang, X.; Gao, S.; Sun, Q.; Gu, X.; Chen, T.; Zhou, J.; Pan, Y. Classification of Maize Lodging Extents Using Deep Learning Algorithms by UAV-Based RGB and Multispectral Images. *Agriculture* **2022**, *12*, 970. [CrossRef]
36. He, X.; Liu, L.; Liu, C.; Li, W.; Sun, J.; Li, H.; He, Y.; Yang, L.; Zhang, D.; Cui, T.; et al. ScienceDirect Discriminant Analysis of Maize Haploid Seeds Using Near-Infrared Hyperspectral Imaging Integrated with Multivariate Methods. *Biosyst. Eng.* **2022**, *222*, 142–155. [CrossRef]
37. Ma, F.; Yuan, M.; Kozak, I. Multispectral Imaging: Review of Current Applications. *Surv. Ophthalmol.* **2023**, *68*, 889–904. [CrossRef] [PubMed]

38. Zhang, W.; Zhu, L.; Zhuang, Q.; Chen, D.; Sun, T. Mapping Cropland Soil Nutrients Contents Based on Multi-Spectral Remote Sensing and Machine Learning. *Agriculture* **2023**, *13*, 1592. [CrossRef]
39. Lu, J.; Tan, L.; Jiang, H. Review on Convolutional Neural Network (CNN) Applied to Plant Leaf Disease Classification. *Agriculture* **2021**, *11*, 707. [CrossRef]

agriculture

MDPI

Article

Simulation and Optimization of a Pendulum-Lever-Type Hole-Seeding Device

Hengshan Zhou [1,2], Fei Dai [1,2,*], Ruijie Shi [2], Cai Zhao [1], Huan Deng [2], Haifu Pan [2] and Qinxue Zhao [2]

[1] State Key Laboratory of Aridland Crop Science, Gansu Agricultural University, Lanzhou 730070, China; zhouhs@st.gsau.edu.cn (H.Z.); zhaoc@gsau.edu.cn (C.Z.)
[2] College of Mechanical and Electrical Engineering, Gansu Agricultural University, Lanzhou 730070, China; shirj@gsau.edu.cn (R.S.); 17797691649@163.com (H.D.); 18198029608@163.com (H.P.); zhaoqx@st.gsau.edu.cn (Q.Z.)
* Correspondence: daifei@gsau.edu.cn

Abstract: The process of hole seeding on the mulch during full-film double-row furrow corn planting faces issues such as poor seed discharge and seed blockage. To address these challenges, a pendulum-lever-type hole-forming mechanism is designed, along with an adjustment device. By analyzing the working principles of the pendulum-lever-type hole seeder and the adjustment device, the structural parameters of the device are determined. Through theoretical analysis and simulation experiments, three-dimensional models of seeds and hole seeders are constructed. Based on MBD-DEM cosimulation, the trajectory of seed movement and the seeding process of the hole seeder are analyzed to elucidate the effects of the hole-former opening and the number of pendulum bearings on seeding quality. To improve the operational performance of the hole seeder, experiments are conducted using the hole seeder's rotating disc speed, lever angle of the hole-former, and the number of pendulum bearings as experimental factors, with the qualification index, miss-seeding index, and reseeding index as experimental indicators. A three-factor, three-level Box–Behnken central composite experiment is performed to obtain mathematical models of the relationships between the experimental factors and indicators. Using Design-Expert 12 software, the regression models are optimized for multiple objectives to obtain the optimal parameter combination: a seeder disc speed of 49 r/min (corresponding to a forward speed of 5.76 km/h), a lever angle of 131°, and four pendulum bearings. Under this optimal parameter combination, the qualification index is 91.70%, the miss-seeding index is 4.57%, and the reseeding index is 3.73%. Experimental validation of the seeding performance of the hole seeder under the optimal parameter combination is conducted. Bench tests show that the qualification index, miss-seeding index, and reseeding index are 90.53%, 5.60%, and 3.87%, respectively. Field tests demonstrate a qualification index of 89.13%, a miss-seeding index of 5.46%, and a reseeding index of 6.41%. The actual results are consistent with the optimized values, providing valuable insights for the design and performance optimization of hole seeders.

Keywords: hole-former; hole seeder; parameter optimization; DEM-MBD

Citation: Zhou, H.; Dai, F.; Shi, R.; Zhao, C.; Deng, H.; Pan, H.; Zhao, Q. Simulation and Optimization of a Pendulum-Lever-Type Hole-Seeding Device. *Agriculture* **2024**, *14*, 750. https://doi.org/10.3390/agriculture14050750

Academic Editors: Xiaojun Gao, Qinghui Lai and Tao Cui

Received: 18 April 2024
Revised: 6 May 2024
Accepted: 9 May 2024
Published: 11 May 2024

1. Introduction

In response to the prevalent "nine droughts in ten years" phenomenon in Northwest China's arid regions, the widespread adoption of the whole-film mulching and double-ridge furrow-sowing drought-resistant tillage technology is currently underway. This approach combines a unique ridge structure with film mulching furrow sowing, offering benefits such as water retention, soil moisture conservation, and temperature elevation [1,2]. This planting method has been widely adopted in the cultivation of crops such as corn and potatoes [3]. Production practice has demonstrated that the whole-film mulching and double-ridge furrow seeding technique increases crop yields by nearly 30% compared to conventional mulch cultivation [4]. Precision seeding on film is vital for achieving mechanized operations throughout the entire process of full-film double-ridge field crop production [3]. Film hole-seeding involves creating planting holes in the film at specific row and hole spacings, effectively minimizing damage to the film caused by seeding machinery, safeguarding the water and thermal systems of the double ridges covered by the film [5], enhancing rainwater collection and moisture retention, boosting seeding efficiency, and reducing labor and resource requirements [6]. Hence, enhancing the operational performance of hole seeders holds significant importance in advancing the mechanization of maize production in full-film double-ridge fields and promoting the evolution of precision seeding technology and equipment [7].

With the advancement of precision seeding technology, high-speed field operations have become the pivotal benchmark for evaluating seeder performance [8,9]. Gao et al. [10,11] explored the influence of particle count and cleaning element angle on seeding performance during high-speed seeding processes. Dong et al. [12] and Ma et al. [13] investigated maize seeding postures and proposed methods for adjusting seed guidance trajectories and filling postures to enhance the high-speed operation performance of seed-metering devices. However, these studies overlooked the impact of the hole-forming device on seeding effectiveness. Accelerating hole-seeder operation speeds leads to shortened seeding times, potentially resulting in hole seeders failing to smoothly dispense seeds or seeds not being dispensed promptly, causing seed blockages and damage. Research on the effect of hole-forming mechanisms on seeding outcomes during hole-seeder operations remains limited. While optimized duckbill hole-forming devices, as proposed by Wang [14], reduce soil plug formation, the incomplete opening of the soft soil pressure plate may impede seed dispersion. Gu et al. [15] suggested a robust opening method using levers and limit blocks to improve seeding success rates, but excessive duckbill opening could increase the damage caused to plastic film and the soil.

Addressing these issues, a pendulum-lever-type hole-seeding device was designed to enhance the operational performance of the seeder and promote the development of precision seeding technology. This study focused on widely used mechanical hole seeders, analyzing the seeding principles of hole-seeder hole-forming components, investigating hole-seeder bench test adjustment requirements, and optimizing structural parameters. Through cosimulation analysis using discrete element software EDEM 2020 [16] and multibody dynamics software RecurDyn V9R4 [17], joint simulations were conducted to identify optimal parameter combinations for hole seeders and key components of the hole-forming mechanism. Bench tests and field tests were conducted to validate the performance improvements.

2. Materials and Methods

2.1. Machine Structure and Working Principle

2.1.1. Machine Structure

The pendulum plate and lever hole-seeding device was mainly composed of a fixed plate, movable shaft, electric actuator, rotating disc, connecting bracket, fixed disc cover, pendulum plate, and hole-former, and its structure is shown in Figure 1.

The fixed plate and connecting bracket were coaxially mounted on the movable shaft with the hole seeder's rotating disc, fixed disc, and fixed disc cover; the hole-former was circumferentially distributed on the movable plate; the seed-discharging wheel dial was coaxially mounted with the seed-discharging wheel; the pendulum mechanism hinged to the lower portion of the fixed disc was adjacent to the limit lever; and the return tension spring was connected to the pendulum plate at one end and was hooked up to the fixed disc at the other end.

2.1.2. Working Principle

When the pendulum paddle hole-seeding device operates, according to the preset sowing depth and the size of the hole-seeding device, the length of the electric push rod is adjusted to change the installation height of the hole-seeding device (the vertical distance between the center of the hole-seeding device axis and the seedbed belt). The adjustment range of the electric push rod was 305~505 mm, and the installation height of the hole-seeding device ranged from 180~471 mm, to meet the agronomic technical requirements of different sowing depths. The adjusting trajectory is shown as a red line in Figure 2a.

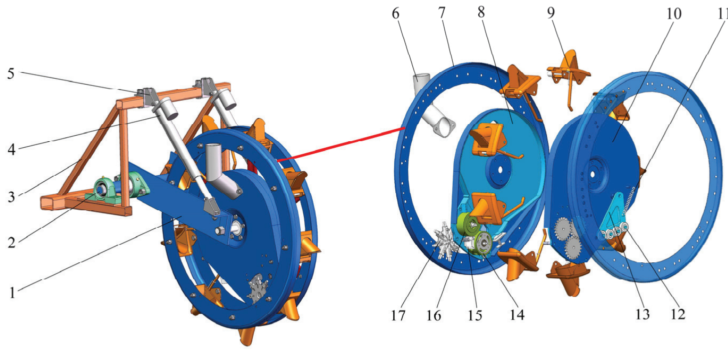

Figure 1. Structural diagram of pendulum-lever-type hole-seeding device: (1) fixed plate; (2) movable shaft; (3) bracket; (4) electric actuator; (5) connecting bracket; (6) seed delivery tube; (7) rotating disc; (8) fixed disc cover; (9) hole-former; (10) fixed disc; (11) return tension spring; (12) pendulum plate bearing; (13) pendulum plate; (14) seed-discharging wheel; (15) guard plate (16) seed brush wheel; (17) seed-discharging wheel dial.

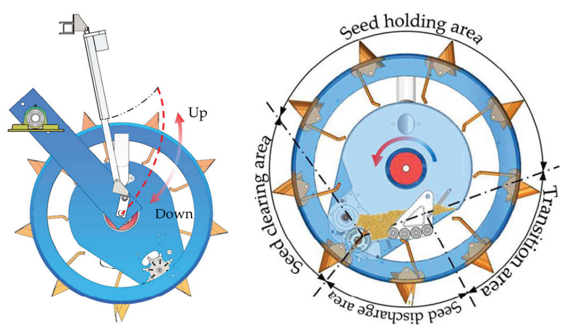

(**a**) (**b**)

Figure 2. Working diagram of wobble plate lever hole-seeding device. (**a**) Adjustment devices; (**b**) hole seeder.

Within the hole-seeding chamber, the corn seed population flows dynamically under the influence of friction and gravity in the seed holding area of the hole seeder's fixed disk chamber. Seeds in the seed holding area rely on gravity and interseed force to enter the holes of the seed discharge wheel. The rotating sleeve contacts the dial of the seed discharge wheel, driving the rotation of both the seed discharge wheel and the seed brush wheel. The brush wheel rotates counterclockwise to clear any seeds that have not fully entered the holes. As the seed discharge wheel rotates to a specific position, seeds fall into the cavity of the hole-forming device under the combined influence of gravity and the seed-clearing plate. At this point, the lever slides around the outer circle of the pendulum plate bearing, while the bearing group acts on the upper end of the lever to keep the movable hole-former open. The seeds then fall into the soil, completing one sowing cycle, as illustrated in Figure 2b.

2.2. Design of Key Components for Hole-Seeding Devices

The hole-seeding device plays a crucial role in the film-sowing process and is primarily composed of the hole-former unit and the swinging disk mechanism. The size and timing of the hole-former's opening are critical factors influencing both the seeding performance of the hole seeder and the moisture retention effect of the full-film hole seeder. Excessive opening size or prolonged opening time may result in film tearing or picking, leading to noticeable soil disturbance around the holes, disrupting the ridge structure of the full-film double-row furrows and reducing soil temperature and water transfer capacity [18]. Therefore, it is essential to minimize the degree of film damage and soil disturbance caused by the hole-former while ensuring smooth seeding, thereby preserving the hydrothermal effect of the full-film double-row production system [19,20].

2.2.1. Design of the Hole-Forming Mechanism

The hole-former shape is mainly conical- and wedge-shaped, and research shows that cone-shaped hole-formers are more effective than wedge-shaped hole-formers in terms of hole formation and soil movement [21]. The structure of the conical hole-forming group, which is mainly composed of a fixed hole-former, base fixed plate, rotating sleeve, lever, return spring, and movable hole-former, is shown in Figure 3.

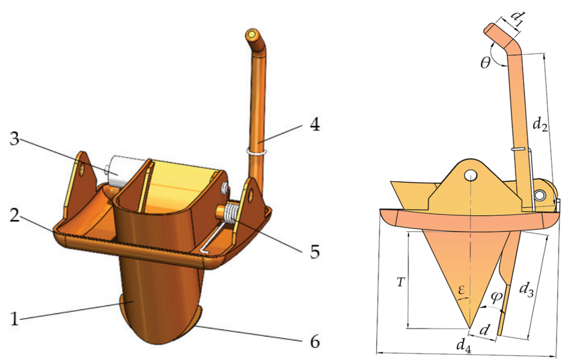

(**a**) 3D diagram (**b**) Schematic diagram

Figure 3. Hole-former structure: (1) fixed hole-former; (2) base fixed plate; (3) rotating sleeve; (4) lever; (5) return spring; (6) movable hole-former.

As shown in Figure 3b, to ensure that the seed drop is smooth and the hole-former works without clogging and film hanging, the hole-former opening degree d satisfies [22]

$$d = 1.2 \sim 1.5 d_{\max} \tag{1}$$

where d is the hole-former opening, mm; $d_{\max}$ is the maximum geometric size of the seed, mm.

To ensure that the seed discharge wheel-type holes are filled with single grains of seeds, the larger Jinsui No. 4 corn seeds were selected [23]. Then, the range of values of hole-former openings d was determined as 15~18.75 mm.

The length of the hole-forming mechanism affects not only the sowing depth but also the effect of the tip scraping when the soil comes out. If the length of the hole-forming mechanism is too short, it is difficult to break the film into holes; if the length of the hole-forming mechanism is too long, it is easy to hang the film, destroying the shape of the film holes, affecting corn seedling emergence. The calculation formula for the length of the dynamic into the hole device is

$$d_3 = \frac{T}{\cos \varepsilon} \tag{2}$$

where d_3 is the length of the movable hole-former, mm; T is the sowing depth. According to the requirements of full-film double-ridge furrow agronomic technology [2], we took 50 mm; ε is the angle between the hole-forming edge line of the fixed hole-former and the line connecting the bottom and the center of the drum, °.

Referring to the literature [24], $\varepsilon = 30°$, which was brought into Equation (5) to obtain $d_3 = 57.74$ mm. After the hole-former opening was determined, the movable hole-former angle φ was determined from the geometrical relationship:

$$\varphi = 2\sin^{-1}\left(\frac{d}{2d_3}\right) \quad (3)$$

where φ is the angle of rotation of the dynamic hole-forming apparatus, °.

From this, the rotational angle φ of the movable hole-former was determined to be 14.93°~18.68°. The long arm of lever d_2 is the distance from the hole-forming part to the pendulum mechanism, which is 100 mm; to ensure the stability of the opening of the dynamic hole-forming mechanism, the value of the short arm of lever d1 should be larger than the radius of the pendulum bearings by 15 mm and smaller than the distance between the centers of the two adjacent bearings by 30 mm, which was taken as $d_1 = 22$ mm.

2.2.2. Design of Pendulum Mechanism

The pendulum mechanism comprises the pendulum plate, pendulum bearing, return tension spring, and limit lever, as depicted in Figure 4. During operation, the return tension spring keeps the pendulum disk mechanism close to the fixed disk limit lever. The lever slides along the outer circle of the pendulum disk bearing, ensuring the hole-forming mechanism remains open for seed deposition into the soil. Furthermore, the limiting device on the pendulum disk regulates the opening and closing of the hole-forming mechanism within an appropriate timeframe, facilitating smooth seeding.

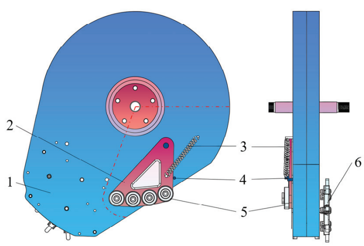

(**a**) Schematic structure

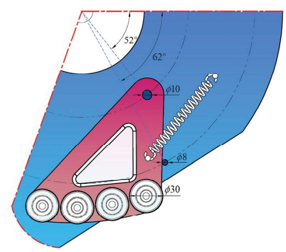

(**b**) Schematic of installation dimensions

Figure 4. Pendulum mechanism: (1) fixed plate; (2) pendulum plate; (3) return tension spring; (4) limit lever; (5) pendulum bearing; (6) seed-discharging wheel dial.

In the pendulum device with reverse rotation protection, as the rotating disc moves backward, the lever glides along the outer perimeter of the bearing, prompting the pendulum disk mechanism to rotate around the pendulum pin in the same direction. Throughout this process, the movable hole-former maintains a tight closure against the fixed hole-former. Upon the lever's disengagement from the outer circle of the bearing, the pendulum disk mechanism reverts to its initial position due to the action of the return spring, as illustrated in Figure 5.

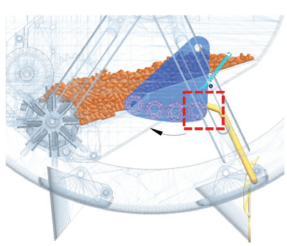

(T_1)

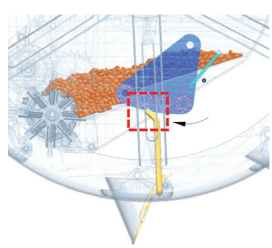

(T_2)

Figure 5. Moments T_1 and T_2 during the reversal process of the hole seeder.

2.3. Design of the Adjustment Mechanism and Test Bench

2.3.1. Design of Adjustment Device

The adjustment device serves the purpose of controlling and regulating sowing depth and is adaptable for altering the bench height to accommodate different sizes of hole-seeder seeding tests. Comprising the bracket, bearing seat, electric actuator, and switch controller, as depicted in Figure 6, the adjustment device is an integral component of the pendulum-lever-type hole-seeding apparatus. During operation, in accordance with various test conditions and hole-seeder dimensions, the electric actuator's stroke is controlled to adjust the hole seeder's height position. Concurrently, the fixed plate rotates along the axis of the movable shaft, providing support and fixation for the hole seeder.

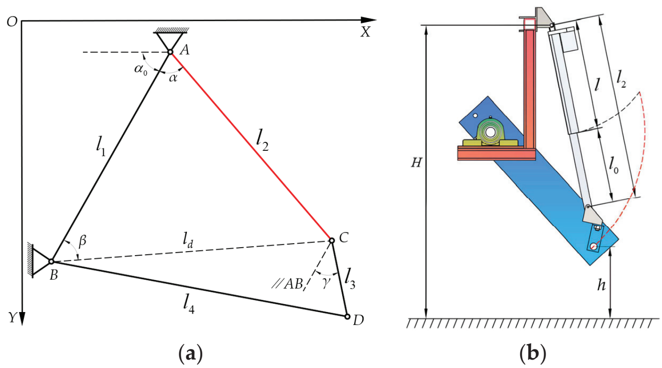

Figure 6. Adjustment trajectory analysis. (**a**) Sketch of the regulating mechanism. (**b**) Hole-seeding axis adjustment track.

Figure 6a shows a sketch of the four-bar mechanism of the mounting bracket, constructing the coordinate system *XOY*, the *X*-axis over point *A*, and the *Y*-axis over point *B*. According to the analytical method [25], the trajectory of the movement of point *D* on the connecting rod can be adjusted to the hole-seeding center-axis trajectory *D*(*x*,*y*):

$$\begin{cases} x_D = l_1\cos\alpha_0 + l_2\cos(\pi-\alpha_0-\alpha) + l_3\cos(\pi-\alpha_0-\gamma), \alpha\in[0,\pi] \\ y_D = l_2\sin(\pi-\alpha_0-\alpha) + l_3\sin(\pi-\alpha_0-\gamma), \alpha\in[0,\pi] \\ {x_D}^2 + (y_D - l_1\sin\alpha_0)^2 = {l_3}^2 \end{cases} \tag{4}$$

$$\begin{cases} \delta = \arccos\frac{{l_1}^2+d^2-{l_4}^2}{2l_1l_d} - \beta \\ \beta = \arcsin\frac{l_2\sin\alpha}{l_d} \\ l_d = \sqrt{{l_1}^2+{l_2}^2-2l_1l_2\cos\alpha} \end{cases} \tag{5}$$

where (x_D, y_D) are the coordinates of point *D*, mm; l is the initial length of the motorized actuator, mm; l_0 is the electric actuator adjustment stroke, mm; l_1 is the length between the bracket fixing points, mm; l_2 is the crank length, mm; l_3 is the length of connecting rod, mm; α_0 is the angle between the line connecting points *A* and *B* and the direction of *X* axis; α is the crank rotation angle, °; δ is the angle between connecting rod *AB* and *CD*, °; l_4 is the rocker length, mm; β is the angle between *AB* and *BC*, °.

The electric actuator stroke l_0 ranges from 0 to 200 mm, i.e., the length of l_2 varies from 305 to 505 mm. Considering the size of the hole-forming mechanism and the radius of the hole-seeding device [26], l_4 = 400 mm, l_1 = 320 mm, l_3 = 100 mm, and α_0 = 60°.

When the minimum adjustment stroke l_0 = 0 mm, the crank angle α = 7 °, calculated using formulas (1) and (2) in the coordinate system *XOY D*, with point coordinates for (328, 279); we adjusted the l_0 maximum to 200 mm, when the crank angle α = 43.2 °, for

D point coordinates for (213, 570). The hole-seeding installation height h and point D longitudinal coordinate relationship formula is

$$h = H - y_D > 0 \tag{6}$$

where h is the vertical distance between the axis of hole seeding to the seedbed belt, mm; H is the vertical distance between the bracket and motorized actuator connecting the axis to the seedbed belt, mm.

When H = 750 mm, the variation range of hole-seeding installation height h is 180~471 mm, which is in line with the range of the hole-seeding radius. The axial trajectory of the hole-seeding installation position is shown as a red line in Figure 6b.

2.3.2. Structure of the Test Bench

We used this regulating device in a test stand; the structure of the test bench mainly included a bench, conveyor belt, drive roller, and roller, as shown in Figure 7.

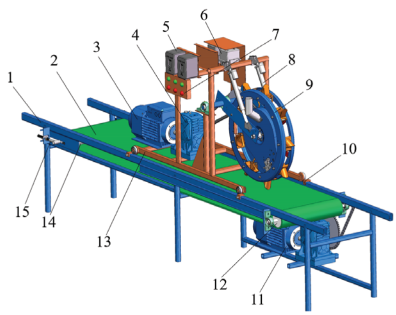

(**a**) 3D diagram

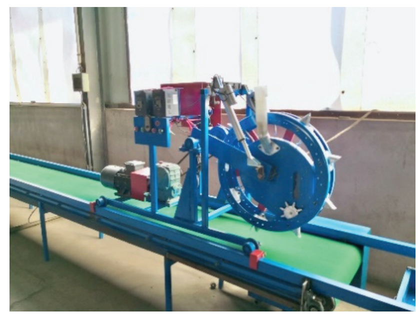

(**b**) Photograph of device

Figure 7. Hole-seeding device test bed: (1) bench; (2) conveyor belt; (3) hole seeder motor; (4) retarder; (5) inverter; (6) contactor; (7) central control panel; (8) electric push rod; (9) hole seeder; (10) bracket restrainer; (11) conveyor belt motor; (12) drive roller; (13) bracket; (14) roller; (15) conveyor belt tensioning device.

The transmission system of the seeding test bench of the hole-seeding device is shown in Figure 8, and the direction of the arrow is the direction of power transmission. The driving motor of the hole seeder is transmitted to the gearbox through a universal transmission shaft. After the gearbox changes direction, it is first transmitted to the movable shaft by belt transmission, and then transmitted to the hole seeder through the coaxial sprocket two-stage transmission. In the same way, the conveyor belt drive motor is transmitted to the conveyor belt drive roller by chain transmission after variable speed commutation of the gearbox.

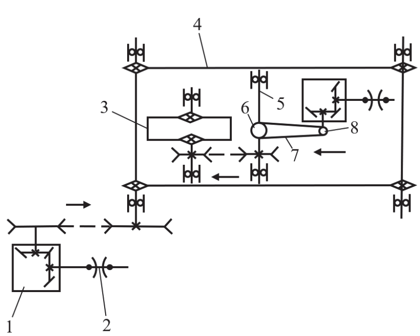

Figure 8. Schematic diagram of the test stand drive system: (1) retarder; (2) coupler; (3) rotating disc; (4) conveyor belt; (5) movable shaft; (6) large pulley; (7) V belt; (8) small pulley.

3. Seeding Process Simulation

3.1. Discrete Elemental Modeling of Corn Kernels

We randomly selected 500 seeds of Jinsui No. 4. Considering the influence of kernel shape on the seed-casting process, the kernels were categorized into flat and round according to the shape contour for counting, and the three-axis dimensions of the maize kernels were determined using digital vernier calipers, which were the length (L), width (W), and thickness (T) of the corn kernels (Figure 9).

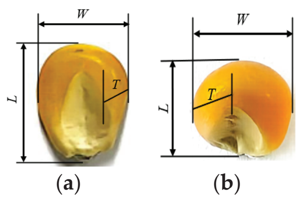

Figure 9. Corn kernel external dimensions. (**a**) Flattened; (**b**) orbicular.

The calculated triaxial geometric mean diameters of the seeds are shown in Table 1. Based on the three-axis geometric mean diameter and shape profile of the corn kernels, 3D modeling software was used to establish a 3D model of the kernel, and the model was imported into EDEM software in .stl format. To more accurately fit the motion of the corn kernels, spheres with unequal diameters were used to fill the kernel. We reduced the number of spherical particles required to fill a single grain to save simulation time, and we established 13 and 14 large-spherical corn grain models, as shown in Figure 10.

Table 1. Triaxial geometric mean diameter of seeds.

Shape	Average Length L/mm	Average Width W/mm	Average Thickness T/mm	Proportion
Flattened	11.65	7.62	4.85	77.4%
Orbicular	10.73	7.68	5.87	22.6%

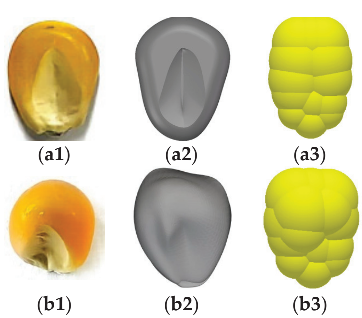

Figure 10. Discrete metamodel of corn kernels. (**a1**) Flat-shaped grain entity; (**a2**) 3D model of flat grain; (**a3**) discrete flat-grain model; (**b1**) circular grain entity; (**b2**) 3D model of circular grain; (**b3**) discrete circular-grain model.

3.2. Modeling of Hole-Seeding Applicator Rows

While ensuring successful sowing with the hole seeder, the 3D model created using SolidWorks 2022 software was simplified to reduce the computational complexity of the simulations. The simplified model was then imported into multibody dynamics simulation software RecurDyn in .x_t format to add constraints, forces, and contact relationships for simulating the trajectory of the hole seeder during seeding. The multibody dynamics model in RecurDyn was imported into EDEM for further analysis using a wall intermediate format file. Simulation tests of the hole-seeding process were conducted based on MBD-DEM. The necessary material and contact parameters for the simulation model in the seed discharge process were obtained by reviewing the literature, as shown in Tables 2 and 3 [27,28].

Table 2. Material parameters of the simulation model.

Material	Poisson's Ratio	Shear Modulus/MPa	Density/(kg·m^{-3})
Corn	0.357	2.17×10^2	1250
Steel	0.28	3.5×10^4	7850
Seed brush	0.40	1×10^2	1150
Rubber band	0.48	1×10^3	1380

Table 3. Contact parameters of the simulation model.

Form of Contact	Coefficient of Restitution	Coefficient of Static Friction	Coefficient of Rolling Friction
Corn–Corn	0.60	0.50	0.10
Steel–Corn	0.60	0.30	0.01
Seed Brush–Corn	0.45	0.50	0.01
Rubber Belt–Corn	0.711	0.784	0.035

After establishing a simplified model for hole-seeding simulation [29], the simulation parameters were set to generate a total of 1000 corn grains, with each type generated at a rate of 300 grains/s, as depicted in Figure 11a. The simulation time was set to 2 min, with a time step of 2.58×10^{-5} s. To observe in detail how the seed model underwent the processes of filling, carrying, and casting during hole-seeding discharge by the hole seeder, kernels with entry hole movement within the corn grain group were selected as the observation objects. The hole-seeding model was set to be displayed in the form of filled objects with an opacity of 0.1, and its trajectory is depicted in Figure 11b. Upon completion of the simulation, Figure 12 illustrates the seedbed with falling seeds.

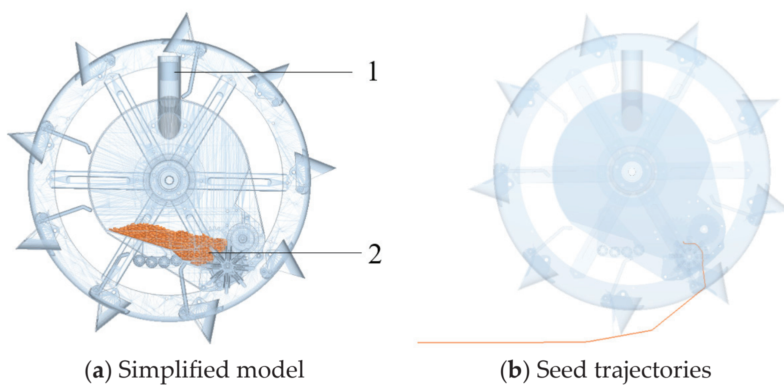

Figure 11. Simulation model. (1) Corn model generation cylinder; (2) corn particles.

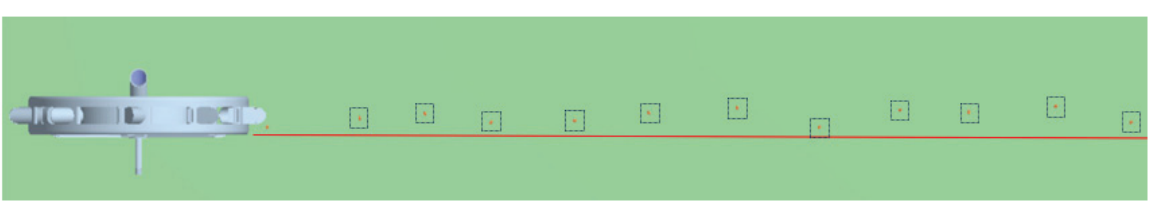

Figure 12. Schematic diagram of simulated seed drop.

3.3. Single-Factor Simulation Test

To determine the range of model operating parameters, single-factor simulation experiments were necessary. Based on the operating principles of the device and relevant operational parameters of the seeder, we separately determined the experimental value range of the seeder's dynamic disc speed, the dynamic forming plate lever angle, and the number of pendulum plate bearings.

3.3.1. Determination of Rotating Speed of Rotating Disc

The seed discharger is the core component of the hole seeder, and its seed supply speed directly determines the rotational speed of the hole seeding. To improve the operation speed of hole seeding, considering the actual seed supply speed of this mechanical seeder, the maximum speed of the hole seeder's rotating disc was set at 80 r/min, which means that the forward speed of the hole seeding was 9.40 km/h. To adapt to different operating conditions of the seeder, we verified the sowing performance at different speeds. Selecting a low speed of 40 r/min, a medium speed of 60 r/min, and a high speed of 80 r/min, the forward speeds of the seeder were 4.72 km/h, 7.06 km/h, and 9.40 km/h, respectively.

3.3.2. Determination of the Angle of the Lever

The angle of the movable hole-former lever primarily affects the size of the hole-former opening, which varies with the lever angle. During operation, Figure 13a,b illustrate that when the lever angle of the hole-forming mechanism is 110°, the opening of the movable hole-former is small, increasing the likelihood of 'stuck seeds' if seeds are not promptly dispensed, leading to seed damage and affecting subsequent seeding strokes. Additionally, when the hole-forming mechanism is used for mulch-hole seeding, a small lever angle narrows the opening of the movable hole-former, preventing seeds from falling into the soil promptly, resulting in decreased seeding quality and an increased empty hole rate. In Figure 13d, when the hole-former lever is at 150°, the turning angle of the movable hole-former λ is 22.72°, elevating the risk of film tearing and soil disturbance. Conversely, in Figure 13c, when the lever is at 140°, the turning angle λ = 18.71°, nearing the maximum range value of 18.69°. Considering these factors, the optimal range for the movable hole-former lever angle was determined to be 110° to 140°.

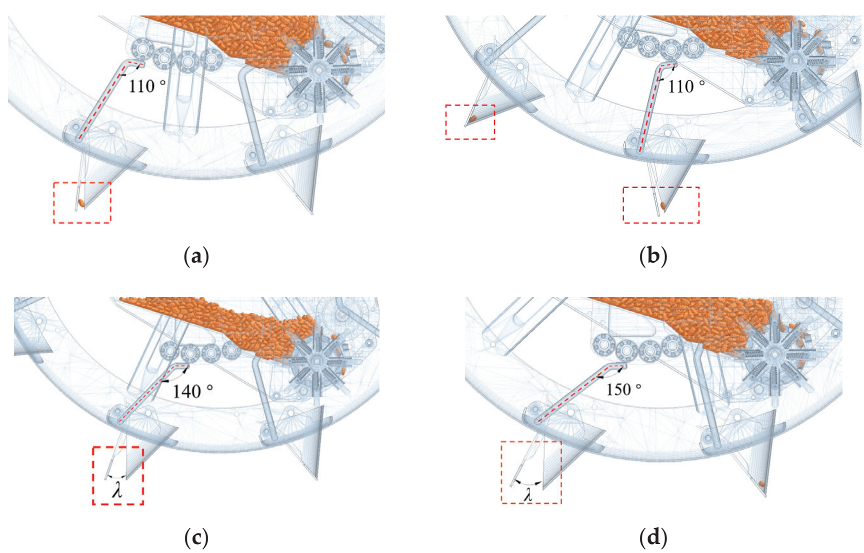

Figure 13. Movable hole-formers with different lever angles: (**a**) for 110° lever; (**b**) seed not dropped for 110°, (**c**) 140°, and (**d**) 150° levers.

3.3.3. Determination of the Number of Pendulum Bearings

The pendulum mechanism serves as the primary opening mechanism of the hole-former, ensuring that it operates within a reasonable timeframe. The number of pendulum bearings is a critical component for controlling the opening and closing times of the hole-forming device. If the number of pendulum bearings is insufficient, it may shorten the opening time of the moving hole-forming device, leading to issues such as seed jamming and the delayed discharge of corn kernels, which can significantly impact the effectiveness of sowing. Conversely, an excessive number of pendulum bearings extends the opening time of hole seeding but increases the risks of film tearing and the disruption of the structure of the whole-film mulching and double-ridge furrow, resulting in lower ground temperature around the seed holes and reduced moisture transfer capability. We calculated the seed drop time to satisfy the following conditions:

$$\begin{cases} \Delta t = \frac{\Delta\theta}{\omega} \\ \omega = \frac{v}{r} = 2\pi n \end{cases} \tag{7}$$

where $\Delta\theta$ is the angle between the drop point of the discharge wheel of the hole seeder and the line connecting the center and the vertical centerline of the hole seeder, (°); Δt is the time for the hole seeding to turn over, s; ω is the hole-forming apparatus's angular velocity, rad.

Considering the seed dispenser had a $\Delta\theta$ of 36° and speeds of 40 r/min, 60 r/min, and 80 r/min, the duration of hole seeding was 0.15 s, 0.1 s, and 0.075 s, respectively. When the speed of the hole seeding was increased from 40 to 80 r/min, the theoretical pulsation period of the seeding time reduced from 0.15 to 0.075 s.

Through simulation testing, we obtained the actual seed drop time of the hole seeder. We set the EDEM data-saving interval to 0.01 s and exported speed data for a single seed to create a two-dimensional line graph, as depicted in Figure 14. We analyzed the seed drop time and speed change graph for different dynamic disc speeds, and we determined the optimal number of pendulum bearings to install. We adjusted the opening and closing time of the hole-former and optimized the seed drop effect of the hole seeder.

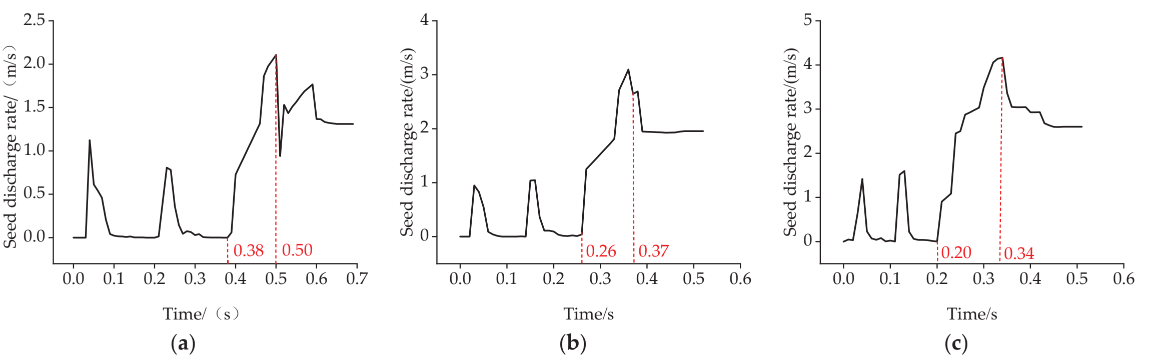

Figure 14. Seed drop time vs. speed at different rotational speeds. (**a**) Speed = 40 r/min; (**b**) speed = 60 r/min; (**c**) speed = 80 r/min.

In the seed movement process, the seed falls into the hole first, the two hole positions are rotated with the seeding wheel, and then the seed contacts the hole-forming device freely, colliding in the cavity of the hole-forming device, and finally reaching the bottom of the hole-forming device. Then, the hole-forming device opens and the seed falls to the seedbed belt. It can be seen from the Figure 14 that when the rotating speed of the hole seeder was 40 r/min, 60 r/min, and 80 r/min, the corn seeds fell freely from the seeding. The time required for this process was 0.12 s, 0.11 s, and 0.14 s, respectively. When the rotating speed of the moving disc was 80 r/min, the seed dropping time did not decrease but increased, because the rotating speed of the moving disc was too fast, and the seed was dragged by the hole-forming device, resulting in delayed falling. The maximum speed of the seeds was more than 4 m/s, and there was an obvious bounce phenomenon that occurred when the seed contacting the seedbed. Figure 15 is the change diagram of the seeding index Y of the hole seeder at different speeds when the number of pendulum bearings ranged from one to six.

$$Y = \frac{m}{M} \tag{8}$$

where Y is the seeding index, %; M is the theoretical number of seeding holes; m is the actual number of seeding holes.

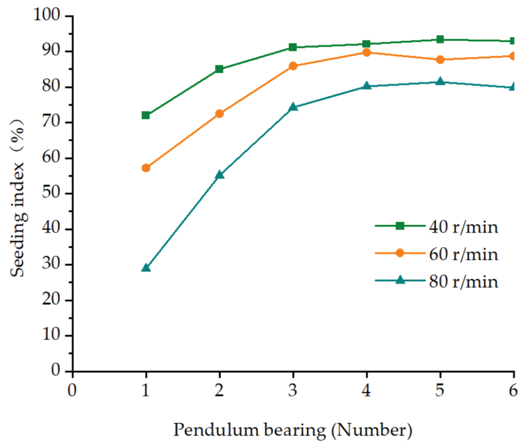

Figure 15. Plot of number of bearings versus row index at different speeds.

It can be seen from the Figure 15 that the number of pendulum bearings was one, the seeding index under different speeds was less than 80%. This is attributed to the brief opening duration of the hole-forming device with a single bearing. When seeds do not reach the bottom of the hole-forming device, the movable hole-former completes its cycle prematurely, resulting in fewer seeding holes. However, the seeding index was 71.94% at 40 r/min. The main reason was that the seeding period of the hole seeder was longer at a slower rotating speed, which prolonged the opening and closing time of the hole-forming device and the falling time, and the seeds could pass through before the closing of the hole-forming device. When the number of bearings was three or less, the seeding index of the hole seeder at different speeds increased significantly. When the number of bearings was more than three, the seeding index at the speed of 40 r/min tended to be stable. The seeding index at the speed of 60 r/min and 80 r/min increased by 4.82% and 5.94%, respectively, and then the seeding index fluctuated within a range of 3%. When the number of bearings was six, the seeding index did not change significantly. From our analysis, the optimal value range of the pendulum plate bearing was found to be between three and five.

3.4. Box–Behnken Experimental Design

To optimize the parameters of the hole-seeding device's oscillating disc mechanism, an experiment was conducted using a Box–Behnken central combination experimental design to determine the optimal parameter combinations of the factors affecting the seed discharge performance. In the test, we took the hole-seeding machine moving disc speed, the angle of the moving hole-forming machine lever, and the number of swing disc bearings as factors, and based on the results of the theoretical analysis and simulation analysis, we set the zero-level value, and we carried out a three-factor, three-level orthogonal test. The experimental factor coding is shown in Table 4. A total of 17 groups of tests were conducted, each group of tests was repeated three times, and the average value was taken as the final test results (X_1, X_2, and X_3 were the factor coding values).

Table 4. Test factor codes.

Levels	Test Factors		
	Rotational Speed of Rotating Disc X_1/(r·min^{-1})	**Lever Angle X_2/(°)**	**Pendulum Bearings X_3/(Number)**
−1	40	110	3
0	60	125	4
1	80	140	5

According to the parameter requirements of each test sequence number, we adjusted the rotational speed of the moving disc, angle of the lever, and number of bearings. We completed the modeling of the hole-seeding machine using SolidWorks, set the rotational speed of the moving disc in RecurDyn software, and carried out simulation tests based on MBD-DEM. We extracted the data of the number of grains in each group of tests and computed the qualification index, the miss-seeding index, and the replanting index. We recorded the test results. According to GB/T 6973-2005 "Test Methods for Single Grain (Precision) Seeders" [30], the test takes the seed discharge qualification index Y_1, miss-seeding index $Y_{2,}$ and replanting index Y_3 as the test indices, which are continuously detected under stable working conditions of the hole-seeding machine, and the test results are shown in Table 5.

$$Y_1 = \frac{n_1}{N} \times 100\% \tag{9}$$

$$Y_2 = \frac{n_0}{N} \times 100\% \tag{10}$$

$$Y_3 = \frac{n_2}{N} \times 100\% \tag{11}$$

where N is the theoretical number of seeds; n_0 is the number of miss-seeded rows; n_1 is the number of single seed rows; n_2 is the number of repeated rows.

Table 5. Experimental project and results.

Test No.	Factors			Response Values		
	X_1	X_2	X_3	Y_1/%	Y_2/%	Y_3/%
1	−1	1	0	89.26	5.42	5.32
2	−1	0	1	90.4	4.54	5.06
3	−1	0	−1	89.98	5.29	4.73
4	−1	−1	0	72.49	25.23	2.28
5	0	1	1	88.02	7.73	4.25
6	0	1	−1	85.03	11.32	3.65
7	0	0	0	87.52	8.73	3.75
8	0	0	0	87.41	9.41	3.18
9	0	0	0	86.61	9.47	3.92
10	0	0	0	86.66	9.57	3.77
11	0	0	0	84.56	11.63	3.81
12	0	−1	1	67.5	29.59	2.91
13	0	−1	−1	64.62	32.73	2.65
14	1	1	0	79.68	17.97	2.35
15	1	0	−1	77.6	20.26	2.14
16	1	0	1	72.56	25.68	1.76
17	1	−1	0	54.33	44.04	1.63

4. Results and Analysis

4.1. Simulation Test Results

4.1.1. Regression Modeling and Testing

Regression fitting and variance analysis were carried out using Design-Expert 12 data processing software. The results are shown in Table 6, and the regression equations of the qualification index Y_1, miss-seeding index Y_2, and replanting index Y_3 with the coded values of the test factors were obtained as follows:

$$Y_1 = 86.55 - 7.25X_1 + 10.38X_2 + 1.42X_3 + 2.15X_1X_2 + 1.15X_1X_3 + 0.0275X_2X_3 - 3.13{X_1}^2 - 9.48{X_2}^2 - 0.7823{X_3}^2 \quad (12)$$

$$Y_2 = 9.76 + 8.43X_1 - 11.14X_2 - 1.61X_3 - 1.57X_1X_2 - 1.17X_1X_3 - 0.1125X_2X_3 + 3.50{X_1}^2 + 9.90X_2 + 0.6790{X_3}^2 \quad (13)$$

$$Y_3 = 3.69 - 1.19X_1 + 0.7625X_2 + 0.1963X_3 - 0.5800X_1X_2 + 0.0125X_1X_3 + 0.0850X_2X_3 - 0.3667{X_1}^2 - 0.4242{X_2}^2 + 0.1032{X_3}^2 \quad (14)$$

Table 6. Variance analysis of the regression coefficients.

Test Index	Sources of Variance	Square of Sum	Degree of Freedom	Mean Square	*F*-Value	*p*-Value
Qualification index	Model	1765.11	9	196.12	207.28	<0.0001 **
	X_1	99.94	1	99.94	105.62	<0.0001 **
	X_2	6.54	1	6.54	6.91	0.0340 *
	X_3	7.58	1	7.58	8.01	0.0254 *
	X_1X_2	18.40	1	18.40	19.45	0.0031 **
	X_1X_3	5.34	1	5.34	5.64	0.0493 *
	X_2X_3	0.0030	1	0.0030	0.0032	0.9565
	${X_1}^2$	41.38	1	41.38	43.73	0.0003 **
	${X_2}^2$	378.18	1	378.18	399.70	<0.0001 *
	${X_3}^2$	2.58	1	2.58	2.72	0.1429
	Residual error	6.62	7	0.9462		
	Lack-of-fit	0.9668	3	0.3223	0.2279	0.8728
	Error	5.66	4	1.41		
	Sum	1771.74	16			
Miss-seeding index	Model	2088.30	9	232.03	190.83	<0.0001 **
	X_1	150.66	1	150.66	123.91	<0.0001 **
	X_2	5.91	1	5.91	4.86	<0.0001 **
	X_3	7.82	1	7.82	6.43	0.0044 **
	X_1X_2	9.80	1	9.80	8.06	0.0251 *
	X_1X_3	5.45	1	5.45	4.48	0.0720
	X_2X_3	0.0506	1	0.0506	0.0416	0.8441
	${X_1}^2$	51.62	1	51.62	42.46	0.0003 **
	${X_2}^2$	412.80	1	412.80	339.49	<0.0001 **
	${X_3}^2$	1.94	1	1.94	1.60	0.2469
	Residual error	8.51	7	1.22		
	Lack-of-fit	3.71	3	1.24	1.03	0.4685
	Error	4.80	4	232.03		
	Sum	2096.81	16	2.12		
Reseeding index	Model	19.05	9	5.19	11.99	0.0018 **
	X_1	5.19	1	0.0157	29.37	<0.0001 **
	X_2	0.0157	1	0.0018	0.0888	0.0014 **
	X_3	0.0018	1	1.35	0.0103	0.2281
	X_1X_2	1.35	1	0.0006	7.62	0.0281 *
	X_1X_3	0.0006	1	0.0289	0.0035	0.9542
	X_2X_3	0.0289	1	0.5663	0.1636	0.6979
	${X_1}^2$	0.5663	1	0.7578	3.21	0.1165
	${X_2}^2$	0.7578	1	0.0449	4.29	0.0770
	${X_3}^2$	0.0449	1	0.1766	0.2542	0.6296
	Residual error	1.24	7	0.2997		
	Lack-of-fit	0.8990	3	0.0843	3.55	0.1262
	Error	0.3373	4	2.12		
	Sum	20.29	16			

Note: ** means very significant ($p < 0.01$); * means significant ($0.01 < p < 0.05$).

The models for the qualification index, miss-seeding index, and reseeding index of the test parameters were all highly significant ($p < 0.01$), with some quadratic and interaction terms also showing significant effects. The regression equations for the three response indicators were not significantly misfitted ($p > 0.05$), indicating that they were well fitted with the experimental data. The quadratic regression equation fitted by the model was consistent with the numerical simulation test results, which thus correctly reflected the relationship between the three response indicators X_1, X_2, and X_3.

(1) Qualification index regression model

According to Table 7, under a significance level $\alpha = 0.05$, the quadratic regression model of the qualification index had a p of < 0.01, extremely significant. The lack-of-fit term was not significant ($p = 0.8728$), indicating that there was no other main factor affecting the qualification index, and the regression equation did not lose fit. The p values of X_2X_3 and $X_3{}^2$ were greater than 0.05, indicating no significant effect on the qualification index. The regression model equation after eliminating the insignificant factors in the interaction term was

$$Y_1 = 86.55 - 7.25X_1 + 10.38X_2 + 1.42X_3 + 2.15X_1X_2 + 1.15X_1X_3 - 3.13X_1{}^2 - 9.48X_2{}^2 \quad (15)$$

Table 7. Results of bench test.

Number	Qualification Index	Miss-Seeding Index	Reseeding Index
1	87.60%	7.60%	4.80%
2	92.40%	4.00%	3.60%
3	91.60%	5.20%	3.20%
Average	90.53%	5.60%	3.87%

Through the test of the regression coefficient in Equation (16), it was concluded that the factors affecting the qualification index in decreasing order of predominance were the angle of the lever X_2, the rotational speed of the rotating disc X_1, and the number of bearings X_3.

(2) Miss-seeding index regression model

According to Table 7, under a significance level α of 0.05, the quadratic regression model $p < 0.01$ for the miss-seeding index was extremely significant. The lack-of-fit term was not significant ($p = 0.4685$), indicating that there was no other main factor affecting the miss-seeding index, and the regression equation did not lose fitting. Among them, the p values of X_1X_3, X_2X_3, and $X_3{}^2$ were greater than 0.05, indicating no significant effect on the miss-seeding index. The regression model equation after eliminating the insignificant factors in the interaction term was

$$Y_2 = 9.76 + 8.43X_1 - 11.14X_2 - 1.61X_3 - 1.57X_1X_2 + 3.50X_1{}^2 + 9.90X_2{}^2 \quad (16)$$

Through the test of the regression coefficient using Equation (17), it was concluded that the factors affecting the miss-seeding index in descending order were the lever angle X_2, the rotational speed of the rotating disc X_1, and the number of bearings X_3.

(3) Reseeding index regression model

According to Table 7, under a significance level α of 0.05, the quadratic regression model of the reseeding index was $p < 0.01$, which is extremely significant. The loss-of-fit item was not significant ($p = 0.1262$), indicating that there were no other main factors affecting the reseeding index, and the regression equation was not lost. Among them, X_1 and X_2 had extremely significant effects, and $X_2{}^2$ had significant effects. The regression model equation after eliminating the insignificant factors in the interaction term was

$$Y_3 = 3.69 - 1.19X_1 + 0.7625X_2 - 0.1963X_3 - 0.5800X_1X_2 \quad (17)$$

Through the test of the regression coefficient using Equation (18), it was concluded that factors affecting the reseeding index in decreasing order were the rotating speed of the moving disc X_1, the lever angle X_2, and the number of bearings X_3.

4.1.2. Analysis of Model Interaction Terms

According to the regression model, a response surface diagram between the significant factors was made, where the shape of the response surface reflects the strength of the interaction factors [31]. This paper mainly analyzed the interaction items that had a significant impact ($p < 0.05$). We drew a response surface diagram of the speed of the hole seeder's moving disc and the angle of the moving hole seeder's lever to the three response indicators (Figure 16); we also drew a response surface diagram of the speed of the hole seeder's moving disc and the number of pendulum bearings to the eligibility index Y_1 (Figure 17).

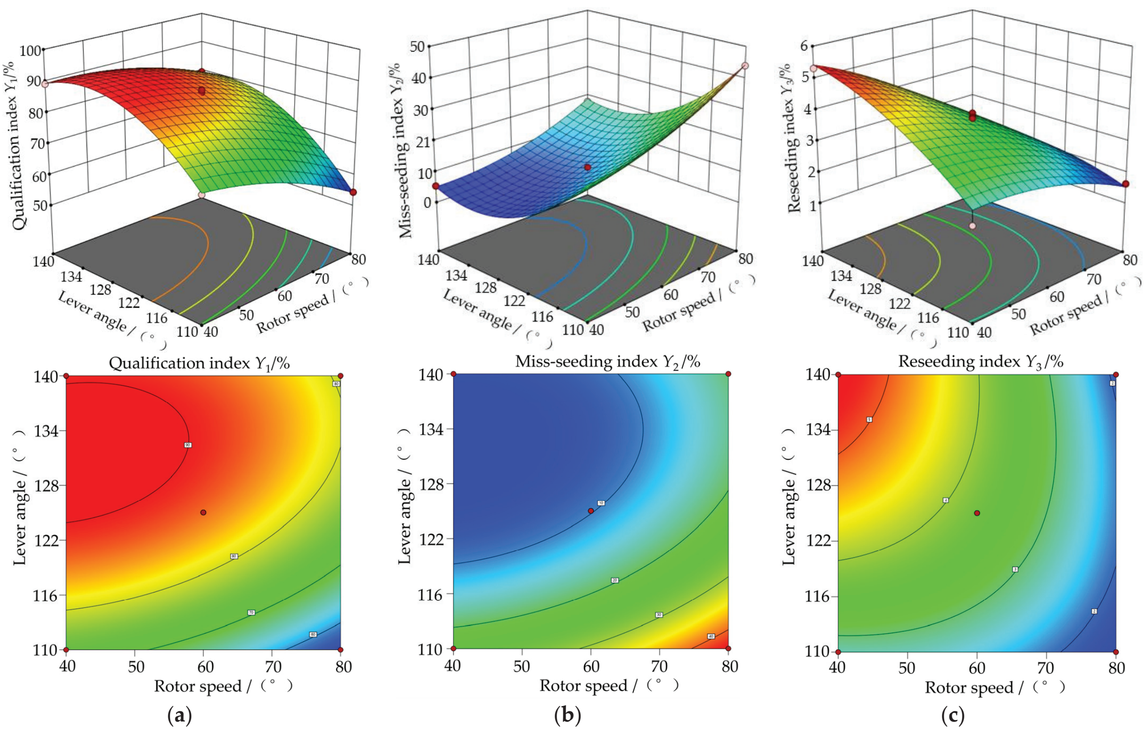

Figure 16. Effect of interaction of rotational speed of the rotating disc and angle of the lever on the response metrics. (**a**) Effect of the interaction of the rotational speed of the rotating disc and angle of the lever on the qualification index; (**b**) effect of the interaction of rotational speed of the rotating disc and angle of the lever on miss-seeding index; (**c**) effect of the interaction of rotational speed of the rotating disc and angle of the lever on the reseeding index.

(1) Interaction of rotational speed of the rotating disc and angle of the lever

Figure 16a illustrates the impact of the interaction between the rotating speed of the moving plate and the lever angle on the conformity index for four pendulum bearings. It can be observed that for a fixed rotation speed of the moving plate, the qualification index initially increases gradually with increasing lever angle, then gradually decreases. Similarly, at a constant lever angle, the qualification index slightly increases with a rising rotating speed of the moving plate before gradually decreasing after reaching its peak. The highest qualification index is achieved at a rotating speed of 40~60 r/min and a lever angle of 122°~134°.

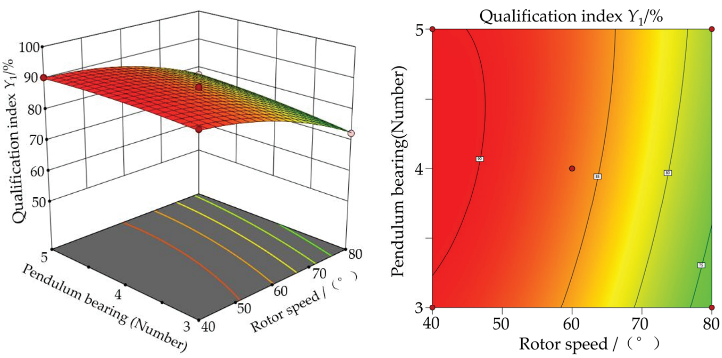

Figure 17. The influence of the interaction between the rotating speed of the moving disc and the number of bearings on the qualification index.

Figure 16b displays the influence of the interaction between the rotating speed of the moving plate and the lever angle on the miss-seeding index with four pendulum bearings. It is evident that at a constant rotation speed of the fixed moving plate, the miss-seeding index initially decreases gradually with increasing lever angle, then gradually increases. Conversely, at a constant lever angle, the miss-seeding index slightly decreases with increasing rotational speed of the moving plate before gradually increasing after reaching its peak. The lowest miss-seeding index was observed at a rotating speed of 40~60 r/min and a lever angle of 122°~134°.

Figure 16c depicts the impact of the interaction between the rotating speed of the moving plate and the lever angle on the reseeding index for four pendulum bearings. It is evident that, at a fixed speed of the moving plate, the reseeding index decreases with increasing lever angle. Similarly, at a constant lever angle, the reseeding index gradually decreases with increasing rotational speed of the moving plate. The lowest miss-seeding index was observed at a rotating speed of 80 r/min and a lever angle of 110 °.

The analysis revealed that when the lever angle remains constant, increasing the rotational speed of the moving plate enhances the rotation speed of the seeding wheel. This results in an accelerated seed delivery rate and an increased resultant force acting on the seeds. Consequently, some seeds fail to interact effectively and fill the designated holes, leading to a decline in both the qualification and reseeding indices, while the miss-seeding index notably escalates. Conversely, when the rotational speed of the moving plate remains constant and the lever angle decreases, the opening of the hole-forming device diminishes. Consequently, some seeds are unable to exit the hole-forming device, resulting in continuous decreases in the qualification and reseeding indices, accompanied by a significant increase in the miss-seeding index.

(2) Interaction between the rotational speed of the rotating disc and the number of pendulum bearings

Figure 17 shows the influence of the interaction between the rotating speed of the moving disc and the number of bearings on the qualification index when the angle of the lever is 125°. From the diagram, it can be seen that the rotating speed of the fixed moving plate is constant. With the increase in the number of bearings, the qualification index increases slightly first and then tends to be stable. The number of fixed bearings remains unchanged. With the increase in the rotating speed of the moving disc, the qualification index increases slightly and then decreases gradually after reaching the highest point. When the rotating speed of the moving disc is 40~60 r/min and the number of bearings is 4, the qualification index is the highest.

The analysis indicates that as the number of bearings increases, the openings of the hole-forming device gradually meet the requirements for discharging corn kernels. Initially, there is a slight increase in the qualification index, followed by stabilization. However, when the rotational speed of the rotating disc exceeds 60 r/min, the performance of the mechanical seed dispenser becomes a limiting factor. This results in an increase in empty holes on the seed-discharging wheel and a reduction in the seed-casting time of the hole-forming device, ultimately leading to a decrease in the qualification index.

4.1.3. Determination of Optimal Operating Parameters

To obtain the best combination of factors under the constraint conditions, the regression model was solved by multiobjective optimization to maximize the speed of the moving plate, minimize the angle of the lever, and minimize the number of bearings as the factor conditions, and to maximize the qualification index, minimize the reseeding index, and minimize the miss-seeding index as the evaluation indices. The regression equation and the constraint conditions were as follows:

$$\begin{cases} \max G(x) = Y_1(X_1, X_2, X_3) \\ \min G(x) = \begin{cases} Y_2 = (X_1, X_2, X_3) \\ Y_3 = (X_1, X_2, X_3) \end{cases} \end{cases} \tag{18}$$

$$\begin{cases} 40\text{r/min} \le \max X_1 \le 80\text{r/min} \\ 110^\circ \le \min X_2 \le 140^\circ \\ 3 \le \min X_3 \le 5, X_3 \in N^+ \end{cases} \tag{19}$$

The optimization solver in Design-Expert 12 software was used to optimize the regression equation models (12), (13) and (14) for objectives (18) and (19). Finally, the optimization test indices Y_1, Y_2, and Y_3 were obtained as the optimal working parameters: the speed of the moving plate was 49 r/min, the angle of the lever was 131°, and the number of the pendulum plate bearings was four. At this time, the seeding qualification index of the hole seeder was 91.70%, the miss-seeding seeding index was 4.57%, and the reseeding index was 3.73%.

4.2. Bench Test Results

To verify the reliability of the hole-seeding device and verify the seeding performance of the hole-seeding device, a bench test was carried out on 10 June 2023, at the Institute of Dry Farming Equipment Experts of Gansu Agricultural University, as shown in Figure 18.

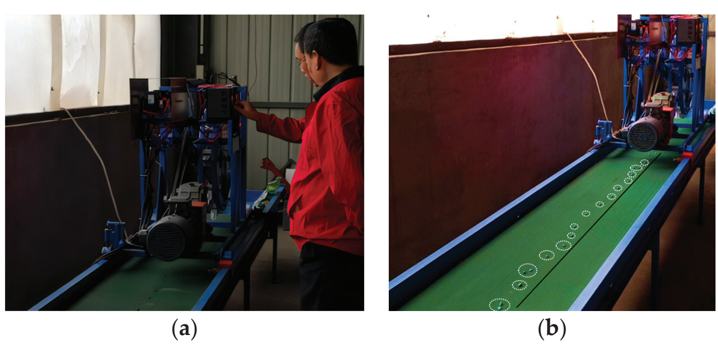

Figure 18. Bench test. (**a**) Diagram of the test bench operation and adjustment; (**b**) seedbed strip seeding maps.

The test was repeated three times, and the average value of 250 holes was counted continuously. The bench test results are presented in Table 7. The results indicate that when the speed of the hole seeder was 49 r/min, that is, the forward speed of the hole seeder was 5.76 km/h; the angle of the lever was 131 °; and the number of the pendulum bearing was four, the seeding qualification index was 90.53%, the miss-seeding seeding index was 5.60%, and the reseeding index was 3.87%.

4.3. Field Test Results

To investigate the field sowing performance of the pendulum-rod-type hole-sowing device, a field sowing test was carried out on 25 June 2023, in the experimental field of Taohe Tractor Manufacturing Co., Ltd., in Lintao County, Gansu Province. The experimental field was flat, north–south, and rectangular, and the soil was loessal soil. According to the agronomic technical requirements of whole-film mulching and double-ridge-furrow sowing, the surface was covered with film after ridging.

The corn planting variety was Jinsui No. 4, and the working power was 404 tractors with a power of 26.5 kW. The forward speed of the whole machine was stable at about 5.76 km/h, and the hole seeder was tested with the optimal working parameters. The unit forward was set to 50 m as the sampling length, referring to GB/T 6973-2005 "Test Methods for Single Grain (Precision) Seeders" [30] to determine the qualification index, miss-seeding seeding index, and reseeding index in the field test. The field sowing test results were averaged, and the field test results of the hole seeder were obtained. The qualification index was 89.13%, the miss-seeding seeding index was 5.46%, and the reseeding index was 6.41%. There was no obvious film tearing, film picking, or film hole dislocation during the test, as shown in Figure 19.

Figure 19. Field test.

5. Discussion

The simulation test results showed discrepancies compared to the indoor bench tests and field trials. The deviation in the qualification index in the simulation test from the bench test was 1.17% and that from the field test was 2.57%. The decrease in the qualification index, along with increases in the miss-seeding and reseeding indices, may be attributed to variations in the size and shape of corn kernels, leading to some holes in the seeding wheel accommodating two smaller kernels. Additionally, the vibrations from the field machinery may have caused larger kernels to fail to enter the seeding wheel holes, affecting the seeding process and slightly reducing the qualification index.

In an effort to enhance the performance of hole seeders, numerous scholars have conducted research on metering devices, proposing various structural designs and performance optimizations [32–34]. However, research on the seeding process of metering devices remains limited. The metering device selected for this study is a widely used mechanical planter with a simple structure [35]. Due to its limitations in high-speed operations, the qualification index decreased as the planter's performance diminished [36].

This was consistent with the significant increase in the miss-seeding index observed during simulation tests conducted at 80 r/min. Future research could focus on pneumatic seeders capable of accommodating higher speeds, aiming to mitigate the adverse effects caused by the seeding process of the hole-forming device during high-speed sowing.

6. Conclusions

1. We designed a pendulum plate and lever-type hole-seeding device, mainly composed of a fixed plate, a movable shaft, an electric actuator, a rotating disc, a connecting bracket, a fixed disc cover, a pendulum plate, a hole-former, and its structure. Bench testing of the hole seeder was conducted to meet different seed size requirements. By analyzing the working principle of the hole seeder, the structural parameters of the hole-forming device were optimized. A height-adjustment device suitable for hole seeders of different sizes was proposed and applied on an experimental bench. The device improved the operational performance of the hole seeder and reduced the rate of empty holes so as to achieve the purpose of improving operational efficiency and increasing production and income.
2. Utilizing Box–Behnken experimental design principles, we employed a three-factor, three-level response surface analysis method to conduct simulation experiments pf the seeding performance of the hole seeder under various combinations of operational parameters. With the aid of Design-Expert 12, we derived quadratic regression models for the qualification index, miss-seeding index, and reseeding index of the seeding process. We investigated the impact of the hole seeder's disc's rotational speed, the lever angle of the movable hole-former, and the number of bearings on the response values of these three indices. The optimal parameter combination identified was a rotating disc rotational speed of 49 r/min for the hole seeder (equating a forward speed of 5.76 km/h), a lever angle of 131° for the movable hole-former, and four bearings for the pendulum plate.
3. Under the optimal working parameters, field test results showed that the qualification index of the pendulum-lever-type hole seeder was 89.13%, the miss-seeding index was 5.46%, and the reseeding index was 6.41%. Compared to the simulation test, the relative errors of the qualification index, reseeding index, and miss-seeding index were 2.57%, 0.89%, and 2.68%, respectively. The small discrepancies between the actual results and the optimized values (<5%) demonstrate the reliability of the obtained working parameters of the pendulum-lever-type hole seeder.

Author Contributions: Conceptualization, F.D. and H.Z.; methodology, H.D. and H.P.; software, H.Z. and R.S.; validation, R.S., C.Z. and H.D.; formal analysis, H.Z. and H.P.; investigation, F.D.; resources, Q.Z. and H.D.; data curation, Q.Z. and C.Z.; writing—original draft preparation, F.D. and H.Z.; writing—review and editing, F.D. and R.S.; visualization, H.Z.; supervision, F.D.; project administration, C.Z.; funding acquisition, F.D. All authors have read and agreed to the published version of the manuscript.

Funding: This research was supported by Key Science and Technology Project of Gansu Province (23ZDNA008), National Natural Science Foundation of China (grant No. 52365029), Central Guide Local Science and Technology Development Fund Project (grant No. 23ZYQF305-1).

Institutional Review Board Statement: Not applicable.

Data Availability Statement: The data presented in this study are available on request from the authors.

Acknowledgments: The authors thank the editor for providing helpful suggestions for improving the quality of this manuscript.

Conflicts of Interest: The authors declare no conflicts of interest.

References

1. Dai, F.; Song, X.F.; Zhao, W.Y.; Sun, B.G.; Shi, R.J.; Zhang, Y. Numerical simulation and analysis of mechanized suppression process of seedbed with whole plastic film mulching on double ridges. *Int. J. Agric. Biol. Eng.* **2021**, *14*, 142–150. [CrossRef]
2. Dai, F.; Guo, W.; Song, X.; Shi, R.; Zhao, W.; Zhang, F. Design and field test of crosswise belt type whole plastic-film ridging-mulching corn seeder on double ridges. *Int. J. Agric. Biol. Eng.* **2019**, *12*, 88–96. [CrossRef]
3. Dai, F.; Zhao, W.Y.; Zhang, F.W.; Ma, H.J.; Xin, S.L.; Ma, M.Y. Research Progress Analysis of Furrow Sowing with Whole Plastic-film Mulching on Double Ridges Technology and Machine in Northwest Rainfed Area. *Trans. Chin. Soc. Agric. Mach.* **2019**, *50*, 1–16. [CrossRef]
4. Xie, J.H.; Zhang, R.Z.; Li, L.L.; Chai, Q.; Luo, Z.Z.; Cai, L.Q.; Qi, P. Effects of plastic film mulching patterns on maize grain yield, water use efficiency, and soil water balance in the farming system with one film used two years. *J. Appl. Ecol.* **2018**, *29*, 1935–1942. [CrossRef] [PubMed]
5. Zhao, W.Y.; Dai, F.; Yang, J.; Shi, Z.L.; Yang, Z.; Shi, L.R. Design and Experiment of direct insert precision hill-seeder with corn whole plastic-film mulching on double ridges. *Trans. Chin. Soc. Agric. Mach.* **2013**, *44*, 91–97. [CrossRef]
6. Dong, J.X.; Gao, X.J.; Zhang, S.L.; Liu, Y.; Chen, X.H.; Huang, Y.X. Design and Test of Maize Posture Control and Driving Precision Metering Device for High-speed Seeder. *Trans. Chin. Soc. Agric. Mach.* **2022**, *53*, 108–119. [CrossRef]
7. Gao, X.J.; Xie, G.F.; Li, J.; Shi, G.S.; Lai, Q.H.; Huang, Y.X. Design and validation of a centrifugal variable-diameter pneumatic high-speed precision seed-metering device for maize. *Biosyst. Eng.* **2023**, *227*, 161–181. [CrossRef]
8. Han, D. Optimization Simulation and Experimental Research of Inside Filling Air-Blowing Maize Precision Seed-Metering Device. Ph.D. Thesis, China Agricultural University, Beijing, China, 2018.
9. Zhang, C.; Xie, X.; Zheng, Z.; Wu, X.; Wang, W.; Chen, L. A Plant Unit Relates to Missing Seeding Detection and Reseeding for Maize Precision Seeding. *Agriculture* **2022**, *12*, 1634. [CrossRef]
10. Gao, X.J.; Cui, T.; Zhou, Z.Y.; Yu, Y.B.; Xu, Y.; Zhang, D.X.; Song, W. DEM study of particle motion in novel high-speed seed metering device. *Adv. Powder Technol.* **2021**, *32*, 1438–1449. [CrossRef]
11. Gao, X.J.; Zhao, P.F.; Li, J.; Xu, Y.; Huang, Y.X.; Wang, L. Design and Experiment of Quantitative Seed Feeding Wheel of Air-Assisted High-Speed Precision Seed Metering Device. *Agriculture* **2022**, *12*, 1951. [CrossRef]
12. Dong, J.X.; Gao, X.J.; Zhang, S.L.; Huang, Y.X.; Zhang, C.Q.; Shi, J.T. Design and Test of Guiding Seed Throwing Mechanism for Maize Posture Control and Driving Metering Device. *Trans. Chin. Soc. Agric. Mach.* **2023**, *54*, 25–34. [CrossRef]
13. Ma, J.; Sun, S.; Wang, J.; Hu, B.; Luo, X.; Xu, X. An Experimental Analysis of the Seed-Filling Mechanism of Maize-Precision Hole-Planter Clamping. *Agriculture* **2024**, *14*, 398. [CrossRef]
14. Wang, K.Y. Optimization Study of Self-Propelled Sunflower Coated Seeder Cavitator. Master's Thesis, Inner Mongolia Agricultural University, Hohhot, China, 2023.
15. Gu, L.L.; Zhang, W.Q.; Liu, M.J. The design and Experiment of the forced opening mechanism on the peanut dibbler. *J. Hunan Agric. Univ. (Nat. Sci.)* **2017**, *43*, 676–679. [CrossRef]
16. Adilet, S.; Zhao, J.; Sayakhat, N.; Chen, J.; Nikolay, Z.; Bu, L.; Sugirbayeva, Z.; Hu, G.; Marat, M.; Wang, Z. Calibration Strategy to Determine the Interaction Properties of Fertilizer Particles Using Two Laboratory Tests and DEM. *Agriculture* **2021**, *11*, 592. [CrossRef]
17. Gummer, A.; Sauer, B. Modeling planar slider-crank mechanisms with clearance joints in RecurDyn. *Multibody Syst. Dyn.* **2012**, *31*, 127–145. [CrossRef]
18. Liu, Q.F.; Chen, Y.; Liu, Y.; Wen, X.X.; Liao, Y.C. Coupling effects of plastic film mulching and urea types on water use efficiency and grain yield of maize in the Loess Plateau, China. *Soil Tillage Res.* **2016**, *157*, 1–10. [CrossRef]
19. Lu, H.D.; Xia, Z.Q.; Fu, Y.F.; Wang, Q.; Xue, J.Q.; Chu, J. Response of Soil Temperature, Moisture, and Spring Maize (*Zea mays* L.) Root/Shoot Growth to Different Mulching Materials in Semi-Arid Areas of Northwest China. *Agronomy* **2020**, *10*, 453. [CrossRef]
20. Wei, W.C.; Dai, F.; Zhang, F.W.; Zhang, S.L.; Shi, R.J.; Liu, Y.X. Numerical simulation on soil water-thermal effect under different film mulching methods of maize in the arid of North-west China. *Agric. Res. Arid Areas* **2020**, *38*, 13–21. [CrossRef]
21. Dai, F.; Gao, A.M.; Zhang, F.W.; Zhao, W.Y.; Han, Z.S.; Wang, S.L. Design and simulation of pneumatic direct insert hill-seeder with corn whole plastic film on double ridges. *Agric. Res. Arid Areas* **2018**, *36*, 284–289. [CrossRef]
22. Wang, G. Design and Test of Duckbill Seed-Metering Device for Rice Film Spreading and Hole Sowing Machine. Master's Thesis, Anhui Agricultural University, Hefei, China, 2023.
23. Shi, L.R.; Zhao, W.Y. Design and test of a rolling spoon type precision hole sower for caraway in northwest cold and arid agricultural region. *J. Jilin Univ. (Eng. Technol. Ed.)* **2023**, *53*, 2706–2717. [CrossRef]
24. Gu, L.L. Desing and Experimental Research on Peanut Dibbling Machine. Master's Thesis, Nanjing Agricultural University, Nanjing, China, 2019.
25. Li, H.; He, T.F.; Liu, H.; Shi, S.; Zhou, J.L.; Liu, X.C.; Wang, B.Q. Development of the profiling up-film transplanter for sweet potato in hilly and mountainous region. *Trans. Chin. Soc. Agric. Eng.* **2023**, *39*, 26–35. [CrossRef]
26. Qu, H.; Shi, L.R.; Xin, S.L.; Zhao, W.Y.; Guo, J.H.; Yang, T.; Liu, F.J. Design and experiment of flax precision hole-seeding combined operation machine with soil storage device. *J. Chin. Agric. Univ.* **2022**, *27*, 186–197. [CrossRef]
27. Shi, L.R.; Wu, J.M.; Sun, W.; Zhang, F.W.; Sun, B.G.; Liu, Q.W.; Zhao, W.Y. Simulation test for metering process of horizontal disc precision metering device based on discrete element method. *Trans. Chin. Soc. Agric. Eng.* **2014**, *30*, 40–48. [CrossRef]

28. Jin, X.N.; Zhang, J.C.; Xue, J.F.; Gou, C.C.; He, C.X.; Lu, L.Q. Calibration of Discrete Element Contact Parameters of Maize Seed and Rubber Belt. *J. Agric. Mach. Res.* **2022**, *44*, 39–43. [CrossRef]
29. Lu, B.; Ni, X.D.; Li, S.F.; Li, K.Z.; Qi, Q.Z. Simulation and Experimental Study of a Split High-Speed Precision Seeding System. *Agriculture* **2022**, *12*, 1037. [CrossRef]
30. *GB/T 6973-2005*; Testing Methods of Single Seed Drills. Standardization Administration of the P.R.C.: Beijing, China, 2005.
31. Zhang, B.; Chen, X.; Liang, R.; Wang, X.; Meng, H.; Kan, Z. Calibration and Test of Contact Parameters between Chopped Cotton Stalks Using Response Surface Methodology. *Agriculture* **2022**, *12*, 1851. [CrossRef]
32. Wang, J.; Yao, Z.; Xu, Y.; Guo, F.; Guan, R.; Li, H.; Tang, H.; Wang, Q. Mechanism Analysis and Experimental Verification of Side-Filled Rice Precision Hole Direct Seed-Metering Device Based on MBD-DEM Simulations. *Agriculture* **2024**, *14*, 184. [CrossRef]
33. Zhang, C.L.; Liu, T.; Zhang, Z.H.; Fang, J.; Xie, X.D.; Chen, L.Q. Design and test of the precision seeding dispenser with the staggered convex teeth for wheat sowing with wide seedling belt. *Trans. Chin. Soc. Agric. Eng.* **2024**, *40*, 47–59. [CrossRef]
34. Zhang, S.; He, H.L.; Yuan, Y.W.; Kuang, F.M.; Xiaog, W.; Li, Z.D.; Zhu, D.Q. Design and experiment of the orifice-groove combined hole of the oriented filling type precision hill-drop seed-metering device for rice. *Trans. Chin. Soc. Agric. Eng.* **2023**, *39*, 39–50. [CrossRef]
35. Yang, L.; Li, Z.M.; Zhang, D.X.; Li, C.; Cui, T.; He, X.T. Design and test of the T-shaped hole of centrifugal high-speed maize precision seed metering device. *Trans. Chin. Soc. Agric. Eng.* **2024**, *40*, 50–60. [CrossRef]
36. Gao, X.J.; Xu, Y.; Zhang, D.X.; Yang, L.; Lu, B.; Su, Y.; Xia, G.Y.; Cui, T. Design and experiment of air-assisted high speed precision maize seed metering device. *Trans. Chin. Soc. Agric. Eng.* **2019**, *35*, 9–20. [CrossRef]

MDPI AG
Grosspeteranlage 5
4052 Basel
Switzerland
Tel.: +41 61 683 77 34

Agriculture Editorial Office
E-mail: agriculture@mdpi.com
www.mdpi.com/journal/agriculture

Academic Open
Access Publishing

mdpi.com

ISBN 978-3-7258-3894-3